DISS. ETH. NO 26227

REMOTE SENSING ANALYSES OF SLOPE INSTABILITIES IN NORTHWESTERN BHUTAN

A thesis submitted to attain the degree of

DOCTOR OF SCIENCES of ETH ZURICH

(Dr. sc. ETH Zurich)

presented by

Benedetta Dini

MSc, UCL

Born on 9 March1983

Italian citizen

Accepted on the recommendation of:

Prof. Dr. Simon Löw, examiner

Dr. Andrea Manconi, co-examiner

Dr. Janusz Wasowski, external co-examiner

2020

Summary

Slope instabilities adversely affect mountainous regions by posing direct and indirect hazards. Landslides can evolve in catastrophic failures that can directly cause loss of lives, damage to properties and to critical infrastructure. Moreover, indirect effects can cause destruction of arable land and, in case of landslide damming of rivers, subsequent floods that can have an impact a long way downstream of the landslide site. A large-scale overview of unstable slopes in mountainous regions is therefore important in order to understand the spatial distribution, to investigate the activity, to create a basis for landslide hazard assessment and to further the science regarding the predisposing and controlling factors. Bhutan was chosen for this study given its relatively poor regional knowledge of unstable slopes, despite its proneness. The main purpose of our work is to understand the spatial distribution of past large rock slope movements in the region, to quantify the recent rates of displacements and to investigate the structural and geological controls. Given the inaccessibility of the region and the large scale of the study, we used remote sensing techniques through all stages of our investigations. In particular, a combination of optical images and high-resolution digital surface model analysis and synthetic aperture radar differential interferometric (DInSAR) techniques was used. The use of DInSAR allowed also to image, quantify and discern slope displacements that are related to soil slide/creep or rock glaciers creep, moreover, it allowed to illuminate areas with reversible displacements related either to freeze-thaw cycles in the permafrost region, or to groundwater table seasonal fluctuations at lower elevations. We produced some new datasets for the region including: 1) a regional rock slope instabilities inventory based on optical images, 2) a rock glaciers inventory based on optical images, 3) an active slope instabilities inventory based on the analysis of individual interferograms, 4) an inventory of active slope instabilities based on multi-temporal DInSAR analyses which includes gravitational and reversible deformation, 5) a regional structural inventory largely based on remote sensing mapping with the inclusion of some in-situ measurements.

We present the analysis of individual interferograms aimed at the identification of actively unstable slopes. We perform a geomorphological classification based on the landslide types and we propose a new method to assess the activity likelihood uniquely based on remote sensing techniques. This methodology is based on an articulated decision tree, which takes into account the number of sensors used for the analysis, the number of interferograms in which displacements are identified, the satellite orbit geometry, vegetation cover, geometrical distortions, estimated velocity and temporal coverage of the data. This method allows lowering or maintaining the confidence regarding the activity of each identified slope instability by analysing what would be the detection expectation. It maximises the

level of information retrievable from standard interferometric analyses and is new and applicable to other mountainous regions.

We use multi-temporal analyses based on SAR data to show the potential of the technique in identifying specific instabilities of which no previous knowledge existed. Here we show a methodology to combine a model-based atmospheric correction and an empirical correction to remove stratified, long wavelength signals from the cumulative displacement maps, without an atmospheric correction on the interferograms used to generate them. This method takes advantage of the local nature of slope processes leading to surface displacements to separate them from the long-wavelengths signals related to artifacts. This method allows to identify small-scale reversible displacements related with freeze-thaw cycles in the permafrost region and, moreover, it provides insights into the possibility of observing the dynamics of natural annual ground water table variations on valley flanks, which, had not yet been explored with multi-temporal satellite based InsAR analyses.

We show the analysis performed with the combination of our structural dataset and landslides dataset aimed at investigating predisposing factors to large rock slope instabilities in the region. The methodologies developed here involve the generation of a compound structural dataset that makes use of different sources of information. The latter include remotely mapped fault traces and planar valley flanks, but also some field measurements of foliation and faults. The methodology used to compile this dataset addresses the biases deriving from uneven sampling of the different data types across the area and allows to make the dataset more balanced for systematic kinematic analyses. We apply kinematic analyses across the structural domains identified in the study region in a probabilistic way, in order to investigate the regional structural control on large rock slope instabilities formation. These methodologies are also new, and applicable to other mountainous regions where remote sensing analyses are the main source of information.

We identify a structural and lithological control on rock slope instabilities across large parts of the study region. A higher predisposition to failure seems to be associated with the presence of specific sets of regional faults and foliation structures. The average orientation of one of such fault sets corresponds to the orientation of the Lingshi fault, a major known structure in the northwest of the region. Moreover, there seems to be a lithological control both on past rock slide activity and on more recent activity in association with shales, quartzite and limestone belonging to the Tethyan sediments and found in the northwest of the region.

The analysis by means of DInSAR of rock slope activity in the recent past (our observation window is between 2006 and 2011) shows that the majority of active rock slope instabilities identified have rates which correspond to the slow to very slow categories, with maximum displacement rates of up to 160 mm/year, with only very few exceptions.

These findings, combined with the field observations of a large number of past rock slide deposits, covered by thick soils, point to the fact that active unstable rock slopes are less abundant in the region in recent times than in the past. We postulate that this may be related to the lack in recent times of major earthquakes that could have previously caused widespread landslide activity at a given point in time. We have also observed that rock glaciers in northwestern Bhutan creep downslope with velocities that are on the whole lower than what has been observed in the Alps in recent years. This could be due to either a less pronounced recent warming trend than at higher latitudes or to less water being available to penetrate into the frozen unconsolidated material supersaturated with interstitial ice and to deeper subsurface shear horizons.

Riassunto

Le instabilità di versante sono fonte di pericolosità causando danni diretti e indiretti nelle zone di montagna. Alcuni tipi di frane possono evolvere in maniera catrastrofica, causando la perdita di vite umane e animali, danni alle proprietà private e a infrastrutture critiche. Inoltre, possono causare effetti indiretti quali la distruzione di terreni agricoli o la chiusura di una valle e conseguenti alluvioni con impatti molto più a valle. Una visione d'insieme di fenomeni di instabilità in zone montagnose è quindi fondamentale per capirne la distribuzione spaziale, per investigarne l'attività, per creare una base per la valutazione di pericolosità e per avanzare le conoscenze scientifiche per quanto riguarda i fattori di controllo e predisposizione. Il Bhutan è stato scelto come area di studio per questa tesi a causa della scarsa conoscenza regionale sui fenomeni franosi e di versante, nonostante l'elevata propensione. Lo scopo principale di questo lavoro è quello di comprendere la distribuzione spaziale di grandi frane in pendii rocciosi, di quantificarne i tassi di movimento recenti e di investigare i controlli sulla distribuzione imposti da fattori strutturali e geologici. L'inaccessibilità e la vastità della regione hanno determinato la scelta di utilizzare techniche satellitari per le varie fasi dell'investigazione. In particolare, è stata utilizzata una combinazione dell'analisi di immagini ottiche e modelli digitali del terreno ad alta risoluzione e di techniche di interferometria radar (DInSAR, Synthetic Aperture Radar Differential Interferometry). L'utilizzo della technica DInSAR ha permesso di identificare, quantificare e discernere movimenti di versante causati da scivolamenti in suolo o di ghiacciai rocciosi (rock glaciers), ha permesso di identificare movimenti reversibili associati o a cicli di gelo e disgelo nelle zone di permafrost o a variazioni della falda idrica di sotto della linea di permafrost. Sono stati prodotti nuovi dataset per l'area di studio, tra cui: 1) un inventario regionale di fenomeni di instabilità in pendii in roccia basato su immagini ottiche, 2) un inventario di ghiacciai rocciosi basato su immagini ottiche, 3) un inventario di instabilità di versante attive basato sull'analisi di interferogrammi singoli, 4) un

inventario di instabilità di versante attive basato su un'analisi di interferometria radar multi-temporale che include fenomeni di versante gravitazionali e reversibili, 5) un inventario regionale delle strutture, basato quasi interamente su una mappatura da satellite con l'inclusione di alcuni dati di terreno. In questo lavoro presentiamo un'analisi di interferogrammi singoli con lo scopo di identificare fenomeni attivi. Viene fatta una classificazione geomorfologica basata sulle tipologie di frane e viene proposta una nuova metolologia per valutare la probabilità di attività basata unicamente su analisi satellitari. Questa metodologia sfrutta un albero decisionale che tiene in conto del numero di sensori utilizzati, del numero di interferogrammi in cui viene identificato uno spostamento, della geometria dell'orbita satellitare, della vegetazione, delle distorsioni geometriche, della stima di velocità e della copertura temporale dei dati. Questo metodo consente di alzare o abbassare il livello di confidenza a riguardo dell'attività di ogni instabilità identificata analizzando l'aspettativa di identificazione. Questa metodologia massimizza il livello di informazione che può essere ottenuto da analisi interferometriche standard, è nuova e può essere applicata a altre regioni montuose. Utilizziamo anche analisi interferometriche multi-temporali per mostrare il potenziale della tecnica nell'identificazione di instabilità precedentemente sconosciute. Mostriamo una nuova metodologia per combinare una correzione atmosferica basata su modelli atmosferici e una correzione empirica al fine di rimuovere gli effetti dell'atmosfera stratificata e segnali a grande lunghezza d'onda senza precedentemente correggere gli interferogrammi utilizzati per l'analisi. Questo metodo utilizza la natura localizzata dei processi di versante che causano movimenti superficiali e li separa dai segnali a grande lunghezza d'onda (quali gli effetti atmosferici, o artefatti di processamento). Questo metodo quindi consente di identificare fenomeni alla scala del versante che causano spostamenti reversibili associati a cicli di gelo e disgelo, inoltre, offre una nuova prospettiva per l'identificazione dei cicli annuali associati a variazioni della falda idrica finora non osservati con l'interferometria radar. Mostriamo l'analisi basata sulla combinazione dei dati strutturali con i dati delle instabilità, al fine di investigare i fattori di predisposizione per grandi frane in versanti in roccia. Le metodologie qui sviluppate includono la generazione di un complesso inventario strutturale che utilizza sorgenti di informazione diverse. Queste ultime includono tracce di faglia mappate con tecniche satellitari, versanti rettilinei, ma anche misure sul terreno di foliazione e faglie. Il metodo di compilazione di quest'ultimo dataset cerca di affrontare il problema generato da bias che derivano da un campionamento disomogeneo dei vari tipi di dato. In questo modo, il dataset ottenuto è adeguato all'utilizzo nelle analisi cinematiche. Le analisi cinematiche vengono svolte per tutta l'area, suddivisa in settori strutturali, in modo probabilistico, per investigare il controllo strutturale a scala regionale sulla distribuzione di frane in roccia. Anche le metodologie relative a questa fase del lavoro sono nuove e applicabili ad altre zone montuose dove informazioni satellitari sono la principale fonte di infomazione. Viene identificato un controllo

strutturale e litologico sulla distribuzione dell grandi frane in roccia identificate per la gran parte dell’area. Un’altra predisposizione al franamento sembra essere associata con la presenza di specifici sets di strutture (faglie o foliazione). L’orientazione media di uno di questi sets corrisponde all’orientazione della Linghi Fault, una grande struttura nel nordovest della regione. Inoltre, viene rilevato un controllo litologico su fenomeni passati e fenomeni recentemente attivi, questi spesso associati a argilliti, quarziti e calcari appartenenti ai sedimenti della Tetide, affioranti per lo più nel nordovest della regione. L’analisi multi-temporale fatta con l’interferometria radar (periodo d’osservazione 2006-2011) mostra che la maggior parte di instabilità attive in pendii rocciosi hanno velocità di spostamento che corrispondono alle categorie di frane lente o molto lente, con velocità massime di 160 mm/year, con rare eccezioni. Questi risultati, in combinazione con l’osservazione di un grande numero di antichi depositi di frana ricoperti da cospicui strati di suolo, indicano nella regione un minor livello di attività recente rispetto al passato. Ipotizziamo che questo possa essere relazionato con la mancanza in tempi recenti di terremoti ad alta magnitudo che possono invece aver causato un’estesa attività franosa in passato. Osserviamo anche che i ghiacciai rocciosi nel nordovest del Bhutan si muovono con velocità che sono in generale meno elevate di quelle identificate per i ghiacciai rocciosi alpini. Questo potrebbe essere collegato a un riscaldamento meno pronunciato rispetto a latitudini più alte oppure dalla minore disponibilità di acqua che possa infiltrare nel materiale inconsolidato sovrassaturato con ghiaccio interstiziale e negli strati più profondi dove avviene lo scorrimento.

Acknowledgements

This research was funded by an ETH grant (ETH-38 15-2) and an ESA Alcantara project (ESA 4000117652/16/F/MOS). During this research, we benefited from the interaction with numerous partners and government departments representatives in Bhutan, among them we would like to mention the College of Natural Resources of the Royal University of Bhutan, particularly in the person of Jigme Thinley, Helvetas, Walo, the National Land Commission, the Department of Disaster Management, the Department of Hydrology, the Department of Roads, the National Soil Science and the Department of Geology and Mines of the Royal Government of Bhutan.

I would like to take the opportunity to thank scientists that I have had the pleasure and luck to meet during this project and who have given me food for thoughts, ideas and encouragement, in particular Djordje Grujic, Wilfried Haeberli and György Hetényi.

Kerry Leith has substantially contributed to writing the successful ETH proposal for this project and has often engaged in fruitful discussions that broadened the context of the research. Kerry Leith and Larissa de Palezieux were also very precious presences during the two field campaigns.

I am very grateful and obliged to Paolo Riccardi, who has supported me with an everlasting friendly attitude during my InSAR processing, definitively going the extra mile.

Thanks of course to Simon Loew for bringing me on board for this project that was so close to his heart and for providing a source of fresh input every time I had something to show. In a cold tent at 4000 m, with Larissa and Kerry, when 7 pm seemed like midnight, but the prospect of a cold sleeping bag wasn’t any more appealing than the dim light of the dinner tent getting fainter by the minute, a game of “Cheat” made Simon call my name almost at every hand. Do Italians have such a bad reputation at card games? I hope that, in time, I have won his trust.

Andrea Manconi has been fundamental not only in this research but in general for my time at ETH. I am grateful to him for keeping me on track, for being always open and patient, for his calm attitude. I may have represented a challenge at times, like “a bomb with a short fuse”, but I hope he knows that I always meant well, that I cherish his opinion and friendship and that I wish our paths will cross again.

Jordan Aaron arrived in the group at the right moment for me, and supported me a great deal through the final phases. I owe so much to his clarity of thoughts, the grace in making suggestions, the positive and constructive criticism and the kindness in formulating them and the willingness to take active part in the work, making him a most precious co-author.

There are always detractors in life, but if for any of them there is someone who believes in your skills and good faith, then things will turn out to be ok. I owe much in the way of helping me keep my motivation through hard times to the timeless Igor Villa who represents the most exquisite and unique combination of wisdom and funniness and who has been there for me at all important turns in my

career, to Chris Kilburn so delightfully Italian in his Britishness who has always believed in me as a researcher and who since the beginning of our friendship taught me to continue to do “my own thing” even when everyone else around me is doing something else, to Eddy Carroll, one of the most clever people I have ever met, who has given me the incentive to leave my interesting, rewarding, permanent and well paid job as a Deputy Chief Meteorologist at the UK Met Office in search of something new and has turned out to be, together with the unmatched Fiona, a much cherished friend.

I have been lucky to find on my new path Georgie Bennett and Aldina Franco, two wonderful women and curious scientists with whom I pride myself to be working with now. Without their support, sensitivity and open mind, the final stages of this thesis would have been extremely difficult.

I should also mention here that a few special friends, old and recent, have helped me a lot through the whole process, being always willing to lend me an ear or give a hug, during many, repetitive rants. These are the eternal Valentina, so far on Earth but so close to my heart, Oli for being always present, Gionata, the best thing that came out of that course we know, and the beautiful Franzi, Larissa and Martin, with whom I enjoyed many coffee breaks, lunches, field work and chats that will always be blissful memories of my time at ETH.

My parents and brother have always been on my side, since I can remember, allowing me the highest possible level of freedom in all of my choices, never complaining about the difficulties I have created for us all through such choices. It is also thanks to them that I have found the courage four years ago to leave something certain to step into the uncertain. My grandad used to tell me, in moments of stress, that a live donkey is better than a dead doctor. Though, whilst I write these words, I cannot yet be sure of the outcome, I wish I could tell him that this is as close as I have ever been to being a doctor. And I am still alive.

I also owe a lot to my partner in life and science, Simon Daout, a brilliant mind and a sensitive heart, with whom I have made and undone the work that went into one of the chapters of this thesis an infinite amount of times. I know I have put your patience to the hardest test, but thanks for listening to all my doubts and thus for allowing us to make things better and better. Thank you for reminding me that I was doing ok, for supporting me and taking care of me also when things got difficult.

But the most special, heartfelt thanks go to my gang, for offering me an extra staggering 16 legs to walk with me through sunshine and rain. You were there always, with your unwavering, unfaltering love and friendship, you were there in all moments when everyone else failed. You listened to all my presentations many times over and every time you looked at me as if you wanted to say: “that was awesome!”. Thanks for teaching me in your humble, sincere, unassuming, faithful, loyal way what friendship is, for being the living examples of strength, patience and tenacity, for being ready to jump up at any “ok let’s go!” and for never making me feel alone. I hope you have forgiven me for all the hours, the minutes that I didn’t spend in your precious company and for all those that you had to watch me at the computer. You were, are and always will be my four-legged rocks with a tail.

Table of contents

Table of figures

Table of tables

1. Introduction

1.1. Context and motivation

When this study was initially undertaken, knowledge regarding the distribution, type and activity of slope instabilities at the regional scale across Bhutan was very limited and fragmentary. The main reason for this dearth of information on unstable slopes is to be found in the inaccessibility of the country, caused by a number of factors. Bhutan is characterised by a variety of landscapes and climatic conditions, ranging from dense forest with tropical climate in the south, to the high mountain region with alpine climate in the north. Topographic gradients are also extreme, with elevations ranging from 100 m to more than 7000 m a.s.l. over a distance of approximately 150 km from the southern to the northern border. Such environmental characteristics, coupled with a basic infrastructure and a long period of political isolationism have made Bhutan historically less studied than neighbouring countries or than countries with similar characteristics.

Regional knowledge of unstable slopes is essential to improve predictive capabilities regarding landslide occurrence in mountainous areas and to establish methods to protect vulnerable communities and a growing infrastructure in developing countries. Moreover, the understanding of controlling factors that affect spatial and temporal distribution of landslides cannot be furthered unless a regional picture of past, recent and ongoing landslides is obtained. Aside from the irreversible deformation caused by landslides in mountainous regions, which may lead to catastrophic failure thus posing direct and indirect hazards, a number of other processes are responsible for displacements on slopes. These include reversible processes that act at depth, either in relation to freeze-thaw cycles in the permafrost region or to seasonal changes in the hydrological conditions at lower elevations. The understanding of such processes is important because multi-annual displacements variations can be used as proxies for climatic changes, and it is also relevant with respect to land use strategies and the development of infrastructure that may susceptible to millimetric, seasonal, reversible deformation.

The choice of a hazard prone, developing country is also relevant in the context of capacity building and knowledge transfer, in order to improve the ability of local communities to monitor their landscape and make informed choices. The need for in depth investigation of slope instabilities has recently come to the fore in Bhutan, where efforts are being made in developing the infrastructure network. Aside from an expanding and vulnerable road network, the demand for hydropower development has led to the planning of several new large hydropower projects, some key ones currently being under construction. Such projects are often associated with significant risk, as large incipient rock slope instabilities provide favorable valley geometries for dam construction (narrow valleys with large, broad catchments upstream). However, when these instabilities are not recognised during the planning and design phases, they can pose significant challenges during reservoir construction and operation and can potentially amplify future landslide hazards in the region.

Recent advances in remote sensing techniques, in particular Synthetic Aperture Radar Differential Interferometry (DInSAR) and time series analysis, open the possibility for relatively inexpensive, large-scale investigations. A regional study case in a challenging environment such as northwestern Bhutan allows demonstrating the full potential of DInSAR for slopes information retrieval, provided suitable expertise. Setting this study in the High Himalaya of northwestern Bhutan thus offers the opportunity to realise a unique combination of societal, regional geological, and fundamental scientific outcomes.

1.2. Research questions and objectives

In this work we aim at performing a regional exploration of unstable slopes across northwestern Bhutan, largely based on remote sensing techniques. We also strive to extract the maximum amount of information from the technique applied (DInSAR), by developing new methods for the usage of the obtained results and for the assessment of their reliability. We use DInSAR in different ways, coupled with geomorphological analyses, in order to identify, quantify and classify different processes acting at the slope scale. We also aim at adding a significant contribution to scientific knowledge regarding processes conditioning large rock slope movements in formerly glaciated mountain belts.
Our main research questions are the following:

I. What is the spatial distribution of past large rock slope movements in the Himalaya of northwestern Bhutan?
II. What are present-day rates of rock slope displacement in DInSAR in northwestern Bhutan?
III. Can we identify and quantify by means of DInSAR both gravitational and irreversible deformation related to large rock slope instabilities and reversible displacements occurring within and below the permafrost region?
IV. How does the observed slope instability distribution relate the lithological, structural and (neo)tectonic pre-disposition?

1.3. Tasks and methods

This project is largely based on remote sensing data, including high resolution optical imagery (GoogleEarth), a high-resolution digital surface model (DSM, ALOS World3d, 5 m horizontal resolution), and satellite-based radar images acquired by different sensors (ESA ENVISAT and Sentinel-

1, JAXA ALOS-1 and ALOS-2). The abundance of radar images over northwestern parts of Bhutan, as well as land cover and presence of populated areas, is a critical factor for the choice of the study area. The choice of the satellites is related in part to availability, given the free access to ESA satellites data and access through proposal to JAXA satellites data. Moreover, a combination of C-band and L-band allows to maximise information retrieval of slower displacements (C-band) and displacements in non-barren areas (L-band). Sentinel-1 data is used for a particular case, showing the increased performance of this recently launched satellite thanks to an increased control over the orbital paths and more frequent repeat pass.

The core tasks of this study include the regional scale mapping of large bedrock landslides in the High Himalaya of Bhutan, the development of methodologies to describe such landslides from satellite data, and the determination of key factors controlling their spatial distribution and activity.

Unstable slopes with active displacements in the period 2006-2011 are mapped through the use of DInSAR, involving the generation of a large number of differential interferograms. Successively, surface velocity maps and displacement time series are generated with the Small Baseline Subset method (SBAS).

Additionally, attention is given to the identification of seasonal, reversible displacements occurring on slopes in mountainous regions, with the aim of discerning between possible underpinning processes. A methodology for extracting slope scale information regarding reversible displacements is thus investigated. In this phase, we show how a regional scale analysis can be performed to extract local slope displacements signal, after removing large scale artifacts in the velocity maps. Among the main limitations to consider for the application of DInSAR techniques in the study area are the high topographic gradients and the related atmospheric phase screen which may introduce consistent artifacts in the results. To mitigate this issue, we use a high resolution DSM instead of more standard, freely available products such as the SRTM (90m) DEM within the DInSAR processing steps. We then introduce post-processing corrections of the stratified delays based on the ERA-Interim (ECMWF) atmospheric model and we explore empirical corrections of long-wavelength artefacts due to orbital errors during the pre-processing or residual stratified delays in the interferometric phase.

Large rock slope instabilities, soil creep and soil slides are mapped through the analysis of optical images and with the use of geomorphological descriptors. A large inventory of past rock slope deformations is produced, including the mapping of instability phenomena and geomorphological and structural features that are indicators of instability. An inventory of rock glaciers in the glaciarised parts of the region is also generated during this phase. The high resolution DMS is used in conjunction with optical images in order to improve the descriptions of landslide geomorphological features.

Finally, a methodology, again almost completely based on remote sensing, is developed to investigate at the large scale lithological and structural controls of the observed rock slope instability distribution. This includes the generation of a large, new dataset of fault traces and possible fault planes obtained through mapping based on the high resolution DSM and GoogleEarth images. Such dataset is then augmented with data derived from previous studies and from own field mapping. This dataset is successively analysed in conjunction with the instability dataset previously generated.

The flow chart in figure 1-1 describes the research questions as well as the tasks and steps to answer them.

1.4. Thesis structure and chapters

This work is organised in four chapters, each of them submitted or planned to be submitted for publication in international scientific journals. This paragraph briefly outlines the rationale of each chapter.

1.4.1. Investigation of slope instabilities in NW Bhutan as derived from systematic DInSAR analyses

In the second chapter of this thesis we aim at identifying in northwestern Bhutan unstable slopes that showed signs of activity between 2006 and 2011. This is done by means of DInSAR and the generation of a large number of differential interferograms obtained with images acquired by ENVISAT and ALOS-1. The 521 interferograms are analysed individually to obtain a picture of active displacements during the observation period. A geomorphological classification is developed to discern between different types of landslides (ranging from mountain slope instabilities, rock slope instabilities, soil slide to soil creep) and to identify a large number of active rock glaciers. Moreover, an articulated decision tree quantifies the reliability of the classification results, by assigning a likelihood to each instability in the inventory in terms of the likelihood of an unstable slope of actually being one, rather than the result of a processing artifact. The regional scale mapping of landslides provides an important first picture of the distribution of unstable slopes, particularly of active rock slope instabilities across the region. The data produced here is very important to establish a basis for futureregional landslide hazard assessment. Moreover, the observed spatial distribution of instabilities can be put in relation with other aspects, such as the presence of large regional faults or the distribution of permafrost.

1.4.2. The Punatsangchhu landslide illuminated by satellite based DInSAR time series

In the third chapter we focus on one particular case, the Punatsangchhu rock slope instability. As mentioned above, in recent years considerable efforts are being made in Bhutan in order to put in place several large hydropower projects. The production of hydropower electricity in Bhutan corresponds to roughly 25% of the country's GDP, with the electricity produced being sold to neighbouring, power-thirsty India. One of such projects is the Punatsangchhu-I hydropower plant, located in the Punakha valley. Excavation and construction works at this site began in February 2009. Insufficient geological investigations in the planning and design phases of the hydropower project allowed for an active unstable slope to go unnoticed. Since excavation began, several difficulties were encountered. The undercutting of the toe and the presence of broken rock prevented the successful emplacement of the dam's right abutment. A series of minor failures led to a catastrophic failure in July 2013, when 1 million m3 of rock (Punatsangchhu Hydroelectric Project Authority (PHPA) estimate) collapsed on the construction site. Since then, excavation and construction halted in favour of stabilisation measurements, leading to significant extra costs and large delays in the delivery of the project. A retrospective DInSAR analysis reveals the importance and the potential of using such technology in the early phase of project design and planning to promptly identify and such geological hazards. Moreover, it allows the assessment of the actual size of the instability and of the evolution of current displacements rates.

1.4.3. Classification of slope processes based on multitemporal DInSAR analyses in the Himalaya of NW Bhutan

In the fourth chapter we aim at quantifying the activity of unstable slopes, by generating velocity maps and time series of displacements at the large scale. Images acquired by ENVISAT and ALOS-1 are processed with the SBAS method. The quantification of creep velocities is performed for the same landslide types identified in chapter 2 (mountain slope and rock slope instabilities, soil slide, soil creep) and rock glaciers. Moreover, we show how DInSAR multitemporal analyses can be used to identify, over a large region, reversible deformation occurring at the slope scale that is either related to freeze-thaw cycles in the permafrost region or to ground water table variations below it. An atmospheric correction based on the ERA-Interim reanalysis data and an empirical correction that allows to reduce long wavelength effects correlated with topography at the scale of the entire frame are applied. The spatial extent of the analysis highlights regional patterns of displacement rates, which will potentially also allow the investigation of the effects of climatic variability in the permafrost region.

1.4.4. Regional scale investigation of preconditioning factors of rock slope instabilities in NW Bhutan

In the fifth chapter we show our last inventory, based on optical images and the ALOS World3D high resolution DSM, in which a large number of identified mountain slope or rock slope instabilities are contained. We also present a structural dataset which allows to investigate the structural control of landslide distribution in NW Bhutan. The data are collected from multiple sources: rock slopes instabilities, fault traces and fault planes derived from satellite optical imagery and the ALOS World3D high resolution DSM were complemented by data from other studies. The study illustrates a new methodology to approach such complex datasets. This approach is based on the combination of the datasets including instabilities and structural information aimed at investigating the structural control on landslide distribution at the regional scale. Investigations of structural controls are carried out by means of kinematic analyses over the entire study area. We also analysed the potential for lithological control, on the basis of a geological map of Bhutan generated in a previous study.

The analysis reveals a structural and lithological control on rock slope instabilities across large parts of the study region. This work is, once again, an example of how large-scale studies of this kind can be carried out largely on the basis of remote sensing data, thus overcoming the problem of inaccessibility of the study region.

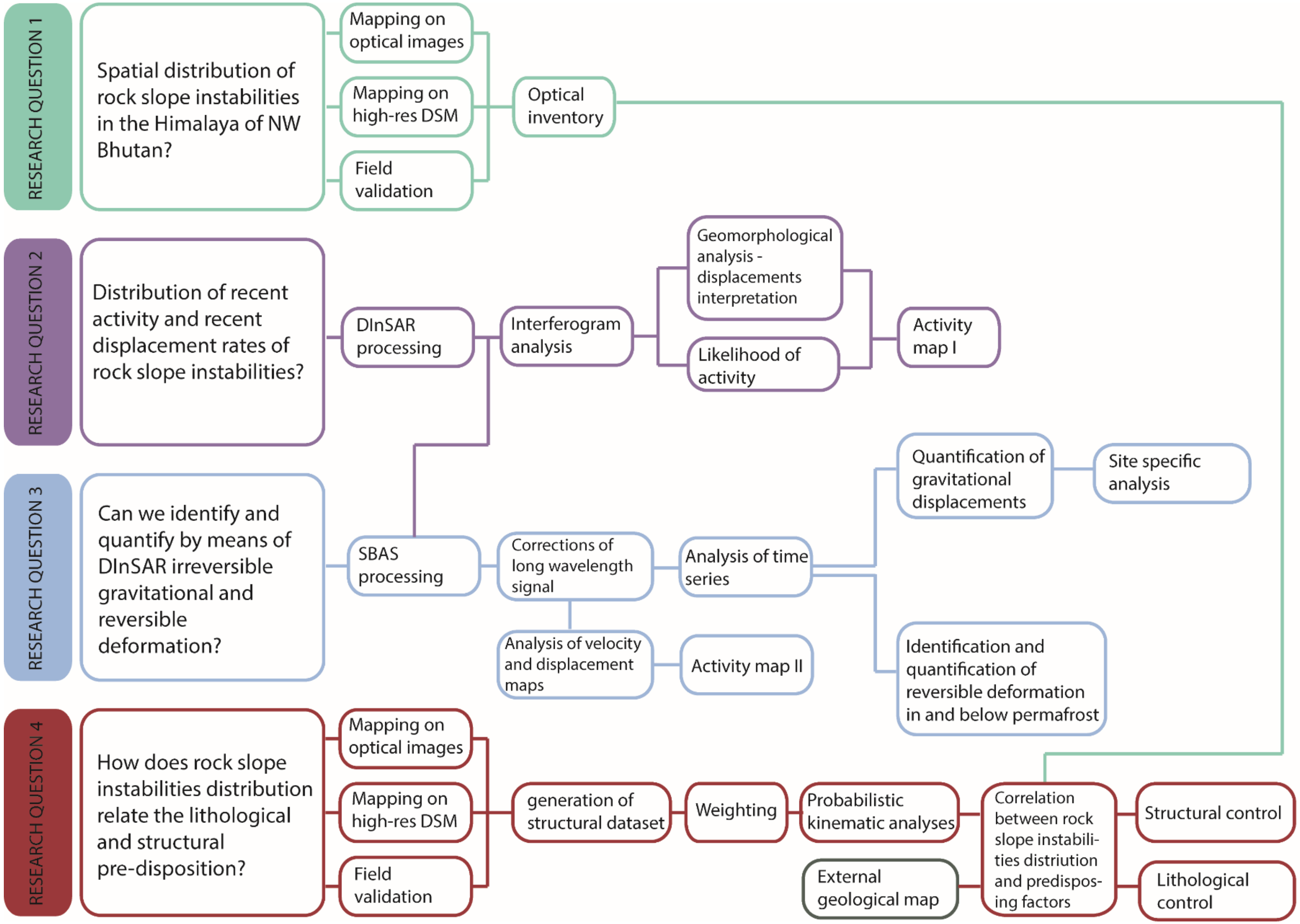

Fig. 1-1. PhD structure

2. Investigation of slope instabilities in NW Bhutan as derived from systematic DInSAR analyses

Benedetta Dini[1], Andrea Manconi[1], Simon Loew[1]

[1] Department of Earth Sciences, ETH Zurich, Zurich, Switzerland

Abstract

In this work we present a methodology based on remote sensing data to map and classify unstable slopes in high alpine areas and apply this methodology to the Himalaya of northwestern Bhutan. We leverage on radar images acquired by the ESA Envisat and the JAXA ALOS-1 satellites between 2007 and 2011. Synthetic aperture radar differential interferometry (DInSAR) is used to identify and quantify recent ground surface displacements associated with potentially unstable slopes. Optical satellite images and a high-resolution digital surface model is used for the geomorphological classification of individual landforms and deposits associated with displacements. The analysis of the geomorphological characteristics reveals that displacements are associated with: rock slides, mountain slope deformation and rock slope deformation (77.5%), soil creep (4%), soil slides (1.9%) and rock glaciers (12.3%); 4.3% of the detected displacements remain of unknown origin. The method applied here for the assessment of activity likelihood uses a very large number of interferograms obtained with images acquired by different satellites. The method, which is new and replicable, takes advantage of the combination of different acquisition geometries and then combines indices of vegetation cover, layover, velocity estimate and temporal sampling associated with each detected active area to assign a weight. The analysis shows that a cluster of unstable slopes exists in the northwest, potentially related to the presence of an important regional lineament and the distribution of permafrost. Comparatively little ongoing activity is detected in the south, but field validation documents substantial landslide activity in the recent geological past. The dataset here generated, containing 700 potentially unstable areas with an associated activity likelihood, is a novel dataset that makes an essential basis of future analysis to investigate rock slope instability distribution and predisposing factors. Moreover, this dataset represents a new important step towards future landslide hazard assessment in the Himalaya of Bhutan.

2.1. Introduction

Reliable inventories of active rockslides, rock slope and mountain slope deformations, rock glaciers, talus and slope debris are critical for regional hazard and risk evaluations in alpine countries (Frattini et al., 2018; Strozzi et al., 2013; Petley, 2012; Kääb et al., 2005b; Wiesmann et al., 2001). A shared characteristic of different types of slope instabilities is ground surface displacement, intended throughout this work as any gravitational movement occurring on a slope. The identification and monitoring of surface displacements are important in order to understand the underlying kinematic behaviour and mechanisms of gravitational slope processes (Cignetti et al., 2016; Huggel et al., 2012; Stoffel and Huggel, 2012; Crozier, 2010; Kääb et al., 2005a). Visual interpretation of aerial images and of high-resolution digital elevation models is a classical approach for the identification and mapping of slope instabilities. This approach is particularly convenient when investigating large and inaccessible mountainous regions (Guzzetti et al., 2012). Despite intrinsic limitations associated with the spatial resolution of the available data, the temporal coverage of the images, and a degree of subjectivity, visual interpretation is widely used to study landforms as deep-seated gravitational slope deformations, rockslides and rock glaciers (Ambrosi et al., 2017; Crosta, 2013; Guzzetti, 2012; Lilleøren and Erzelmüller, 2011; Ambrosi and Strozzi, 2008; Van Westen C.J., 2006). On the other hand, this method provides only a qualitative or semi-quantitative picture of the current activity associated with the mapped phenomena. Instead, surface displacements can be quantified with different methods, ranging from standard in situ sensors (Mazzanti and Pezzetti, 2013) to ground-based, air- and spaceborne remote sensing (Wasowski and Bovenga, 2014). Among remote sensing methods, satellite based synthetic aperture radar differential interferometry (DInSAR) has been increasingly explored and successfully applied to identify and monitor different types of slope deformation (Wasowski and Bovenga, 2014; Colesanti and Wasowski, 2006; Massonnet and Feigl, 1998). DInSAR allows to accurately measure small variations on the Earth surface topography of the order of a cm or less, along the line of sight (LOS) of the satellite, with higher sensitivity to vertical deformation (Wasowski and Bovenga, 2014; Bovenga et al., 2013; Ferretti et al., 2007; Casu et al., 2006). This technique has several advantages, including the capability to cover large areas as well as the increasing data availability (Nagler et al., 2016; Aschbacher and Milagro-Pérez, 2012). Moreover, compared to other techniques DInSAR does not need for in situ installations and is thus convenient to monitor surface displacement in inaccessible and/or remote areas.

In the last two decades, advanced DInSAR methods have been proposed by various authors to process multitemporal SAR acquisitions and generate average velocity maps and surface displacement time series. The most widely used approaches to combine multitemporal SAR acquisitions are Persistent Scatterers interferometry (PS, Ferretti et al., 2001(Werner et al., 2003) and Small Baseline Subset

(Berardino et al., 2002; Ferretti et al., 2001). Obtainable accuracies are in general of the order of 1-2 mm/year for annual velocities and 5-10 mm for displacement (Catani et al., 2014; Wasowski and Bovenga, 2014; Meisina et al., 2008; Casu et al., 2006). In mountainous terrain, standard and advanced DInSAR techniques have been often exploited for detection and inventorying of slope instabilities (Delaloye et al., 2010; Delaloye et al., 2008; Lambiel et al., 2008; Meisina et al., 2008; Delaloye et al., 2007), for the interpretation and quantification of various types of surface displacements (Cignetti et al., 2016; Plank et al., 2012; Colesanti and Wasowski, 2006; Catani et al., 2005; Kenyi and Kaufmann, 2003; Massonnet and Feigl, 1998) and for the identification the geomorphological processes leading to the observed displacements (Strozzi et al., 2010; Lambiel et al., 2008).

As far as slope instabilities are concerned, DInSAR techniques work better for the detection of large phenomena (the extent of which is considerably higher than the pixel resolution used) showing slow displacements (Frattini et al., 2018; Hölbling et al., 2012; Strozzi et al., 2010; Strozzi et al., 2005). Such phenomena would fall within the very slow to slow categories ((Hungr, 2014), with displacements between 16 mm per year up to 1.6 m per year. This is due to intrinsic limitations associated to the SAR phase, namely spatial and/or temporal phase aliasing, when surface displacements are characterised by sharp spatial gradients and/or very rapid evolution (Manconi et al., 2018). However, DInSAR has been also successfully applied to phenomena implying relatively large and/or rapid displacements, as for example rock glaciers, by considering high-resolution SAR imagery and/or pairs with short temporal baselines (Strozzi et al., 2004).

In this paper we present a DInSAR based methodology for the creation of regional scale slope instabilities inventories in alpine settings and we apply it to the Himalaya of northwestern Bhutan. The dearth of available data on active slopes in northwestern Bhutan hinders the understanding of processes responsible for ground displacements in the region and prevents future regional landslide hazard assessments. The extent as well as the largely inaccessible nature of the study area have hindered the development of background knowledge on geology, structural geology, landslides and natural hazard and make both photointerpretation DInSAR among the better suited techniques to fill the existing gap.

The first slope instability inventory generated for the Himalaya of northwestern Bhutan proposed here provides a basis to investigate orogen-scale processes controlling mass wasting activity and landslide hazards in the Himalayas and other high alpine regions.

The primary goals of this paper are to present a method to assess the likelihood of activity based on the analysis of DInSAR data and to show a new regional data base of active slopes in the Himalaya of northwestern Bhutan which relies almost entirely on EO data. The inventory was obtained by maximizing the extraction of information in a way that would result as objective as possible, through the addition of a methodology that focuses on how to use the DInSAR results in an engineering geological context. The detailed analyses of the factors controlling slope instabilities distributions and hazards in the Himalaya of Bhutan will be the focus of subsequent papers.

In the following, we first describe the geographic, geologic and climatic conditions in the study area (chapter 2). We show the criteria used for mapping and for classifying slope instabilities and we explain the method used to generate the activity likelihood map (chapter 3). We then present in chapter 4 the inventory of different types of slope instabilities obtained through the analysis of differential interferograms and we show the spatial occurrence and frequency of the different objects mapped. Finally, in chapter 5 we illustrate and discuss processes identified as responsible for the observed displacements.

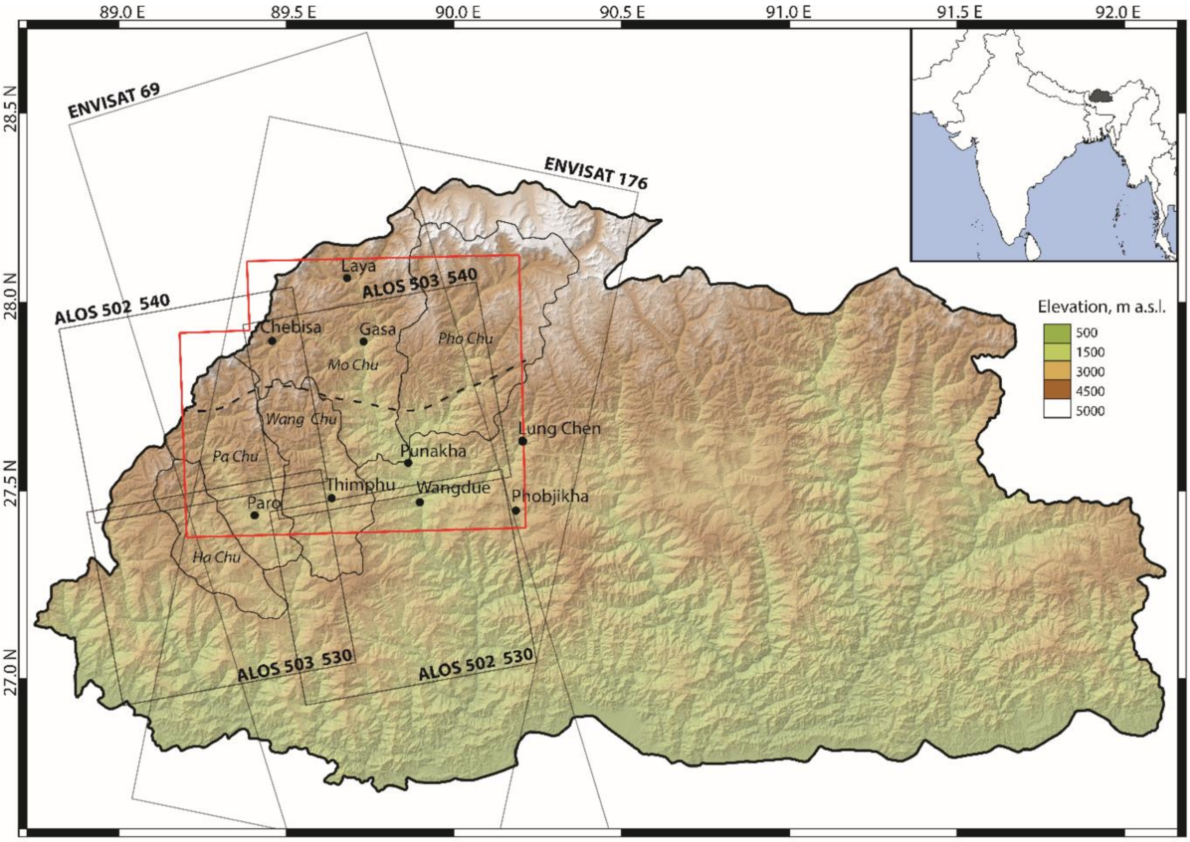

Fig. 2-1. Geographical setting of Bhutan, with area of study within red polygon. Black rectangles represent the satellite footprints of the SAR tracks and frames used for interferometric processing. Black lines are catchments in the study area, modified after Gurung et al. (2011).

2.2. Area of study

2.2.1. Geographic setting and choice of study area

The small kingdom of Bhutan, nested between Tibet and India, roughly between 26N and 28N and 88E and 92E (Figure 2-1), is characterised by a unique variability of landscapes and climatic zones. The elevation ranges from just over 1000 m a.s.l. in the far southeast of the region to over 7000 m a.s.l., over a north south extent of only 90 km approximately, bringing about extreme topographic gradients (Dunning et al., 2009; Dunning et al., 2006). The study area covers around 7550 km2 (Fig. 2-1), stretching from the northern border to Thimphu in the south, and from the western border to Phobjikha in the east. The north of the study area is characterised by the high peaks of the Higher Himalaya, with average elevations of 4400 m a.s.l., whilst in the south the ranges have average elevations of 2800 m a.s.l. and are separated by mainly north-south oriented valleys (Norbu, 2003). The choice of the study area is to 1) include a variety of landscapes, geological and geographical settings (from high mountain regions to more populated areas), 2) avoid the completely forested southern regions that are not suitable for investigations with DInSAR and 3) take advantage of the relatively higher availability of SAR data.

2.2.2. Geological setting

From a geological point of view, our study region spans Lesser Himalayan and Greater Himalayan rocks (Molnar, 1984). In the south Lesser Himalayan rocks are separated from the structurally higher Greater Himalaya by the Main Central Thrust (MCT). In the north of the region, the South Tibetan detachment system separates Tethyan Himalayan strata from the structurally lower crystalline sheets of the Greater Himalaya (Gansser, 1983). The study area lies almost entirely within the crystalline rocks of the Greater Himalaya, largely composed of orthogneiss, paragneiss, quartzite, schists of Precambrian and early Paleozoic ages and Miocene leucogranitic intrusions (Long et al., 2011; McQuarrie et al., 2008); (Gansser, 1983). Tethyan sediments of different ages (Paleozoic to Eocene) are found in the northwest of the region, largely comprised of limestones, shales and sandstones. These cover roughly 24% of our study region and are found mostly north of 27.5° N and west of 89.6° E, in the Lingshi area, and in the far southeast in the Dang-Chu Klippe (Long et al., 2011). In the Paro area, Lesser Himalayan rocks exposed within the Paro window are largely composed of quarzites and schists (Neoproterozoic to Ordovician). Other important structures, found all along the Himalayan arc, are the Main Boundary Thrust (MBT) and the Main Frontal Thrust (MFT). These thrusts are found along the southern border of Bhutan, thus outside of our study region. However, these structures are related to the Main Himalayan Thrust (MHT), a basal décollement separating the orogen from the basement, with some authors indicating that the MFT is a ramp of the MHT (Diehl et al., 2017). An important regional lineament striking NE-SW is found in the northwest of the region, the Lingshi Fault (Antolín et al., 2012; Long et al., 2011; Gansser, 1983). The LF accommodates sinistral slip associated with the clockwise rotation of the southeastern parts of the Tibetan plateau and presents as well a normal component, with upthrow of the northwestern block.

The Quaternary history of the Bhutan Himalaya is not as well-known as that of other Himalayan countries (Iwata et al., 2002), due to the lack of quantitative dating. Recently glaciated valleys (Last Glacial Maximum (LGM) and later re-advances) in our study region are not found at elevations lower than 3000 m a.s.l.. Below these elevations, valleys present V-shaped cross section, typical of fluvial incision. Between 3000 m a.s.l. and 3700 m a.s.l., only badly preserved remnants of moraines, largely destroyed by glacial lake outburst floods, obliterated by landslides or completely reworked by erosion during present uplift, are observed sporadically (Gansser, 1983). Above 3700 m a.s.l. impressive moraine systems are clearly visible, likely associated with LGM (Iwata et al., 2002), rising up to around 300 m and 500 m from the valley bottom. Above 4000 m a.s.l. late LGM, early Holocene, late Holocene and Little Ice Age moraines are observed (Iwata et al., 2002).

Catchment		Place/ area	Elevation, m a.s.l.	Precipitation, mm/year	Mean annual snow cover (area %)	Snowfall onset	Snowfall peak	Snowmelt onset	Snowmelt ends
Northwest	Ha Chu	Haa	2700	1227	15	Sep-Oct	Jan	Mid-Jan	Apr
	Pa Chu	Paro	2200	1800					
	Wang Chu	Thimphu	2500	1600					
Northeast	Mo Chu	Laya	3900	450	45	Sep	Feb	Feb	end May
		Chebisa	3800	500					
		Gasa	2400	1000					
	Pho Chu							end Feb	end May

Table 2-1. Rainfall and precipitation data for catchments and some locations in the area of study. Sources: Gurung et al. (2011), www.climate-data.org, www.worldweatheronline.com.

2.2.3. Climate

The geographical setting of Bhutan is associated with large precipitation variations, both spatial as well as seasonal. The Higher Himalaya is characterised by a relatively dry, continental, alpine climate, with annual precipitation as low as 400 mm, cool summers and severe winters (Banerjee and Bandopadhyah, 2016; ICIMOD, 2016; Dunning et al., 2009). Precipitation falls as snow in winter but in summer snow falls only at higher elevations, with the perennial snowfields found at 5000 m a.s.l. and above. Most of the annual precipitation falls during the monsoon season between May and October, with the wettest months being July and August.

The middle ranges lie under a temperate climate, with cool winters and hot summers and receive between 1000 and 2000 mm of annual rainfall (Banerjee and Bandopadhyah, 2016; ICIMOD, 2016; Bookhagen and Burbank, 2009). Rainfall and snowfall data for the catchments and some locations in the study area are shown in Table 1.

2.3. Data and methods

To detect and map active slope instabilities in the area of study, we integrated the information of SAR imagery acquired from different sensors, a high-resolution Digital Surface Model and high-resolution satellite optical imagery. We used data acquired by the ESA Envisat satellite in ascending and descending orbits and by the JAXA ALOS-1 satellite in ascending orbit. The acquisition parameters, geometry, number of images and spatial and temporal coverage of the data used for the analysis are summarised in table 2. Aside for Envisat track 176, for which an average revisit time of 50 days over a period of 3 years 4 months is available, the rest of the used tracks are not very populated.

Only a handful of images are available for the ascending Envisat track 69, whilst the four ALOS-1 frames have each between 15 and 18 acquisitions over a period of between 3 years 9 months or 4 years depending on the track. The digital surface model (DSM) available, ALOS World 3D, has ground sample distance (GSD) of 5m and vertical accuracy of 5 m (JAXA, 2017). This has been used for both DInSAR processing as well as morphological interpretations of the retrieved displacement for its higher resolution and accuracy in comparison with other available DSM (SRTM 30m, ASTER 30m and Tandem-X 12m). Finally, high-resolution optical images from Google Earth were extensively used to classify the phenomena associated with displacements, as it will be explained in the following sections.

2.3.1. DInSAR analysis and activity likelihood

The methodology followed for this study is outlined in its main points in the flowchart in figure 2-2. We start by generating interferograms with a broad range of temporal baselines, the longest varying between 700 and 1500 days for ALOS-1 and 400 and 600 days for Envisat. Instead, the maximum perpendicular baselines are constrained to 45% of the critical baselines, i.e. around 300 m for Envisat 176, 600 m for Envisat 69 and 3500 m for ALOS-1. The phase is then analysed for 521 interferograms distributed across the 6 frames for the identification of objects compatible with surface displacements occurring on slopes using a visual procedure. Layover and shadow masks are calculated for each geometry and incidence angle (appendix 2-1) and attention is paid to avoid artefacts related to

Satellite/ sensor	Band	Incidence angle	Track/ frame	Orbit type	Images number	Period	Interf. number	% winter images	Temporal sampling (days)
Envisat ASAR	C	~23°	176	D	25	20070415-20100822	105	40	49
Envisat ASAR	C	~23°	69	A	9	20050820-20090516	24	66	152
ALOS 1 PALSAR	L	~34°	502/530	A	18	20070201-20110212	81	55	82
ALOS 1 PALSAR	L	~34°	502/540	A	18	20070201-20110212	115	55	82
ALOS 1 PALSAR	L	~34°	503/530	A	15	20070218-20110301	105	66	98
ALOS 1 PALSAR	L	~34°	503/540	A	15	20070218-20102911	91	66	98

Table 2-2. Data used for interferometric processing.

geometric distortion, topographic residuals or atmospheric effects. Examples of the mapped potential slope instabilities can be seen in figure 2-3.

Phase gradients (in radians) allow to establish clear boundaries between potentially stable and unstable areas. The visual analysis of interferograms, although time consuming, is crucial to maximise the detection of unstable slopes (Przyłucka et al., 2015) that can be lost applying more advanced multitemporal approaches due, for example, to phase decorrelation. However, the identification of displacements in a single interferogram does not directly lead to the conclusion that a slope is unstable during the entire observation time. Indeed, displacements related to an unstable slope can be detected or not in one interferogram depending on: (1) exposition of the valley flank with respect to sensor line-of-sight (layover/shadowing), (2) presence of vegetation and its changes over time, 3) displacement rates and sensor’s wavelength, 4) effects of snow cover (and its variations) between considered pairs. In our investigation, we aim at identifying processes associated with a relatively long period of activity. Thus, to increase the confidence on our analysis, we adopt a weighting system based on an articulated decision tree, yet straightforward in concept, that takes into account (1) the number of interferograms in which displacement over a potentially unstable slope is identified, then (2) if in the same area displacements are detected by more than one sensor, (3) if the displacements are detected with different satellite orbits (ascending/descending). Figure 2-4 shows an example of a landslide that was observed in 33 different interferograms, this contributing to the high likelihood of

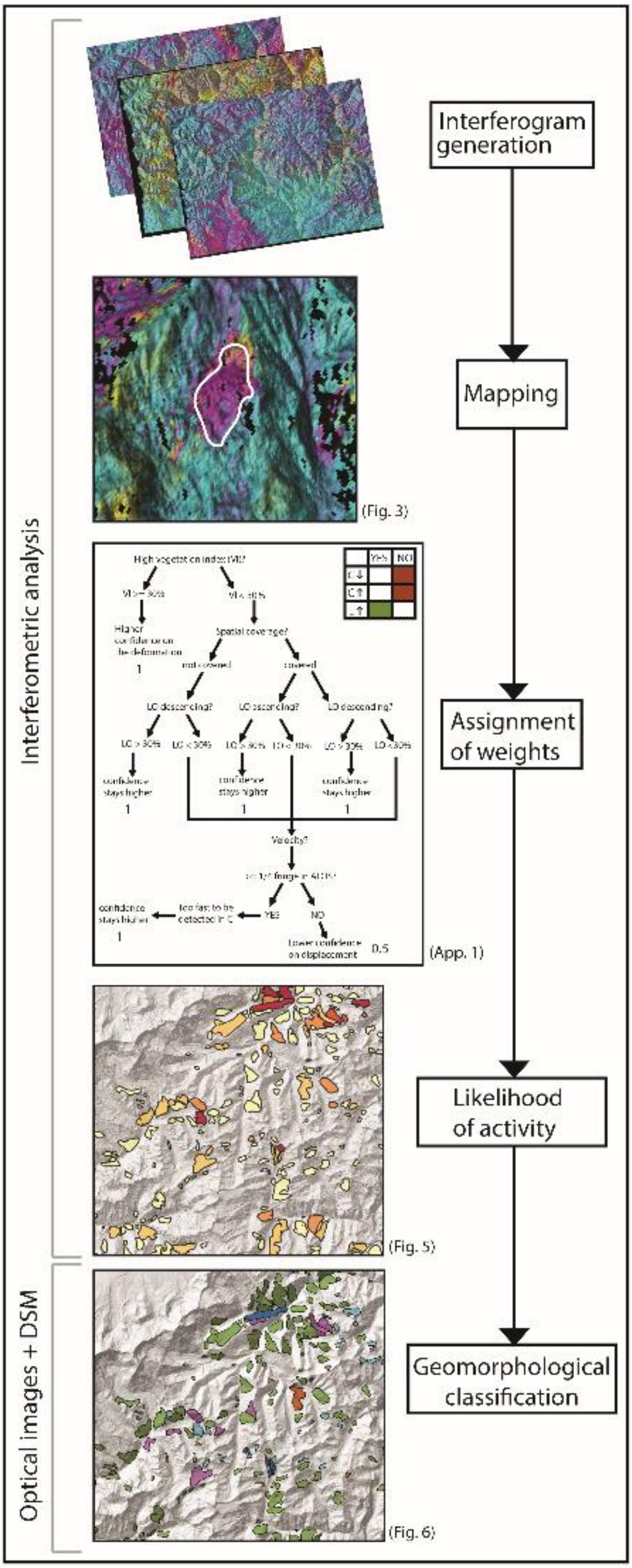

Fig. 2-2. Steps of the analysis.

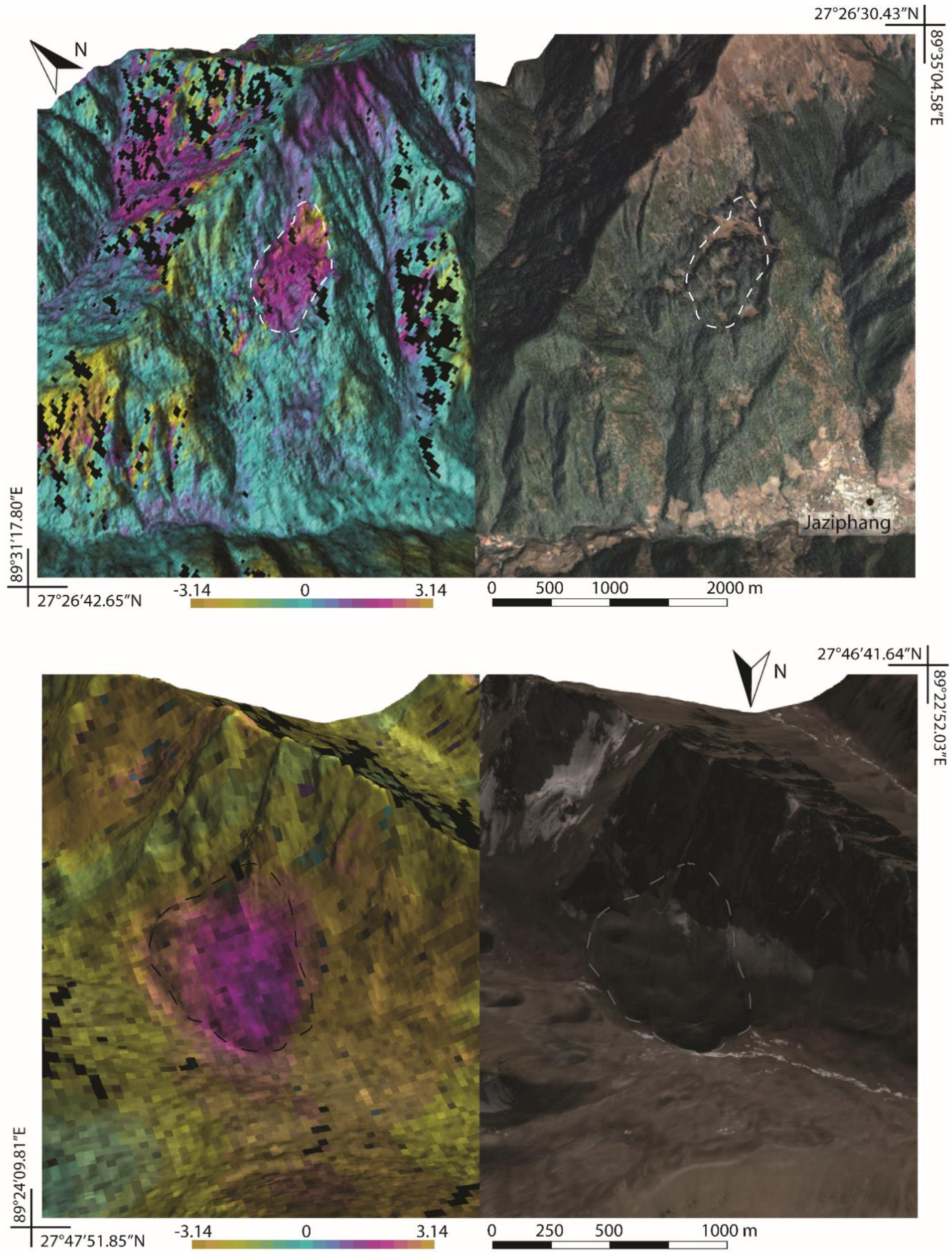

Fig. 2-3. Two examples of objects mapped on single wrapped interferograms. At the top, a rockslide is observed. In the white dashed area the mapped active object, which occupies a small portion of the landslide. The interferogram obtained with ALOS acquisitions covers the period 20080807-20091011 (~14 months) and it indicates a displacement corresponding to roughly a third of the phase cycle (≈3.9 cm). Layover areas with typical bright bands are also visible, with black pixels representing layover mask calculated on SRTM (30m). Atmospheric effect following topography are also present away from the landslide. Below, displacement is identified on a rock glacier. In the dashed lines the mapped active object. In this case two Envisat acquisitions were used, covering the period 20070624-20070729 (~1 month). The wrapped interferogram indicates a displacement corresponding to roughly between 1/2 and 4/5 of the phase cycle (≈1.4 to 2.2 cm).

activity related to the unstable slope. Overlapping polygons, as mapped on different interferograms, are then used to define one polygon for a given unstable slope. The highest the count of observations of the displacement areas occurring at the same slope location in different interferograms, the highest the likelihood on the activity. The applied weighting factor assigns to each potential slope instability a relative level of confidence and allows the comparison between different sensors. We multiply the count (recurrence of displacements over the same slope, as shown in figure 2-4) by a weight which is assigned to every possible combination of sensors and acquisition geometry: 1) ALOS, 2) Envisat descending, 3) Envisat ascending, 4) ALOS and Envisat descending, 5) ALOS and Envisat ascending, 6) Envisat ascending and Envisat descending 7) Envisat descending, Envisat ascending and ALOS ascending. The lowest weight was assigned to combinations 1, 2 and 3 (single track), the intermediate weight to combinations 4, 5 and 6 (at least two tracks) and the maximum weight to combination 7 which includes all tracks. In order to take into account important factors such as layover, effects of land cover and displacement detectability thresholds the weights are refined through a decision tree and shown in detail in appendix 2-2. Layover indices (considering ascending and descending geometries) and vegetation index are calculated for all potentially unstable slopes. The decision tree allows lowering or maintaining the confidence regarding the activity of each identified slope instability by analysing what would be the expectation of observing it also in tracks in which it was not observed. Confidence is considered to be lower in those cases for which the various calculated indices show a relatively high expectation to observe a slope instability with a given sensor/geometry, but this is actually not observed. For example, if displacements over the same unstable slope are observed a number of times in interferograms obtained with ALOS, layover effects for Envisat ascending can be ignored (same geometry) but the vegetation index in the area has to be taken into account. In our decision tree, if more than 30% of the area is vegetated, it can be assumed that the reason for which a given instability is not observed with Envisat is decorrelation due to vegetation cover.

In this case, confidence on the activity does not get lowered. This is because the high vegetation index makes the expectation of detection with Envisat low. The same reasoning is applied to all combinations and parameters. It is difficult to quantitatively take into account the fact that, in comparison with Envisat track 176 and all ALOS frames, the ascending track of Envisat (69) has a much poorer temporal sampling and the highest percentage of winter images (November to April). This may induce to think that the expectation of observing with Envisat track 69 the same instabilities as those observed with the other tracks should be indeed in general low. Following this reasoning, the fact that an instability observed with ALOS or Envisat 176 but not with Envisat 69 does not necessarily imply a lower confidence on the activity, due to the poorer temporal sampling and high percentage of winter images which may decrease the chances of detecting it.

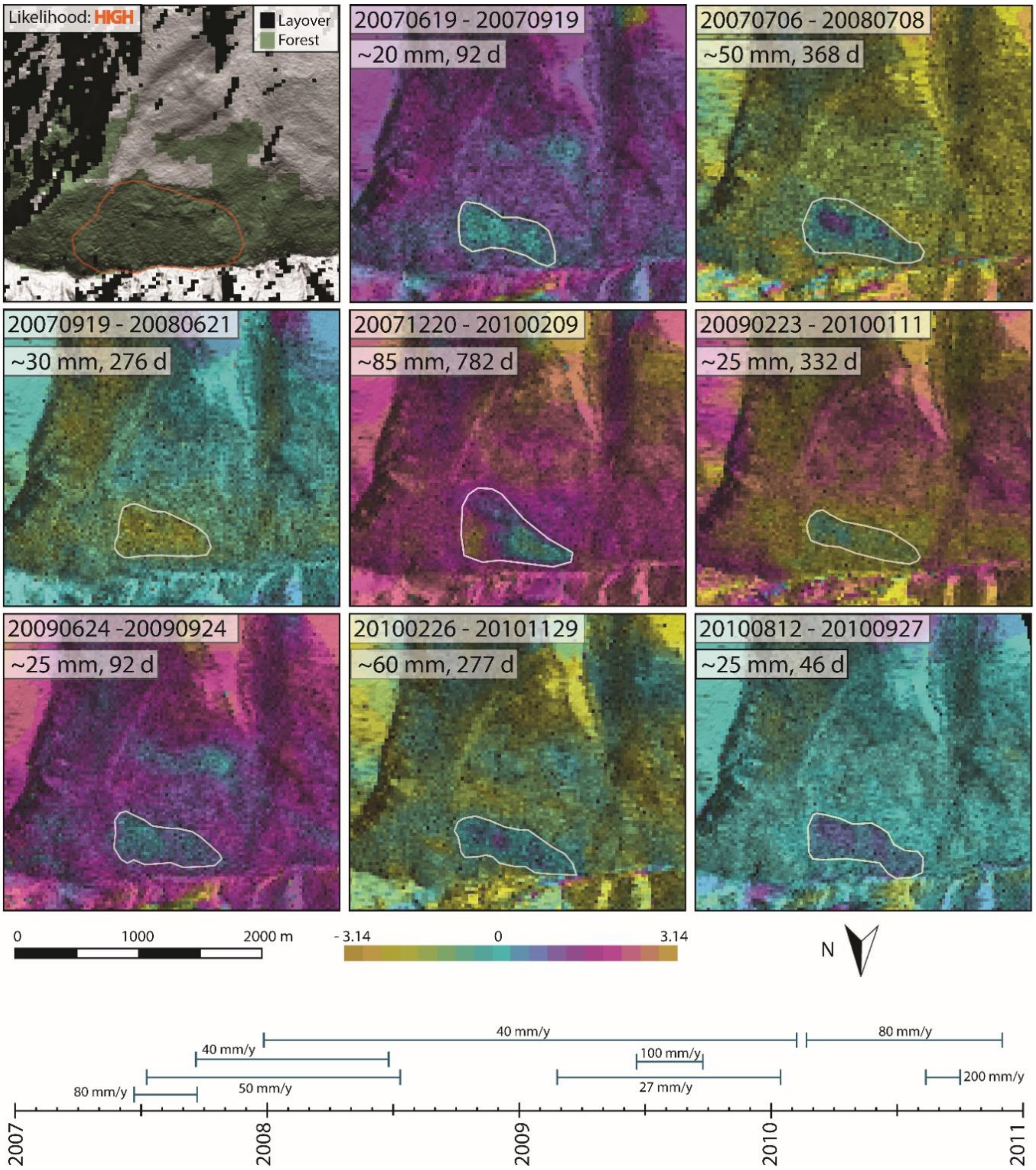

Fig. 2-4. An example of active area is shown here. The top left panel shows the forest cover in green, the layover mask in black and the final polygon with its associated likelihood level. The likelihood level is primarily based on the count of the number of interferograms in which the same object is observed. Here, 8 interferograms of ALOS-1 tracks 502 and 503 and frame 540 are shown. These are a selection of 33 interferograms in which the object within the white polygons was observed. An estimate of the displacement was made based on the fraction of fringe observed in the gradients. Some of these interferograms show also a likely tropospheric artifacts affecting the lower portion of the slope following a pattern parallel to elevation and that leave the deformation gradient largely unaffected. Another area of deformation can be seen (20070619-20070919 and 20090624–20090924), although its more sporadic occurrence corresponds to a lower activity likelihood level. A timeline of the shown interferograms is also presented, with estimated mean annual velocities for comparison.

2.3.2. Morphological classification based on optical imagery and DSM analysis

After the identification of potential slope instabilities on the interferograms, we investigate available high-resolution optical imagery (Google Earth) and the high resolution ALOS DSM. This step is crucial to assign a plausible type to each mapped slope instability. The classification presented strives to include rock slope instabilities, landforms (moraines, rock glaciers) and deposits affected by surface displacements (talus cones, debris mantled slopes). In order to homogenise the classification as much as possible, considerations regarding the material involved and their origin are made as shown in table 3.

Material ► Descriptor ▼		ROCK	COLLUVIUM (or residual soil)	DILUVIUM	ICE/ROCK
MORPHOLOGY	SLOPE INSTABILITY	Rock slope instability			
	LANDFORM		Debris cone	Moraine	Rock glacier
	DEPOSIT		Debris mantled slope		
LANDSLIDE TYPE (Hungr et al., 2014)		Rock slide Rock slope deformation Mountain slope deformation	Soil creep	Soil slide Soil creep	-

Table 2-3. Descriptors and slope materials, leading to the final classification.

Five classes of either landslide type (following the classification of Hungr et al., 2014), unstable slope debris or talus deposits, or active landforms (i.e. rock glaciers) were thus defined:
a) rock slides, rock slope deformations and mountain slope deformations, b) soil creep, c) soil slide or soil creep, d) rock glacier, with the addition of e) unknown type.
Potentially unstable slopes were assigned to the different classes on the basis of the following criteria:

a) Depending on the type of slope instability, different morphological phenomena prevail on ground surface. Large mountain slope deformations are deep seated landslides affecting rock slopes at the scale of an entire valley flank which are characterised by scarps, trenches, grabens and double ridges in the upper parts of the slope and bulging toes and secondary slope failures at the valley bottom (Agliardi et al., 2009; Ambrosi and Crosta, 2006). They often form a concave-convex profile from crest to slope toe and contain linear depressions parallel or oblique to the slope strike. Morphological features of rock slides and rock slope deformations are in general more difficult to detect. Tensional cracks of the order of tens of centimetres are too small to be detected in the high-resolution DSM available, but occasionally may be visible in the optical images on bare rock slopes not covered by dense vegetation. Rock fall activity (Rosser et al., 2007) as well as channels affected by debris flows (Gschwind and Loew, 2016) can also be indicators of rock slides.

b) The coarse clastic material composing talus cones gives repose angles between 30° and 40° (Migoń et al., 2010; Carson, 1977). A distinctive fan like shape, as well as the presence of large blocks are often clear in the optical images. Profiles usually show a slope angle change, reflecting the steep cliffs from which the material originates and the deposits below. Debris mantled slopes are deposits of loose, finer material. The presence of such deposits is normally associated with muted morphologies and topographic profiles appear often very linear, from crest to valley floor. The optical images show frequent changes in colour and texture across the slope indicating small and superficial soil slips. Both talus cones and debris mantled slopes are largely composed of colluvium and the nature of the surface displacements observed on them can be defined according to Hungr et al. (2014) as soil creep.

c) Occasionally, elongated surface displacements have been observed to follow moraine ridges. The displacements observed in the interferograms are either decorrelated patches within an area of good coherence, or small phase fractions of smooth gradients. These displacements are in all cases seen in association with the presence of moraine ridges and/or extending downslopes to their flanks. In general, ground displacements on moraines could be either associated with permafrost degradation, variations in the ice core thickness in the moraine itself or slumping or sliding of the moraine sediments. In this study, we have been able to link surface displacements on these landforms with either soil creep of loose sediments or deeper soil slides (see section 2.5).

d) Rock glaciers are tongue-shaped structures with flow lobes composed of perennially frozen unconsolidated debris. Rock glaciers move as the ice contained in them, either in the form of lenses or filling spaces between clasts, deforms under the action of gravity (Gärtner-Roer and Nyenhuis, 2010). Alpine rock glaciers are found near the lower limit of discontinuous permafrost, with temperatures around 0° C (Delaloye et al., 2010) and generally move with velocities comprised between a few cm/y to 1 m/y (Cignetti et al., 2016; Gärtner-Roer and Nyenhuis, 2010; Haeberli, 1985). Typical characteristics are blocky texture, lobes, furrows and, in the most active cases, steep sides and front (Cignetti et al., 2016; Roer et al., 2008), whilst inactive rock glaciers tend to be covered by turf (if not vegetation), have less pronounced fronts and are characterised by gentler slopes (Martin and Whalley, 1987). Though rock glaciers can be affected by rock fall activity and landslides, we did not observe such phenomenon and the displacements observed are directly related to rock glacier creep through gravitational processes. For this reason, in our classification rock glaciers maintain a class on their own. This class is associated with the landform and not with a landslide type as defined by Hungr et al. (2014).

e) The unknown category is a collection of displacements for which no distinctive cause or property could be provided. This includes areas at the valley bottom, which show patterns of localised activity, and no clear signs for specific phenomena were found in the optical imagery.

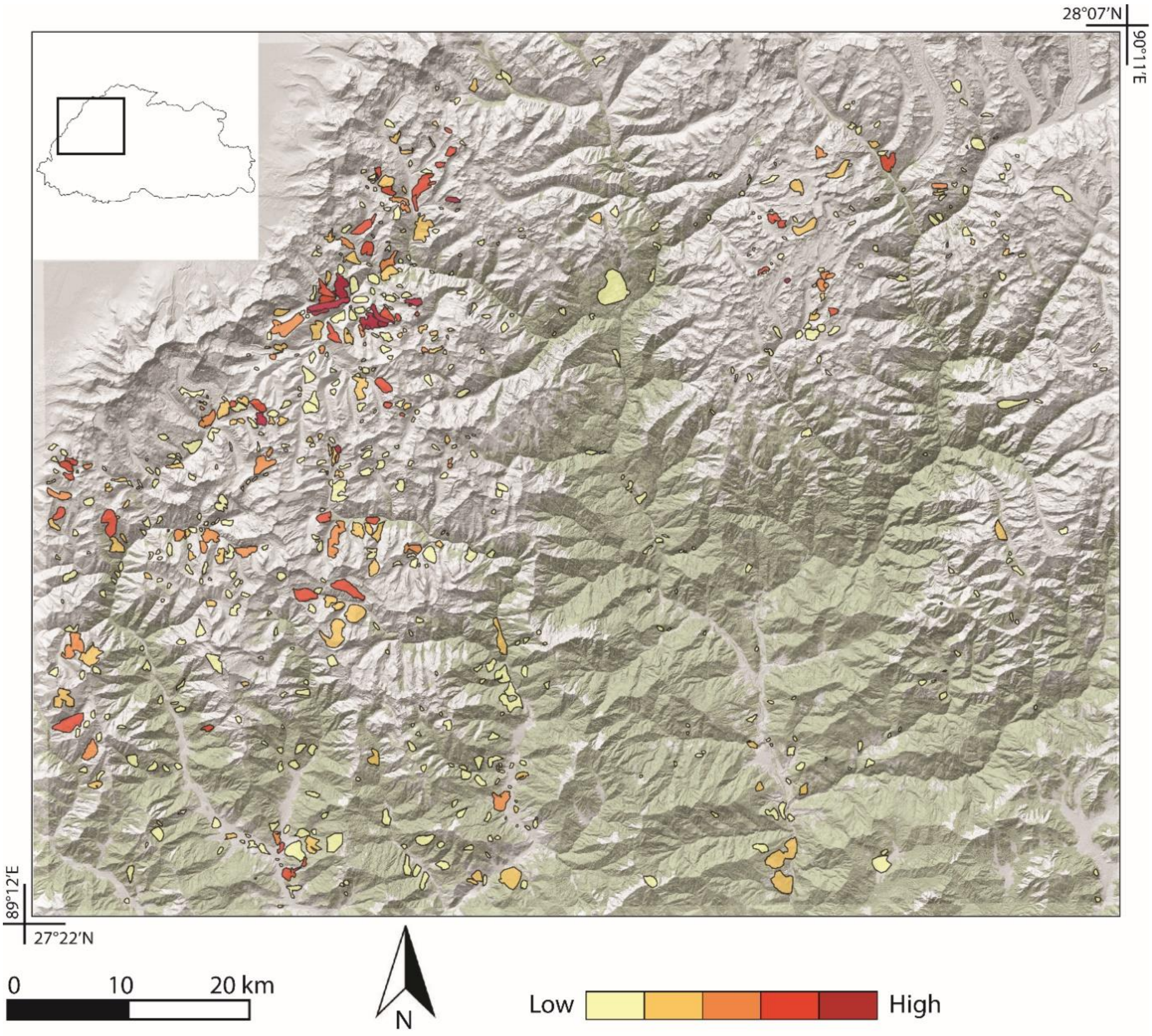

Fig. 2-5. Likelihood of activity obtained for active objects mapped on single interferograms. The weight applied allows for the generation of a relative likelihood level for each potentially active area.

2.4. Results

The detailed analysis of 521 wrapped phase interferograms revealed the presence of over 2,800 areas affected by displacements. After applying our strategy to increase confidence on the displacements, 693 potentially unstable slopes are classified (Fig. 2-5). The total area covered by the areas mapped is 388 km2, roughly 5% of the entire study area, with clear clusters in the northwest of our study area (north of N 27.61° and west of E 89.58°, see figure 2-5). The majority of the observed displacements have been associated with rock slope instabilities, representing 77.5% of the mapped objects (Fig. 2-6), 12.3% are associated with rock glaciers, soil creep occurring on talus cones or slope debris represents around 4%. In a small number of cases, elongated displacement patterns due to soil creep or soil slides are observed over moraines, representing roughly 1.9% of all mapped displacements. The rest 4.3% remain currently unclassified (unknown). Additional information is listed in table 4.

<table>
<tr><th></th><th>Barren/urban areas</th><th colspan="2">Shrubland/ grassland</th><th>Forested areas</th></tr>
<tr><td>Objects detected (%)</td><td>17</td><td colspan="2">55</td><td>28</td></tr>
<tr><td>Detected objects/square km</td><td>0.15</td><td colspan="2">0.11</td><td>0.06</td></tr>
<tr><td rowspan="2">Detection in forest (%)</td><td colspan="2">L-band</td><td colspan="2">C-band</td></tr>
<tr><td colspan="2">92</td><td colspan="2">8</td></tr>
<tr><td rowspan="4">Objects in urban areas (%)</td><td colspan="2">Rock slope instabilities</td><td colspan="2">Unknown</td></tr>
<tr><td colspan="2">63</td><td colspan="2">37</td></tr>
<tr><td colspan="2">Within 500 m of a road</td><td colspan="2">≤ 5 km upstream of hydropower plant *</td></tr>
<tr><td colspan="2">10</td><td colspan="2">6</td></tr>
</table>

Table 2-4. Additional information regarding the detection of unstable slopes through single interferogram analysis. *) planned or existing (Walker, 2016).

The elevation of detected rock slope instabilities ranges from 1200 m a.s.l. to 5200 m a.s.l., with two clear peaks between 2300 and 2900 m a.s.l. and between 4000 and 5000 m a.s.l.. However, the majority are observed at elevations above 4000 m a.s.l., with a much stronger peak in the frequencies at higher elevations. Displacements associated with rock glaciers are found between 4200 and 5300 m a.s.l., above the tree line, 83% of which lies in areas where the permafrost index is lower than 0.5

(Gruber, 2012), thus in the region of discontinuous permafrost or at the lower limit of continuous permafrost. Potential displacements observed in correspondence of moraines have been detected between 3850 and 5050 m a.s.l., this suggesting that moraines from LGM to Holocene are subjects to changes either at surface or at depth. Displacements on talus have been observed up to 5200 m a.s.l., whilst the lower limit, around 4000 m a.s.l., appears to correspond to the tree line. Large areas in the southeast of our area of study, where dense forest cover is present, are characterised by a clear dearth of polygons (see Discussion). Landcover type (NSSC, 2010) was used to assess the detectability of unstable slopes on different land types. We found that 17% of the mapped instabilities are observed in urban or barren areas, 28% in forested areas and 55% in shrubland or grassland. Given the large extent of forested areas in comparison to other types of land cover, it appears clear that only 0.06 instabilities per square km can be detected in forested areas and that 92% of the instabilities mapped within forest cover were indeed detected with the L-band sensor of ALOS.

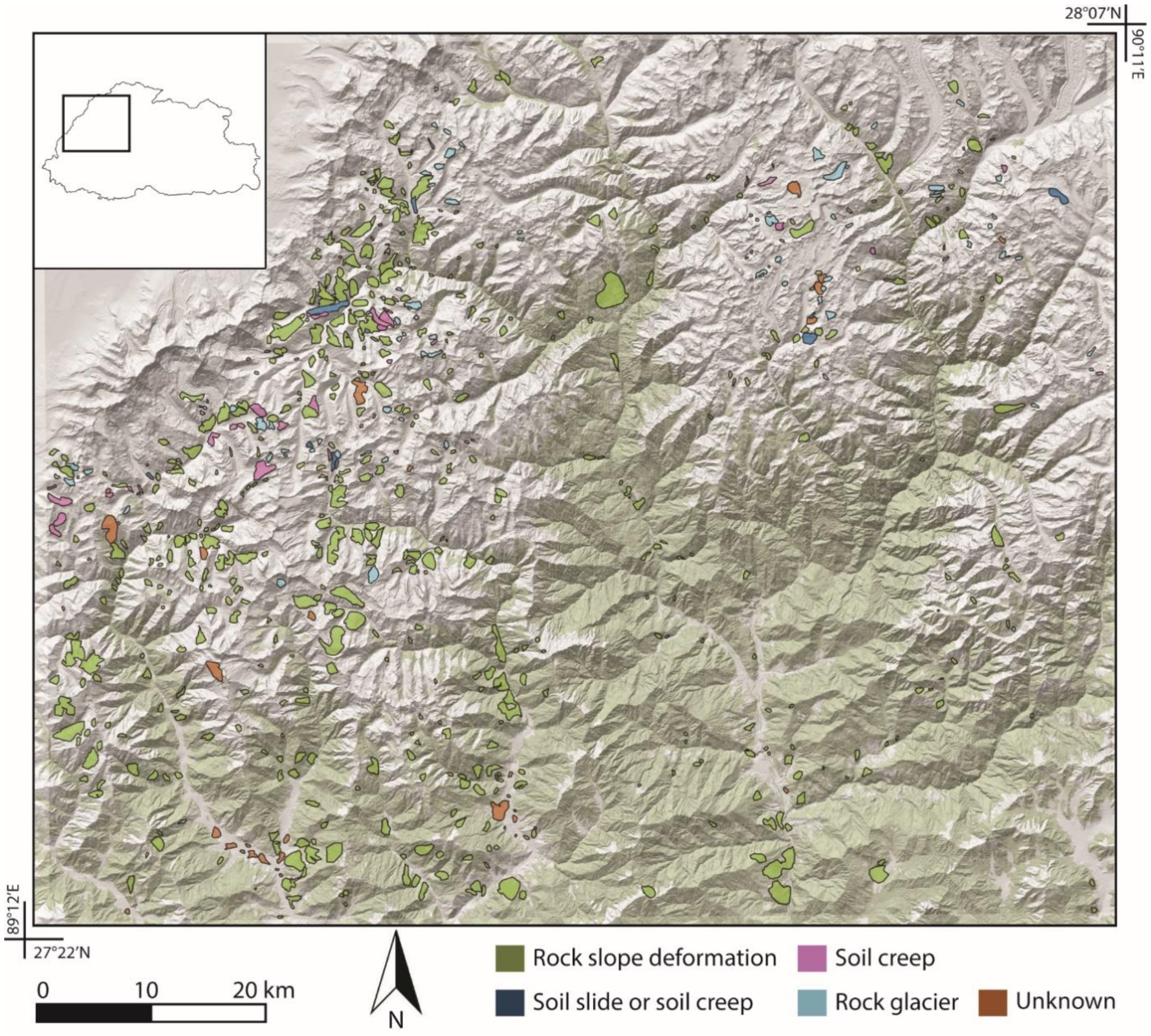

Fig. 2-6 Inventory of active objects obtained through the analysis of single interferograms. Classification of landform is based on visual interpretation of optical images. Light green shading shows forest cover.

Displacements associated with potential rock slope instabilities cover individual areas that range from a few thousand m2 up to 6 km2, although 85% have areas smaller than 0.5 km2. 97% and 78% of areas affected by displacements associated with rock glaciers and talus or slope debris respectively are smaller than 0.5 km2, the remainder not exceeding 1.5 km2 in both cases. As far as the activity likelihood is concerned, 25% of the mapped instabilities have a weighted count of more than 6 times, thus the majority have been observed a small number of times (Fig. 2-5).

Whilst the lowest limit of displacement detectability is more difficult to pin point, but it is not lower than roughly 1/5-1/6 of a fringe for a single interferogram (around 5 mm for Envisat and 20 mm for ALOS-1), the highest bound has never reached, for any of the mapped instabilities, a full fringe. Indeed, the actual velocity depends on the history of each area affected by displacements over the observation period. Only for some rock glaciers, displacements corresponding to a gradient of almost a full fringe have been observed. Occasionally, debris mantled slopes and talus cones show patterns that appear to be decorrelated within a more coherent area, this showing that the maximum detectability threshold is reached by faster displacements.

2.5. Discussion

In this work, we leverage on high-resolution satellite images, a high-resolution digital elevation model and DInSAR to systematically identify, quantify but also classify morphological types of potentially unstable slopes (rock slope instabilities, rock glaciers, soil creep or soil slides occurring on moraines and talus or slope debris) in the area of study. In the following sections, we will discuss these slope instability types and their spatial distribution, special attention will be given to paraglacial and periglacial conditioning. Finally, we will discuss the representativeness and completeness of our inventory, also considering results from two field validation campaigns.

2.5.1. Regional distribution of unstable slopes

With the exception of the southeastern quadrant, we believe that the observed distribution of unstable slopes may reflect the real distribution. First of all, the comparable land cover and topographic gradients between the northwestern and the northeastern quadrant and the fact that the same sensors were used indicate that the relative dearth of slope instabilities in the northeast in comparison to the northwest is not an artifact of the dataset. Moreover, the southwestern quadrant, showing a relative scarcity of unstable slopes was analysed also by Ambrosi et al. and was object of two field campaigns carried out in this study (see section 2.5.5). Field observations reveal indeed that more relict rock slides are present in the region than active ones.

Figure 2-7 shows the distribution of mapped unstable slopes with permafrost, glaciers, seismicity and regional fault structures. Only few regional faults have been mapped and identified in our study area. The Lingshi fault and the Lingshi thrust are shown in red (solid and dashed lines respectively), modified from Grujic et al. (2011) and Kellett et al. (2013). The Lingshi fault is a sinistral strike-slip fault with a normal component, trending NE-SW. Neotectonic activity levels of these major structures are not clear. Although Antolín et al. (2012) suggest that this fault is seismically active, studies focusing on recent seismicity in Bhutan are not conclusive in this respect. Two local networks have been installed in the region in 2002-2003 (Velasco et al., 2007) and 2012-2013 (Diehl et al., 2017). Whilst the first study did not record any seismicity in the northwest of our interest region, Diehl et al. (2017) indicate that two shallow events occurred in the proximity of the Lingshi fault during their observation period. These events, both M2, with depths of 11.70 and 15.96 km respectively, may be associated to the Lingshi fault, for which shallow activity may be expected. However, the low magnitudes and the epicenters outside of the local network made their detectability challenging and the generation of a reliable focal mechanism not possible (Diehl, pers comm). In 2013, the USGS recorded another shallow event (M3.9, depth 10 km) and located it very close to the southwestern mapped tip of the Lingshi fault. However, this event, also found in the catalogue published by Diehl et al. (2017) was placed by their local network 100 km to the northeast (out of our study region) and with a much higher depth (~76 km). The large incongruence between the location of this event in the two catalogues casts some doubts on whether this event may be associated to the Linsghi fault. Moreover, the fragmentary observations obtained from the local networks (due to the short periods in which these were in place) do not allow a reliable determination of seismotectonic activity that may be ongoing along this regional structure. However, as shown in Figure 2-7, the Lingshi fault could influence the dense distribution of unstable slopes in this part of the study area. It is possible that not only its presence has preconditioned the rock slopes to failure (Ambrosi and Crosta, 2006; Gupta, 1989), but also that the possible activity and past seismicity has led to the higher number of potentially unstable slopes detected in this area. It is also likely that lithology is another important factor. The Lingshi Faults runs through the Tethyan sediments, with shales in its immediate proximity (Long et al., 2011; Gansser, 1983). 48% of our detected unstable slopes fall within the sedimentary rocks of the Tethyan sequence, which correspond to roughly only 24% of the entire study area. Activity in this cluster may therefore also be influenced by weaker rock types. Recent seismicity in Bhutan appears to indicate that activity concentrates in southern parts (outside of the study region) (Diehl et al., 2017; Velasco et al., 2007), with the exception of cluster of microseismicity in the Punakha area (Fig. 2-7). This cluster shows variable focal depths but generally deeper than the depths associated to the three events in the

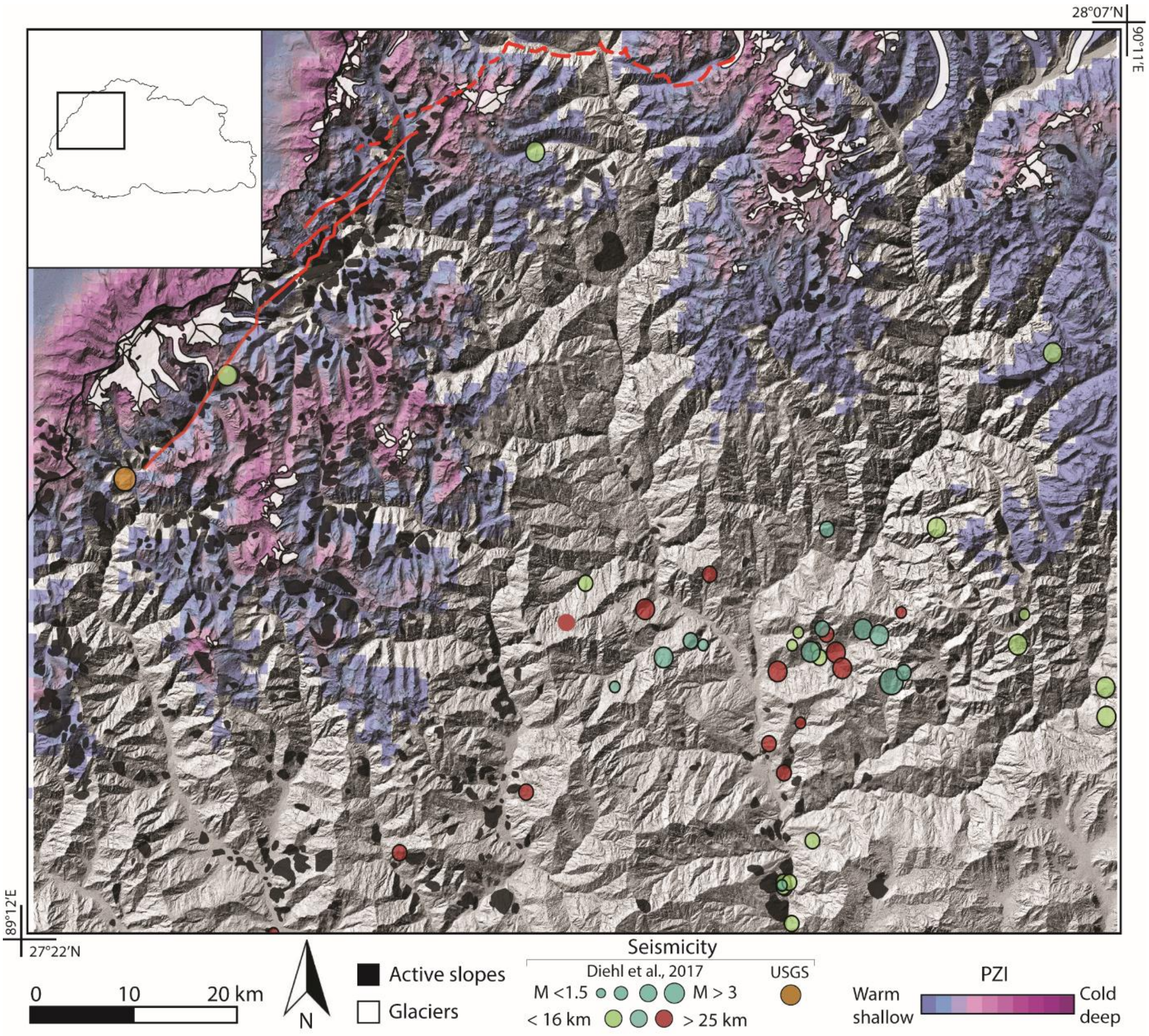

Fig. 2-7. Black polygons represent active slopes distribution (this study), white polygons are present-day glaciers from GLIMS database (GLIMS and NSIDC, 2005). The purple colour scale describes the global permafrost index zonation (modified from Gruber, 2012). Circles represent seismicity between 2012 and 2013 (modified from Diehl et al., 2017), with size increasing with magnitude and colour scale to show depths. Orange circle represent one event recorded in the USGS catalogue. Solid red lines Lingshi fault, dashed red line Lingshi thrust (Kellett et al., 2013; Grujic et al., 2011).

northwest mentioned above, and it is shown by both studies of Velasco et al. (2007) and Diehl et al. (2017), this indicating persistent activity (Diehl et al., 2017). The microseismicity of this cluster is associated with the hanging wall of the mid-crustal ramp of the Main Himalayan Thrust (Diehl et al., 2017 and references therein). The higher depths and thrust plane orientation associated to these low magnitude events most likely reflect the dearth of unstable slopes in our analyses, although the difficulty in detecting activity in densely forested areas may enhance this effect.

The global permafrost map generated by Gruber (2012) is also shown in figure 2-7. The distribution of permafrost in the region seems to have an effect on the density of detected unstable slopes, with a higher percentage of them being detected in regions of relatively shallow and warm permafrost. This may reflect that annual melting cycles and ongoing retreat in the permafrost cover in the region may be associated with displacements on slopes. Periglacial processes in the region will be illustrated and discussed in a companion paper in detail. Several studies (see Ballantyne, 2002 and references therein) have pointed out that slopes adjacent to retreating glaciers are increasingly prone to failure and recognised rock slope instability as a characteristic paraglacial response to glacier retreat. The descending track of Envisat, 176, covers almost the entire area around present-day glaciers within our study region (with the exception of the far northeast). This means that the identification of relatively slowly moving rock slopes should be possible if displacements occurred within the observation period, given the relatively low vegetation index. The available ALOS frames cover the areas occupied by glaciers only for about half, therefore not providing full coverage. The analysis of the interferograms has revealed 9 potentially unstable slopes, with likelihood of activity (described in section 2.3.1) resulting low (7) to medium (2). For two of these objects (with low likelihood) the displacements observed seem be related to a diffuse activity of the entire slope on which they are found, whereas for the others it could be associated with local rock slope instability. Even if this suggests that 70% of potential rock slope instabilities at glacier terminuses show signs of rock slope instability in the observation period of this work, the scarcity of detected objects and the low likelihood levels indicate that such activity is in general low.

2.5.2. Rock slides, rock slope and mountain slope deformations

Outside the glaciarised regions, more rock instabilities were identified. An example of a mountain slope deformation from a recently non-glaciated valley, with diagnostic features as explained in section 2.3.2, is shown in figures 2-4 (section 2.2.3) and 2-8. The main scarp is very clear in the optical images, along with three marked secondary scarps downslope. A rather linear eastern boundary is also evident down to ~4070 m a.s.l. where it appears possibly obliterated by a shallower, smaller secondary failure. This elevation corresponds also to the lowermost scarp observed (figure 2-8c-d). The profile indicates a slight bulging of the toe with a very steep lowermost part. The surface displacements observed on this landslide are quite clear, as shown in figure 2-4. The most active part appears to be corresponding very well with the lowermost scarp marked in figure 2-8c. Some interferograms indicate activity also for the second scarp from the top, suggesting that the entire landslide may be active, although with different zones being affected by different activity levels. The displacements observed in the interferograms in figure 2-4 (which are only a part of the interferograms in which the same instability can be detected) can be used to estimate an average velocity, in order to have a comparable measure among interferograms with different temporal baselines. It is worth noting that the displacements estimated from the interferograms area relative

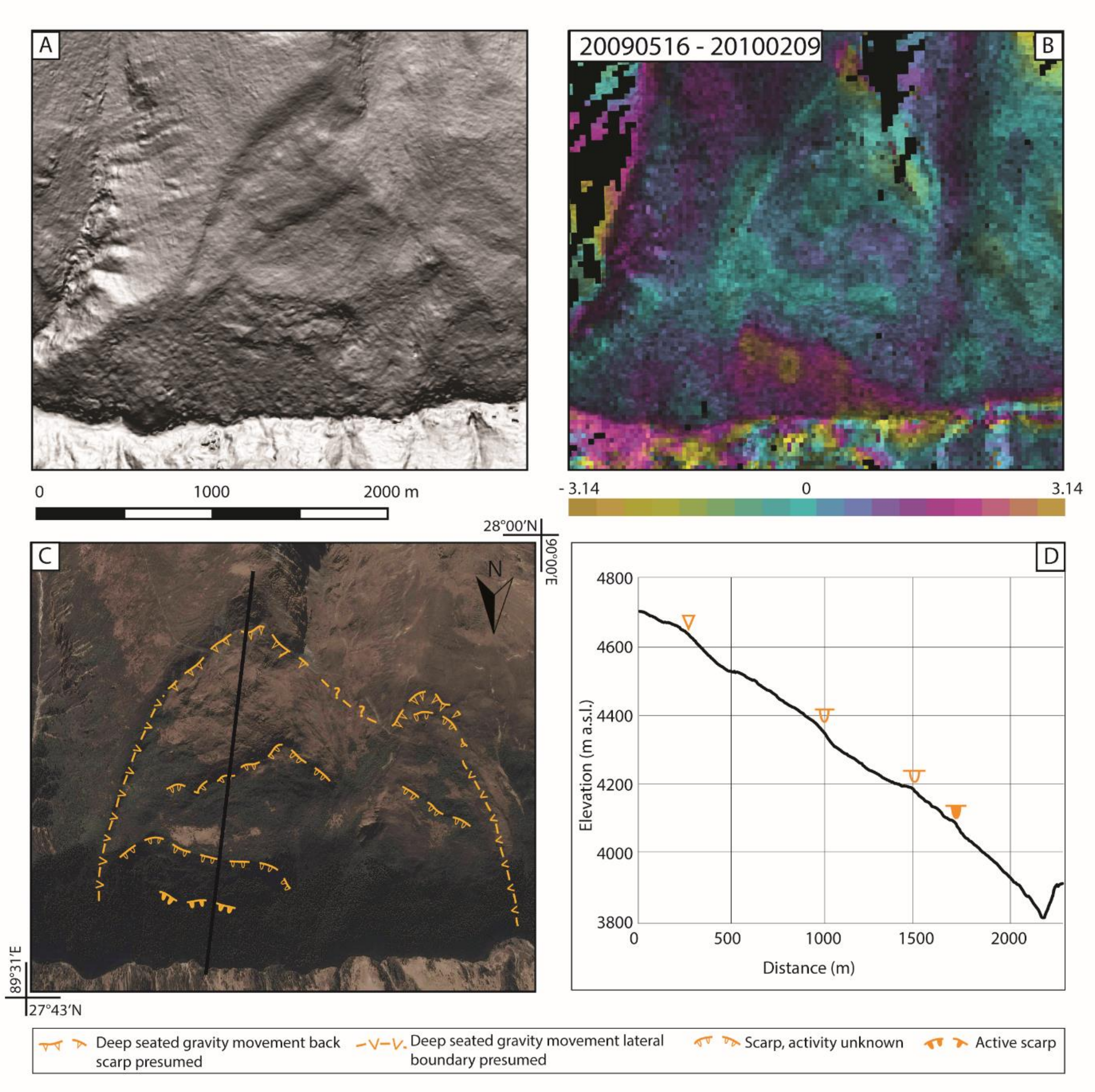

Fig. 2-8. The mountain slope deformation also shown in fig. 2-4 is illustrated here with its geomorphological characteristics. A) ALOS 5m DSM, B) another example of differential interferogram obtained with an ALOS-1 pair. C) GoogleEarth image, with mapped gravitational features, D) ALOS 5m DSM profile with indicated the mapped features of (C)

rough estimate of the displacement in mm occurred in each time interval, retrieved from the fraction of fringe (in radians) observed and then rounded to the nearest 5. Moreover, there are clear atmospheric effects that were uncorrected for and that are visible for example in two interferograms in figure 2-4. The reliability of the level of activity and of the observed displacements is given by the repeated detection. What can be observed in figure 2-4 is that short baselines interferograms covering the months of July, August and September have higher estimated mean annual velocities, whereas longer baselines show the shortest estimated mean annual velocities. This clearly indicates that the activity is concentrated during the monsoon period and that the landslide undergoes accelerations likely in response to high rainfall intensities. Provided a suitable set of connections, the periods of accelerations and higher activity can thus be pin pointed and correlated with meteo-climatic

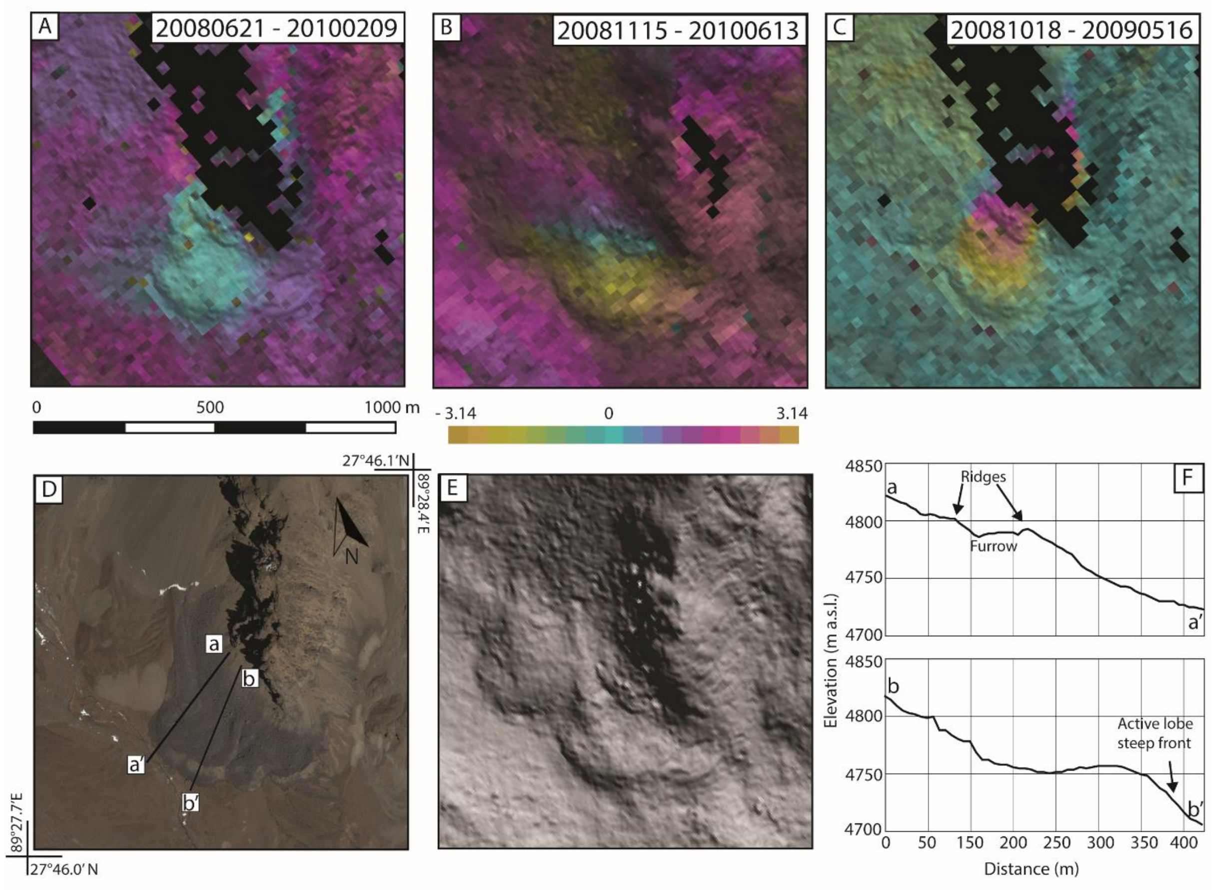

Fig. 2-9. Three wrapped interferograms from A) ALOS-1 track 503 frame 540, B) Envisat track 176, C) Envisat track 69 showing displacements over a rock glacier. D) GoogleEarth image, E) ALOS 5m DSM, F) profiles, traces shown in (D).

conditions. The estimated mean annual velocities are therefore compatible with what could be the history of this instability through the period of observation.

2.5.3. Rock glaciers

Creeping rock glaciers are defined by very clear patterns which follow remarkably well the boundaries of the landform. Our analysis of individual interferograms revealed 92 active rock glaciers. Elevation seems to have an influence on creep velocities, with highest estimated displacements rates observed mostly above 4700 m a.s.l.. We can also observe that the lowest detected displacements occur below 4700 m a.s.l. (below this altitude, rock glaciers are still visible in optical images but only a small percentage of them (16%) is detected with DInSAR). Rock glaciers below such elevations are either inactive or characterised by levels of activity closer to the lower threshold of detectability of DInSAR. Our data show that around 90% of the detected rock glaciers fall within regions where the Permafrost Zonation Index (PFI) (Gruber, 2012) is less than 0.5, indicating areas where permafrost is present only

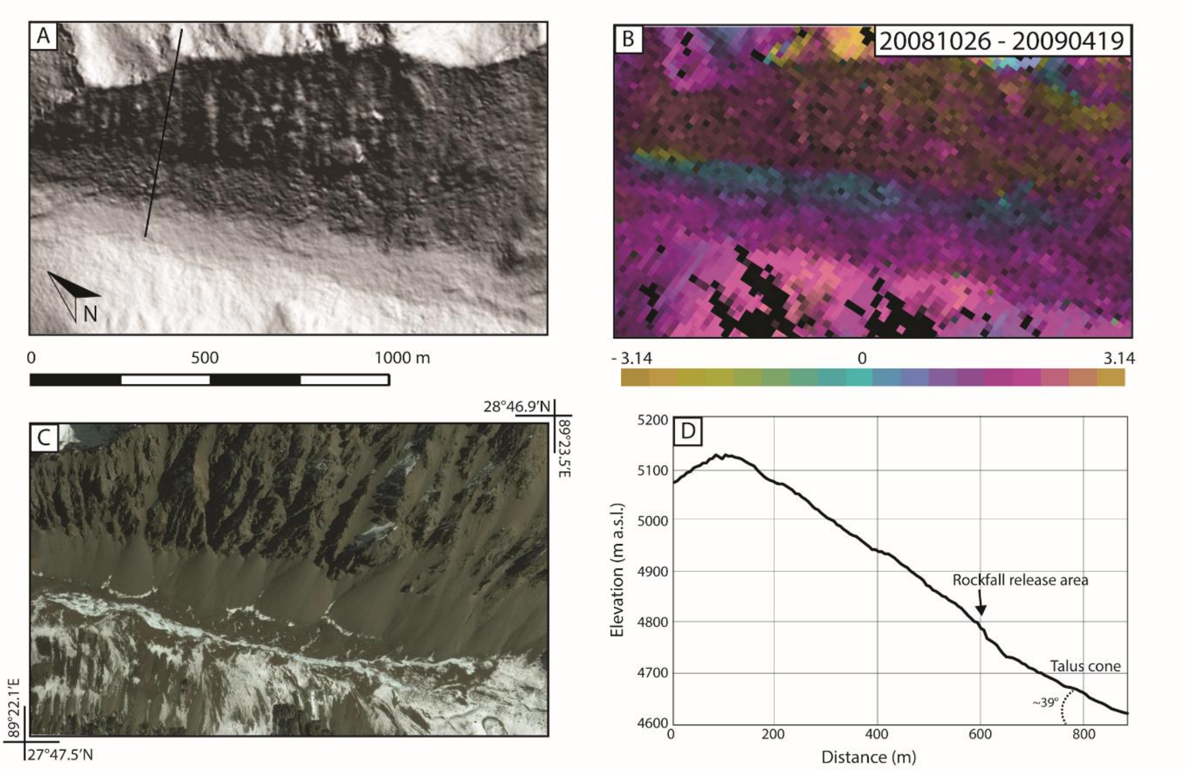

Fig. 2-10. A) ALOS 5m DSM, B) Wrapped interferogram from Envisat track 176, showing displacements over talus or scree cones C) GoogleEarth image, D) Profile, trace shown in (A).

in favourable conditions and thus relatively shallow and warm. Just over 60% in fact are in areas where the PZI is less than 0.3, thus near the lower limit of discontinuous permafrost. This is similar to what is observed for rock glaciers in the Alps (Delaloye et al., 2010).

Examples of such rock glaciers are given in figures 2-3 (section 2.2.3) and 2-9. In the majority of the cases, the displacement patterns allow to identify the active lobes and to distinguish them from inactive lobes. Figure 2-9 shows typical ranges of displacements observed. Figure 2-9a indicates roughly 5/6 of a full fringe for ALOS-1 in roughly 20 months, this corresponding to an average estimated annual velocity of 2.3 cm/year; in figure 2-9b and 2-9c interferograms from Envisat descending and ascending tracks are shown respectively, these indicating almost a full fringe (~1.8 cm/year) and almost 3/4 of a fringe (~3.5 cm/year).

2.5.4. Soil creep and soil slides

All of the instabilities classified as soil creep in our dataset are found within the permafrost region. On one hand, vegetation cover below the permafrost region hinders the detection of displacements, on the other hand the thick vegetation may act as damper on large displacements of loose material on slopes. Soil creep associated with unstable slope debris or talus deposits accounts for 4% of observed displacements. This low percentage may have two different explanations. On one hand, often talus feeding rock glaciers has been mapped within the rock glacier itself, if the area was not sufficiently large (at least as large as the rock glacier itself) to be assigned another polygon; moreover, often we observe clear shallow movements of debris and loose material on slopes that have been classified as potential rock slope instabilities or moraines due to the presence of other morphological characteristics. On the other hand, displacements involving loose materials on slopes may be around the upper threshold for detectability. Figure 2-10 shows the typical displacement pattern associated with talus or scree cones as observed in wrapped interferograms. The resolution of the interferograms does not allow to identify the individual cones shapes, which are a few tens of meters to a hundred meters across. The typical observed pattern is elongated in correspondence to a series of such cones. The upper part of the signal usually corresponds with the apexes of the cones and the lower boundary of the feeding cliff. This would induce some similarities with atmospheric delays; however, the perfect correspondence to the cones position and lateral extent are indicative of true ground displacements. This may indicate that the cliffs acting as release areas are still active. Therefore, they are a useful indicator of ongoing rockfall activity, phenomenon that could not be observed with DInSAR due to its extremely high velocities (Wasowski and Bovenga, 2014).

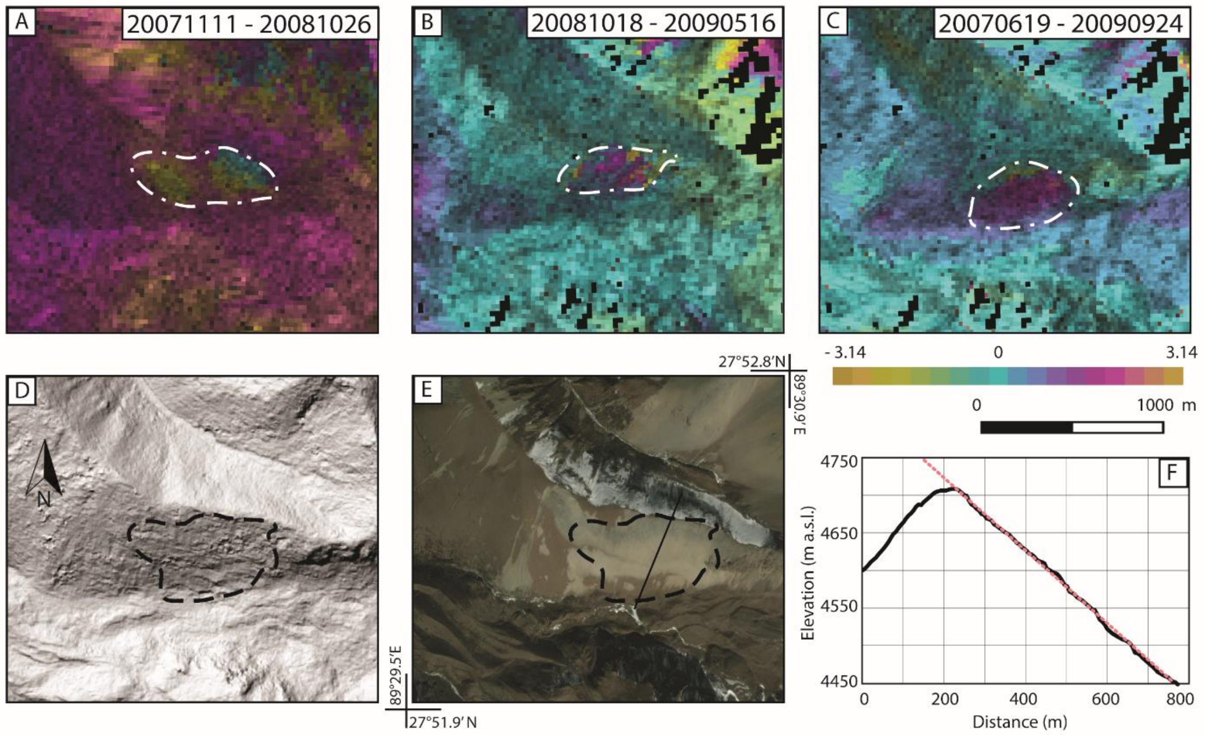

Fig. 2-11. Examples of interferograms from A) Envisat track 176, B) Envisat track 69, C) ALOS-1 track 502 frame 540 showing displacements over a debris mantled slope. In white the individual polygons of the mapped objects contributing to the final overlap. D) ALOS 5m DSM, in black the final polygon of the active area. E) GoogleEarth image, F) Profile, trace shown in (E).

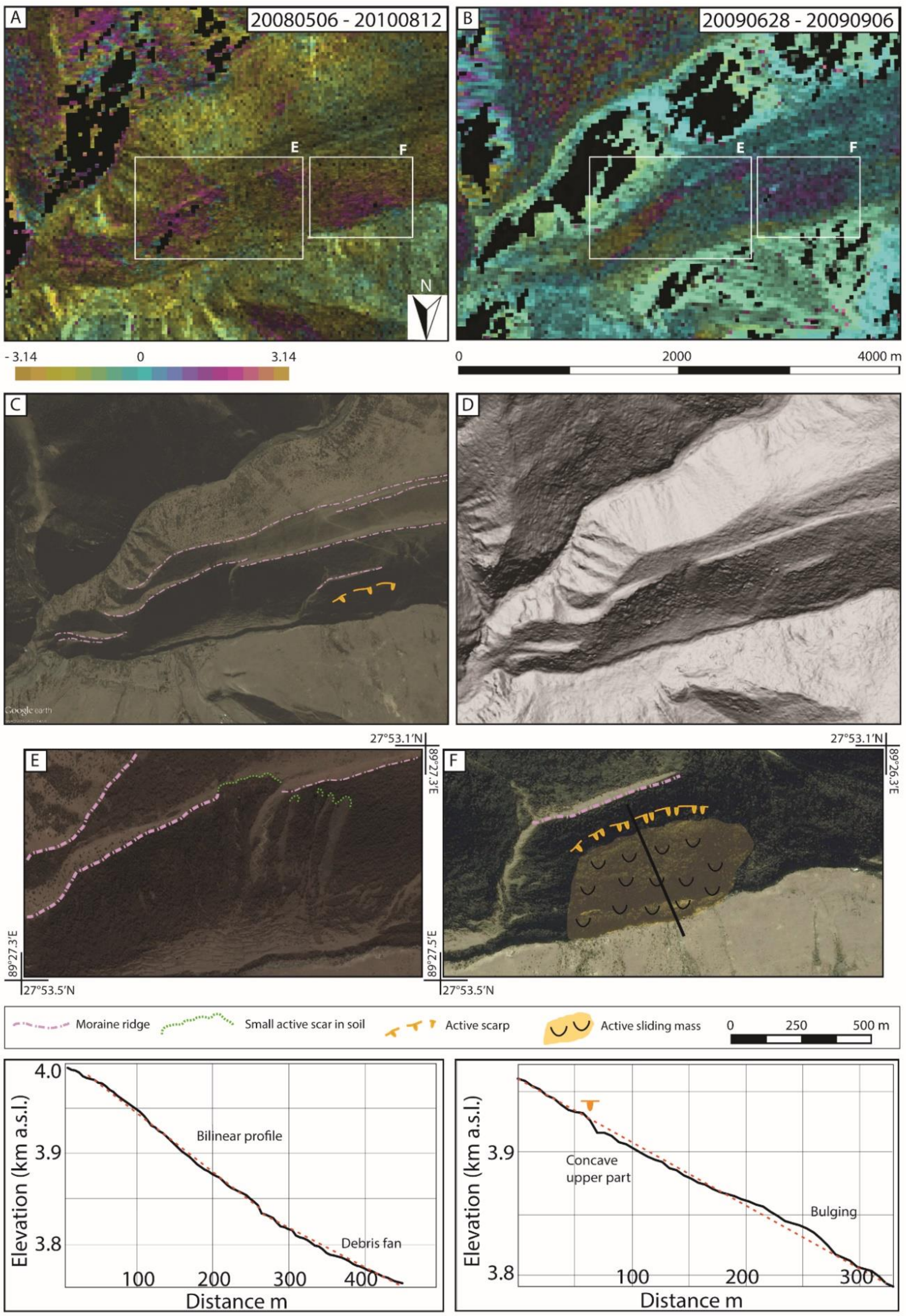

Fig. 2-12. Examples of interferograms from A) ALOS-1 track 503 frame 540, B) Envisat track 176 showing displacements over a large moraine system. C) GoogleEarth image with mapped features, D) ALOS 5m DSM, E) GoogleEarth image, zoom showing superficial scars in loose material (box shown in A-B), F) GoogleEarth image, zoom showing a large landslide, likely in soil (box shown in A-B); the inset shows the profile which illustrate the presence of the scarp and an accumulation zone in the lower parts of the slope.

Figure 2-11 shows a debris mantled slope, with a featureless aspect with the exception of changes in colour of the loose material as observed in the optical images (figure 2-11e). The draping of loose soil and debris gives the slope a smooth appearance and the profile is very linear due to the complete coverage with debris at a uniform angle of repose. This linearity of the profile also indicates that the nature of any displacements is most likely to be shallow, and no deeper, internal rock deformation causes convexities in the profile.

Surface displacement was also observed in association with lateral moraines, albeit this is a rarer occurrence. We observed 13 areas of soil creep or soil slide on moraine flanks, all falling outside of areas with cold and deep permafrost. The displacement patterns observed in the interferograms are not always clear, especially regarding the boundaries and how these fit to the underlying morphology. Ice melting in ice-cored moraines is an increased factor for periglacial slopes instability. Displacements occurring in association with large moraines related to the LIA have been observed in the Swiss Alps with 35-day ERS interferograms and interpreted as related to creep of frozen sediments or subsidence-inducing melting of ice at depth (Delaloye et al., 2007).

Figure 2-12 shows examples of displacements detected on moraines. Here we distinguish two different types of gravitational processes. Figure 2-12e is a zoom on an area where many superficial scars in soil are observed in the images. The displacements observed here, noisy in nature, could be the response to superficial debris movements. Figure 2-12f is another zoom, this time on a flank of a lower moraine ridge that is likely affected by a soil slide. Although we have no information regarding the materials involved and vegetation cover conceals any geomorphological features in the optical images, the occurrence on a large moraine flank suggests a large soil slide. The depth is also unknown (hence the volume) however, the scarp observed in the profile (figure 2-11f) is ~20m high and the bulging shows also an accumulation above the linear profile of ~10-15 m. This would make it for a completely different phenomenon when compared with the displacements observed in figure 2-11e, but would most likely also point towards a gravitational process affecting moraine deposits, most likely unrelated to melting of an ice core at depth.

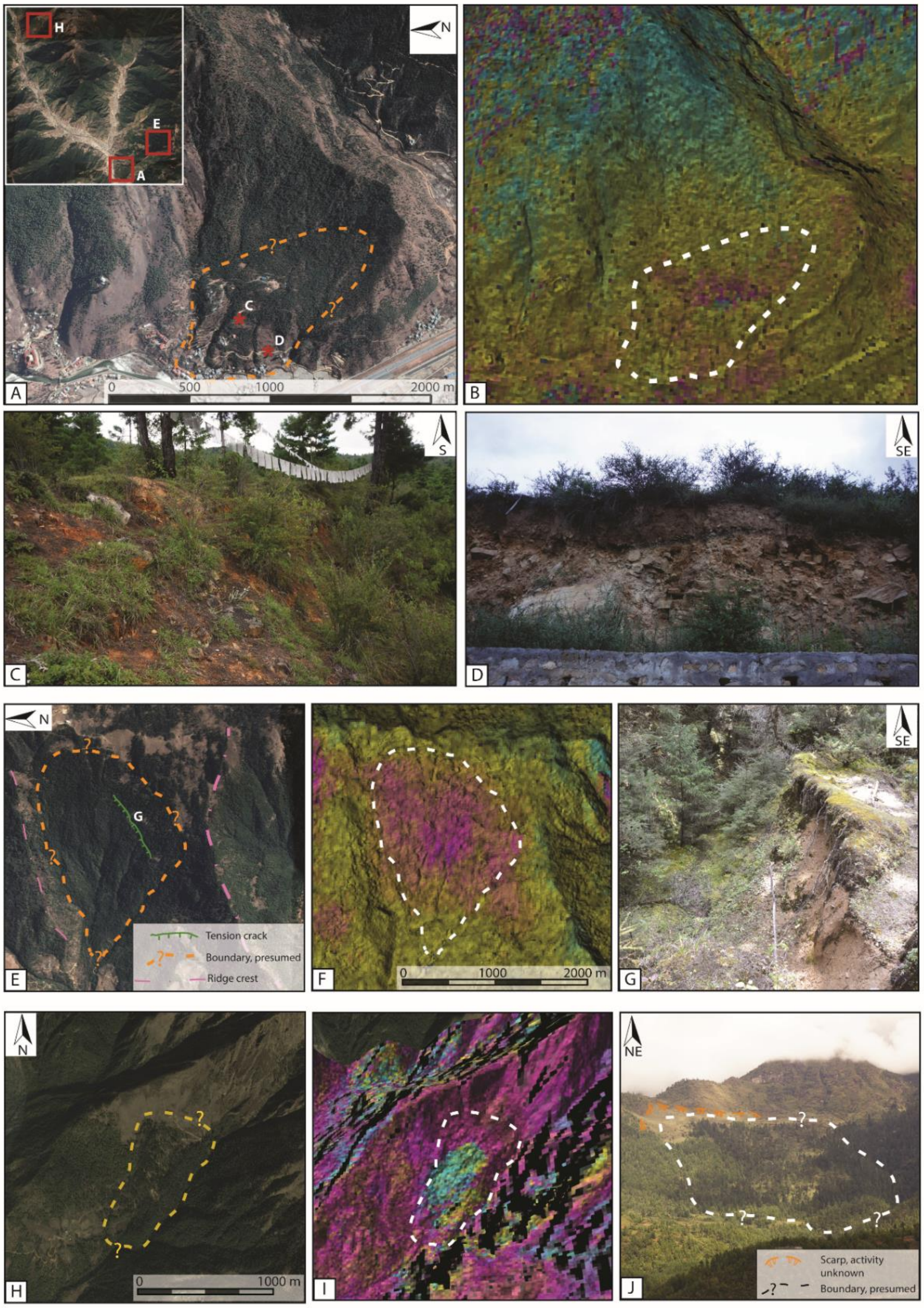

Fig. 2-13. Examples of active landslides validated during field campaign. A large, slow moving landslide near Paro airport, A) GoogleEarth images showing presumed boundaries and location of photos shown in C and D; B) Example of wrapped interferogram from Envisat track 69 for the period 0060211-20061223; C) fresh, secondary scarp observed in the field, D) rockslide deposit observed along the road within the landslide boundaries. Another landslide in the Paro area shown in E) in a GoogleEarth view, with boundaries, observed crack and location of photo shown in G; F) example of wrapped interferogram from ALOS-1 track 503 frame 530 covering the period 20071006-20091011; G) observed crack with tension roots. A third example is shown in H) GoogleEarth image with presumed boundaries, I) example of wrapped interferogram from ALOS-1 covering the period 20070218-20090108; J) Photo taken from a point of view in the main valley from which the main scarp and the landslide body where visible.

2.5.5. Field validation

Two field campaigns in the valleys of Paro, Thimphu and Punakha were carried out in October 2016 and 2017 to validate part of the inventory. This allowed to refine the remote sensing data interpretation across other parts of the study area. Figure 2-13 shows three examples of landslides in the valley of Paro for which validation was possible. A relatively large, slow moving landslide to the northeast of the Paro airport (figure 2-13a-d) was observed in Envisat interferograms, an example of which is shown in figure 2-13b. Field observations revealed the presence of rockslide deposits on the road (figure 2-13c) within the landslide boundaries and also several, fresh secondary scarps (figure 2-2-13d) only a few meters high. Due to the short wavelength of Envisat, many interferograms are noisy. Nevertheless, displacements of a few mm/year can be observed, whilst no displacements were detected with ALOS, probably due to the lower sensitivity. The second example (figure 2-13e-g) illustrates a landslide covered by a dense vegetation cover, with fewer morphological features visible. However, many ALOS interferograms showed a clear phase gradient likely related to ground displacements. Phase gradients as those shown in figure 2-13f are not attributable to atmosphere, since they do not cross the ridges to the north and to the south, but some parts of the slope are in layover, therefore caution has to be taken when interpreting the data. In this case, field investigations revealed also other indicators of recent or ongoing activity. Large fissures oriented northeast-southwest were observed, these a few meters large, two meters deep and many tens of meters long. In these depressions occasionally tension roots were also observed.The landslide in the last example (figure 2-13g-j), unequivocally showing displacements in the interferograms, was observed from a point of view 3 km to the southwest. A large scarp, secondary scarps and rockfall activity were observed and the mass appears as bending the lateral valley outwards. Ambrosi et al. (2018) identified slope instabilities through SAR interferometry and photointerpretation in the western branch of the Paro valley. Within this area Ambrosi et al. (2018) identified 35 slope instabilities, however all of these through photointerpretation, this suggesting that no displacements were found, either due limitations intrinsic to the technique or for lack of activity. In the same area, we identified 13 potentially unstable slopes, however 12 of this with very low likelihood and only 1 with high likelihood (figure 2-13g-j). In general, in this area, in general DInSAR did not reveal extensive recent activity, thus supporting the findings of Ambrosi et al. (2018) and in line with the many rock slide deposits observed in the field, often draped by thick soil covers.

2.5.6. Limitations and challenges

High topographic gradients, ice and snow cover, and dense vegetation cover are examples of factors that can hinder the potential of DInSAR techniques. The high topographic gradients lead to layover effects in unsuitably exposed valley flanks, however, this problem can in some cases be overcome with the use of ascending and descending geometries (subject to acquisitions availability). Moreover, a topography mainly consisting of north-south oriented valleys is optimal for the DInSAR technique (Delaloye et al., 2007), which this is the case for our study region in north-western Bhutan. In this work, Envisat tracks of both ascending and descending geometries were used for the interferograms generation, which ensured some coverage on most valley flanks in the areas where the tracks overlap. The presence of wet snow and snow cover variations have a strong influence on coherence Cignetti et al., 2016). At longer time intervals, interferograms can become unusable if temporal changes in the snow cover occurred. When a sufficiently large amount of images is available, then a choice may be to discard winter images, however it is very difficult to define winter images over several years of observation due to climate variability (Cignetti et al., 2016). In any case, the lack of a large dataset for this study has prevented this possibility and all images were retained. For all our ascending tracks, on average 57% of the images are winter acquisitions, whereas for Envisat 176 only 28% are acquired in winter (see table 1).

Atmospheric delays are also one of the main causes for signal deterioration which is exacerbated by the high topographic gradients (Cignetti et al., 2016; Ding et al., 2008). In alpine terrains, homogeneous tropospheric delays can affect the whole scene and appear to follow the topography (Doin et al., 2009; Hanssen, 2001). The interferograms used in this study were not corrected for atmosphere; however, since turbulent atmospheric effects are poorly correlated in time (Doin et al., 2009) the likelihood strategy applied helped to mitigate this problem. Moreover, phase changes due to the layered atmosphere are long-wavelength (Doin et al., 2009) and can be ignored when the size of the investigated area is smaller (slope scale) than the scale of tropospheric variations (Kenyi and Kaufmann, 2003).

Vegetation cover can severely impact the retrieval of interferometric information. The growth of crops and the re-working of fields impacts the dielectric properties of the ground and creates variations that cause coherence loss (Engelbrecht et al., 2014; Massonnet and Feigl, 1998), especially at short wavelengths, such as those of C- and X-band sensors. Shrubland and forest are volumes composed of parts of different sizes (tree trunks, branches and leaves) and the degree of penetration of the radar signal depends on the wavelength, with longer wavelengths less affected by smaller individual scatterers. Indeed, we find that one of the most challenging problems in our study area is vegetation cover, responsible for severe decorrelation even at short revisit times in C-band but also in L-band over thick forest, and for other types of vegetated surfaces for longer revisit time intervals. The gap of detected instabilities observed roughly between 3000 and 3500 m a.s.l. corresponds to the mixed forest, favouring the hypothesis that the observed distribution is highly influenced by the type of vegetation.

Data availability is also a problem, and it is certainly a challenge in our region where acquisitions have not been systematic for the used tracks. Many interferograms are characterised by large areas of low coherence (either due to snow or vegetation changes), whilst the largest the number of high quality interferograms the more reliable the analysis is (Lambiel et al., 2008).

DEM inaccuracies can be another source of errors or misinterpretations of the signal, even if these appear to be clearly correlated with topography and can be identified. The availability of a high-resolution DEM allows for the generation of interferograms with no noticeable artefacts even for longer perpendicular baselines (Massonnet and Feigl, 1998). For our processing and analysis we used the ALOS World3D DSM with high spatial resolution and relatively high vertical accuracy in order to minimise errors derived from this phase of the processing.

As mentioned above, the irregular distribution of detected potentially unstable slopes presented in this study is largely attributable to land cover, which seems to be the strongest limitation for the analysis. However, a very large number of unstable slopes were identified with the analysis of single interferograms. The analysis of individual interferograms only offers a snapshot view of potentially unstable slopes but, as these are identified in more than one interferogram, confidence increases on the overall quality and reliability of the dataset.

2.6. Conclusions

In this work, we developed a new methodology for a reliable evaluation of unstable slopes activity likelihood at the regional scale and the determination of slope instability types in high alpine terrain. The methodology, based on the generation of a large number of interferograms and on a novel decision tree that takes into account various indices (such as layover, vegetation, estimated velocity and temporal coverage of the data), assigns a weight to each detected active area. Through this methodology, entirely based on remote sensing data, we obtain a new map of potentially unstable slopes over a large region in northwestern Bhutan and are able to scale the likelihood of activity of each area in the dataset in an objective way, for the observation period between 2007 and 2011. We used a combination of remote sensing data, from satellite based radar images to optical images and a high resolution DSM. DInSAR, in combination with the recognition of geomorphological characteristics, has proven extremely useful in generating a new inventory of potentially unstable slopes in the area of study. Considering the intrinsic limitations of DInSAR that were discussed above, particularly with respect to difficult terrain in terms of land cover and topographic gradients, we show how to maximise the amount of information extracted for a region for which very little was initially known. Estimates of lower and upper bounds of displacement rates can be made for different types of active landforms or unstable deposits, this allowing comparisons with similar gravitational mass movements in other alpine regions. Moreover, we could identify slopes on which displacements occur most likely at greater depth, distinguishing them from more strictly surficial displacements. Despite the fact that our dataset is unlikely comprehensive of all (large) slope instabilities in the study area (due to detectability issues and the limited observation period discussed above), the information that we retrieved sheds some light on the spatial distribution of unstable slopes, which appears to concentrate in the northwest of the region, and indicates that slope instability in such areas is influenced by the presence of important tectonic structures and lithology, and to a lesser degree by periglacial and paraglacial processes. Regarding the distribution of displacements, we note that the factor that hinders the most the detectability of slope instabilities is indeed related to the presence of thick forest. This is most likely causing the dearth of information in the southeast of the region, which is unlikely reflecting a true distribution. However, due to the comparable landcover in the northwest and northeast of the area, our data indicates most likely real enhanced slope instability in the northwest. This could be related to rock damage, active tectonic displacements and seismic activity along the Lingshi fault. Regarding the southwest of the region, where forest cover is dense but less so than in the southeast, field observations and comparison with the results obtained by Ambrosi et al. (2018), our data clearly points to a relatively low level of slope instability in recent times, as opposed to higher past levels of activity.

The new dataset that we generated here will be used in future work, in combination with other datasets, to investigate large rock slope failures in the region in association with lithology and tectonic structures. In particular, a separately generated rock slope instabilities inventory based on the analysis of optical images will be associated to the findings of the present work in order to understand landslide predisposition and controlling factors in the study region. Multitemporal analyses through advanced DInSAR processing will also be a valuable continuation of the present work, to better identify processes responsible for displacements through time series analysis. This will enable to further improve our understanding of predisposing factors and causes of large rock slope instabilities in the Himalaya of Bhutan and of landscape evolution in the area. Moreover, our findings can serve as a basis for the hazards related to mass wasting phenomena in the region that can adversely affect a growing infrastructure and that are currently still poorly monitored, understood and mitigated for.

Acknowledgements

We would like to express our gratitude to Paolo Riccardi from Sarmap for his precious support in processing the SAR data. We thank our colleagues Larissa de Palezieux, Kerry Leith, Djordje Grujic and Tobias Diehl for the fruitful discussions. We are also grateful for the support and interest of the College of Natural Resources of the Royal University of Bhutan, Helvetas, Walo and of National Land Commission, Department of Disaster Management, Department of Hydrology, Department of Roads, National Soil Science and Department of Geology and Mines of the Royal Government of Bhutan. This work was funded by an ETH grant (ETH-38 15-2) and an ESA Alcantara project (ESA 4000117652/16/F/MOS).

2.7. References

Agliardi, F., Crosta, G. B., Zanchi, A., and Ravazzi, C. (2009). Onset and timing of deep-seated slope deformation kinematics. Engineering Geology, 59, 83-102. doi:10.1016/j.geomorph.2007.09.015

Ambrosi, C., and Crosta, G. B. (2006). Large sackung along major tectonic features in the central italian Alps. Engineering Geology, 83, 183-200. doi:10.1016/j.enggeo.2005.06.031

Ambrosi, C., Strozzi, T., Scapozza, C., and wegmüller, U. (2018). Landslide hazard assessment in the Himalayas (Nepal and Bhutan) based on Earth-Observation data. Engineering Geology, 237, 217-228. doi:10.1016/j.enggeo.2018.02.020

Antolín, B., Schill, E., Grujic, D., Baule, S., Quidelleur, X., Appel, E., and Waldhör, M. (2012). E-W extension and block rotation of the southeastern Tibet: Unravelling late deformation stages in the eastern Himalayas (NW Bhutan) by means of pyrrhotite remanences. Journal of Structural Geology, 42, 19-33. doi:dx.doi.org/10.1016/j.jsg.2012.07.003

Aschbacher, J., and Milagro-Pérez, M. P. (2012). The European Earth monitoring (GMES) programme: Status and perspectives. Remote Sensing of Environment, 120, 3-8.

Banerjee, A., and Bandopadhyah, R. (2016). Biodiversity hotspot of Bhutan and its sustainability. Current Science, 110(4). doi:10.18520/cs/v110/i4/521-528

Berardino, P., Fornaro, G., Lanari, R., and Sansosti, E. (2002). A New Algorithm for Surface Deformation Monitoring Based on Small Baseline Differential SAR Interferograms. IEEE transactions on geoscience and remote sensing, 40(11).

Bookhagen, B., and Burbank, D. W. (2009). Towards a complete Himalayan hydrological budget: Spatiotemporal distribution of snowmelt and rainfall and their impact on river discharge. Journal of Geophysical Research, 115. doi:10.1029/2009JF001426

Bovenga, F., Nitti, D. O., Fornaro, G., Radicioni, F., Stoppini, A., and Brigante, R. (2013). Using C/Xband SAR interferometry and GNSS measurements for the Assisi landslide analysis. . International Journal of Remote Sensing, 34(11), 4083-4104. doi:dx.doi.org/10.1080/01431161.2013

Carson, M. A. (1977). Angles of repose, angles of shearing resistance and angles of talus slopes. Earth surface Processes, 2, 363-380.

Casu, F., Manzo, M., and Lanari, R. (2006). A quantitative assessment of the SBAS algorithm performance for surface deformation retrieval from DInSAR data. Remote Sensing of Environment, 102(3-4), 195-210.

Cignetti, M., Manconi, A., Manunta, M., Giordan, D., De Luca, C., Allasia, P., and Ardizzone, F. (2016). Taking advantage of the ESA G-POD service to study ground deformation processes in high mountain areas: a Valle d'Aosta case study, northern Italy. Remote sensing, 8(852). doi:10.3390/rs8100852

Crozier, M. J. (2010). Deciphering the effects of climate change on landslide activity: a review. Geomorphology, 124, 260-267. doi:10.1016/j.geomorph.2010.04.009

Delaloye, R., Lambiel, C., and Gärtner-Roer, I. (2010). Overview of rock glacier kinematics research in the Swiss Alps. Geographica Helvetica, 65, 135-145. doi:doi.org/10.5194/gh-65-135-2010

Delaloye, R., Lambiel, C., Lugon, R., Raetzo, H., and Strozzi, T. (2007). ERS InSAR for detecting slope movement in a periglacial mountain environment (western Valais Alps, Switzerland). Paper presented at the HMRSC-IX. Grazer Schriften der Geographie und Raumforschung.

Diehl, T., Singer, J., Hetényi, G., Grujic, D., Clinton, J., Giardini, D., and Kissling, E. (2017). Seismotectonics of Bhutan: Evidence for segmentation of the Eastern Himalayas and link to foreland deformation. Earth and Planetary Science Letters, 471, 54-64. doi:dx.doi.org/10.1016/j.epsl.2017.04.038

Ding, X., Li, Z., Zhu, J., Feng, G., and Long, J. (2008). Atmospheric effects on InSAR measurements and their mitigation. Sensors, 8, 5426-5448. doi: 10.3390/s8095426

Doin, M.-P., Lasserre, C., Peltzer, G., Cavalié, O., and Doubre, C. (2009). Corrections of stratified tropospheric delays in SAR interferometry: Validation with global atmospheric models. Journal of Applied Geophysics, 69(1), 35-50. doi:doi.org/10.1016/j.jappgeo.2009.03.010

Dunning, S. A., Massey, C. I., and Rosser, N. J. (2009). Structural and geomorphological features of landslides in the Bhutan Himalaya derived from Terrestrial Laser Scanning. Geomorphology, 103, 17-29. doi:10.1016/j.geomorph.2008.04.013

Dunning, S. A., Rosser, N. J., Petley, D. N., and Massey, C. R. (2006). Formation and failure of the Tsatichhu landslide dam, Bhutan. Landslides, 3, 107-113.

Engelbrecht, J., Musekiwa, C., Kemp, J., and Inggs, M. (2014). Parameters affecting interferometric coherence - the case of a dynamic agricultural region. IEEE transactions on geoscience and remote sensing, 52(3), 1572-1582.

Ferretti, A., Prati, C., and Rocca, F. (2001). Permanent scatterers in SAR interferometry. IEEE transactions on geoscience and remote sensing, 39(1), 8-20. doi:10.1109/36.898661

Ferretti, A., Savio, G., Barzaghi, R., Borghi, A., Musazzi, S., Novali, F., . . . Rocca, F. (2007). Submillimeter accuracy of InSAR time series: experimental validation. IEEE transactions on geoscience and remote sensing, 45, 1142-1153. doi:dx.doi.org/10.1109/TGRS.2007.894440.

Frattini, P., Crosta, G. B., Allievi, J., and Rossini, M. (2018). Activity and kinematic behaviour of deep-seated landslides from PS-InSAR displacement rate measurements. Landslides, 15, 1053-1070. doi:10.1007/s10346-017-0940-6

Gansser, A. (1983). Geology of the Bhutan Himamalya.

Gärtner-Roer, I., and Nyenhuis, M. (2010). Volume estimation, kinematics and sediment transfer rates of active rockglaciers in the Turtmann valley, Switzerland. In R. D. e. J.-C. Otto (Ed.), Landform - Structure, Evolution, Process Control (Vol. 115): Springer-Verlag Berlin Heidelberg.

GLIMS, and NSIDC. (2005). Global Land Ice Measurements from Space glacier database. Compiled and made available by the international GLIMS community and the National Snow and Ice Data Center, Boulder CO, U.S.A. doi:DOI:10.7265/N5V98602

Gruber, S. (2012). Derivation and analysis of a high-resolution estimate of global permafrost zonation. The Cryosphere, 6, 221-233. doi:10.5194/tc-6-221-2012

Grujic, D., Warren, C. J., and Wooden, J. (2011). Rapid syn-convergent exhumation of Miocene-aged lower orogenic crust in the Eastern Himalaya. Litosphere, 3(5), 346-366. doi:doi.org/10.1130/L154.1

Gschwind, S., and Loew, S. (2016). Reconstruction of the long-term evolution of a catastrophic slope failure at the Preonzo rock slope instability complex (TI, Switzerland). Paper presented at the 12th International Symposium on Landslides, Napoli.

Gupta, R. P. a. J., B.C. (1989). Landslide hazard zoning using the GIS approach - A case study from the Ramganga catchment, Himalayas. Engineering Geology, 28, 119 - 131.

Guzzetti, F., Mondini, A. C., Cardinali, M., Fiorucci, F., Santangelo, M., and Chang, K. T. (2012). Landslide inventory maps: new tools for an old problem. Earth-Science Reviews, 112(1-2-), 42-66. doi:10.1016/j.earscirev.2012.02.001

Haeberli, W. (1985). Creep of mountain permafrost: internal structure and flow of Alpine rock glaciers. Mitteilungen der VAW-ETH Zürich, 17.

Hanssen, R. F. (2001). Radar interferometry: data interpretation and error analysis. . Dordrecht: Kluwer Academic Publishers.

Huggel, C., Clague, J. J., and Korup, O. (2012). Is climate change responsible for changing landslide activity in high mountains? Earth Surface Processes and Landforms, 37, 77-91. doi:10.1002/esp.2223

Hungr, O., Leroueil, S., Picarelli, L. (2014). The Varnes classification of landslide types, an update. Landslides, 11, 167-194. doi:10.1007/s10346-013-0436-y

ICIMOD. (2016). Bhutan Climate Change. Thimphu, Bhutan: Bhutan Media and Communications Institute (BMCI).

Iwata, S., Narama, C., and Karma. (2002). Three Holocene and late Pleistocene glacial stages inferred from moraines in the Lingshi and Thanza village areas, Bhutan. Quaternary International, 97-98, 69-78.

JAXA. (2017). ALOS World 3D. Retrieved from http://www.eorc.jaxa.jp/ALOS/en/aw3d30/index.htm

Kääb, A., Huggel, C., Fischer, L., Guex, S., Paul, F., Roer, I., . . . Weidmann, Y. (2005b). Remote sensing of glacier and permafrost-related hazards in high mountains: an overview. Natural Hazards and Earth System Sciences, 5, 527-554.

Kääb, A., Reynolds, J. M., and Haeberli, W. (2005a). Glacier and permafrost hazards in high mountains. In U. M. H. e. a. (eds) (Ed.), Global Change and Mountain Regions (pp. 225-234): Springer.

Kellett, D. A., Grujic, D., Coutand, I., Cottle, J., and Mukul, M. (2013). The South Tibetan detachment system, Sikkim Himalaya facilitates rapid cooling, not rapid exhumation. Tectonics, 32(3), 252-270. doi:doi.org/10.1002/tect.20014

Kenyi, L. W., and Kaufmann, V. (2003). Estimation of rock glacier surface deformation using SAR interferometry data. IEEE transactions on geoscience and remote sensing, 41(6), 1512-1515.

Lambiel, C., Delaloye, R., Strozzi, T., Lugon, R., and Raetzo, H. (2008). ERS InSAR for assessig rock glacier activity.Paper presented at the 9th International Conference on Permafrost University of Alaska, Fairbanks.

Long, S., McQuarrie, N., Tobgay, T., Grujic, D., and Hollister, L. (2011). Geologic map of Bhutan. Journal of Maps, 7(1), 184-192.

Martin, E., and Whalley, W. B. (1987). Rock glaciers. Part 1. Rock glacier morphology: classification and distribution. Progress in Physical Geography: Earth and Environment, 11(2), 260-282. doi:doi.org/10.1177/030913338701100205

Massonnet, D., and Feigl, K. P. (1998). Radar interferometry and its application to changes in the Earth's surface. Reviews of Geophysics, 36(4), 441-500. doi:10.1029/97RG03139

Mazzanti, P., and Pezzetti, G. (2013). Traditional and innovative techniques for landslide monitoring: dissertation on design criteria. . Paper presented at the Tagung für Ingenieurgeologie mit Forum für junge Ingenieurgeologen.

McQuarrie, N., Robinson, D., Long, S., Tobgay, T., and Grujic, D. (2008). Preliminary stratigraphic and structural architecture of Bhutan: implications for the along strike architecture of the Himalayan system. Earth and Planetary Science Letters, 272, 105-117. doi:doi.org/10.1016/j.epsl.2008.04.030

Migoń, P., Knapik, R., Jała, Z., and Remisz, J. (2010). Contemporary Evolution of Talus Slopes in the Wielki Śnieżny Kocioł Glacial Cirque. Opera Corcontica, 47.

Molnar, P. (1984). Structure and tectonics of the Himalaya: constraints and implications of geophysical data. Annual Review of Earth and Planetary Sciences, 12, 489-518.

Nagler, T., Rott, H., Ripper, E., Bippus, G., and Hetzenecker, M. (2016). Advancements for Snowmelt Monitoring by Means of Sentinel-1 SAR. Remote sensing, 8(348). doi:doi:10.3390/rs8040348

Norbu, C., Baillie, I., Dorji, T., Tamang, H. B., Tsherin, K., Hutcheon, A. (2003). A provisional physiographic zonation of Bhutan. Journal of Bhutan Studies, 8, 54-87.

NSSC. (2010). Technical report Bhutan land cover assessment. Retrieved from Thimphu, Bhutan:

Petley, D. (2012). Global patterns of loss of life from landslides. Geology, 40, 927-930. doi:10.1130/G33217.1

Przyłucka, M., Herrera, G., Graniczny, M., Colombo, D., and Béjar-Pizarro, M. (2015). Combination of Conventional and Advanced DInSAR to Monitor Very Fast Mining Subsidence with TerraSAR-X Data: Bytom City (Poland). Remote sensing, 7, 5300-5328. doi:doi.org/10.3390/rs70505300

Roer, I., Haeberli, W., Avian, M., Kaufmann, V., Delaloye, R., Lambiel, C., and Kääb, A. (2008). Observations and considerations on destabilizing active rockglaciers in the European Alps. Paper presented at the 9th International Conference on Permafrost, University of Alaska, Fairbanks.

Rosser, N., Lim, M., Petley, D., Dunning, S., and Allison, R. (2007). Patterns of precursory rockfall prior to slope failure. Journal of Geophysical Research: Earth Surface, 112(F4). doi:10.1029/2006jf000642

Stoffel, M., and Huggel, C. (2012). Efects of climate change on mass movements in mountain environments. Progress in Physical Geography, 36(3), 421-239. doi:10.1177/0309133312441010

Strozzi, T., Ambrosi, C., and Raetzo, H. (2013). Interpretation of aerial photographs and satellite SAR interferometry for the inventory of landslides. Remote sensing, 5(5), 2554-2570. doi:10.3390/rs5052554

Strozzi, T., Kääb, A., and Frauenfelder, R. (2004). Detecting and quantifying mountain permafrost creep from in situ inventory, space-borne radar interferometry and airborne digital photogrammetry. International Journal of Remote Sensing, 25(15), 2919-1931.

Velasco, A. A., Gee, V. L., Rowe, C., Grujic, D., Hollister, L. S., Hernandez, D., . . . Harder, S. (2007). Using Small, Temporary Seismic Networks for Investigating Tectonic Deformation: Brittle Deformation and Evidence for Strike-Slip Faulting in Bhutan. Seismological Research Letters, 78(4), 446. doi:10.1785/gssrl.78.4.446

Wasowski, J., and Bovenga, F. (2014). Investigating landslides and unstable slopes with satellite Multi Temporal Interferometry: Current issues and future perspectives. Engineering Geology, 174, 103-138. doi: 10.1016/j.enggeo.2014.03.003

Walker, B. (2016). Erratic weather spells, tough time ahead for Bhutan's hydropower. Retrieved from https://www.thethirdpole.net/2016/04/22/erratic-weather-spells-tough-time-ahead-for-bhutans-hydropower/

Werner, C., Wegmüller, U., Strozzi, T., and Wiesmann, A. (2003). Interferometric point target analysis for deformation mapping. Paper presented at the IGARSS, International Geosciences and Reomte Sensing Symposium, Toulouse, France.

Wiesmann, A., Wegmüller, U., M, H., Strozzi, T., and Werner, C. (2001). Potential and methodology of satellite based SAR for hazard mapping. Paper presented at the IGARSS Scanning the Present and Resolving the Future. Proceedings. IEEE 2001 International Geoscience and Remote Sensing Symposium, Sydney, NSW, Australia, Australia.

2.8. Appendix

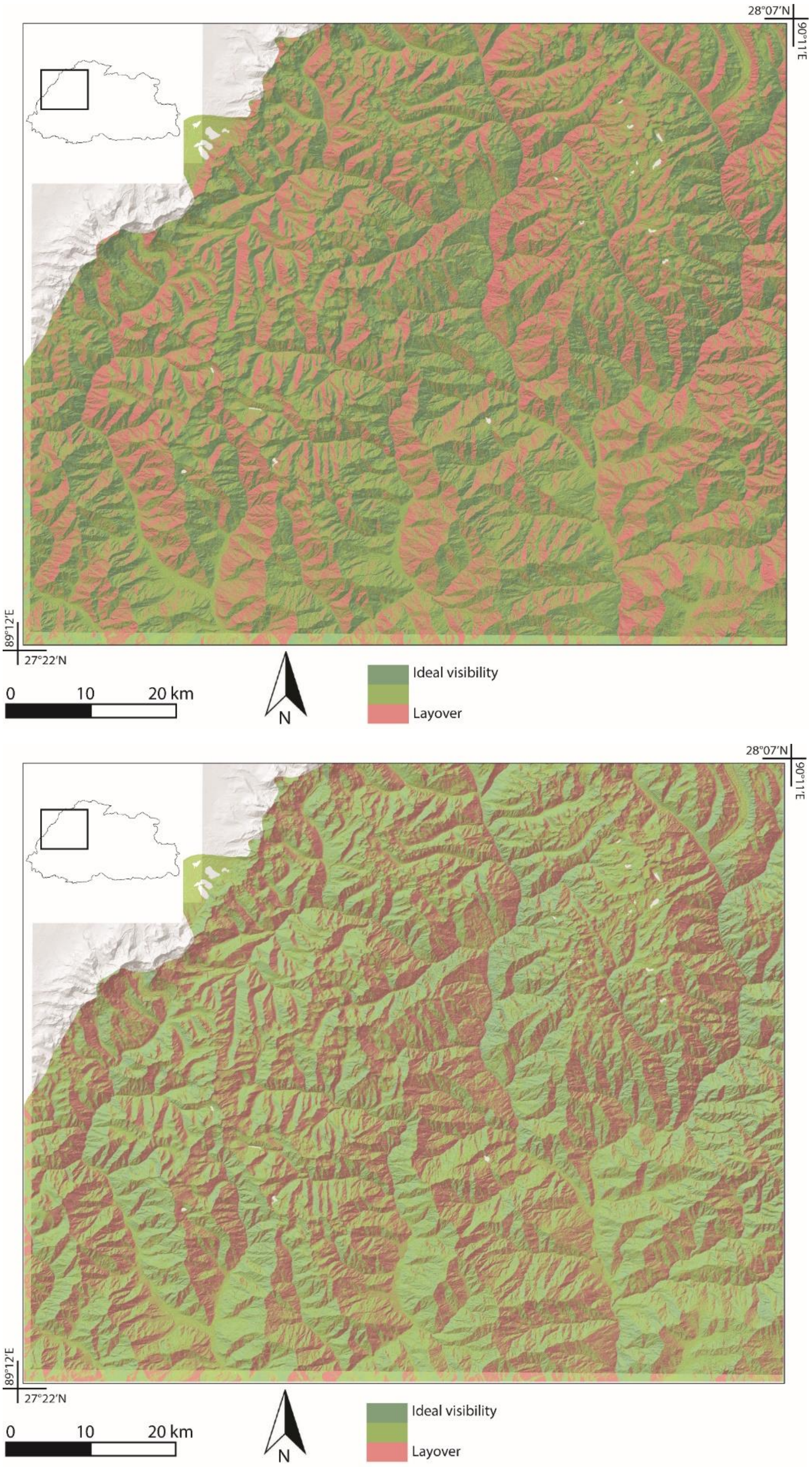

App. 2-1. Layover maps for ascending (top) and descending (bottom) geometries.

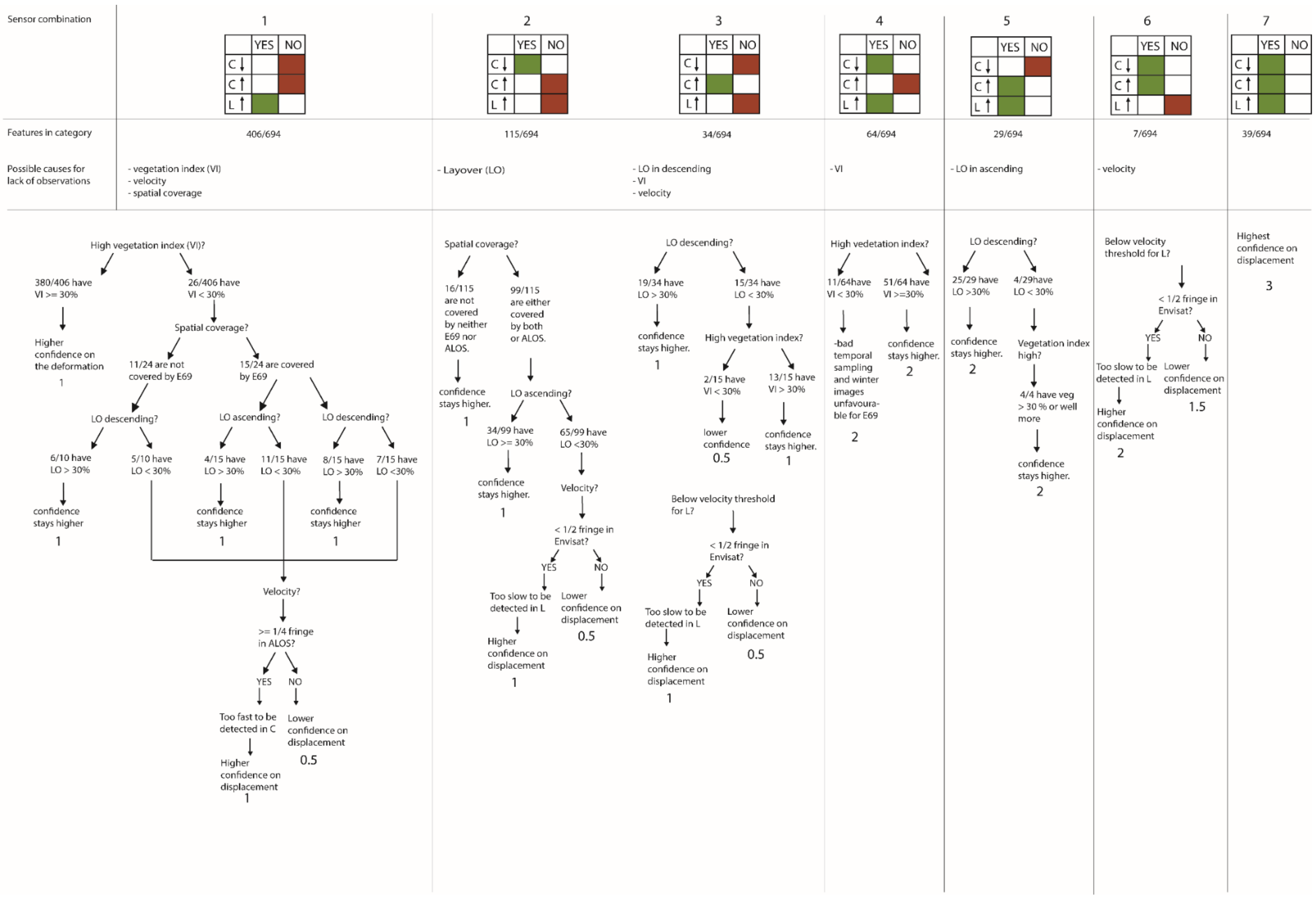

App. 2-2 Decision tree used to identify weights to apply to the active areas identified through analysis of the interferograms. Each column corresponds to a combination of sensors.

3. The Punatsangchhu-I dam landslide illuminated by a multi-sensor InSAR time series analysis

Benedetta Dini1, Andrea Manconi[1], Simon Loew[1]

[1] Department of Earth Sciences, ETH Zurich, Zurich, Switzerland

Abstract

Recent developments in Bhutan have led to the planning of several hydropower plants within an initiative aimed at reaching a capacity of 10000 MW by 2020. Works at the Punatsangchhu-I plant began in 2009. A large failure occurred in 2013 on the right flank, immediately upslope of the dam, likely as consequence of toe undercutting of a previously unrecognised rock slope instability. Stabilisation efforts have been undertaken, leading to increased costs and delays. Our multitemporal Synthetic Aperture Radar interferometric (InSAR) analysis indicates that downslope displacements affected various sectors of the valley flank already since 2007. Moreover, the unstable area impinging on the dam site has continuously increased in size, exhibiting accelerating creep into 2017. Not only the unstable area is much larger than expected (and thus the volumes involved), but the effects of the stabilisation measures, focused on a small portion of the unstable flank, are also questionable. Our analysis shows that InSAR can be used to identify instabilities, without previous site knowledge, and it can be used to assess the real extent, magnitude and evolution of the displacements and the effectiveness of stabilisation measures, shedding light on the suitability of a given site and the feasibility of a project.

3.1. Introduction

The narrow valleys of deeply incised mountainous ranges represent an ideal set-up for the construction of dams, because they allow to create large reservoirs with the minimum structure width. When valley flanks are affected by landslides, they offer, at least at first sight, the picture of an appealing site for building a dam (Schuster, 2006; Legget, 1939), as the valley constriction that landslides cause provides a deep, narrow gorge bounded by steep sides. However, gravitational movements at the abutment of a dam can also have critical consequences. A notable case of a dam built directly on a landslide is the Beauregard dam, in northwest Italy. Here, a deep-seated gravitational slope deformation impinges directly on a 132 m high concrete arch-gravity dam (Barla et al., 2010). The landslide, with a depth of 240 m in the lower parts (Barla et al., 2010) and a volume of 200 millions m3 (Marcello and Meda, 2013), had its onset about 10 ka ago and it experienced reactivation after the filling of the reservoir in 1958, showing significant displacements across a large portion of the slope. Though this dam is still operational, the recognised necessity of maintaining safety and avoiding a potential catastrophic failure, has led to a substantial decrease of the dam maximum operating capacity. With a planned reservoir capacity of 70 hm3 and a height of 1765 m a.s.l., the dam has been kept in operation at a capacity limited to 2.3 hm3 and a reservoir height 62.5 m lower than originally intended. Landslides and dams interact also when the dam is built in the vicinity of pre-existing instabilities. The modifications in the hydrological conditions at the toe of a slope caused by induced river flow changes and by the presence of a reservoir are associated with variations in the distribution of pore water pressure within the slope, leading to new water table conditions and fluctuations that get superimposed to natural seasonal cycles (Havaej et al., 2015; Liu et al., 2013; Barla et al., 2010). The consequences of catastrophic slope failures into a dammed lake can be extremely serious and have impacts a long way downstream of the site. Though the list of landslides built in close proximity to dams is long (Schuster, 2006), a notable case is the Vajont dam, in northeast Italy, the story of which is tragically known for its devastating epilogue. In October 1963, a 250 million m3 rock mass slid into the Vajont reservoir, causing a wave that destroyed an entire village and killed around 2000 people. It has been accepted in the literature that the failure was caused by the reactivation of a prehistoric rock slide (Wolter et al., 2014), the identification of which was not disclosed nor fully investigated at the design stage (Barla and Paronuzzi, 2013). In the first half of the past century, in a rapid growth of the hydropower sector, a large number of dams were built around the world without adequate investigations and without a full understanding neither of the geological and geotechnical problems nor of the potential catastrophic consequences that negligence in addressing them could cause (Schuster, 2006). However, nowadays, little space for disagreement is found in the literature regarding the utmost importance of carrying out appropriate investigations in the leading up to the choice of a dam site. The monitoring of slopes impinging on or in the vicinity of a planned or existing hydropower plant is an important aspect in the identification of potential instabilities.

In the past two decades, synthetic aperture radar differential interferometry (DInSAR) has gained increasing importance in imaging unstable slopes, due to its suitability to retrieve information over large and inaccessible areas, whilst potentially ensuring a continuous, versus point-like, overview of the displacements affecting the illuminated ground surface (Colesanti and Wasowski, 2006; Luzi et al., 2006; Tralli et al., 2005). The usage and usefulness of this technique have been demonstrated, in the specific cases of the interaction between dams and landslides, for example for the Beauregard landslide (Ground Based InSAR, Barla, 2010) and for various landslides in China, such as the Guobu landslide upstream of the Laxiwa power station (Li et al., 2019), the Badong county landslides (Liu et al., 2013) and the Xintan landslide (Xia et al., 2004) upstream of the Three Gorges dam. These studies show that DInSAR is able to detect displacements over sectors of the monitored instability for which no prior knowledge existed and that the widespread information of displacements can facilitate the interpretations of the landslide’s behaviour and mechanisms. Moreover, DInSAR allows to monitor the spatial and temporal evolution of the displacements and to make correlations between water level changes and seasonal landslide movements, enabling the understanding of the impact of water level variations on the reactivation of pre-existing landslides.

Developing countries characterised by mountainous terrain and high relief, such as many Himalayan countries, are experiencing an increase push towards the expansion of hydropower, which is seen as a promising revenue source, thanks to the exploitation of a seemingly favourable geographical setting. In recent years, a large initiative jointly launched by the governments of Bhutan and India, has led to the planning of several hydropower plants to be built in Bhutan by 2020, with an expected overall power output of 10000 MW (World Bank Group, 2016). 80% of the energy produced will be sold to India (Roychoudhury and Srinivasan, 2016; Walker, 2015), the revenue coming from this sector already amounting to 25% of Bhutan GDP (Kirchherr et al., 2016; Walker, 2016) and being expected to soar in the future. As India largely controls the planning and construction of hydropower plants, is the main consumer of most of the electricity produced and grants loans to Bhutan to cover for project costs, the political aspect of this rapid hydropower growth has a profound effect on the assessment and management of environmental hazards. Recent studies have shown that risk management and disaster preparedness have been sidelined in hydropower planning processes across the Himalaya (Huber, 2019). This may be due not only to failure in producing adequate geological and geotechnical assessments, but in fact, more gravely, to the fact that “a blind-eye to environmental risks facilitates the appropriation of economic benefits by powerful interest groups” (Huber, 2019). In the same study, the author highlights the importance to influence the increase of knowledge about risks in order to create a basis for a more aware and informed debate around hazardous hydropower projects. Bhutan, despite its recent hydropower history, is not free from related disasters. In August 2015, for example, a landslide occurred at the Mangdechhu dam site burying 6 workers (Dolkar, 2019; Petley, 2015). Another potentially hazardous project is the Punatsangchhu-I, object of the present work. The 1200 MW Punatsangchhu-I hydropower project, located 20 km south of Punakha and 50 km east of the capital Thimphu, is part of the 10000 MW initiative and it comprises a 136 m high gravity concrete dam (Sati et al., 2017), two diversion tunnels and a 10 km long headrace tunnel (International Rivers, 2015). The project began in November 2009 and it was initially scheduled to be completed by 2015. Inadequate geological and geotechnical investigations have, however, caused large delays and a soaring in the overall costs (Lamsang, 2017), with the project not yet being completed as of today. A large failure, estimated at 1 million m3 (PHPA pers. comm.) occurred in July 2013 on the east facing slope (Palden, 2017), causing the construction works to come to a halt in favour of a huge effort aimed at stabilising the lower portion of the slope (Dolkar, 2017). More recently, in January 2019, another failure injured a worker and caused additional damage (Dema, 2019). The lack of knowledge and understanding on the part of all parties involved regarding the nature and extent of the real problem, during planning, design, excavation and construction phases, has led to costly delays and the potential future amplification of an existing natural hazard. It is reported that, for example, in 2012 the risk perceived or acknowledged was minimal: "With the completion of the Punatsangchhu-I head race tunnel excavation on August 21 we aren't left with any geological uncertainty" (Norbu, 2012).

In this study, we measure the spatial and temporal evolution of the surface displacements over an area of 15 km2 at the Punatsangchhu-I dam site (Fig. 3-1). Our observations cover a period before and during the construction works, with 11 years of SAR data, acquired by ALOS-1, ALOS-2 and Sentinel-1 between 2007 and 2018. A multi-temporal InSAR analysis highlights that the valley flank was already affected by creep before the start of the construction of the dam and shows an increase of the surface displacement rates subsequent to the beginning of the works. The spatial coverage of the measurements also highlights that the instability is not only affecting the area immediately around the 2013 failure, but it covers a much larger area of about 8 km2 in total. This could have critical implications for the volumes of rock involved, which could be of the order of tens or even hundreds of millions of m3 in the worst-case scenario. Our measurements underline that remote sensing techniques, and in particular InSAR, could have allowed stakeholders to identify a potential problem at this site and understand its extent before the instalment of such critical infrastructure. The increased availability of remote sensing data has now the potential to play an important role in filling

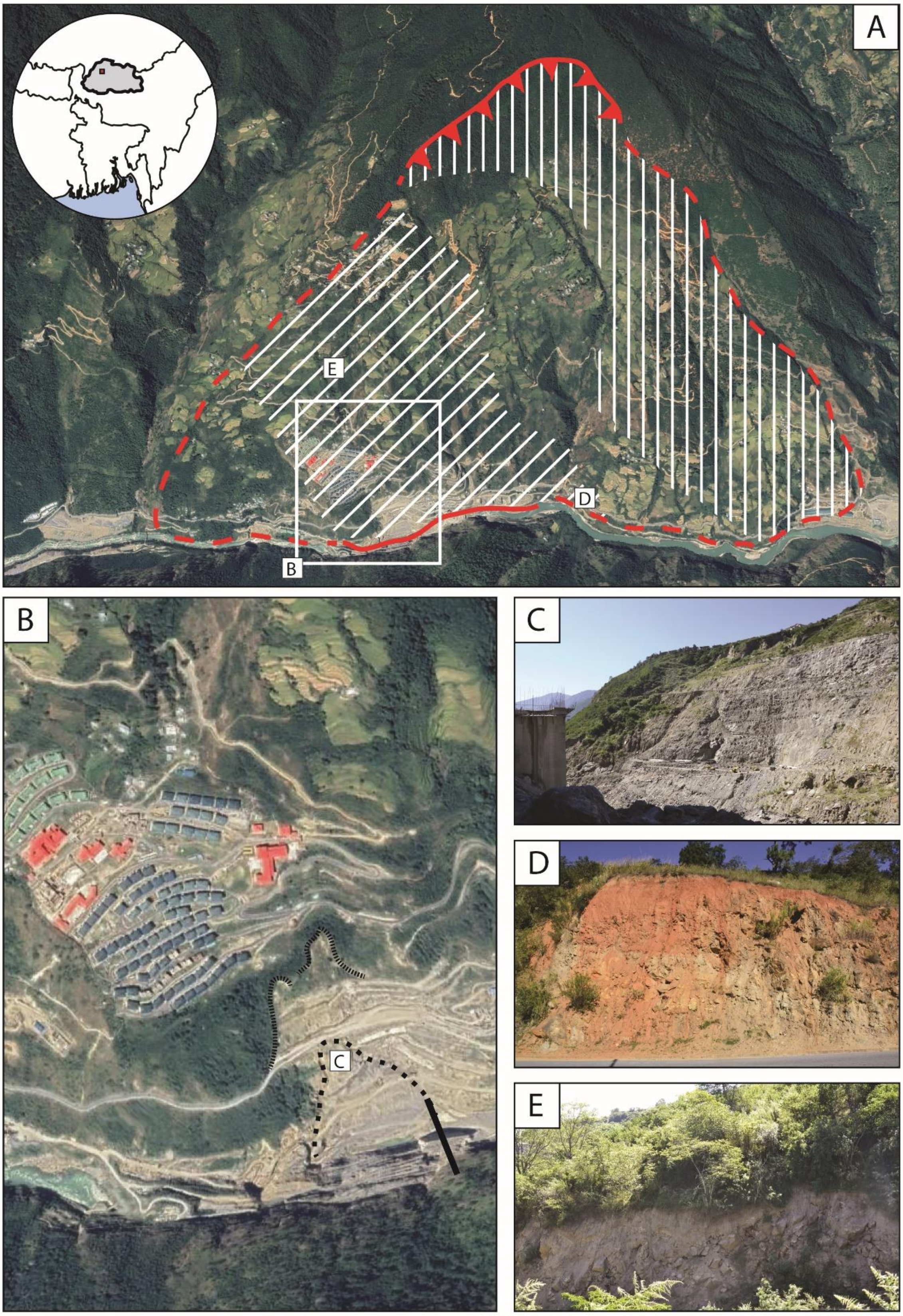

Fig. 3-1. A) Area of study. Red lines represent head scarp (with triangles), presumed (dashed) and known (continuous) boundaries. Hatch areas represent damaged rock (diagonal) and undisturbed residual soil (vertical). White square is the area in B. Inset shows regional setting. B) Black line represents dam axis, thick dotted line indicates 2013 failure area, thin dotted lines indicate fresh scarps. C) Photo of 2013 failure area. D-E) Intensely damaged rock.

a gap in the site-specific knowledge caused by insufficient or inadequate investigations and can significantly increase the transparency and public awareness around such large projects and the associated risks.

3.2. Results

The observation period starts in February 2007 and ends in October 2018 (table 1), with ALOS-1 covering a four years period between February 2007 and February 2011, ALOS-2 a two and a half years period between September 2014 and March 2017 and Sentinel-1 a four years period between October 2014 and October 2018. Our results show that there are different sectors of the entire valley flank that are affected by displacements through the observation period (Fig. 3-2). Such sectors are identifiable because they are characterised by spatially continuous patterns of downslope displacements. Each of these sectors shows changes in the areal extent and significant cumulative displacements during the periods illuminated by the three sensors and some of them also show displacement rates changes in the time series.

3.2.1. Areas and cumulative displacements

The sectors observed are described in detail in this section, and shown in the upper panels in Fig. 3-2. Cumulative displacements described in this section are in line of sight (LOS) and away from the satellite. Given that the used tracks are all ascending, and the LOS is almost west to east, the displacements observed are compatible with downslope movements. The visibility coefficient calculated for the slope (section 3.4) indicates that, on average, about 70% of the downslope component is detected. Thus, assuming that the main component is downslope, then the real displacements could be more than 40% higher than observed.

Sector A, as seen by ALOS-1 is characterised by an area of cumulative displacements > 100 mm covering about 0.44 km2. A larger area of 2.35 km2, encompassing the higher displacements zone and extending 1200 m upslope from its upper margin, shows cumulative displacements between 50 mm and 100 mm. This larger extent is well matched by the observations retrieved with ALOS-2, where the areal extent of cumulative displacements higher than 20 mm is approximately 1.9 km2. However, the cumulative displacements are on the whole lower than those observed with ALOS-1, with maxima reaching 70 mm. The extent of the displacements in this sector becomes patchier in Sentinel-1 observations, and the boundaries less well traceable. Cumulative displacements do not exceed 100 mm through Sentinel-1’s observation window and the highest values are restricted to the toe of the slope and at around 1360 m of elevation.

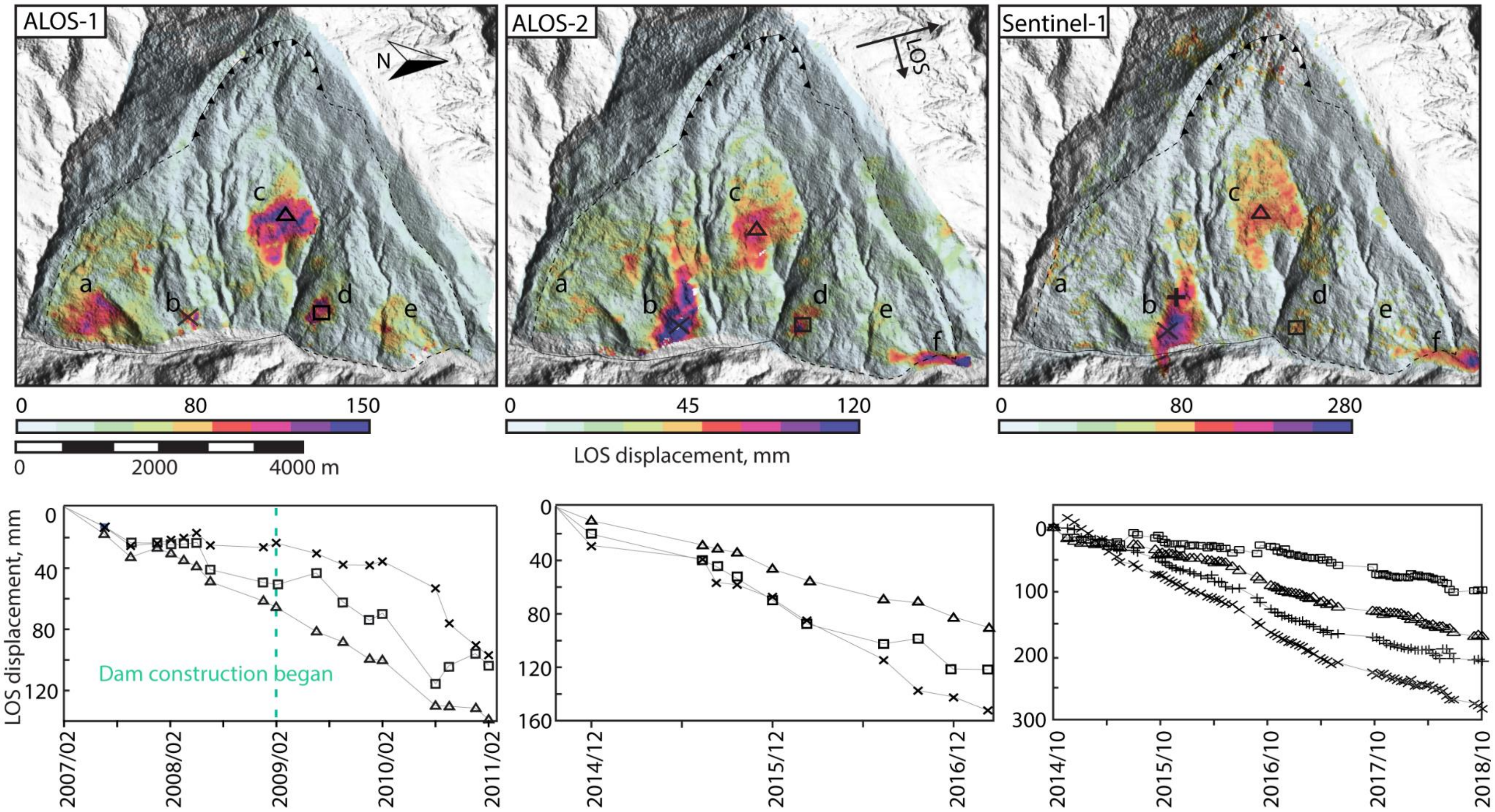

Fig. 3-2. The top three panels show LOS cumulative displacements in the three sensors. Colour scales are different and non-symmetrical to highlight areas of highest displacements. Letters indicate the sectors described in section 3.2. Panels at the bottom show the time series of three points in sectors B, C, and D. Points shown in panels above.

Sector B in ALOS-1 shows two different areas with displacements above 50 mm, both with extent of approximately 0.1 km2. The higher one presents lower cumulative displacements with maxima around 70 mm, the lower one, at the toe of the slope, is characterised by larger displacements, reaching 150 mm. ALOS-2 shows a marked areal increase of 900%, the overall extent reaching 1 km2, comprising the two areas observed with ALOS-1. Displacements are largely above 80 mm and reaching up to 220 mm in the lowest half. Although the boundaries are more jagged in the upper parts in Sentinel-1 data, the area is comparable to that seen in ALOS-2 and displacements exceed 300 mm in the lower half.

ALOS-1 displacements in sector C cover an area of 1.2 km2. Cumulative displacements have a very coherent appearance and gradients increasing towards the middle of the area. Displacements are largely above 50 mm and exceed 150 mm in the central parts. This area increases to 2 km2 in ALOS-2 displacements map, with values largely above 30 mm and exceeding 90 mm in places. The area of higher cumulative displacements appears shifted towards the south in comparison to ALOS-1. The area observed with Sentinel-1 is similar in extent (1.9 km2), though again it presents a shift, this time upslope and towards the north. Displacements are largely above 50 mm and reach up to 170 mm in the centre.

Sector D covers an area of 0.4 km2 in ALOS-1 cumulative displacements map. Displacements are on the whole above 50 mm and increasing up to 130 mm towards the lower half of the area. The area is comparable in size in the ALOS-2 displacements map, covering approximately 0.3 km2, with displacements above 30 mm and up to 130 mm. A small decrease in extent and a patchy appearance of the displacements is seen in Sentinel-1, with a 0.2 km2 area and with displacements on the whole above 50 mm but up to 110 mm.

Sector E as illuminated by ALOS-1 is characterised by an area of 0.5 km2. Cumulative displacements lie between 70 and 100 mm. ALOS-2 suggests that the area shrinks in its period of observation to 0.3 km2, with cumulative displacements above 30 mm in general and up to 70 mm at elevations between 1250 and 1280 m a.s.l.. Sentinel-1displacements over this sector appear patchy, with unclear boundaries. Cumulative displacements between 100 and 120 mm represent the maxima and are found again between 1250 and 1280 m a.s.l..

Sector F is not visible in the cumulative displacements map of ALOS-1, but it appears in the period of observation of the other two sensors. With ALOS-2 the area is seen as covering an extent of 0.16 km2, with cumulative displacements up to 160 mm. The area increases to 2.4 km2 and is affected by cumulative displacements of up to 320 mm, as observed with Sentinel-1.

3.2.2. Time series

Time series are analysed and described here for sectors B, C and D, and are shown in the lower panels in Fig. 3-2.

In sector B, the ALOS-1 time series of a point at 1300 m of elevation shows a non-linear trend. In the first half of the period, from February 2007 to February 2009, the trend is shallow, followed by two acceleration phases during the second part of the period, from February 2009 until February 2011. The trend for the same point as seen with ALOS-2 and Sentinel-1 shows an increase in creep velocity in comparison to the previous period and linearity between September 2014 and June 2017. Sentinel-1 shows then a decrease in the displacement velocity after June 2017, though linearity is again seen through this last period. Velocities in this sector and their variations in time are described in detail in section 3.3.3. On the whole, the time series in the centre of sector C show linear trends. The cumulative displacements observed over the different periods of observation of the three sensors show that the creep velocity remained similar throughout the whole period, lying relatively steady between 32 mm/year (ALOS-1) and 37 mm/year (ALOS-2 and Sentinel). Short periods of acceleration which deviate from the linear trend are observed between three pairs of ALOS-2 images and in Sentinel-1 time series.

The time series of a chosen point in sector D generated with ALOS-1 images is non-linear. An initial phase with a lower velocity is visible up to end of June 2009. After that, a period of acceleration is observed until August 2010. Assuming linear trends, we observe a change in velocity from 20 mm/year, to 70 mm/year for ALOS-1 in the periods identified, to around 50 mm/year as observed with ALOS-2 and then decreasing again to 30 mm/year through the rest of the period.

3.2.3. Velocities across profile intersecting sector B

Velocities were calculated along a profile intersecting sector B (inset in Fig. 3-3), from west to east and from 1620 to 1150 m a.s.l., using ALOS-1 and Sentinel-1 data, given the partial overlap between ALOS-2 and Sentinel-1. Fig. 3-3 shows the LOS velocity calculated assuming linear displacement rates over four different periods, the latter defined by changes in the observed trends (as seen in the lower panels in Fig. 3-2). Between February 2007 and February 2009, the velocity remained relatively constant along the profile, at around 20 mm/year or less. From February 2009 the velocity increased remarkably between 1450 and 1350 m a.s.l. from less than 20 mm/year to 60 mm/year, and below 1250 m a.s.l. it increased to about 30 mm/year. A further acceleration is observed from October 2014 to May 2017. During this period, we observe that between 1600 and 1450 m a.s.l. the velocity shows a downslope increase, reaching 70 mm/ year. Moreover, after a 100 m wide bench at 1450 m a.s.l., the velocity increases downslope up to 90 mm/year at 1350 m a.s.l.. Although downslope of 1300 m of elevation the velocities appear lower than in the upslope sections during this period, we still observe an overall increase from the previous period. Only in the last period, from May 2017 to October 2018 we observe a decrease in creep velocities: although there are still parts of the slope with increasing downslope gradients, the overall velocities along the profile are lower in comparison to the previous interval, though remain higher in comparison to the beginning of the observation.

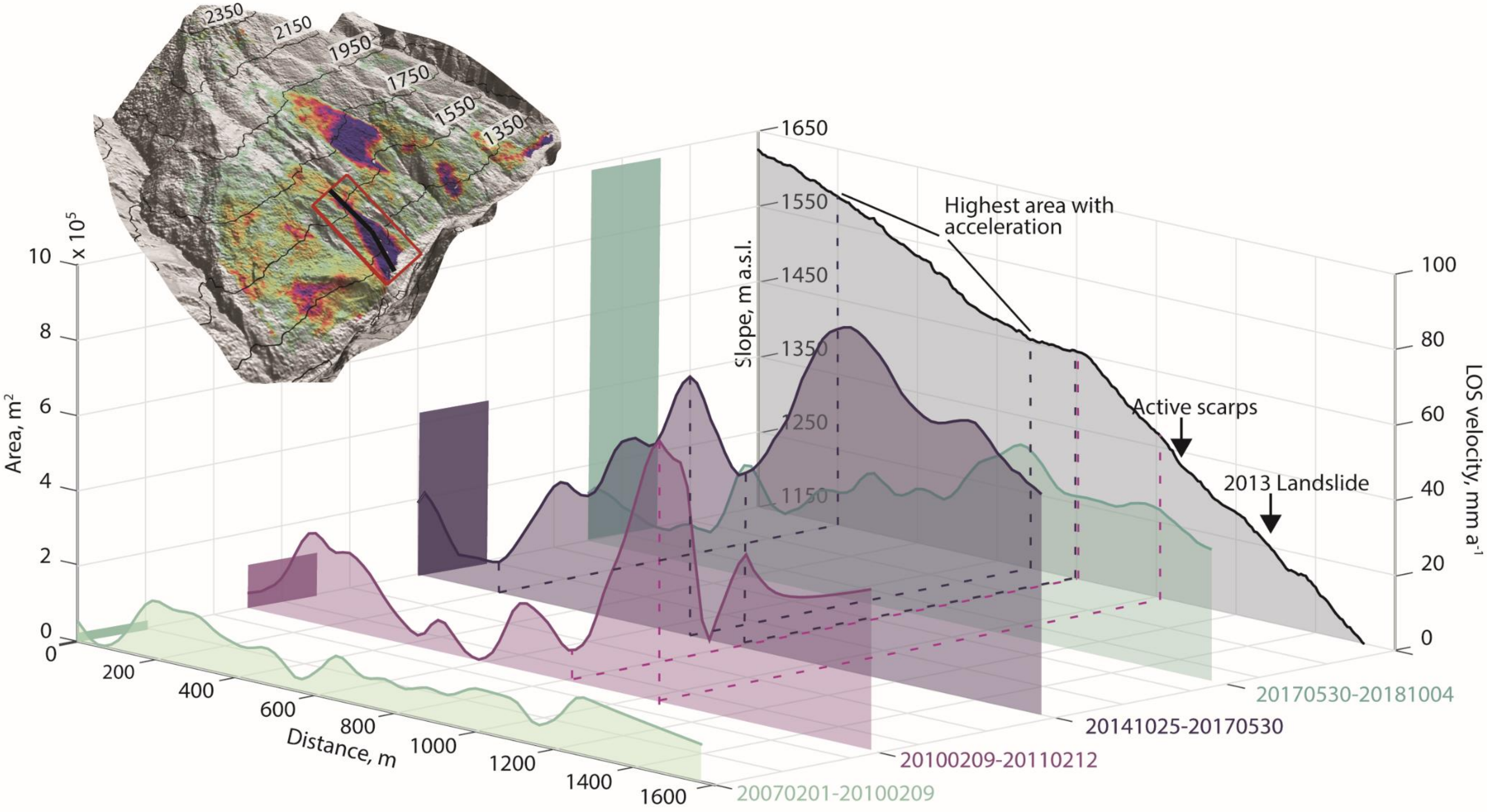

Fig. 3-3. 3D illustration of velocities along a profile intersecting sector B. Distance along the profile shown on left horizontal axis. Slope profile shown in black. The periods over which velocities are calculated are shown on the right horizontal axis. Histogram of the area size is shown on the left vertical side, whilst velocity is shown on the right vertical axis. Inset shows the sum of cumulative displacements (stack) of all sensors over the entire slope, in red polygon the area of sector B and in black the profile are shown.

3.2.4. Geomorphological observations

Analysis of the high-resolution DSM (see section 3.4) reveals the presence of an old head scarp, with heights varying between 30 and 100 m. The scarp can be followed for an arched path of 3 km, from 2030 m a.s.l. in the south, to 2430 m a.s.l. at its highest point below the ridge top, to 2080 m a.s.l in the north (Fig. 3-1A). A convex profile is also present below 1600 m a.s.l., with bulging in the lower parts of the slope. Erosion at the toe, visible in a GoogleEarth image prior to 2009, indicates active river incision, particularly evident in the south; moreover, in the northern half of the slope, a marked curvature in the river bed towards the opposite side of the valley is also present. An abundance of deeply incised channels, visible both in the DSM and in the optical images, suggests high erodibility of the material (Fig. 3-1A). This dense network of channels is coupled with a high roughness of the topography, which confers an irregular morphology to the slope.

During a field visit in October 2017, some more observations were made. We observed intensely damaged rock across a large part of the slope (Fig. 3-1 A-C-D-E). This extends from the village's area, upslope to the smaller settlement on the southern flank of the slope at around 1800 m a.s.l. and then north into the middle of the slope. Outcrops along the farm road in the northern half of the slope show relatively undisturbed residual soils, with preserved parent rock structure. Fresh scarps were observed below the village at elevations going from 1250 m a.s.l. in the south, intersecting the road, to 1340 m a.s.l.at the highest point, to 1290 m a.s.l. in the north (Fig.3-1B). These scarps, with an estimated height between 10 and 20 m, are also visible in Google Earth images. A large deposition is also observed below the village, this corresponding to the accumulation of the 2013 event (Fig 3-1B). The lower parts of such deposits are intensely reworked by activity at the site.

The opposite valley flank has a very different aspect, as it can be seen in the DSM and on the field. Analysis of the DMS indicates a smoother morphology and steeper slope angles. This is consistent with the fact that intact rock was observed in the field. Faults were not directly observed on the right flank, but measurements were collected on the left valley flank. Here, we observed faults dipping generally towards the northwest (average dip direction 330°) at an average angle of 55°.

3.2.5. In-situ data (section not for publication)

A total station installed at the site on the left abutment on the dam has recorded the movements of reflectors placed within the 2013 failure area. 39 reflectors were installed between the deposit of the 2013 failure and the scarps below the village, thus covering an area 300 m wide and 400 m high (Fig.3-4). The data from these reflectors was converted into the line of sight of the satellites for comparison. In Fig. 3-4, the corrected time series of 24 of these reflectors are shown, along with 2 ALOS-2 and 2 Sentinel-1 time series of points sampled in the area. From December 2014 to June 2015 a very fast downslope displacement is recorder by all reflectors and such acceleration is not captured by the satellites. However, from June 2015, the velocity shown by the reflectors decreases and the time series obtained with the satellite data reproduces very well this trend. An acceleration in June 2016 is shown by the reflectors and captured by ALOS-2 time series.

3.3. Discussion and conclusions

3.3.1. Displacements in relation to site history

A detailed history of the events occurred at the site is not known to the authors, however, a few key points are established. Works at the site began in November 2008 (Chattopadhyay, 2012), large floods occurred in 2009 (Norbu, 2012), in summer 2013 a significant failure occurred on the east facing slope (Palden, 2017), in correspondence with the dam axis. Since then, and at least up to October 2017, stabilisation measures were under way (Dolkar, 2017), and no further construction was carried out. The first acceleration phase in sector B, thus in the area of the 2013 failure, is observed in our time series from 2009. This acceleration could be a response of the slope to either high rainfall totals or to the undercutting of the toe caused by excavation works or, more likely, to a combination of these factors. Another sector of the slope shows acceleration in a similar period, sector D, in an area largely unaffected by works at the site. This seems to indicate that rainfall totals, and increased river erosion during the monsoon and the reported floods, may be at least partly responsible for the increasing creep velocities. However, whilst sector D remains largely unchanged through 2018 in terms of areal extent of displacements and displacements rates, these parameters both increase substantially for sector B. This seems to suggest that undercutting of the toe in sector B and the disturbances due to excavation works have played a substantial role. The gap in our time series between February 2011 and September 2014 does not allow for speculations regarding the fact that the continued acceleration period in sector B between 2009 and 2011 is precursory of the 2013 failure. From September 2014 until mid-2017, ALOS-2 and Sentinel-1 show two main phases of acceleration. These two acceleration phases appear to be largely independent from rainfall rates, given the continuous trends that each of them sets the scene for which is independent from seasonality. However, short periods of even faster acceleration likely related to monsoonal rainfall can also be seen superimposed on the overall trends of ALOS-2 time series (between September and November 2014, July and August 2015 and July and September 2016). The period between end-2014 and mid-2017 seems to indicate that the stabilisation measures undertaken at the toe of sector B from 2013 onwards have not dampened the slope displacement rates and, in fact, accelerations post 2013 are observed together with an increase in the extent of the displacements area The last period in our time series, from.

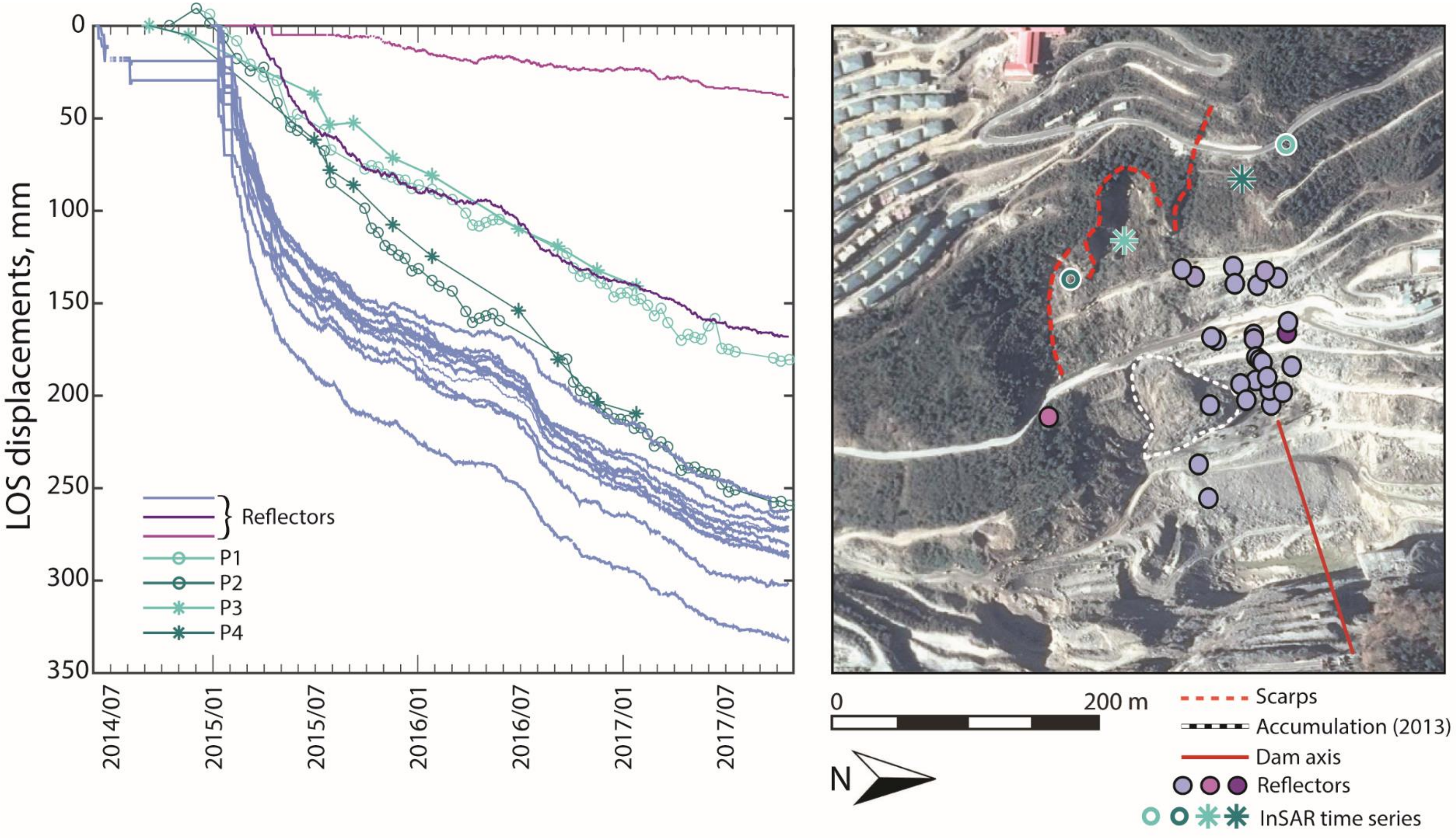

Fig. 3-4. Left: comparison between in-situ data (solid lines) and satellite based time series (lines with markers). Right: area of 2013 failure with location of reflectors and sampling points of satellite observations. (Not for publication)

mid-2017 to end 2018 shows a decrease in the creep velocities in comparison with the previous three years. The question could be raised as to whether the stabilisation activity at the site has, at that stage, contributed to a decrease of displacement rates. However, there are indications that the monsoon seasons of 2017 and 2018 were characterised by lower rainfall totals than in previous years (see appendix 3-1), which may have contributed to a reduction in the displacement rates associated with lower pore water pressures and river erosion power. Despite the lower displacement rates observed through the last period, a new failure occurred on January 22nd 2019 (Dema, 2019), outside the period of our time series, in the same area of the 2013 failure, indicating that the problem is still persisting.

3.3.2. Instability type, size and implications for potential volumes

The overall area affected by displacements is approximately 8 km2, when all sectors are considered, which is about 60% of the areal extent of the valley flank. The well-defined, separate boundaries of the identified sectors may suggest that different, potentially shallow instabilities are present. However, there are a number of important observations that suggest that the entire valley flank may be affected by a deep-seated instability, on which secondary rock slides have developed. First of all, the head scarp and the morphology of the valley flank, including the bulging of the toe and the roughness of the terrain are compatible with one large, deep seated instability. Moreover, intensely fractured and damaged rock was observed in outcrops scattered over an area estimated to be between 4 and 5 km2, encompassing sectors A and B. Although sector C was not accessed during the field visit, the displacements observed here would suggest a similar degree of internal deformation as that observed in the southern portion of the slope. Sporadic observations in the northern half of the slope indicated undisturbed residual soil, hence suggesting a lesser degree of internal deformation as opposed to the southern half. Indeed, the lower displacements and the smaller areas of sectors D, E and F indicate a lower degree of activity. Nonetheless, the northern part of the slope could also be part of the large instability, though a complex geometry of the basal shear plane would be required to explain the different activity levels and surface observations.

Our data shows that the area affected by significant downslope displacements in sector B reached a maximum extent of 1.5 km2. The 2013 failure was estimated at 1 million m3 (PHPA pers. comm.). The area that is targeted for stabilisation as seen in Google Earth is about 4000 m2, immediately to the north of the 2013 accumulation zone and approximately between 1220 m and 1190 m a.s.l., this is three order of magnitude smaller than the area covered by sector B. Moreover, assuming that the area of the 2013 failure is considered to be between 50000 and 100000 m2, if extending the upper and lateral boundaries to the scarps observed (Fig.3-1B), then depth would be between 10 and 20 m to obtain a 1 million m3 volume. Since the scarps observed are compatible with such depths, then it can be assumed that the depth of the instability in sector B alone is at least that. An area of 1.5 km2 with a depth of 10 to 20 m would imply volumes comprised between 10 and 30 million m3, thus an order of magnitude larger than the estimated volume of the 2013 failure. In the scenario in which the entire valley flank is affected by a deep-seated instability, then the volumes involved would dwarf the volumes of the 2013 failure and would potentially be an order of magnitude larger than the scenario presented here for sector B. The depth of an instability affecting the entire valley flank could be associated with higher depths than those hypothesised here, and sector B could in fact be a shallower, secondary rock slide.

3.3.3. Displacements in relation to geomorphological observations

We observe that features of the displacement gradients are in some cases associated with secondary scarps or with deeply incised channels. For example, in sector A, the highest displacements are observed below a scarp at 1360 m a.s.l., quite evident under the village. The more diffused region of lower displacements extends upslope, and is bounded in the south by the flank of the presumed larger instability and by a channel in the north. In sector D and sector E, two scarps observed in the DSM mark the upper boundary of the maximum displacements. These scarps have a height of 7 and 16 m and the base at 1452 m a.s.l. and 1272 m a.s.l. respectively. In sector B, the first acceleration phase (February 2009 – February 2011) also corresponds to highest accelerations over a portion of the slope between 1350 and 1450 m a.s.l. This area shows a steep, linear profile just downslope of a flat bench and immediately upslope of the fresh scarps likely related to the 2013 failure (Fig. 3-3). In the following acceleration phase, again creep velocities increasing downslope are observed in the same slope sector, between 1350 and 1450 m a.s.l.. Moreover, in this period, accelerating creep is observed also over a section upslope of this, between 1450 and 1600 m a.s.l.. These observations, suggesting successive acceleration phases over increasingly high portions of the slope, could point to a response of the slope to a retrogressive failure. Finally, the displacements observed in sector E, which are absent in the period of ALOS-1 and appear later, are related to intense modifications occurring at the ground surface, due to human activity, as shown by Google Earth images between 2002 and 2013. The correlation of the location of the displacements with such geomorphological or surface features suggests that the sharp gradients observed are unrelated to artifacts, but real. Notably, however, the total areas affected by displacements of sectors A and B, D and E do not appear to be bounded by specific morphological features nor correlated on the whole with slope gradients, which supports the hypothesis that the instability could have a significant depth.

Sati et al. (2017) state that no major landslide area can be observed on the right slope, with the exception of one location. This is found 1.3 to 1.5 km upstream of the dam axis and between 1260 and 1225 m a.s.l. and is associated with an extent of 230 by 90 m. The location of this area seems to coincide with our sector D, though the area indicated by Sati et al. (2017) is much smaller. Another vulnerable zone that they recognise is 1.9 to 2.3 km upstream of the dam axis, thus possibly coinciding with our sector E. Though their analysis indicates that no major stability problems around the reservoir rim should be encountered, our analyses points to a different direction. In particular, our study shows that 1) several areas show significant downslope displacements across the entire valley flank, 2) such displacements are already visible from 2007, thus before works at the dam site began, 3) an acceleration is visible in the lower parts of the slope, immediately upslope of the dam axis, from 2009 onwards, thus around the time excavation began, 3) since stabilisation efforts began in 2013 accelerations continued with increasing velocities observed in the lower parts of the slope well into 2017, this indicating the ineffectiveness of stabilisation efforts, 4) even disregarding the possibility that the whole valley flank is affected by a deep seated instability, the lowermost part of the slope, directly above the dam axis, is affected by significant displacements over an area that is much larger than the area affected by the 2013 landslide, 5) field observations of intensely fractured and deformed rock in different areas of the larger slope seem to point to the fact that the whole valley flank may indeed be affected by a large instability. Multitemporal InSAR analyses were able to reveal the presence of an instability previously unrecognised, moreover, despite the relatively small observation window, InSAR analyses alone would have allowed to raise concern regarding the location of the dam. This analysis shows the potential of InSAR for 1) the assessment of the suitability of a site for a large hydropower project, 2) targeting of stabilisation measures and investigating their effectiveness, 3) understanding the spatial and temporal evolution of displacements and 4) long-term monitoring of the entire valley flank.

3.4. Data and methods

Data from Envisat, ALOS-1, ALOS-2 and Sentinel-1 were processed over the area. Only one descending track was used (Envisat 176), the rest are all ascending geometries. Data is summarised in table 1. Initially, a number of interferograms were generated, across the entire available frames. Due to limitations associated with the landcover, initially the wrapped phase was screened. Successively, velocity and cumulative displacements map were generated with the Small Baseline Subset (SBAS) method. The time series were constructed only for ALOS-1, ALOS-2 and Sentinel-1 (connection graphs are shown in appendix 3-2). The level of decorrelation achieved with Envisat did not allow for multitemporal processing. Maximum temporal baselines were set at 750, 365 and 48 days for ALOS-

1, ALOS-2 and Sentinel-1 respectively, whilst maximum perpendicular baselines are 3500, 280 and 190 m respectively. The high control over perpendicular baselines of ALOS-2 allowed for the generation of SBAS time series even with an exiguous number of images. Temporal baselines were kept at 48 days for Sentinel-1 due to the highest sensitivity to changes in land cover given by the shorter wavelength of C-band. Disconnected blocks of images were used to construct the Sentinel-1 time series. This was necessary due to several images being discarded, given the low coherence of the interferograms that they generated. The model fits a linear velocity, interpolating between blocks of images, where no connections exist. The topographic model used for interferometric processing is the 5 m horizontal resolution ALOS World3d digital surface model. In order to improve the results over the study area, the images were cut around the unstable valley flank. This is because the site is within a densely vegetated area and increasing the size of the processed images would deteriorate the results, due to unwrapping difficulties. Reference points were chosen on the crest of the slope and on the ridges to the south and north, bounding the instability. Areas of cumulative displacements > 100 mm in the period of observation of each sensor were mapped and time series of points within such areas were analysed. 3 trend changes were identified in the time series of ALOS-1 and Sentinel-1. Linear velocities before and after such changes were estimated and the velocities analysed along a profile across the instability impinging on the dam.

A field visit in October 2017 allowed for the identification of some important morphological features. Moreover, in situ data was obtained from the Punatsangchhu Hydroelectric Project Authority (PHPA). The data includes time series of displacements occurring at 39 reflectors placed within and upslope of the 2013 instability and measured by a total station installed on the left side of the dam. The data of 24 of these reflectors was converted with trigonometrical calculaltions into the line of sight (LOS) of the satellites and then compared to the DInSAR time series. Depending on the acquisition geometry, the downwards, eastwards and northwards components of the displacement vector are:

$$d = \sin\vartheta \qquad \text{(Equation 1)}$$

$$e = \cos\vartheta \cos\varphi \qquad \text{(Equation 2)}$$

$$n = \cos\vartheta \sin\varphi \qquad \text{(Equation 3)}$$

where ϑ is the complementary angle to the incidence angle and φ is the angle between the LOS and the east (or heading angle from the north). The components of the vectors for correction of the in-situ data are shown in table 2. After the three components are corrected, the new vector projected on the LOS is obtained throught the sum of the three components.

A visibility coefficient was also calculated, following the approach of Notti (2011), in order to evaluate the percentage of displacement detectable, assuming a main downslope component. The angle of incidence used for the calculations is the average of the incidence angles of the three sensors.

Satellite	Band	Incidence angle	Track/ frame	Orbit type	Images number	Period
ALOS-1	L	~38.75°	502/530	A	18	20070201-20110212
ALOS-2	L	~31.39°	154/540	A	11	20140919-20170302
Sentinel-1	C	~39°	114	A	79	20141025-20181004

Table 3-1. Data used for the interferometric analysis.

	ALOS-1	ALOS-2	Sentinel-1
ϑ	90°-39°	90°-31°	90°-39°
φ	16°	16°	12°
d	0.77	0.85	0.77
e	0.131	0.44	0.131
n	0.615	0.53	0.615

Table 3-2. Parameters used for LOS conversion of in-situ data.

3.5. References

Barla, G., Antolini, F., Barla, M., Mensi, E., and Piovano, G. (2010). Monitoring of the Beauregard landslide (Aosta Valley, Italy) using advanced and conventional techniques. Engineering Geology, 116, 218-235. doi:10.1016/j.enggeo.2010.09.004

Barla, G., and Paronuzzi, P. (2013). The 1963 Vajont landslide: 50th anniversary. Rock Mechanics and Rock Engineering, 46(6), 1267-1270. doi:10.1007/s00603-013-0483-7

Chattopadhyay, S. S. (2012). Power from rivers. Frontline. Retrieved from https://frontline.thehindu.com/static/html/fl2921/stories/20121102292111600.htm

Colesanti, C., and Wasowski, J. (2006). Investigating landslides with space-borne Synthetic Aperture Radar (SAR) interferometry. Engineering Geology, 88, 173-199.

Dema, T. (2019, 24/01/2019). Another slide at PHPA I. KuenselOnline. Retrieved from http://www.kuenselonline.com/another-slide-at-phpa-i/

Dolkar, D. (2017). PHPA-I awaits second-party opinion on sliding right bank. pressreader.

Dolkar, D. (2019). PHPA-II dam block construction comes to a halt. pressreader.

Havaej, M., Wolter, A., and Stead, D. (2015). The possible role of brittle rock fracture in the 1963 Vajont slide, Italy. International Journal of Rock Mechanics and Mining Sciences, 78, 319-330. doi:doi.org/10.1016/j.ijrmms.2015.06.008

Huber, A. (2019). Hydropower in the Himalayan hazardscape: strategic ignorance and the production of unequal risk. Water, 11(414). doi:10.3390/w11030414

International Rivers (2015). Status of hydropower dams in Bhutan Retrieved from https://www.internationalrivers.org/resources/8703

Kirchherr, J., Charles, K. J., and Walton, M. W. (2016). The interplay of activists and dam developers: the case of Myanmar's mega-dams. International Journal of Water Resources Development, 111-131. doi:doi.org/10.1080/07900627.2016.1179176

Lamsang, T. (2017). Punatsangchu I to be delayed to Dec 2022 and Punatsangchu II till Sept 2019. The Bhutanese.

Legget, R. F. (1939). Geology and Engineering. New York: McGraw-Hill.

Li, M., Zhang, L., Shi, X., Liao, M., and Yang, M. (2019). Monitoring active motion of the Guobu landslide near the Laxiwa hydropower station in China by time-series point-like targets offset tracking. Remote Sensing of Environment, 221, 80-93. doi:doi.org/10.1016/j.rse.2018.11.006

Liu, P., Li, Z., Hoey, T., Kincal, C., Zhang, J., Zeng, Q., and Muller, J.-P. (2013). Using advanced InSAR time series techniques to monitor landslide movements in Badong of the Three Gorges region, China. International Journal of Applied Earth Observation and Geoinformation, 21, 253-264. doi:10.1016/j.jag.2011.10.010

Luzi, G., Pieraccini, M., Mecatti, D., Noferini, L., Macaluso, G., Calgaro, A., and Atzeni, C. (2006). Advances in ground based microwave interferometry for landslide survey: a case study. International Journal of Remote Sensing, 27(12), 2331-2350. doi:doi.org/10.1080/01431160600554975

Marcello, C., and Meda, P. (2013). The rehabilitation design of the Beauregard Dam. Paper presented at the 9th ICOLD European Club Symposium, Venice.

Norbu, P. (2012). Hydro Electric Projects - Punatsangchu I & II: Ahead of schedule. Raonline. Retrieved from https://www.raonline.ch/pages/bt/ecdu/bt_ecohydel0105.html

Notti, M., Zucca, Colombo. (2011). Models to predict persistent scatterers data distribution and their capacity to register movement along the slope.

Palden, T. (2017). Remedial measures worth Nu 3.7B to stabilise PHPA-I damsite. KuenselOnline. Retrieved from http://www.kuenselonline.com/remedial-measures-worth-nu-3-7b-to-stabilise-phpa-i-damsite/

Petley, D. (2015). Mangdechu in Bhutan – another significant landslide at a hydroelectric power plant site. Retrieved from https://blogs.agu.org/landslideblog/2015/08/14/mangdechu/

Roychoudhury, S., and Srinivasan, S. (2016). India’s Hydropower Investments in Bhutan: Environmental Impacts and the Role of Civil Society. India In Transition. Retrieved from https://casi.sas.upenn.edu/iit/roychoudhurysrinivasan

Sati, S. K., Khazanchi, R. N., Mishra, A., and Gautam, A. K. (2017). Reservoir rim stability: a case study of Punatsangchhu-I H. E. project, Bhutan. Paper presented at the INDOROCK 201: 7th Indian Rock Conference, New Delhi.

Schuster, R. L. (2006). Interaction of dams and landslides, case studies and mitigation: U.S. Geological Survey Professional Paper 1723, 107 p. Retrieved from Reston, Virginia:

Tralli, D. M., Blom, R. G., Zlotnicki, V., Donnellan, A., and Evans, D. L. (2005). Satellite remote sensing of earthquake, volcano, flood, landslide and coastal inundation hazards. ISPRS Journal of Photogrammetry and Remote Sensing, 59(4), 185-198. doi:doi.org/10.1016/j.isprsjprs.2005.02.002

Tropical Rainfall Measuring Mission (TRMM) (2011), TRMM (TMPA/3B43) Rainfall Estimate L3 1 month 0.25 degree x 0.25 degree V7, Greenbelt, MD, Goddard Earth Sciences Data and Information Services Center (GES DISC), Accessed: 10/06/2019, 10.5067/TRMM/TMPA/MONTH/7

Walker, B. (2015). Will mega dams turn Bhutan's happiness sour? The Guardian. Retrieved from https://www.theguardian.com/sustainable-business/2015/may/20/will-mega-dams-turn-bhutans-happiness-sour

Walker, B. (2016). India Bhutan hydropower cooperation fraying at the edges. Understanding Asia's water crisis. Retrieved from https://www.thethirdpole.net/en/2016/10/04/india-bhutan-hydropower-cooperation-fraying-at-the-edges/

Wolter, A., Stead, D., and Clague, J. J. (2014). A morphologic characterisation of the 1963 Vajont Slide, Italy, using long-range terrestrial photogrammetry. Geomorphology, 206, 147-164. doi:doi.org/10.1016/j.geomorph.2013.10.006

World Bank Group (2016). Managing Environmental and Social Impacts of Hydropower in Bhutan. Retrieved from http://documents.worldbank.org/curated/en/254821470402939614/pdf/107462-REVISED-PUBLIC-HydropowerforBhutanWebCORRECTED.pdf

Xia, Y., Kaufmann, H., and Guo, X. F. (2004). Landslide monitoring in the Three Gorges area using D-InSAR and corner reflectors. Photogrammetric Engineering and Remote Sensing, 70(10), 1167-1172.

3.6. Appendix

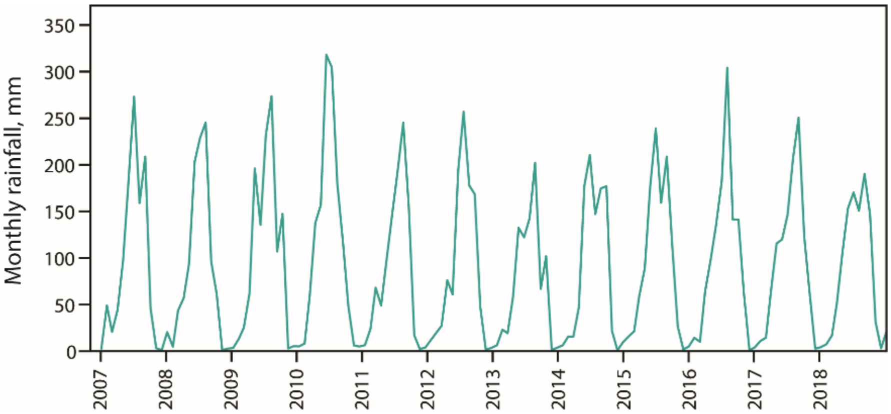

App. 3-1. .Estimated rainfall from TMPA multi-satellite precipitation analysis for 27.375° N, 89.875° E. The monthly rainfall is estimated based on the average hourly rates (TRMM, 2011).

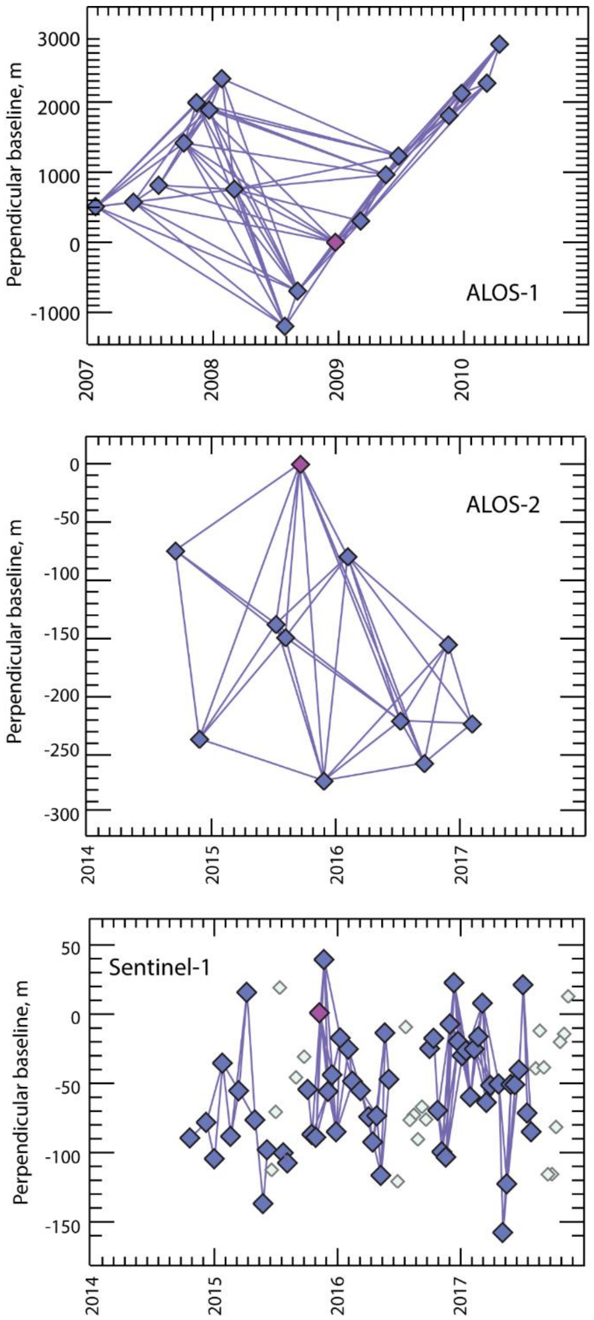

App. 3-2. Connection graphs of the SBAS processing for the three sensors.

4. Classification of slope processes based on multitemporal DInSAR analyses in the Himalaya of NW Bhutan

Benedetta Dini[1], Simon Daout[2], Andrea Manconi[1], Simon Loew[1]

[1] Department of Earth Sciences, ETH Zurich, Zurich, Switzerland, [2] Department of Earth Sciences, University of Oxford

Abstract

Slope deformation in mountainous terrain can be driven by different processes, the nature of which is either gravitational and irreversible or seasonal and reversible, the latter induced by permafrost variations or by hydromechanical or thermomechanical effects. The importance of identifying such deformations is not only related to the hazard they can pose, but also to the understanding of changes that permafrost or local hydrological conditions undergo. We here carry out a multi-temporal InSAR analysis over an 8000 km2 large mountainous area affected by a variety of slope processes, straddling north-western Bhutan and southern Tibet. We propose a methodology to separate locally deforming areas from the effects of long-wavelengths signals through the analysis of the spatio-temporal behaviour of the time series of surface displacements. We present the mapping of hundreds of small-scale features that appear to be actively deforming, as well as several examples of reversible deformation rarely detected at this scale in such a challenging and vast region. The analysis of the multi-annual trend of ground deformation shows a relatively small number of irreversible gravitational movements clearly related to rock slides which attests a low level of recent activity of large rock slope instabilities in the region. In the southernmost, lower elevation parts of the study area, we quantify surface displacements ranging between 5 and 17 mm, and showing maximum seasonal peaks in summer months compatible with hydro-mechanical effects related to groundwater table variations. In addition, the ground movement induced by the active layer's response to melting and freezing over the gentler slopes and high-elevation permafrost regions of Bhutan and southern Tibet is on average around 10 mm, with maxima up to 28 mm. This displacement appears to be largely associated to braided stream plains, glacier outwash plains or low angle fine sediment covered slopes.

4.1. Introduction

Mountainous regions are affected by surface deformation caused by a variety of processes (Ballantyne, 2002; C-K., 2002; Kääb, 2002; Haeberli, 1985; Barsch and Caine, 1984). Among these, gravitational movements affecting permanently rock, rock and ice, and soil slopes can result in rapid slope failures and direct and indirect losses (Petley, 2012; Kääb, 2002). In addition, non-gravitational processes can be characterised by reversible surface deformation related to permafrost freeze-thaw cycles (Daout et al., 2017; Liu et al., 2009; Gruber and Haeberli, 2006; Wegmann and Gudmundsson, 1999), ground water table elevation changes (Rouyet et al., 2017; Hansmann et al., 2012; El Tani and Bremen, 2005), or thermomecanical effects (e.g. Gischig et al., 2011). The ability to identify and distinguish between such processes is crucial not only to assess primary and secondary hazards that gravitational, potentially catastrophic phenomena can pose, but it is also relevant in relation to land use strategies and the development of infrastructure susceptible to millimetric to centimetric seasonal deformation (e.g. concrete arch dams, pressure shafts, or sensitive transport infrastructure).

Space borne differential synthetic aperture radar interferometry (DInSAR) techniques allow the observation of displacements at regional scales within the same acquisition frame (Tang et al., 2018) and without the need for any in situ installation. In the past 20 years DInSAR techniques have been applied to a variety of geological problems (Massonnet and Feigl, 1998), including monitoring of irreversible ground deformation related to landslides and rock glaciers with millimetric accuracy (Catani et al., 2014; Wasowski and Bovenga, 2014; Strozzi et al., 2005; Nagler et al., 2002) or ground water exploitation (Crosetto et al., 2018; Ruiz-Constán et al., 2016; Le Mouélic et al., 2002). Observation of reversible deformation associated with permafrost variations has been shown with DInSAR over relatively low elevation regions (Liu et al., 2014; Liu et al., 2012; Short et al., 2011; Liu et al., 2009) or, more recently, over the large sedimentary basins of the Tibetan Plateau (Daout et al., 2017). However, in high relief regions (e.g. elevations more than 2000 m), the technique suffers from seasonal variability of atmospheric conditions, which may overprint reversible deformations (Doin et al., 2009). Multitemporal radar interferometry (MT-InSAR) allows to reconstruct the timeline of cumulative ground movements with centimetric accuracy (Hooper et al., 2004; Berardino et al., 2002), and provides opportunities to map and characterise slow, reversible or transient processes.

In this study, we present a MT-InSAR analysis of ALOS-1 and Envisat data in a challenging, broad and mountainous area between northwestern Bhutan and southern Tibet (Fig. 4-1) to measure, identify and characterise slope processes at high spatial resolution. In the following sections, we first describe how we construct the timeline of ground displacement maps in line of sight (LOS) and then present an empirical approach to separate surface slope processes (which usually occur at very local scales) from the long-wavelengths signals. The, displacement time series are then analysed for multiannual

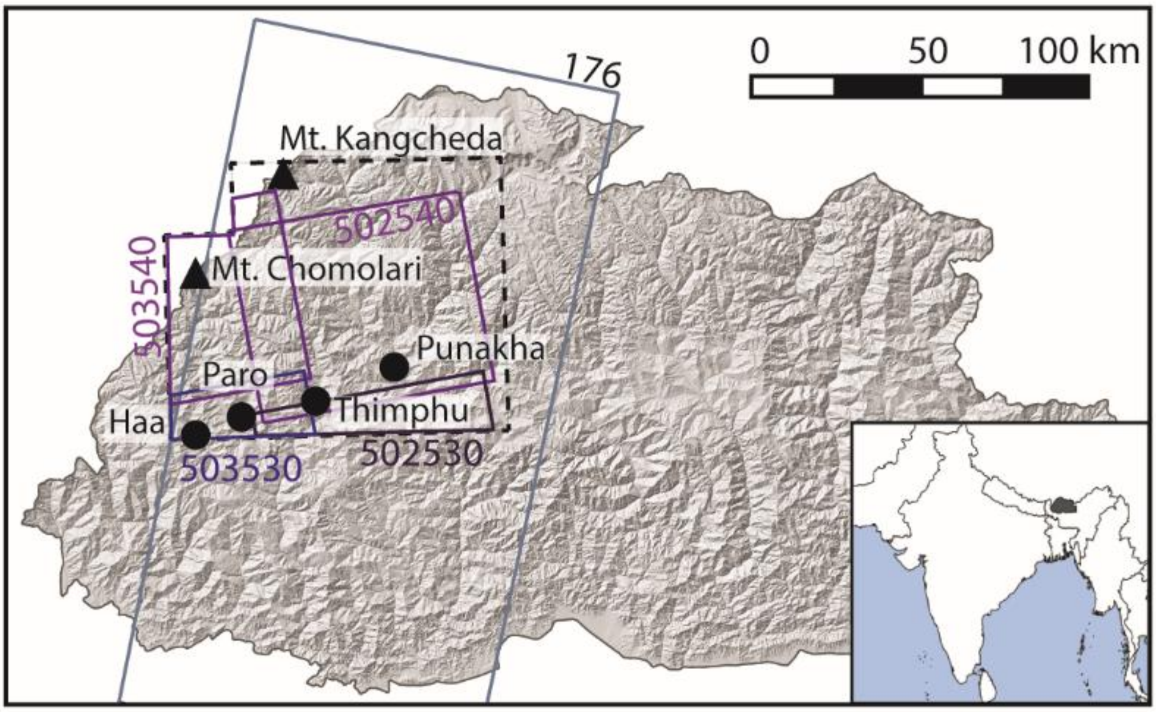

Fig. 4-1. Black dashed line, area of study. Dark blue polygon, ALOS track 503 frame 530, dark purple polygons, ALOS track 502 frame 530, lighter purple polygons ALOS tracks 502 and 503, frame 540. Grey box, Envisat track 176. Hillshade is from SRTM 30m over the whole country, but from ALOS World3D 5m resolution digital surface model within black dashed line. In insert the geographical setting of Bhutan.

trends and seasonality, in order to distinguish between gravitational processes and reversible deformation occurring below (e.g hydromechanical effects) or within the permafrost region (e.g. frost heave and thawing effects). The methodology is illustrated in section 4.2, while section 4.3 presents the results of our analysis. In section 4.4 we discuss the multi-annual trends detected, as well as amplitude and timing of seasonal ground surface displacements over other landforms. Section 4.4 is organised in three sub-sections, each one respectively focusing on specific processes: gravitational deformations, reversible deformations below permafrost regions, and reversible above permafrost regions.

4.2. Data and methods

4.2.1. State of the art

Since the generation of the first interferograms, numerous developments in InSAR have allowed to improve the S/N ratios and extract small or slow deformations in challenging regions (Schlögel, 2015; Manconi and Casu, 2012). More particularly the development of the time series analysis of a collection of interferograms (Lopez-Quiroz et al., 2012; Hooper et al., 2012) offers wide ranges of opportunities to detect slow deformations over a long period of time (e.g Daout et al., 2016, Grandin et al., 2012, Wasowski & Bovenga 2014), transient (e.g Jolivet et al., 2013) or reversible deformations (Daout et al., 2017; Chang and Hanssen, 2015; Liu et al., 2014). However, over broad mountainous areas, the technique suffers from limitations such as those related to land cover type, snow cover and the associated temporal decorrelation. Moreover, the ambiguities linked to the long-wavelength artefacts can reach up to a few centimetres within an interferogram and can severely affect the unwrapping, the suitability of stable points and, consequently, the time series of surface displacements. Large-scale artefacts within the interferometric phase arise from various contributions. These appear uniform along one direction of the track and can be related to orbital errors or to the effects of clock drift (Fattahi and Amelung, 2014), long-wavelength errors in the digital elevation model, or changes in atmospheric or ionospheric conditions. More particularly, atmospheric disturbances are well known to cause major delays on the radar waves propagation, either related to turbulent effects or to the stratified component of the atmosphere (Hanssen, 2001). Whilst turbulent atmospheric effects are local in nature, random in space and time, the stratified component of the atmosphere is correlated to the topography over large areas (several km scale) and its temporal behaviour is dominated by a seasonal term with amplitude depending on temperature, pressure and relative humidity that can overprint small-scale ground deformations (Doin et al., 2009; Hanssen, 2001). Cumulative displacements and velocity maps based on a relatively small number of acquisitions are known to be polluted by poorly sampled atmospheric seasonal signal (Daout et al., 2018; Bekaert et al., 2015; Doin et al., 2009). In case of large surface displacement rates (>10mm/y) such as those related to localised (slope-scale) gravitational movements, the long-term trend remains almost unaffected. However, if time series are affected by atmospheric cycles associated with seasonal stratified delays, the detection of reversible slope deformation can be severely hindered due to its cyclical nature.

Several methods have been proposed for correction of atmospheric delays in particular. The use of ERA-Interim reanalysis data has been proven useful to estimate the atmospheric delay in areas where the deformation is correlated to topography (Jolivet et al., 2011). However, one limitation is related to accuracy and spatial resolution due to the coarse grid (~75 km) of the model. Other authors proposed the use of MODIS and MERIS water vapour observations (Walters et al., 2013), however these are only available during day time and in cloud free conditions and require the availability of an image around the time of each SAR acquisition date. Methods based on the use of GPS and radiosonde data also exist (Li et al., 2003), with sparse nature of observations being the main drawback (Walters et al., 2013). On other hand, empirical methods for atmospheric correction do not require external data and estimate the relationship (linear, quadratic or power law) between the interferometric phase and topography (Bekaert et al., 2015; Jolivet et al., 2011). However, these methods entail that deformation and topography are uncorrelated. The choice of parametrisation is therefore critical in case of topography correlated deformation such as mountain belt uplift or volcanic inflation (Jolivet et al., 2011).

4.2.2. Dataset and DInSAR time series generation

We processed 91 SAR images acquired between February 2007 and February 2011 by one Envisat and four ALOS-1 tracks partly overlapping (see appendix 4-1). Given the position of the satellite frames with respect to the study area, the two northernmost ALOS scenes were processed in their entirety, thus covering roughly 60 km in latitude. The two southernmost scenes were only processed over a roughly 10 km north-south extent. A total of 497 differential interferograms were generated with the software SARScape (Sarmap) (see also Dini et al., 2019). The multi-looking was chosen to retain maximum resolution for ground range pixel spacing for both sensors, i.e. around 15 m and 20 m for ALOS-1 and Envisat respectively. The interferograms were flattened with the high-resolution digital surface model ALOS World3D, with a ground sample distance of 5 m (JAXA, 2017). The interferograms were filtered using the Goldstein method (Goldstein and Werner, 1998) to improve the S/N ratio. The filtering strength was kept to a minimum, in order to avoid the loss of small-scale displacement signal and keep the high-frequency content. This choice likely reduced the final coverage of temporally coherent areas, but allowed to minimise unwrapping errors. Unwrapped interferograms were then approached with the SBAS algorithm (Berardino et al., 2002) to generate mean velocity maps and displacement time series (appendix 4-1).

4.2.3. Extraction of atmospheric patterns

Initially, we aimed at correcting the atmospheric artefacts by taking advantage of external information. To this end, we considered the Generic Atmospheric Correction Online Service (GACOS) for DInSAR (Yu et al., 2018), see also appendix 4-2). GACOS integrates high-resolution European Centre for Medium-Range Weather Forecast (ECMWF) data and continuous GPS tropospheric delay estimates. Although the correction removes part of the atmospheric delays, we observe significant residual long wavelength signals correlated to the topography.

Thus, in order to identify and mitigate any residual, large-scale artefacts, we made also use of the spatial information contained in the cumulative displacements to determine an empirical correction on each time series map (Doin et al., 2015; Cavalié et al., 2007). This approach takes advantage of the large spatial coverage of the results to iteratively estimate long wavelength spatial ramps and artefacts correlated to the topography. In addition to removing the long-wavelength residual signals, this procedure also refers the surface displacements of the whole map to common areas, which is crucial before the analysis of the temporal behaviour of a specific feature. Figure 4-2 shows examples of the

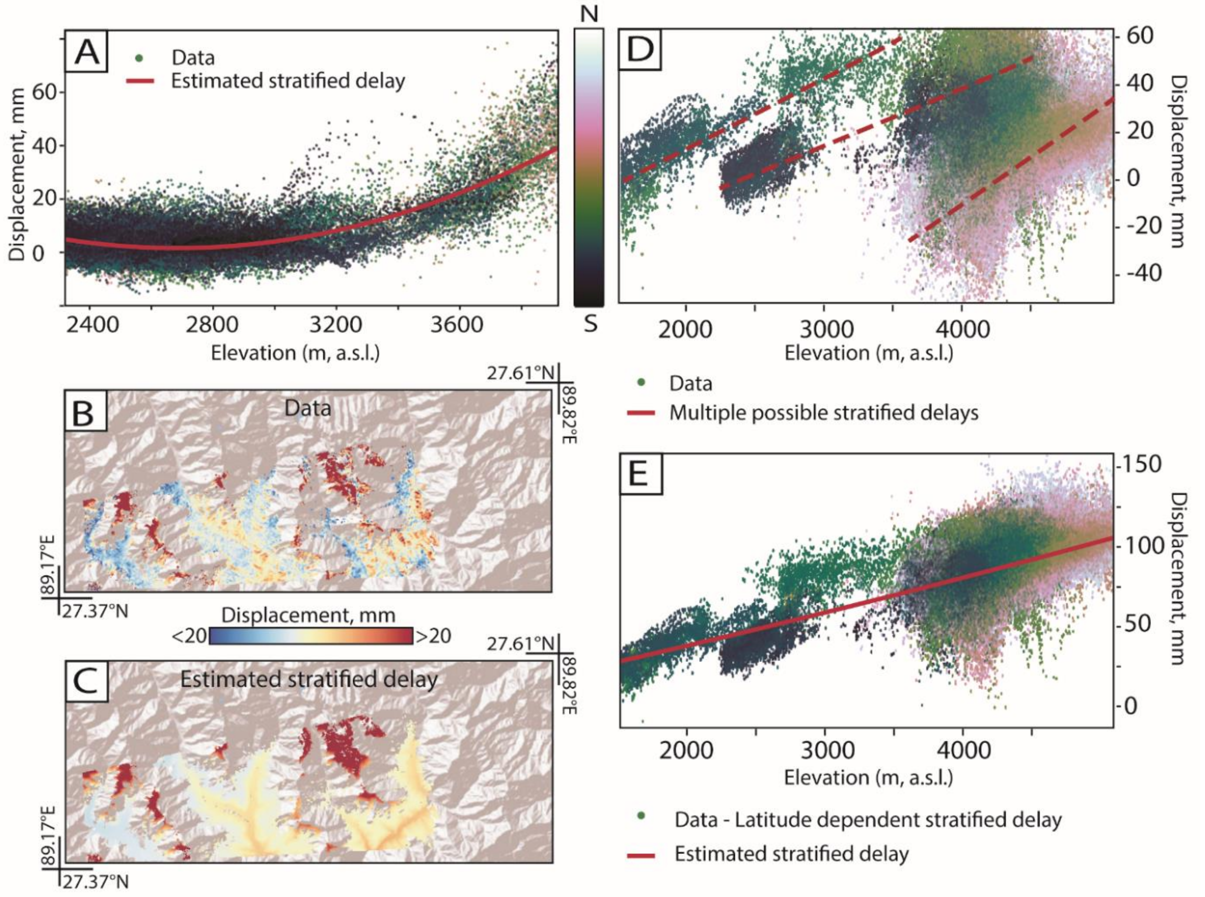

Fig. 4-2. *A) Displacement-elevation relationship for one acquisition of the small N-S extent ALOS track-frame 503530. A quadratic relationship is observed. Each point represents a displacement-elevation estimation for a single pixel in the frame with a colour scale depending on the latitude within the frame. Given the small N-S extent of this frame, colours are similar. B) Map view of uncorrected displacement data for ALOS 503530. C) Map view of the estimated large-scale stratified delay for ALOS 503530 following the relationship observed in A. D) Displacement-elevation relationship for one acquisition of the ALOS track 503540, with large N-S extent (full frame extent processed), showing displacement-elevation relationships as multiple polynomial fits varying with latitude. Dark colours (valleys the south and vegetated areas) shows a different phase/elevation dependency than light colours (high-elevations plateau in the north desertic areas). E) Displacement-elevation relationship for ALOS 503540 after removing the latitudinal component of the delay.*

correlation between displacement and topographic relief for all coherent targets obtained from the SBAS time series analysis of two ALOS tracks, with a small (Fig. 4-2A) and large (Fig. 4-2D) north-south final coverage (as mentioned above). Each point represents a displacement-elevation estimation for a single pixel in the frame with colour scale depending on the latitude. We use a quadratic polynomial function (red line) such as:

$$LOS(x,y) = A*z2 + B*z + C \qquad \text{(equation 1)}$$

where LOS(x,y) are the LOS displacements within a time series map, z, the topography, and A, B, C the inverted parameters (Fig. 4-2A). The inverse problem is solved with a sequential least-square algorithm after cleaning the data from outliers. By plotting in map view the LOS displacements-elevation relationship derived from this operation (Fig. 4-2C), we can observe the correspondence with a stratified large-scale bias affecting the whole map, also observed in the data in map view (Fig. 4-2B).

For the larger track (Fig. 4-2D), we observe a variability of the displacement-elevation relationship, which cannot be explained by a single polynomial function. For example, dark colours, which correspond to valleys and vegetated areas in the south, indicate a different displacement-elevation dependency than that corresponding to light colours, which are high-elevations areas in the plateau of the northern desertic region. Here, the displacement data can be fitted by multiple polynomial fits, which reflect the lateral variability of the stratified delay (Jolivet et al., 2011). In order to capture this north-south variability of the displacement-elevation relationship, we include for the two larger tracks in the north (ALOS 502-530 and 502-540, see figure 4-1) a latitudinal cross dependency (Doin et al., 2015) such as:

$$LOS(x,y) = A*z2 + B*z + C*z*y + D*y2 + E*y + F \qquad \text{(equation 2)}$$

where LOS(x,y), are the LOS displacements for each acquisition date, y and z are latitude and topography, respectively. We observe that after removing this latitudinal cross dependency of the displacement-elevation correlation from the data (data points in Fig. 4-2E), a quadratic polynomial function (red) also provides a good fit to the data.

This post-processing step is of particular importance for three reasons. First, to attenuate the effects of the stratified and seasonal atmospheric delays within the displacement time series. Second, to remove residual long-wavelength ramps due to orbital errors, ionospheric or atmospheric large-scale patterns. Third, to define a common reference for all cumulative displacement maps, which were previously biased by residual long-wavelength signals.

4.2.4. Time series decomposition

As a second step for our analysis, we decompose the corrected cumulative displacement data of each pixel defined by their x, y positions with a parametric approach. Each time series of cumulative LOS displacements, LOS(x,y,t), are expressed as follows:

$$LOS(x,y,t) = V * t + A \cos (wt + B) \qquad \text{(equation 3)}$$

where t is the acquisition time, V is the best estimate of the pixel LOS velocity, A is the amplitude of the seasonal signal (mm), and B is the timing of the seasonal function, corresponding therefore to the month of the maximum displacements (Fig. 4-3). Based on the misfit of the inverse problem, we also derive the uncertainty for each explored parameter V, A, B, and therefore produce velocity, amplitude and timing of maximum displacement error maps, respectively. In the following analysis, we only consider pixels with small uncertainties and amplitudes, A, greater than 5 mm.

4.2.5. Validation of the approach

To validate the approach and quantify the effects of the predictive and empirical corrections in our measurements, we compare the time series decomposition results with time series data that have neither been corrected with GACOS nor with empirical long-wavelength corrections. Without atmospheric correction, the multiannual LOS displacements are dominated by a single seasonal peak between July and September (Fig. 4-3B, C, H, I). The amplitude of the uncorrected seasonal signal ranges between 5 and up to 90 mm and in map view the uncorrected time series data show a clear correlation with topography at large scale, with highest values at higher elevations (Fig. 4-3A, G). This behaviour reflects the long wavelength and spatially-correlated signal associated with the layering of the troposphere. In comparison, after predictive and empirical corrections of the atmospheric artefacts, the amplitude maps of the seasonal signal show lower values, ranging between 5 and 20 mm and a lower correlation with topography (Fig 4-3D, J) whilst maps and histograms of the timings of maximum seasonal deformation indicate a more uniform distribution, highlighting the partial removal of the previously dominating, likely atmospheric seasonal pattern (Fig. 4-3E, F, K, L).

4.2.6. Mapping of displacements

Corrected displacement and velocity maps were analysed in order to map areas showing displacements during the observation period. These were classified on the basis of their geomorphological characteristics (the criteria used are the same as those used for objects mapped on individual interferograms illustrated in Dini et al., 2019), their multiannual trend and amplitude and timing of seasonal cycles. A sinusoidal function offers a first-order linear fit to the data and is used here to detect reversible deformations and map their lateral variability. However, to better characterise the reversible deformation pattern, we also compute the de-trended and normalised seasonal signal over a 12 months period, $(LOS(t) - V*t) / A$, where LOS(t) are the time seires of LOS displacements for each pixel and A, V, are the inverted amplitudes and velocities previously obtained from eq. 3, respectively.

Both multiannual trend of the LOS ground velocity and seasonal ground displacements were also analysed with respect to the slope aspect. This allows to assess whether the ground deformation is more likely to include a horizontal component or whether it is mostly vertical, like in the case of objects in flat topography, and to discern between the components normal to valley axis directed towards

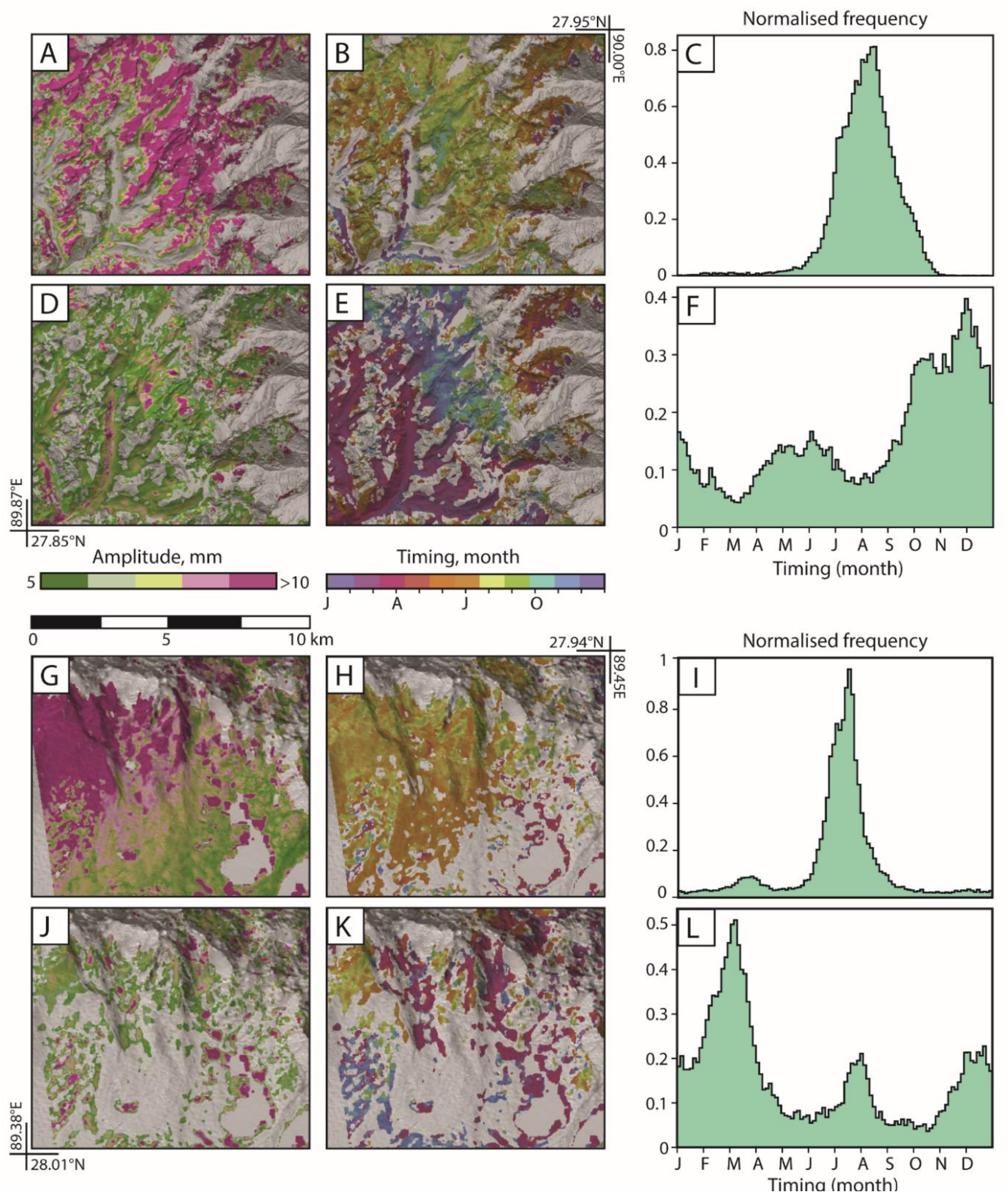

Fig. 4-3. A-B-G-H) Amplitude and timing of seasonal cycles before empirical correction for two areas within ALOS track/frame 503540. The increase of amplitude is correlated to the increase of topography at large scale and at long-wavelength with an homogeneous timing across the area, corresponding to the atmospheric delay. C-I) Histograms of timings of maximum seasonal displacements without corrections showing a Gaussian distribution centred on the Monsson atmospheric peak in August. D-E-J-K) Amplitude of seasonal cycles after correction. Small-wavelength high amplitude areas appear and correspond to potential reversible deformation. F-L) Histograms of timings of maximum seasonal displacements after corrections. Timings of maximum seasonal displacements do not correspond to the Monsson time anymore and are less homogeneous.

and away from valley centre, for objects located on slopes. This analysis allows better characterising the mapped processes.

Areas of unequivocal non-zero velocity or cumulative displacements are mapped across the whole region, which is subdivided into a 10 km grid. Rock slides, rock slope deformation and mountain slope deformation are grouped to indicate gravitational movements associated with instability of a rock slope, and classified according to Hungr et al. (2014). The terms soil creep and/or soil slide are used in association with talus cones, debris mantled slopes and moraines, where gravitational movements of loose soil and coarse debris are expected to lead to the observed displacements. Rock glaciers constitute a class on their own, as they represent a landform and not a landslide type. This choice is related to the fact that though landslides and rockfall can occur on a rock glacier, active rock glaciers move downslope as a result of permafrost creep. A class is associated with reversible seasonal displacements that may be associated either to permafrost melt-thaw cycles and to hydromechanical effects induced by annual groundwater table variations in the permafrost-free region. Finally, an unknown class is associated with areas that show displacements but are located in areas that do not exhibit clear morphological characteristics nor unambiguous time series trends.

4.3. Results

The analysis of the seasonality, the velocity and the cumulative displacement maps revealed the presence of 550 areas over which ground displacement is detected in the observation window (Fig. 4-4). Around 22% of the objects are associated with rock glaciers creep, 19% are soil creep occurring on talus slopes or shallow debris on slopes, 10% are rock slope instabilities, around 1% seem to be associated with soil creep or soil slides occurring on moraine flanks, 34% are possible reversible deformation (either related to permafrost or possible hydromechanical effects) and 14% remain unclassified for lack of evident geomorphological characteristics or due to unclear time series. The distribution of these objects is very irregular across the study area, with clusters in the northwest of the region, in the northeast and south of Thimphu. Table 1 summarises information regarding size, elevation, relief, and displacement rates of the areas affected by linear displacements. Rock slope instabilities represent the category with the largest elevation range. Moreover, the distribution is bimodal with two peaks at different elevations.

If the displacement vector is assumed to be oriented downslope along the maximum gradient, which is a generally acceptable first assumption for gravitational slope movements, then it is possible to estimate the percentage of displacement detectable in the LOS (Notti, 2011) and thus to estimate a downslope velocity closer to the true velocity. Table 1 shows the displacement rates so calculated for rock slope instabilities, soil creep and rock glaciers creep. As far as rock slope instabilities are

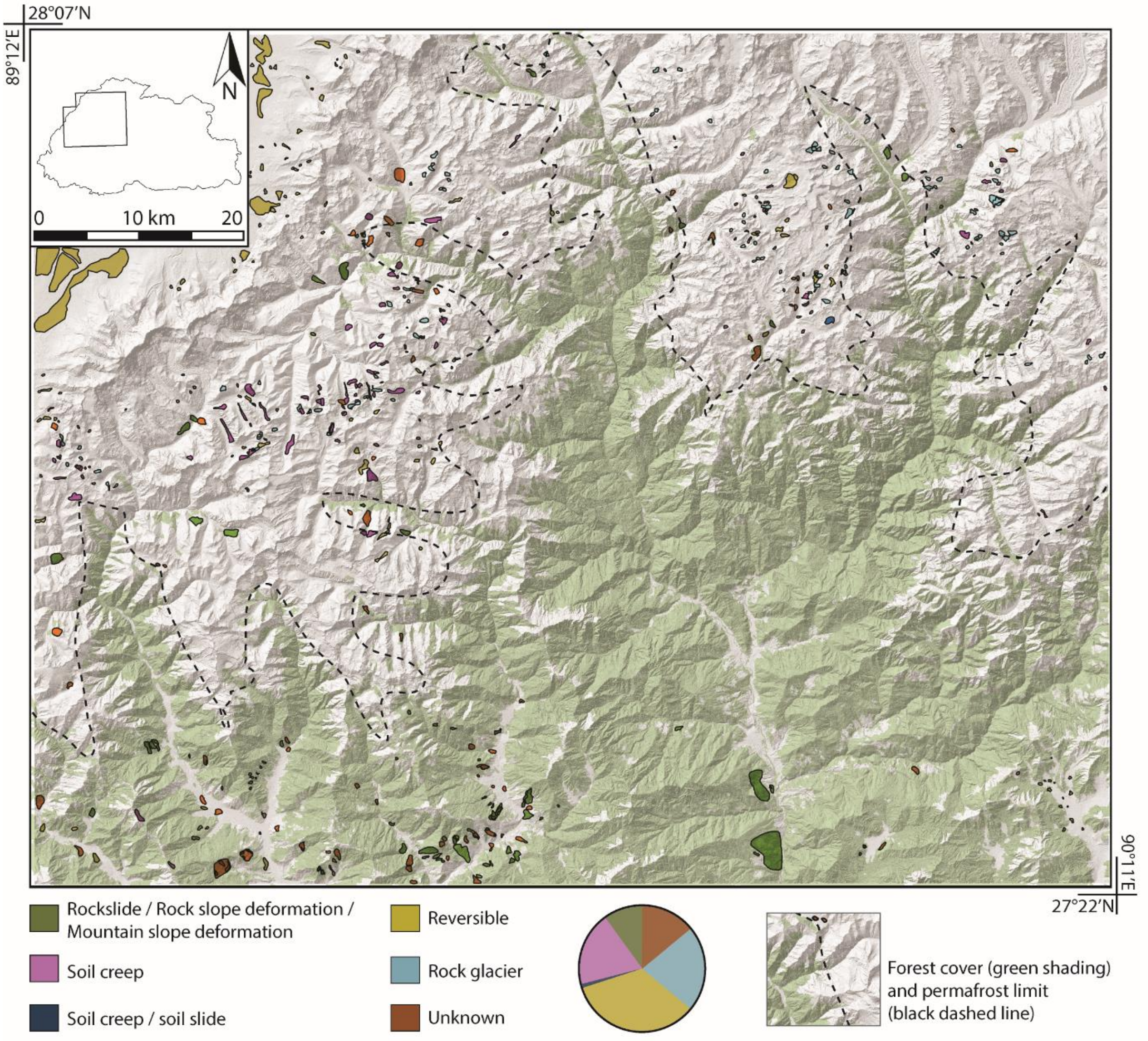

Fig. 4-4. Displacement areas mapped on the SBAS velocity and displacement maps. Pie chart shows proportions of different types of processes.

concerned, we observe that the vast majority falls within the category "very slow" and "slow" of the landslide classification (Hungr, 2014), with displacements rates rarely exceeding 160 mm/year. This is in agreement with the expected intrinsic limitations of DInSAR time series analyses (Wasowski and Bovenga, 2014). Only one observed rock slope instability has a much higher displacement rate than the others, exceeding the upper end of the main velocity range by more than three times, with about 700 mm/year of estimated downslope displacement rates. Rock glaciers' creep velocities are, as expected, considerably higher than those detected for rock slope instabilities, but relatively low in comparison with rock glaciers in other alpine regions (see section 4.4). Downslope displacement rates are of the order of 300 mm/year or less and only 3 cases above 500 mm/year. However, velocities

		Linear trends				Reversible
		all	rock slope instabilities	rock glaciers	talus/ debris	below permafrost/ within permafrost
AREA	min	1500 m^2				8000 m^2
	max	0.7 km^2				2.6 km^2
	95th perc	0.2 km^2				
ELEVATION, m a.s.l.	min	1000	1000	4700	4400	2500
	max	5100	5100	5000	5000	5000
	preferential ranges		2500 - 3000 4000 - 4500			2500 - 3000 4200 - 5000
RELIEF, m	min		100			
	max		1000			
	mode		300			
	95th perc		800			
DISPLACEMENT RATES, mm/y	range		5 - 200	5 - 760	10 - 160	
	95th perc		160	330		
	outliers		700			
AMPLITUDE, mm	range					2 - 28
	90th perc					15
	max					17 / 28
SLOPE, ° / ASPECT						30-35, SW-NW <15, ESE

Table 4-1. Relevant descriptors of the different processes observed.

above 250 mm/year are less reliable because these correspond to rock glaciers oriented almost perpendicularly to the LOS, this severely affecting the detectability of movement.

66% of the areas affected by reversible deformation are found within the permafrost region as defined by the global permafrost zonation (Gruber, 2012), 62% of which in deep and continuous permafrost, whilst the remaining 34% are in the permafrost free region. The specific elevation ranges covered by these areas, as well as their sizes are summarised in table 1. In general, we observe that the largest ones are found in permafrost. These areas are characterised by a localised increase in the amplitude of seasonal cycles towards their centre, with a clear and sharp gradient when compared to the surrounding areas. Amplitudes of the seasonal cycles within and below permafrost, as well as slope angles and preferential aspects are shown in table 1.

In general, the detection of displacements is higher with L-band, as it can be expected given the presence of vegetation over large parts of the region. The proportions of detectability in different landcover types (appendix. 4-3) is similar to what was observed in Dini et al. (2019) for individual interferogram analysis. The analysis of the velocity and displacement maps presented herein, shows that 19% of the active areas observed in Dini et al. (2019) in individual interferograms also show activity in the multitemporal analyses results.

4.4. Interpretation of the results

Due to their high-rates of surface displacements, long-term multiannual trends of slope instabilities are likely to be detectable, even when atmospheric effects pollute the signal. Indeed, as mentioned in the previous section, we observe linear displacement trends in a large number of cases, either superimposed or not to seasonal cycles. On the contrary, areas of reversible deformations are more difficult to detect due to artefacts, as for example the delays caused by the layered atmosphere.

The strategy applied in this work shows that by taking advantage of both spatial and temporal characteristics of the expected deformation, it is possible to identify and map with DInSAR reversible processes in a large and difficult mountainous region, such as Bhutan, and disentangle them from atmospheric delays that present different spatio-temporal characteristics. However, further limitations relative to the LOS observation, to the temporal sampling but also to the discontinuous coverage of the SBAS data due to the land cover and its influence on coherence and unwrapping, make it relatively difficult to disentangle individual processes that may cause reversible deformation. For example, hydromechanical and thermomechanical effects may lead to reversible deformation that shows the same sign in a similar time of the year. This makes the disentangling of such effects difficult, unless information of temperature and hydrology is known. However, the amplitude of seasonal deformation induced by purely thermomechanical effects is substantially lower than that caused by hydromechanical effects (Grämiger et al., 2018), thus whilst it is possible that such effects superimpose, the contribution of the former alone would be possible to detect with DInSAR due to their low amplitude. In the following, we illustrate with examples the objects that correspond to displacements related to gravitational processes, seasonal behaviour in permafrost and below the permafrost region.

4.4.1. Linear trends and gravitational processes

4.4.1.1. Landslides

Linear displacement trends compatible with downslope movements have been observed in relation to rock slope instabilities (rock slides, rock slope deformations or mountain slope deformations, as described in the landslide classification of Hungr et al. (2014)), soil creep or soil slides occurring on talus cones, debris mantled slopes and moraines and rock glaciers creep. Occasionally, objects in the unknown category also show linear trends. Figure 4-5 shows 4 examples of landforms on which linear

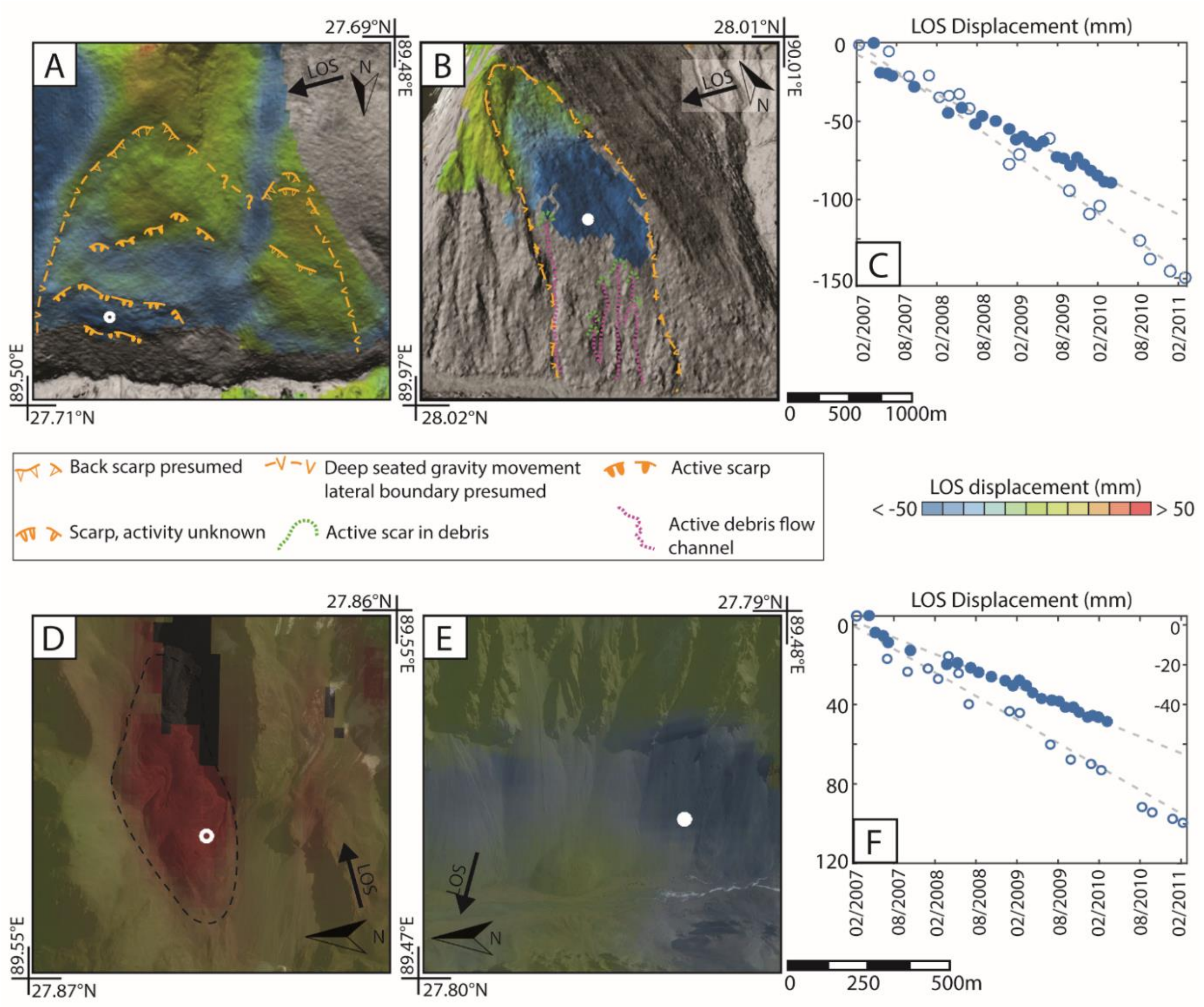

Fig. 4-5. Examples of time series showing example of linear trends observed on different types of landforms. A) Cumulative displacement map obtained with ALOS track 503540 for a large and likely deep-seated mountain slope deformation with different sectors of activity visible. B) Cumulative displacements of a large rockslide obtained with Envisat track 176. C) Time series of the instabilities in A and B. Open circles correspond to the time series of the circle in A. Filled circles correspond to the time series of the circle in B. D) Cumulative displacement of a rock glacier obtained with ALOS track 503540. E) Cumulative displacement over large talus cones obtained with Envisat track 176.

displacement trends were detected. Figure 4-5A shows the cumulative displacements observed with ALOS over a large and possibly deep mountain slope deformation. A clear displacement area is visible on the north facing flank affected by the instability. Displacements can be observed also on eastern facing slopes, surrounding the main instability. Such elongated areas of displacements are most likely related to debris on the slope. Only a minor portion of the slope shows clear displacements, however, due to decorrelation effects in the lower parts caused by vegetation, the total deforming area is difficult to estimate. For these reasons, analysing the relief of the area characterised by displacement may be misleading, if used to infer the type of rock slope instability and other observations are necessary. The lowermost scarp seen in figure 4-5A had already been identified as active through the analysis of the interferograms (Dini et al., 2019). The cumulative displacement map, however, also reveals the previously unidentified activity of two other scarps. The corresponding time series trend shown in figure 4-5C indicates an average velocity for the lower parts of the slope of 100 mm/year (when LOS component is projected on maximum slope gradient). Another large rock slope instability is shown in figure 4-5B. Here a gradient of the displacement rates is observed, with the fastest velocities around 53 mm/year. The lower half of the slope is covered with forest, hence the coherence loss. Faster movements in the lower parts of the slope could also be responsible of decorrelation, this is supported by the increasing downslope displacement gradient. Many small superficial secondary failures as well as active debris flow channels, identified on optical imagery, are also indicative of the ongoing activity of the slope.

In the work presented in Dini et al. (2019), a relatively low rockslide activity level in northwestern Bhutan was observed in the short temporal window of the dataset (2007-2011) and the multitemporal analyses presented here are another indication in support of the same finding. The rockslides shown here are among the most active that were found and the velocities observed are in the ranges of the very slow to slow categories (Hungr et al., 2014). Moreover, we observed that only 10% of the objects mapped in the present work through the analysis of the time series maps are unambiguously attributable to rock slides. Though it is possible that decorrelation due to faster movements hinders the detection of high activity slopes, the systematic analysis over a 10 km grid carried out for the identification of unstable areas would limit the risk of overlooking clear gaps due to decorrelation. These findings open the question regarding the factors controlling recent landslide activity in northwestern Bhutan. A lack of significant earthquakes occurrence within or in the proximity of the study area in the last 300 years (Hetényi and Phuntsho, 2016) may at least in part explain the generally low level of large rock slope instabilities activity.

4.4.1.2. Rock glaciers

An example of rock glacier is shown in figure 4-5D. Here, the LOS is oriented parallel to the maximum slope gradient looking into the slope and displacements appear to be towards the satellite. This may either indicate a strong horizontal component or the overriding of individual lobes and thickening of the rock glacier's body or a combination of the two. The velocity in the LOS is around 100 mm/year, however the visibility of displacement component in the downslope direction is only partial, given the ~65° angle between the slope and the LOS. The velocity along the maximum slope gradient could thus be higher than 100 mm/year. Indeed, Envisat data for the same rock glacier shows downslope velocities of around 200 mm/year, with Envisat acquisition being opposite in orbit (descending) and its LOS generating a lower angle with the slope (~52). This velocity corresponds to the 90th percentile of the velocities of all observed rock glaciers. Faster velocities may lead to decorrelation and hence a loss of information on fast moving rock glaciers. However, in Dini et al. (2019) 86 rock glaciers were identified on interferograms and of these only 13 have no information in the SBAS velocity maps. The analysis of the fringes of the wrapped interferograms for these 13 rock glaciers however does not suggest higher velocity estimates. This seems also in agreement with the fact that no cracks were observed in any of the mapped rock glaciers in the optical images, which would indicate that no destabilising rock glaciers are present. As shown by (Delaloye et al., 2010)), cracks develop in the rooting zone or close to the rock glacier's front in response to high horizontal velocities, deep shear-zones and changes at the front. In general, we observe that there are no fast moving rock glaciers in the region in the period of observation, with velocities comparable to what has been observed for example in the Alps in recent years, up to 4 m/y in a few cases (Scotti et al., 2017; Delaloye et al., 2008). This could be due to either a less pronounced recent warming trend than at higher latitudes (Alps, Norway, Alaska) or to less water being available to penetrate into the frozen unconsolidated material supersaturated with interstitial ice (Barsch, 1992) and to deeper subsurface shear horizons (Haeberli, pers. comm.). Analysis and linear interpolation of ERA5 temperature data at 850 hPa, 700 hPa and 500 hPa shows that rock glaciers that lie at elevations between the mean annual 0°C and -2°C isotherms have slower velocities than those lying at elevations where the mean annual air temperature is between -2°C and -3.5°C, with a decrease in velocities again for colder mean annual temperatures. Due to snow and vegetation effects, mean subsurface temperatures are generally warmer than mean air temperatures. Rock glaciers at temperatures of 0 to -2°C may therefore not be perennially frozen any more (some could be becoming relict), whilst those at air temperatures of -2°C to -4°C are more likely to have permafrost near 0°C.

4.4.1.3. Talus cones

Finally, in figure 4-5E, talus cones are observed with downslope velocity of about 25 mm/year. The activity on talus cones suggests that there may be ongoing settling of the debris which could be related to current activity of the cliffs from which rockfall initiates. Of course, permafrost creep also affects talus slopes displacements, which we observe mostly within the permafrost region. However, the temporal sampling of our data does not allow to observe seasonal accelerations and decelerations of creep velocity on such landforms. In order to observe such behaviours, a temporal sampling offered by more recent satellites could help, such as for example Sentinel-1 with a 12 days repeat cycle.

4.4.2. Seasonal cycles below permafrost

As mentioned above, seasonal reversible displacements below the permafrost region would be either related to a response of slopes to annual ground water table variations or to thermomechanical effects. In the Alps, it has been observed that a recharge of fractures rock aquifers happens within 2

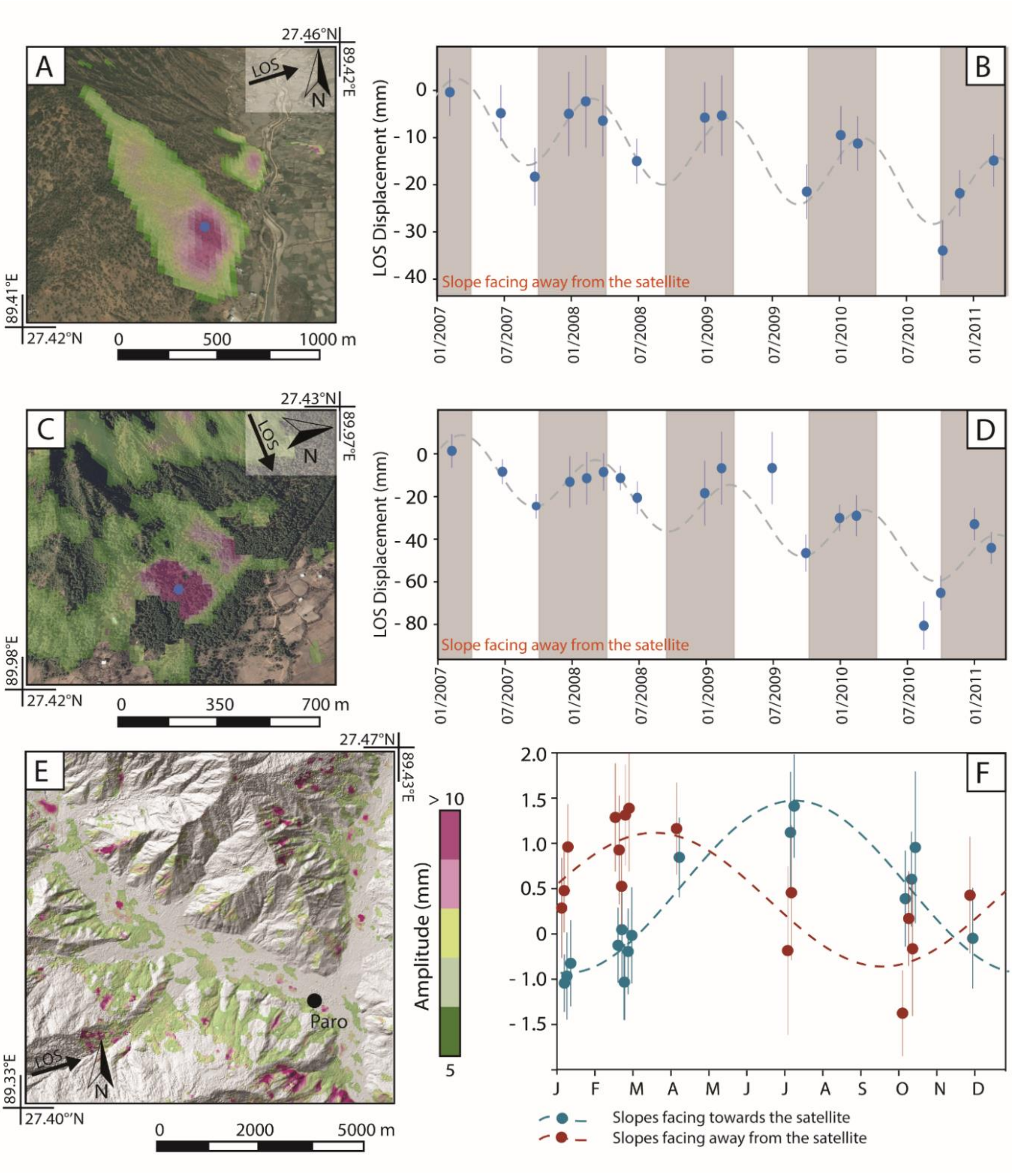

Fig. 4-6. Examples of possible reversible slope deformation below permafrost. A-C) Amplitudes of seasonal cycles over a slope near Paro and one in the far east of the study region, both slopes facing away from the satellite. B-D) The time series relative to these slopes (blue circles in A and C) obtained with ALOS tracks 503530 and 502530. E) Larger region in the Paro valley showing small areas of high amplitudes after corrections, these potentially related to seasonal ground deformation. F) Seasonality of all pixels in E wrapped between January and December and separated for slopes facing the satellite and slopes facing away from the satellite. It shows a clear aspect dependency with a maximum seasonality in summer and winter for slopes facing towards and away from the satellite respectively. This is compatible with valley closure in summer and opening in winter and is likely related to ground water table variations.

to 3 months during spring snow melt and summer rainstorms causing rock slope deformations. During this type of events, opposite slopes move towards each other with a strong horizontal component perpendicular to the valley axis by as much as 10-15 mm (Hansmann et al., 2012). In the remainder of the year, a slower phase of aquifer depletion causes reversible slope displacements and the valley to open again. In figure 4-6 (more examples are shown in appendices 4 and 5) we show two examples of slopes over which seasonal reversible deformation is detected. In figure 4-6A and 4-6C the amplitudes of the reversible signal are shown, with a gradient increasing towards the centre of the area and maximum amplitude around 15 mm. The time series in figure 4-6B and 4-6D show that these slopes, oriented away from the satellite, move away from the sensor in summer and towards the sensor in winter. Figure 4-6E shows a larger area around Paro, with a discontinuous signal of reversible deformation. To further analyse the seasonal behaviour of this area, we compute the de-trended seasonal signal for each year, between January and December for both slopes towards and away from the satellite (see section 4.2.6) (Fig. 4-6F). We observe that the seasonal signal has in this case a strong dependency on the aspect: slopes that face towards and away from the sensor move towards the satellite in summer and winter respectively. Atmospheric delays are not aspect dependent and thus the seasonality for slopes facing towards or away from the satellite would show no difference, as opposed to what we observe here. The strong aspect dependency observed is compatible with valley closure during summer and valley opening during winter and also with the fact that the strongest component of the deformation is horizontal. Given the poor temporal sampling of our time series (appendix 4-1), we could not observe the asymmetry of the seasonality shown for example in Hansmann et al. (2012) and due to the discontinuous coverage obtained through SBAS over the vegetated region, the examples we have are not for directly opposite valley flanks.

4.4.3. Seasonal cycles within permafrost region

In the permafrost region, we observed reversible deformation mostly over sediment covered valley floors in braided stream plains, on glacier outwash plains and on the alluvial fans developing from the north facing slopes from Chomolari to Kangcheda (see location in Fig. 4-1) into the Tibetan plateau and in correspondence to thermokarst basins. More rarely we observed them at the terminuses of glaciers around the equilibrium line altitude and on gentle debris covered slopes. Figure 4-7 shows examples on a glacier outwash plain (Fig. 4-7A-B) and on a gentle debris covered slope (Fig. 4-7 D-E). The time series of the cases illustrated here are shown in figure 4-7C and 4-7F. Here it can be observed that the seasonality, with amplitude between 15 and 25 mm, has a maximum in winter and a minimum in summer. The time series show a good fit with the seasonal model (dashed lines) despite the poor temporal sampling. Figure 4-8 shows two examples on braided stream plains (one shown in figure 4-8A-C and the other in figure 4-8B-D). Here rock glaciers can also be seen in the optical image (Fig. 4-8C), these remaining unaffected by seasonal deformation. In both examples in this figure, the deformation seems to correspond to areas of finer alluvial sediments, away from coarser talus. Most of such areas are on gentle slopes, thus a dominant horizontal component of the deformation is unlikely. As opposed to what was observed for reversible deformation below the permafrost region (section 4.4.2), here we find that the mode of the seasonality does not depend on aspect, supporting the hypothesis of a stronger vertical component of the deformation. This is illustrated in figure 4-9, where higher amplitudes of seasonal cycles (9A) correspond to a clear band of darker sediments (9B) and where, in general, there are no linear displacements (9C), this indicating that in the period of observation no long-term change in permafrost conditions can be observed. Both the amplitudes that we observed and the lack of aspect dependency are compatible with seasonal cycles of uplift and subsidence related to frost heave and thaw settlement. The good correspondence found with the amplitude signal and either

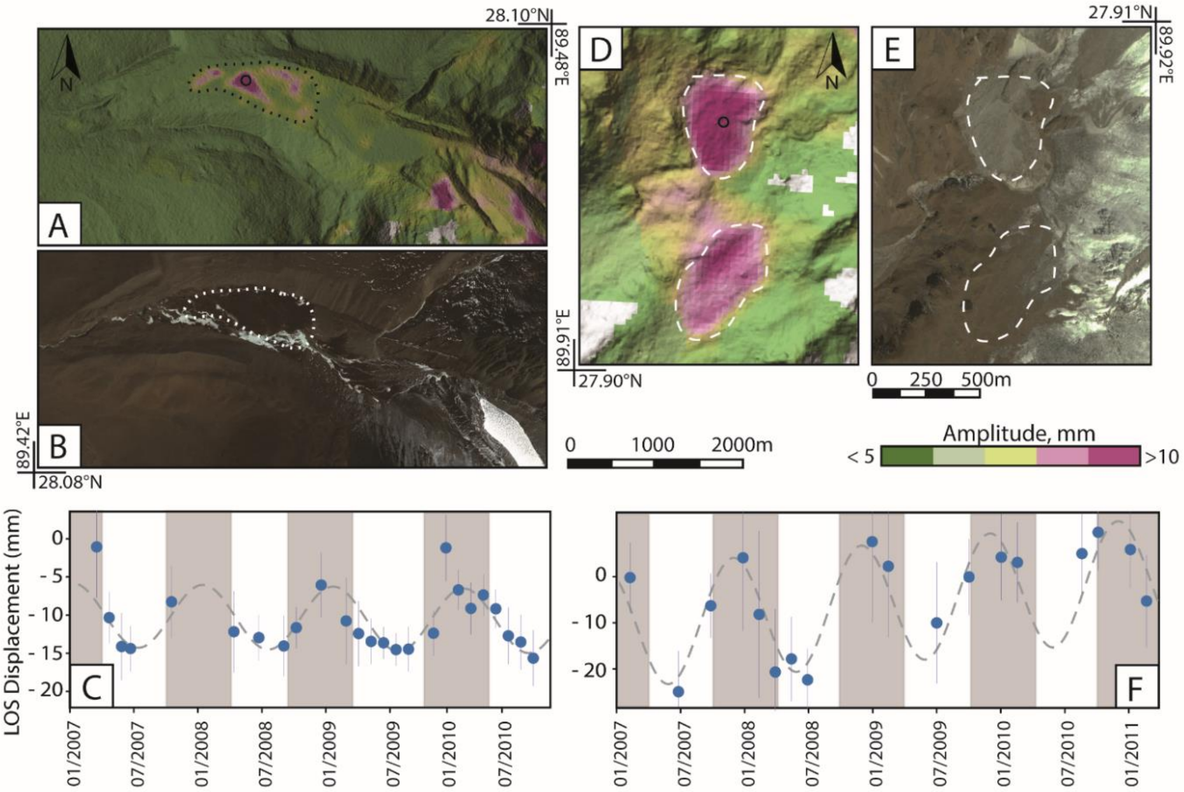

Fig. 4-7. Examples of areas of reversible deformation in permafrost. A) higher amplitudes of seasonal cycles over a glacier outwash plain, seen with Envisat track 176 after corrections. B) GoogleEarth image showing the finer sediments covering the valley floor. C) Time series for circle in A. D) higher amplitudes of seasonal cycles over a small outwash plain (top) and a gentle debris covered slope (bottom) seen with ALOS track 502540. E) GoogleEarth image showing the appearance of the sediments in these areas. F) Time series for circle in D showing a maximum uplift between December and January, compatible with frost heave.

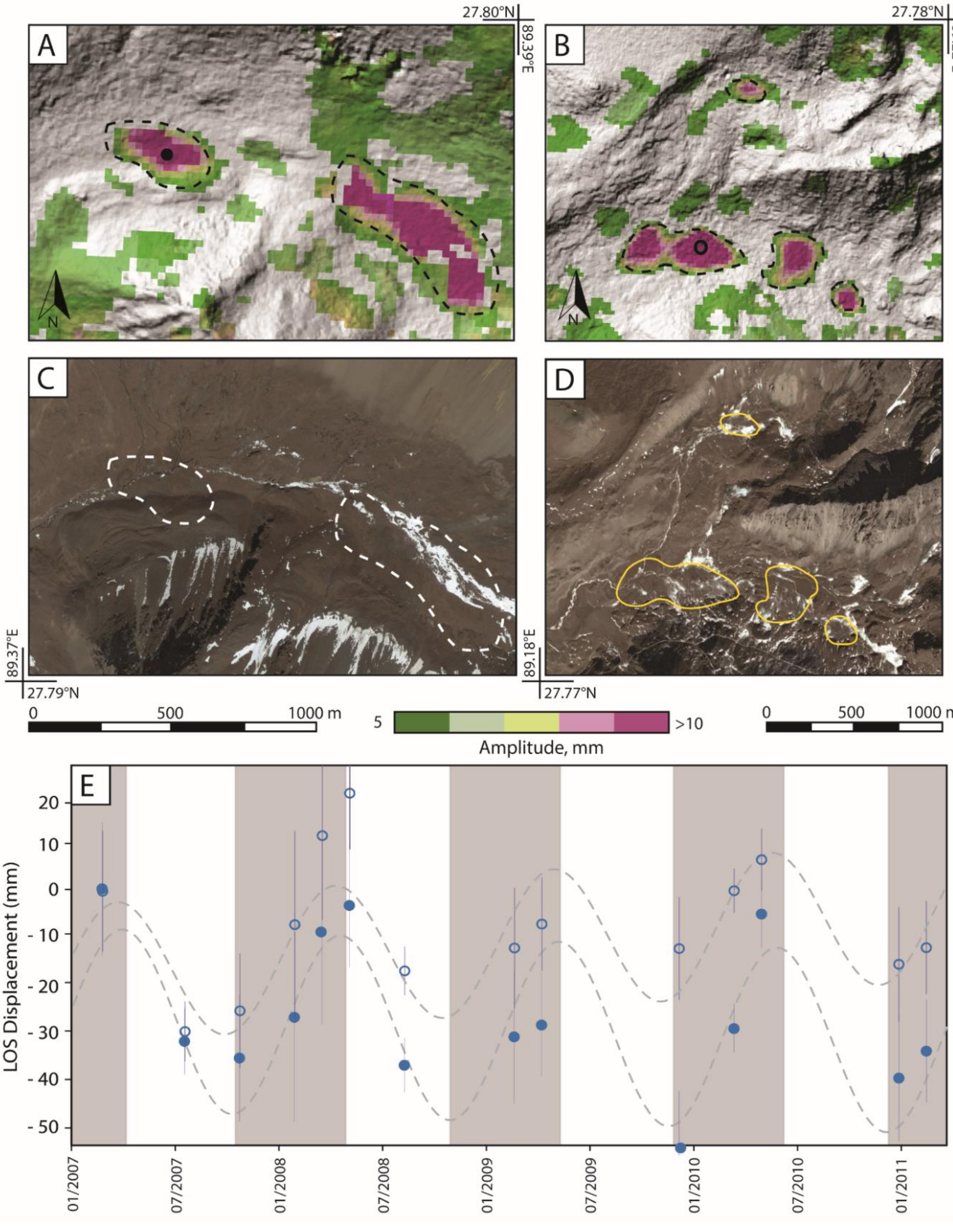

Fig. 4-8. A-B) Two examples of higher amplitudes areas observed with ALOS track 503540 after correction over braided stream planes. C-D) Corresponding GoogleEarth images to show the nature of the sediments involved. Note that rock glaciers visible in C are not affected by seasonal cycles. E) Time series: filled circles corresponding to filled circle in A; empty circles corresponding to empty circle in B.

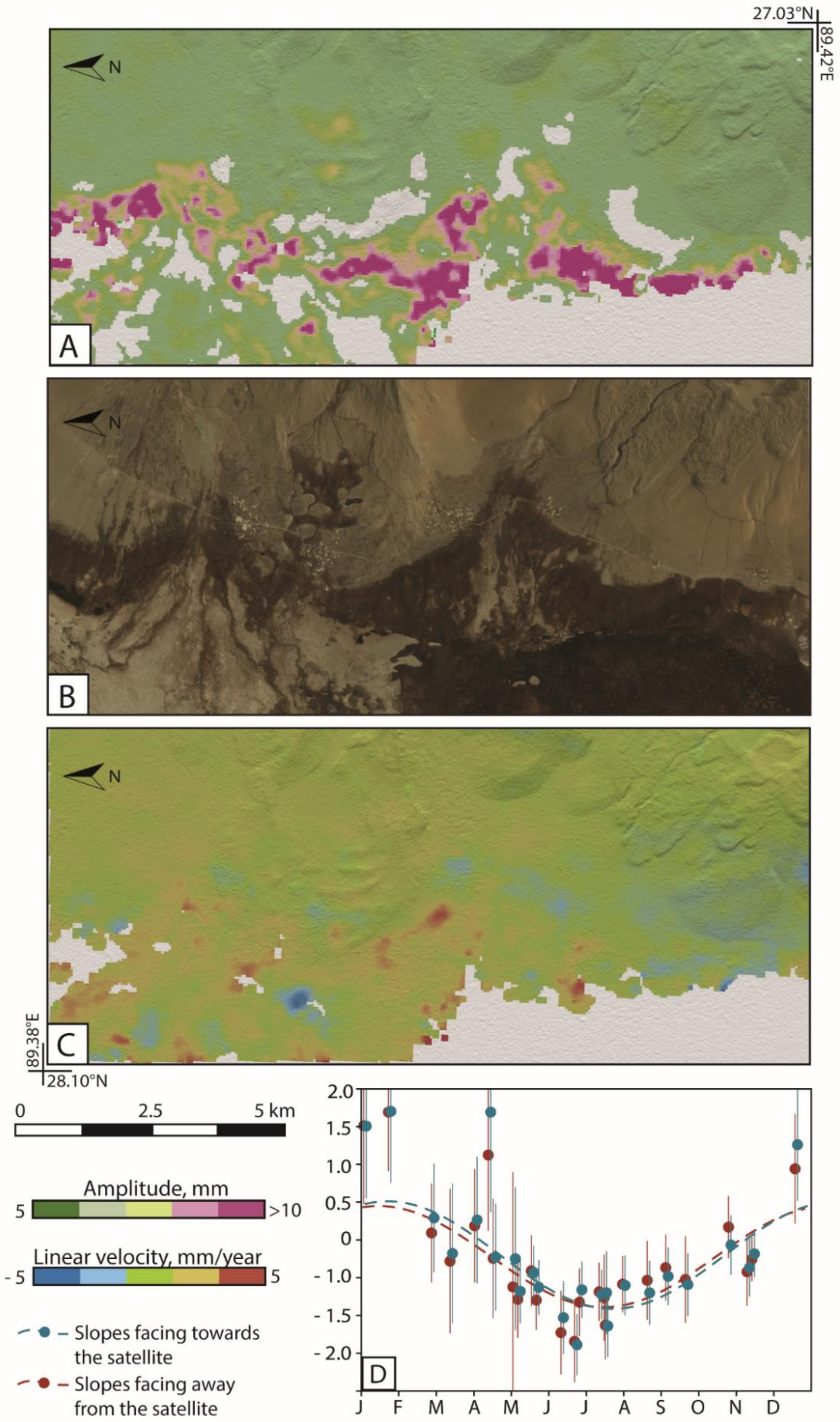

Fig. 4-9. A) Large area affected by seasonal cycles of ground deformation as observed with Envisat track 176. B) Corresponding GoogleEarth image showing that the higher amplitudes are observed over an area of darker sediments, the colour indicating the different nature of the material. C) Average velocity map showing that no large scale, long term trends are observed. D) Seasonality of de-trended pixels in A wrapped between January and December and separate in slopes facing towards and away from the satellite. It shows a maximum uplift in winter and the absence of aspect dependency for deformations occurring in the flat permafrost sedimentary basins.

areas of different sediments or clear morphologies, such as thermokarst basins (appendix 4-6 panels E-H and appendix 4-6 panels K-L) and glacial outwash plains (e.g. appendix 4-6, panels I-J) is a strong indication of the fact that such detected reversible displacements are not simply uncorrected atmospheric artefacts. Notably, we also observe heterogeneity of timing of seasonal cycles associated with the heterogeneity of amplitudes (appendix 4-6, panels C-D) which may be related to spatial variations in sediments and/or water content and consequent seasonal behaviour. Limitations in this case are related again to the relatively poor temporal sampling which does not allow, here with ALOS-1, to observe any asymmetry in the seasonality. For example, Daout et al. (2017) note that in winter months, when the active layer is completely frozen, a hiatus in the deformation occurs causing a flattening of the time series trend curve. Though in the figure in the appendix 4-7 (panels I-F) we suggest that our observations may hint at a similar behaviour, between February and April, the temporal sampling allows no more than a speculation. Further limitations are associated with the lack of detailed information regarding the type of sediments involved. In order for frost heave and thaw settlement to occur, relatively high proportions of fine-grained sediments need to be present, allowing for water to be hosted within the pore spaces. Coarse to very coarse grain material is not suitable for frost heave processes, due to the large spaces between blocks. For this reason, this type of effects is not expected in rock glaciers, given the coarse nature of the debris that forms them. This is supported by our findings as rock glaciers have never been observed in association with seasonal deformation. Seasonal reversible deformation in permafrost areas has been observed by other authors (e.g. Liu et al., 2014 and references therein). The melting of pore ice (thaw settlement) and the subsequent freezing (frost heave) can result in seasonal deformation of a few cm, for example 1 to 4 cm of seasonal reversible displacements have been observed in the arctic lowlands (Liu et al., 2014). This is of the order of magnitude of our observations.

4.5. Conclusions

We analysed in detail DInSAR time series over a large mountainous region that extends from northwestern Bhutan into southern Tibet, and extracted information regarding the type of processes responsible for the detected displacements. We established a methodology to retrieve information on potentially reversible ground deformation by separating this signal from the large-scale seasonality likely related to atmospheric delays or other processing artefacts such as long wavelength ramps. In particular, we distinguished between gravitational and reversible processes either linked to permafrost or hydromechanical effects. The MT-InSAR analysis approach that we applied here has the advantage of covering large areas and can potentially retrieve the timeline ground deformation measurements with millimetric accuracy. The procedure presented in this study allows to identify local slope processes (1) by mitigating the effect of long-wavelength artefacts uniform in one direction of the track or correlated at large scale to the topography, (2) by mapping the spatial variations of the amplitude and timing of the seasonal signal, and (3) by classifying categories of slope processes. We quantified the displacements observed on rock slides, rock glaciers and talus slopes associated with gravitational processes. Aside from the identification of gravitational movements, we are able to observe across a large region small-scale reversible deformation areas. More particularly, we provide insights into the possibility of observing with DInSAR the dynamics of natural annual ground water table variations on valley flanks, which, had not yet been explored with MT-DInSAR.

We also observe and quantify a large number of active areas on which freeze and thaw cycles are likely to occur, often in relation to fine grained alluvial sediments.

This work aims to maximise information on deformation types and processes acting on slopes in the Himalaya of northwestern Bhutan, however, similar approaches can be applied to other mountainous regions as well. Future work should involve validation, particularly in relation to reversible deformation caused by hydromechanical effects below the permafrost region. This could be done with in situ measurements or with the installation of corner reflectors that may allow a higher visibility over vegetated slopes (provided suitable position with respect to vegetation) and thus the use of higher temporal sampling C-band data like Sentinel-1. A higher temporal sampling could in fact allow the identification of non-sinusoidal cycles and confirm the slope response to hydrological conditions and possibly temperatures. If the reliability of InSAR data to distinguish between slope processes of different nature can be proven with either in-situ or more remote sensing data, then this methodology could represent a step forward for monitoring of slopes in mountainous regions and/or development countries with relatively little economical effort and high spatial coverage, supporting future infrastructure developments.

Acknowledgments

We are grateful to Paolo Riccardi from Sarmap for his generous and valuable support during the processing of SAR data. We also thank Wilfried Haeberli for his encouragement and ideas and Christophe Lambiel for the fruitful discussions. The project was funded by an ETH grant (ETH-38 15-2) and an ESA Alcantara project (ESA 4000117652/16/F/MOS). Simon Daout’s contribution was supported by the Emmy-Goethe grant of the German Research Foundation (DFG).

4.6. References

Ballantyne, C. K. (2002). Paraglacial Geomorphology. Quaternary Science Reviews, 21(18-19), 1935-2017. doi:10.1016/S0277-3791(02)00005-7

Barsch, D. (1992). Permafrost creep and rockglaciers. Permafrost and periglacial processes, 3(3), 175-188. doi:10.1002/ppp.3430030303

Barsch, D., and Caine, N. (1984). The nature of mountain geomorphology. Mountain Research and Development, 4(4), 287-298.

Bekaert, D. P. S., Walters, R. J., Wright, T. J., Hooper, A. J., and Parker, D. J. (2015). Statistical comparison of InSAR tropospheric correction techniques. Remote Sensing of Environment, 170, 40-47. doi:http://dx.doi.org/10.1016/j.rse.2015.08.035

Berardino, P., Fornaro, G., Lanari, R., and Sansosti, E. (2002). A New Algorithm for Surface Deformation Monitoring Based on Small Baseline Differential SAR Interferograms. IEEE transactions on geoscience and remote sensing, 40(11).

Catani, F., Canuti, P., and Casagli, N. (2014). The use of radar interferometry in landslide monitoring: Springer.

Cavalié, O., Doin, M.-P., Lasserre, C., and Briole, P. (2007). Ground motion measurement in the Lake Mead area, Nevada, by differential synthetic aperture radar interferometry time series analysis: Probing the lithosphere rheological structure. Journal of Geophysical Research Solid Earth, 112(B3). doi:doi.org/10.1029/2006JB004344

Chang, L., and Hanssen, R. F. (2015). Detection of permafrost sensitivity of the Qinghai–Tibet railway using satellite radar interferometry. International Journal of Remote Sensing, 36(3). doi:oi.org/10.1080/01431161.2014.999886

Crosetto, M., Devanthéry, N., Monserrat, O., Barra, A., Cuevas-González, M., Mróz, M., . . . Crippa, B. (2018). A Persistent Scatterer Interferometry Procedure Based on Stable Areas to Filter the Atmospheric Component. Remote sensing, 10(1780). doi:10.3390/rs10111780

Daout, S., Doin, M.-P., Peltzer, G., Lasserre, C., Socquet, A., Volat, M., and Sudhaus, H. (2018). Strain Partitioning and Present-Day Fault Kinematics in NW Tibet From Envisat SAR Interferometry. Journal of Geophysical Research, 123(3), 2462-2483. doi:http://dx.doi.org/10.1002/2017JB015020

Daout, S., Doin, M.-P., Peltzer, G., Socquet, A., and Lasserre, C. (2017). Large-scale InSAR monitoring of permafrost freeze-thaw cycles on the Tibetan Plateau. Geophysical Research Letters, 44, 901-909. doi:10.1002/2016GL070781

Delaloye, R., Lambiel, C., and Gärtner-Roer, I. (2010). Overview of rock glacier kinematics research in the Swiss Alps. Geographica Helvetica, 65, 135-145. doi:doi.org/10.5194/gh-65-135-2010

Delaloye, R., Perruchoud, E., Avian, M., Kaufmann, V., Bodin, X., Hausmann, H., . . . Thibert, E. (2008). Recent interannual variations of rockglacier creep in the European Alps. Paper presented at the 9th International Conference on Permafrost, University of Alaska, Fairbanks.

Dini, B., Manconi, A., and Loew, S. (2019a). Investigation of slope instabilities in NW Bhutan as derived from systematic DInSAR analyses. Engineering Geology, 259. doi:doi.org/10.1016/j.enggeo.2019.04.008

Doin, M.-P., Lasserre, C., Peltzer, G., Cavalié, O., and Doubre, C. (2009). Corrections of stratified tropospheric delays in SAR interferometry: Validation with global atmospheric models. Journal of Applied Geophysics, 69(1), 35-50. doi:doi.org/10.1016/j.jappgeo.2009.03.010

Doin, M.-P., Twardzik, C., Ducret, G., Lasserre, C., Guillaso, S., and S, J. (2015). InSAR measurement of the deformation around Siling Co Lake: Inferences on the lower crust viscosity in central Tibet. Journal of Geophysical Research Solid Earth, 120(7). doi:doi.org/10.1002/2014JB011768

El Tani, M., and Bremen, R. (2005). Val Termine cyclic deformation due to seasonal variation of water table. Paper presented at the The 41st U. S. Symposium on Rock Mechanics, Golden, Colorado.

Fattahi, H., and Amelung, F. (2014). InSAR uncertainty due to orbital errors. Geophysical Journal International, 199(1). doi:doi.org/10.1093/gji/ggu276

Gischig, V., Moore, J. R., Evans, K. F., Amann, F., and Loew, S. (2011). Thermomechanical forcing of deep rock slope deformation: 2. The randa rock slope instability. Journal of Geophysical Research, 116. doi:10.1029/2011JF002006

Goldstein, R. M., and Werner, C. L. (1998). Radar interferogram filtering for geophysical applications. Geophysical Research Letters, 25(21), 4035-4038. doi:doi.org/10.1029/1998GL900033

Grämiger, L. M., Moore, J. R., Gischig, V. S., and Loew, S. (2018). Thermomechanical Stresses Drive Damage of Alpine Valley Rock Walls During Repeat Glacial Cycles. Journal of Geophysical Research: Earth Surface, 123(10), 2620-2646. doi:10.1029/2018jf004626

Gruber, S. (2012). Derivation and analysis of a high-resolution estimate of global permafrost zonation. The Cryosphere, 6, 221-233. doi:10.5194/tc-6-221-2012

Gruber, S., and Haeberli, W. (2006). Permafrost in steep bedrock slopes and its temperature-related destabilization following climate change. Journal of Geophysical Research, 112. doi:10.1029/2006JF000547

Haeberli, W. (1985). Creep of mountain permafrost: internal structure and flow of Alpine rock glaciers. Mitteilungen der VAW-ETH Zürich, 17.

Hansmann, J., S., L., and Evans, K. F. (2012). Reversible rock-slope deformations caused by cyclic water-table fluctuations in mountain slopes of the Central Alps, Switzerland. Hydrogeology journal, 20(1), 73-91.

Hanssen, R. F. (2001). Radar interferometry: data interpretation and error analysis. Dordrecht: Kluwer Academic Publishers.

Hetényi, G., Le Roux-Mallouf, R., Berthet, T., Cattin, R., Cauzzi, C.,, and Phuntsho, K., Grolimund, R. (2016). Joint approach combining damage and paleoseismology observations constrains the 1714A.D. Bhutan earthquake at magnitude 8±0.5. Geophysical Research Letters, 43. doi:doi:10.1002/2016GL071033.

Hooper, A., Zebker, H., Segall, P., and Kampes, B. (2004). A new method for measuring deformation on volcanoes and other natural terrains using InSAR persistent scatterers. Geophysical Research Letters, 31(23). doi:doi.org/10.1029/2004GL021737

Hungr, O., Leroueil, S., Picarelli, L. (2014). The Varnes classification of landslide types, an update. Landslides, 11, 167-194. doi:10.1007/s10346-013-0436-y

JAXA. (2017). ALOS World 3D. Retrieved from http://www.eorc.jaxa.jp/ALOS/en/aw3d30/index.htm

Jolivet, R., Grandin, R., Lasserre, C., Doin, M.-P., and Peltzer, G. (2011). Systematic InSAR tropospheric phase delay corrections from global meteorological reanalysis data. Geophysical Research Letters, 28. doi:10.1029/2011GL048757

Kääb, A. (2002). Monitoring high-mountain terrain deformation from repeated air- and spaceborne optical data: examples using digital aerial imagery and ASTER data. ISPRS Journal of Photogrammetry and Remote Sensing, 57, 39-52.

Le Mouélic, S., Raucoules, D., Carnec, C., King, C., and F., A. (2002). A ground uplift in the city of Paris (France) detected by satellite radar interferometry. Geophysical Research Letters, 29(17), 34-31, 34-34. doi:https://doi.org/10.1029/2002GL015630

Li, Z., Muller, J.-P., and Cross, P. (2003). Comparison of precipitable water vapor derived from radiosonde, GPS, and Moderate-Resolution Imaging Spectroradiometer measurements. Journal of Geophysical Research, 108(D20). doi:10.1029/2003JD003372

Liu, L., Schaefer, K., Gusmeroli, A., Grosse, G., Jones, B. M., Zhang, T., . . . Zebker, H. (2014). Seasonal thaw settlement at drained thermokarst lake basins, Arctic Alaska. The Cryosphere, 8, 815-826. doi:10.5194/tc-8-815-2014

Liu, L., Schaefer, K., Zhang, T., and Wahr, J. (2012). Estimating 1992-2000 average active layer thickness on the Alaskan North Slope from remotely sensed surface subsidence. Journal of Geophysical Research, Earth Surface, 117(1). doi:10.1029/2011JF002041

Liu, L., Zhang, T., and Wahr, J. (2009). InSAR measurements of surface deformation over permafrost on the North Slpe of Alaska. Journal of Geophysical Research, 115. doi:10.1029/2009JF001547

Manconi, A., and Casu, F. (2012). Joint analysis of displacement time series retrieved from SAR phase and amplitude: Impact on the estimation of volcanic source parameters. Geophysical Research Letters, 39(14w). doi:doi.org/10.1029/2012GL052202

Massonnet, D., and Feigl, K. P. (1998). Radar interferometry and its application to changes in the Earth's surface. Reviews of Geophysics, 36(4), 441-500. doi:10.1029/97RG03139

Nagler, T., Mayer, C., and Rott, H., and Nagler, T. (2002, 11-14 September 2001). Feasibility of DInSAR for mapping complex motion fields of alpine ice- and rock-glaciers. Paper presented at the 3rd international symposium, Retrieval of bio- and geophysical parameters from SAR data for land applications, Sheffield, UK.

Notti, M., Zucca, Colombo. (2011). Models to predict persistent scatterers data distribution and their capacity to register movement along the slope.

Petley, D. (2012). Global patterns of loss of life from landslides. Geology, 40, 927-930. doi:10.1130/G33217.1

Rouyet, L., Kristensen, L., Derron, M.-H., Michoud, C., Blikra, L. H., Jaboyedoff, M., and Lauknes, T. R. (2017). Evidence of rock slope breathing using ground-based InSAR. Geomorphology, 289, 152-169. doi:doi.org/10.1016/j.geomorph.2016.07.005

Ruiz-Constán, A., Ruiz-Armenteros, A. M., Lamas-Fernández, F., Martos-Rosillo, S., Delgado, J. M., Bekaert, D. P. S., . . . Sanz de Galdeano, C. (2016). Multi-temporal InSAR evidence of ground subsidence induced by groundwater withdrawal: the Montellano aquifer (SW Spain). Environmental Earth Sciences, 75(242). doi:https://doi.org/10.1007/s12665-015-5051-x

Schlögel, R., Doubre, C., Malet, J.-P., and Masson, F. (2015). Landslide deformation monitoring with ALOS/PALSAR imagery: A D-InSAR geomorphological interpretation method. Geomorphology, 231, 314-330. doi:10.1016/j.geomorph.2014.11.031

Scotti, R., Crosta, G. B., and Villa, A. (2017). Destabilisation of Creeping Permafrost: The Plator Rock Glacier Case Study (Central Italian Alps). Permafrost and periglacial processes, 28(1), 22-236. doi:doi.org/10.1002/ppp.1917

Short, N., Brisco, B., Couture, N., Pollard, W., Murnaghan, K., and Budkewitsch, P. (2011). A comparison of TerraSAR-X, RADARSAT-2 and ALOS-PALSAR interferometry for monitoring permafrost environments, case study from Herschel Island, Canada. Remote Sensing of Environment, 115(12), 3491-3506. doi:10.1016/j.rse.2011.08.012

Strozzi, T., Farina, P., Corsini, A., Ambrosi, C., Thüring, M., Zilger, J., . . . Werner, C. (2005). Survey and monitoring of landslide displacements by means of L-band satellite SAR interferometry. Landslides, 2(3), 193-201. doi:10.1007/s10346-005-0003-2

Tang, W., Yuan, P., Liao, M., and Balz, T. (2018). Investigation of ground deformation in Taiyuan Basin, China from 2003 to 2010, with atmosphere-corrected time series InSAR. Remote sensing, 10. doi:10.3390/rs10001499

Walters, R. J., Elliott, J. R., Li, Z., and Parsons, B. (2013). Rapid strain accumulation on the Ashkabad fault (Turkmenistan) from atmosphere-corrected InSAR. Journal of Geophysical Research Solid Earth, 118, 3674-3690. doi:doi.org/10.1002/jgrb.50236

Wasowski, J., and Bovenga, F. (2014). Investigating landslides and unstable slopes with satellite Multi Temporal Interferometry: Current issues and future perspectives. Engineering Geology, 174, 103-138. doi: 10.1016/j.enggeo.2014.03.003

Wegmann, M., and Gudmundsson, H. G. (1999). Thermally induced temporal strain variations in rock walls observed at subzero temperatures. In W. Y. Hutter K., Beer H. (Ed.), Advances in Cold-Region Thermal Engineering and Sciences. Lecture Notes in Physics. (pp. 511-518): Springer, Berlin, Heidelberg.

Yu, C., Li, Z., Penna, N. T., and Crippa, P. (2018). Generic Atmospheric Correction Model for Interferometric Synthetic Aperture Radar Observations. Journal of Geophysical Research: Solid Earth, 123. doi:10.1029/2017JB015305

4.7. Appendix

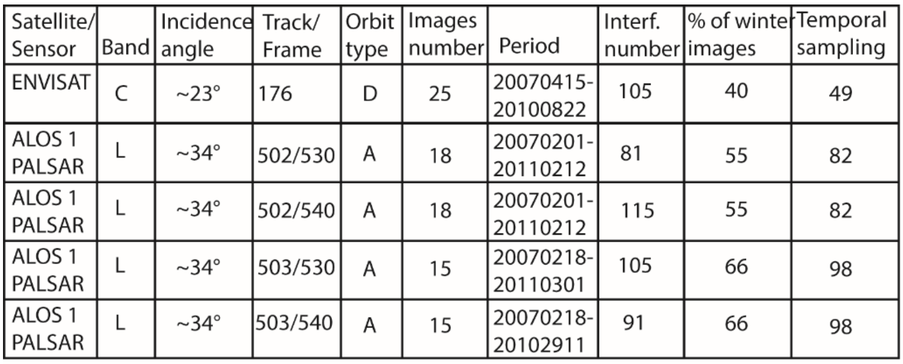

Satellite/ Sensor	Band	Incidence angle	Track/ Frame	Orbit type	Images number	Period	Interf. number	% of winter images	Temporal sampling
ENVISAT	C	~23°	176	D	25	20070415-20100822	105	40	49
ALOS 1 PALSAR	L	~34°	502/530	A	18	20070201-20110212	81	55	82
ALOS 1 PALSAR	L	~34°	502/540	A	18	20070201-20110212	115	55	82
ALOS 1 PALSAR	L	~34°	503/530	A	15	20070218-20110301	105	66	98
ALOS 1 PALSAR	L	~34°	503/540	A	15	20070218-20102911	91	66	98

App. 4-1. Table showing the data used for SBAS processing.

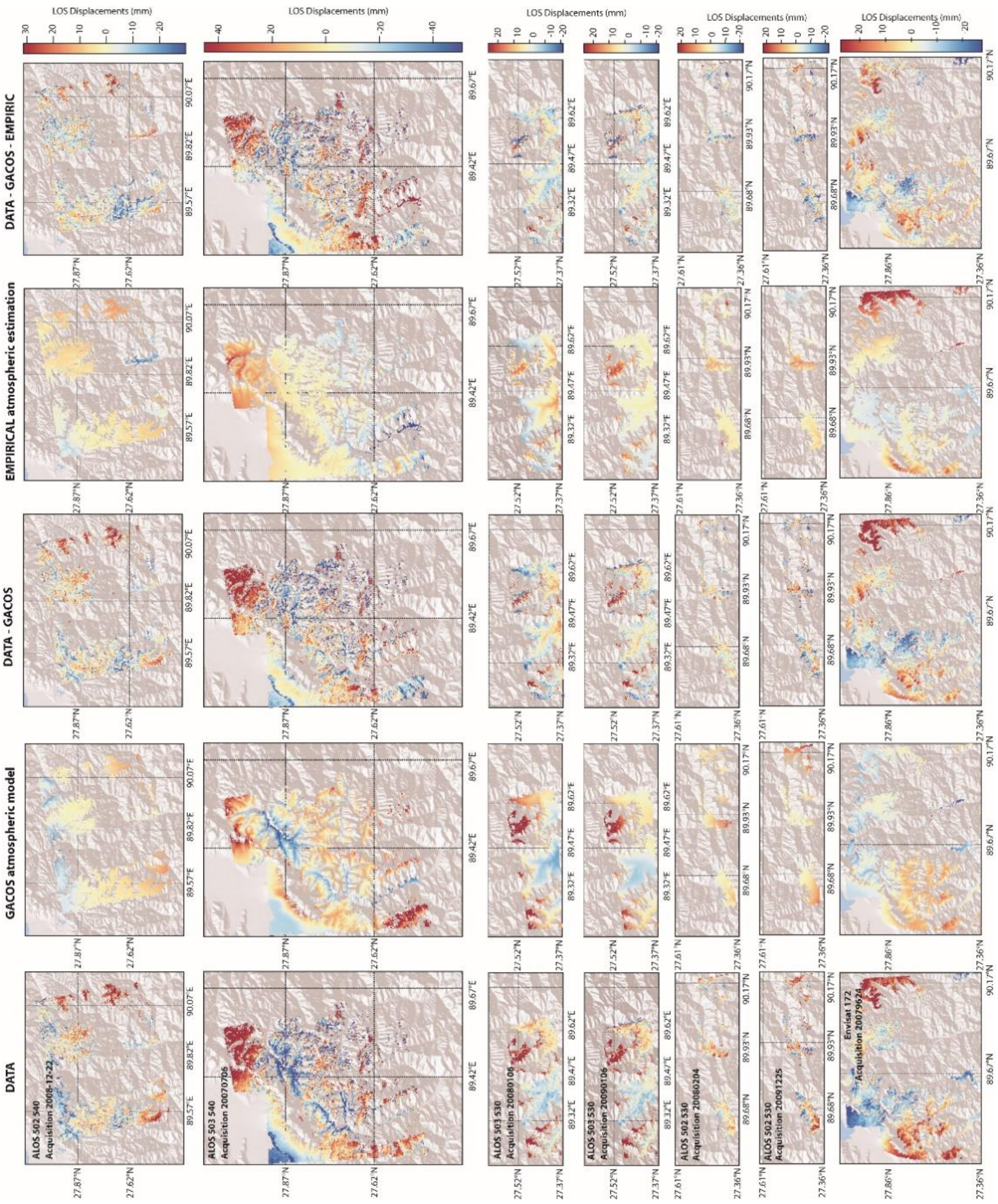

App. 4-2. Examples of applied corrections: one sample date for each used track.

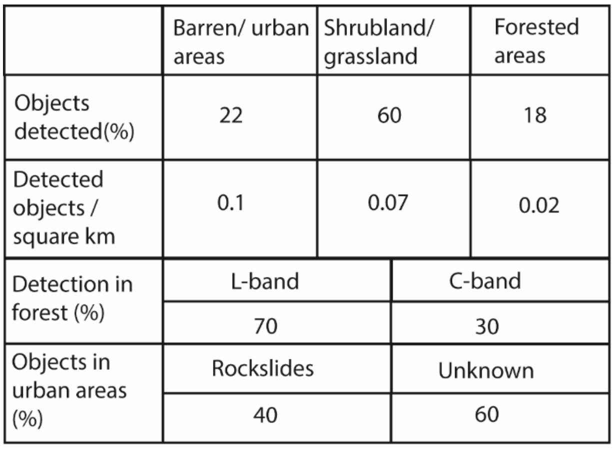

<table>
<tr><th></th><th>Barren/ urban areas</th><th colspan="2">Shrubland/ grassland</th><th>Forested areas</th></tr>
<tr><td>Objects detected(%)</td><td>22</td><td colspan="2">60</td><td>18</td></tr>
<tr><td>Detected objects / square km</td><td>0.1</td><td colspan="2">0.07</td><td>0.02</td></tr>
<tr><td rowspan="2">Detection in forest (%)</td><td colspan="2">L-band</td><td colspan="2">C-band</td></tr>
<tr><td colspan="2">70</td><td colspan="2">30</td></tr>
<tr><td rowspan="2">Objects in urban areas (%)</td><td colspan="2">Rockslides</td><td colspan="2">Unknown</td></tr>
<tr><td colspan="2">40</td><td colspan="2">60</td></tr>
</table>

App. 4-3. Percentage of objects detected in different land cover with L and C band.

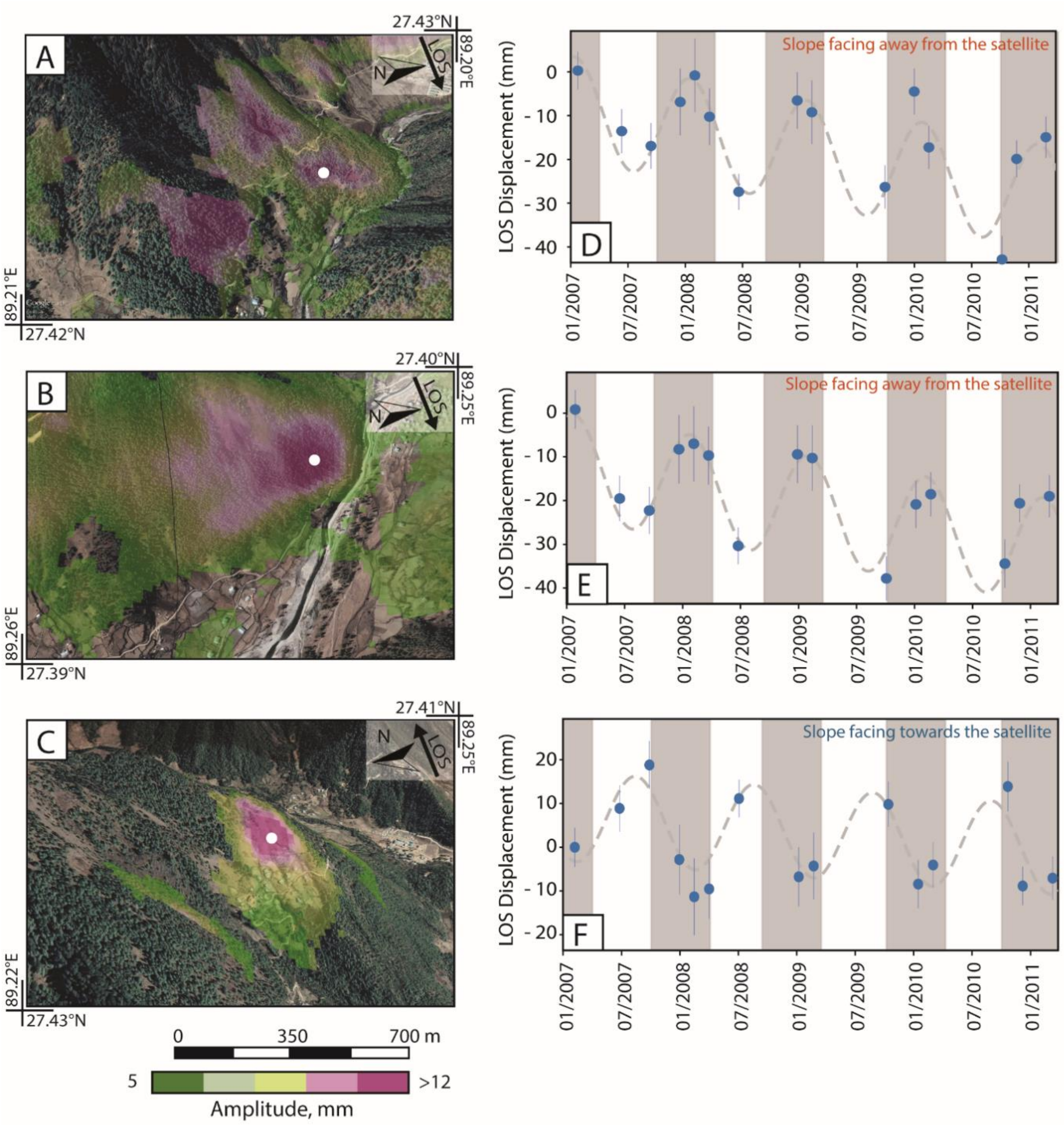

App. 4-4. A-B-C) amplitudes of seasonal cycles obtained with ALOS track 503530 over three slopes in the valley of Haa, A-B face away from the satellite, C faces towards the satellite. D-E-F corresponding time series.

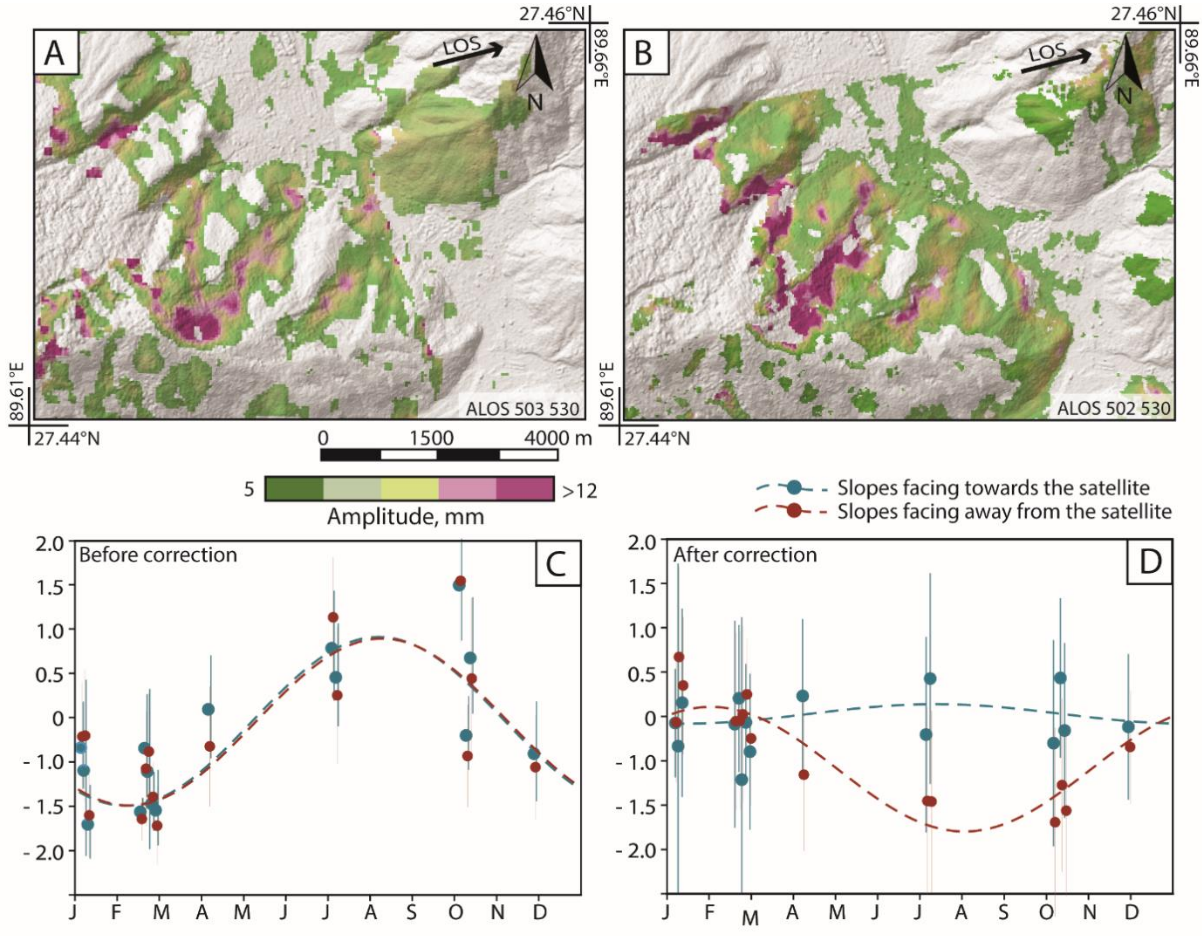

App. 4-5. An area in the valley of Thimphu seen with ALOS track 503530 (A) and 502530 (B), showing higher amplitudes of seasonal cycles potentially related to reversible ground deformation. C) mode of seasonality for pixels in the area before correction, after separating by slopes facing towards and away from the satellite. Seasonality is dominated by atmosphere. D) mode of seasonality after correction, this showing no seasonality for slopes facing the satellite and strong seasonality with movement towards the satellite in winter for slopes facing away from the satellite, compatible with valley closure and strong component away from valley axis in winter.

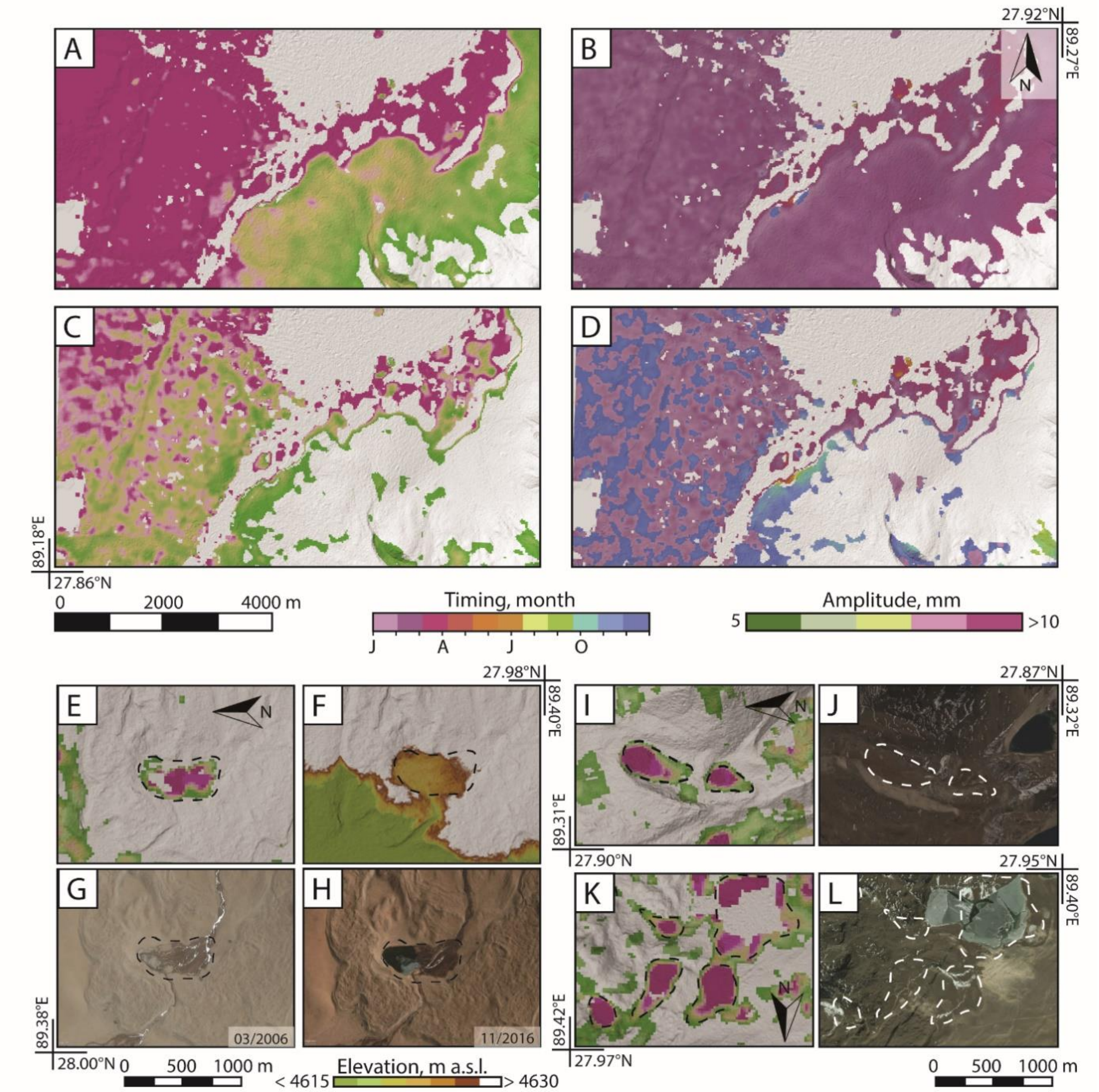

App. 4-6. A-B) amplitude and timing of seasonal cycles over an area within ALOS track 503540 before correction. C-D) amplitude and timing of seasonal cycles over the same area after correction. In A the amplitudes are really large and saturated, in C, smaller areas of high amplitudes appear. The timing, although within the same ranges (winter) is also less homogeneous. In E-F-G-H a termokarst basin, with amplitudes (E), elevation (F) and GoogleEarth images (G-H) showing the formation of the basin. I-K) areas of high amplitudes over fine sediments with GoogleEarth images (J-L) showing the correspondence with areas of sediments defined by texture or colour change and over a glaciated lake. Irrespective of the periglacial processes acting upon these landforms, these images show that the amplitudes are not associated with atmospheric cycles.

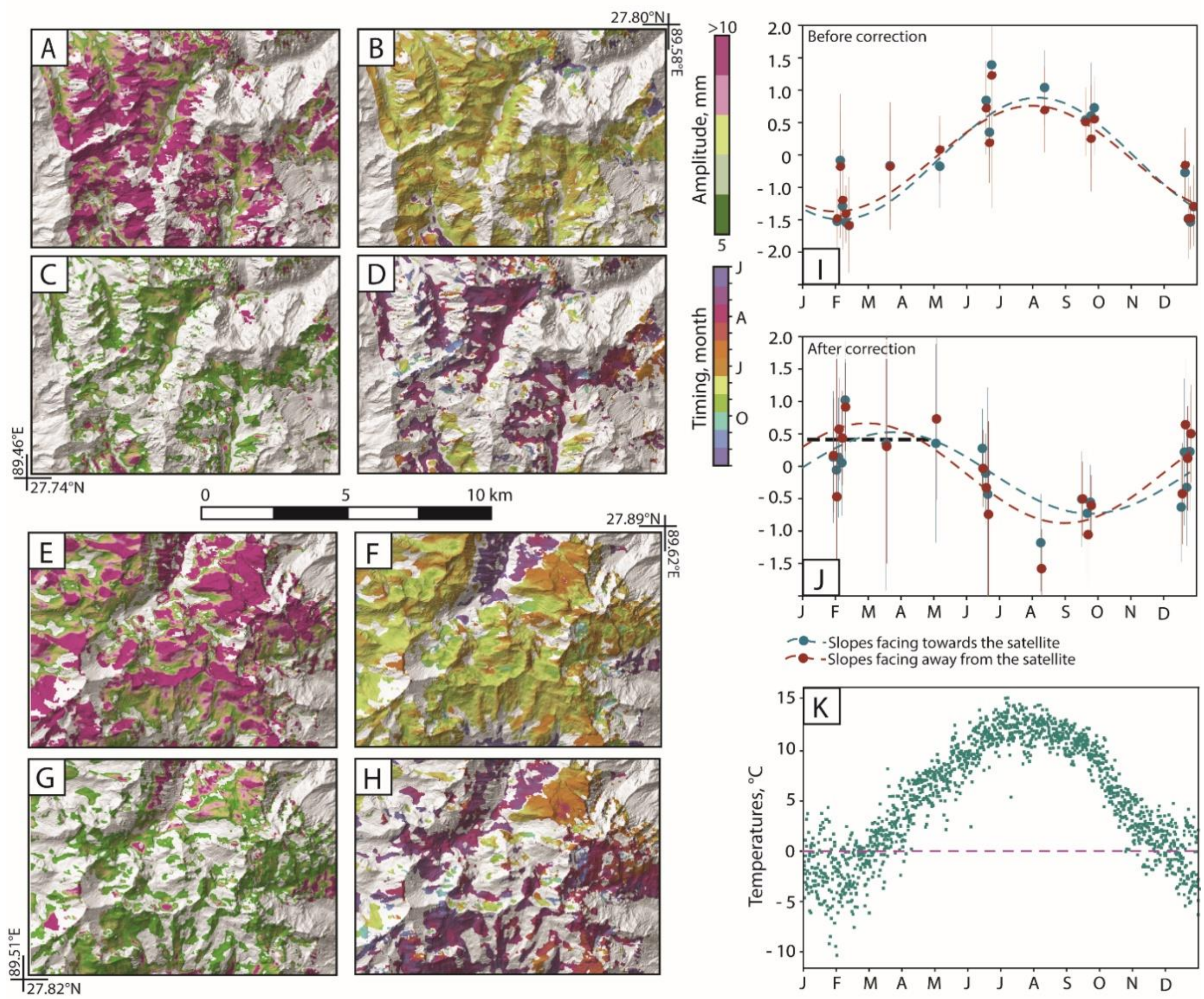

App. 4-7. Two areas taken from ALOS track 502540, showing amplitudes (A-E) and timing (B-F) of seasonal cycles before corrections. Same areas after corrections with amplitudes (C-G) and timing (D-H) of seasonal cycles. I) shows the mode of the seasonality collapsed over a year (wrapped between January and February) and separated by slope facing towards and away from the satellite, with all pixels falling within the atmospheric delay. J) mode of seasonality of pixels in the same areas, again separated by slopes facing away and towards the satellite and collapsed over a year, this time showing maximum uplift in winter and no aspect dependency. K) ERA-Interim reanalysis 2m average temperatures for a 75km grid square centred over 27.75°N, 89.25° E, collapsed over a year.

5. Regional scale investigation of preconditioning factors of rock slope instabilities in NW Bhutan

Benedetta Dini[1], Jordan Aaron[1], Simon Loew[1]

[1] Department of Earth Sciences, ETH Zurich, Zurich, Switzerland

Abstract

Large rock slope instabilities have the potential to evolve into catastrophic failure and pose direct and indirect hazards to communities and infrastructure located in their proximity or up to several km downstream. Furthering the knowledge of the factors that govern the distribution of large rock slope instabilities is thus important in order to better understand the hazard related to them. Preconditioning factors, such as lithological and structural characteristics of a slope, have been recognised by many authors as exerting an important control on landslide distributions in various mountain belts. Often structural controls are studied at the site scale, with the use of kinematic analyses based on some knowledge of existing joint and fault sets. Some authors have investigated the structural control on soil or rock slides distribution over larger areas, though with limitations related to unknown regional fracture orientations distribution or to limited structural datasets. In this work we compile a new, large rock slope instability inventory and an extensive structural dataset for northwestern Bhutan. Given the large extent and inaccessibility of the study region, methodologies built on remote sensing data are most suitable and applicable to similar regions. Our dataset is thus largely based on remote sensing (optical images, high resolution digital surface model (DSM)), with the inclusion of some field observations. In order to account for the variability in the density of different layers of our dataset, we apply a weighting system to the structural data. Successively, kinematic analyses over all structural domains of the study region are carried out to investigate structural controls over landslide distribution at a regional scale. We observe that structural control exists in 6 of 7 domains, with foliation strongly influencing sliding mechanisms. A lithological control appears also evident, with sedimentary rocks showing the highest landslide densities in the region.

5.1. Introduction

Large rock slope instabilities are ubiquitous in mountainous regions (Crosta et al., 2013; Hutchinson, 1988; Heim, 1932). These features can have remarkably large volumes (Clayton et al., 2017; Fey et al., 2017), and can transition into extremely-rapid rock slides or rock avalanches (Hungr et al., 2014). Hungr et al. (2014) note that a large number of deforming mountain slopes remain stable in historical time, whereas a small number of cases transition into catastrophic failures. Many developed regions are located in close proximity to deforming slopes, with high population densities and developed infrastructure often lying in elevated risk areas. In less developed countries, or remote mountainous regions, although lower population and infrastructure densities are often related to lower exposure, direct and indirect landslide hazards can adversely affect an already weak infrastructure, interrupt lifelines and turn arable land unusable. Thus, understanding the mechanisms that control large rock slope instabilities is crucial to manage the risk posed by these events in different geographical settings. The factors that govern the occurrence and evolution of large rock slope instabilities can be broadly subdivided into preconditioning, preparatory and triggering factors (e.g. Finlayson and Statham, 1980). Preconditioning factors, such as lithology and structural geology, can be investigated by looking at landslide occurrence at a regional scale (Ivy-Ochs et al., 2017; Pedrazzini et al., 2016; Stead and Wolter, 2015; Tonini et al., 2014; Agliardi et al., 2013; Crosta et al., 2013). Preparatory factors, such as glacial cycles (Grämiger et al., 2017; McColl and Davies, 2013) can be studied by combining detailed field observations with advanced numerical modelling at both the regional and site scale. Triggering factors, such as heavy precipitation or strong seismic events, are often studied with detailed investigation at the site scale (Clayton et al., 2017; Glueer and Loew, 2015). The understanding of the interaction between preconditioning and preparatory factors is important for reconstructing the history of a slope, to identify failure mechanisms, quantify volumes and, ultimately, to better identify methods for hazard assessment (Agliardi et al., 2013).

For a given area, the regional structural regime is an important preconditioning factor for rock slope instabilities. Important regional faults have been recognised to influence the formation and geometry of landslides, these ranging from soil slides in saprolites (Cerri et al., 2018) to large and deep-seated rock slope instabilities (Agliardi et al., 2009; Hermanns, 2006; Agliardi et al., 2001). Moreover, distance to faults has been considered an important factor controlling landslides distribution as a proxy for rock damage (Robinson et al., 2015).

Regional scale analyses have been performed to understand rock slope instability occurrence (Francioni et al., 2018; Mishra et al., 2018; Park et al., 2016; Santangelo et al., 2015; Di Maggio et al., 2014; Gokceoglu et al., 2000). A subset of these studies uses prominent regional structural sets to identify slope instabilities prone to the four kinematic failure modes: planar sliding, sliding wedge, block topple and flexural topple (Hudson and Harrison, 1997). Kinematic analyses have been applied to larger areas (Cerri et al., 2018; Park et al., 2016; Gokceoglu et al., 2000). In these studies, the main uncertainties arise from unknown geotechnical parameters, such as friction angle, from uncertain location and orientations of discontinuities into the rock mass and from variations in slope orientation that cannot be accounted for. Therefore, this type of approach is less reliable in cases in which non-systematic discontinuities interact adversely with a slope, potentially leading to failure. Thus, few studies exist in which spatially distributed data of observed discontinuities have been used, especially over a very extensive region, normally due to the difficulties in acquiring detailed structural data (Park et al. 2016).

In this work, we perform a regional analysis of the preconditioning factors that govern the occurrence of large landslides in the higher Himalaya of northwestern Bhutan, over a 7200 km2 large area. The extent and remoteness of the study area require the development of new methodologies largely based on remote sensing techniques, supplemented and verified by local field measurements. The derivation of the landslide database has been described in previous contributions (Dini et al., 2019a; Dini et al., 2019b). In this paper we develop and apply a probabilistic approach for a regional scale kinematic analysis using a structural dataset and slope morphology derived from satellite optical and DSM data. We provide a new regional dataset of steeply dipping brittle fault planes which influence the stability of rock slopes, and can serve as a basis for landslide susceptibility mapping in our inaccessible, and high alpine study region.

In the following we first briefly describe the geological and tectonic setting of the study area, we then present in detail the different layers composing the dataset and how they were obtained (landslide inventory, structural data), we show the methodology used to weight the unevenly recorded structural measurements and to perform the regional kinematic analyses. We finally present and discuss the results, which show that for 6 out of 7 domains a structural control exists and that landslides cluster around specific ranges of slope aspects and slope angles.

5.2. Geology and tectonics of the study area

The study area is located in northwestern Bhutan, between the settlements of Haa, Paro, Timphu and Punakha in the south and the border with Tibet in the north (roughly between 27.3° and 28.0° N and 89.0° and 90.0° E, see inset in Fig. 5-1). The geology of the study region includes rocks from the Grater Himalayan sequence, which are orthogneiss and generally higher grade metasediments, mainly, paragneiss, schist and quartzite. The Tethyan Himalayan sequence represents the sedimentary sequence of the Tethyan Ocean, deposited at the northern margin of the Indian continent. These rocks

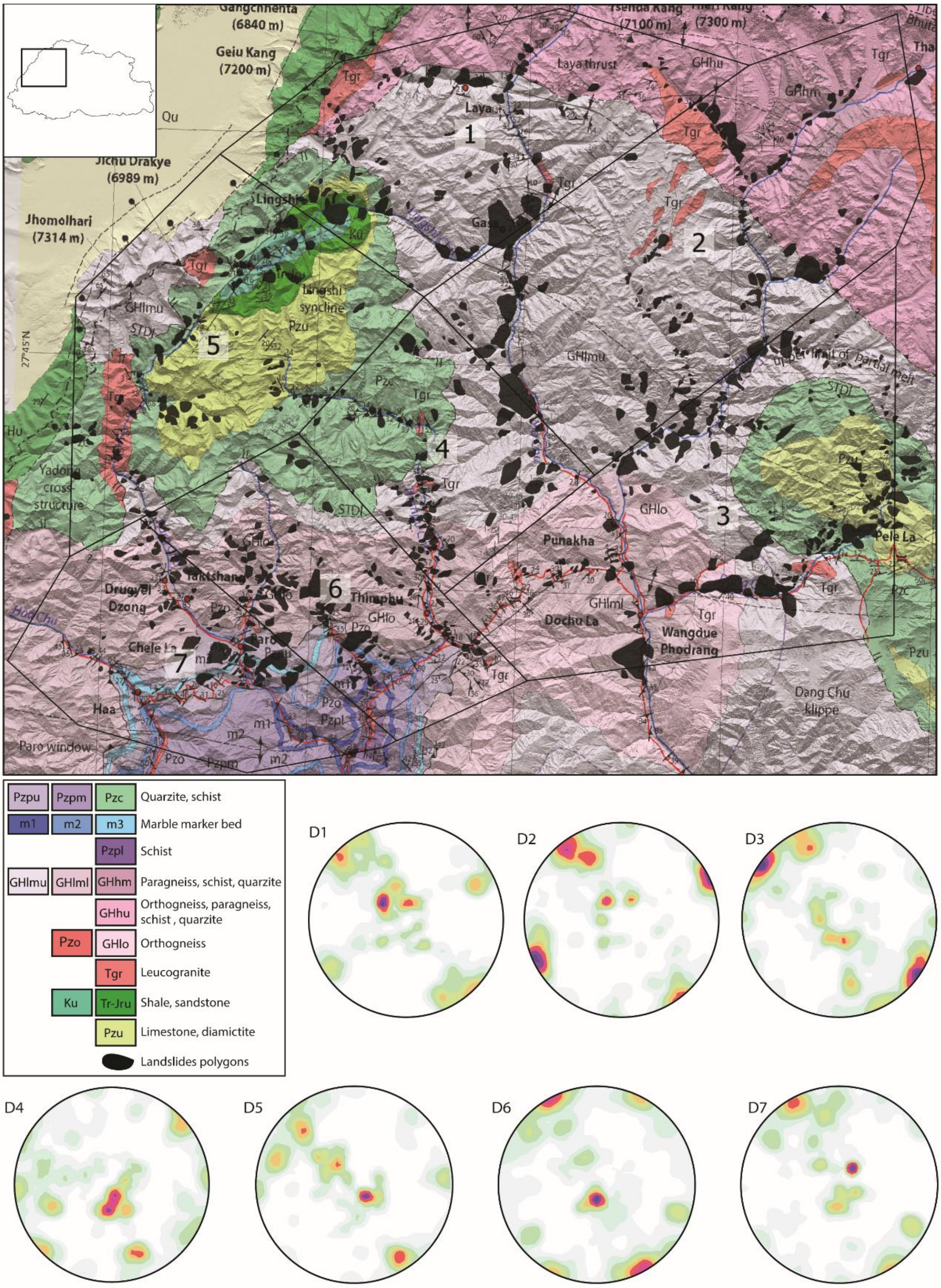

Fig. 5-1. Geological map of the area of study (Long et al.,2011). Black polygons represent the landslide inventory generated in this study. Stereoplots represents the main structural sets found in the domains. Domains are marked as black lines and numbers in the main figure. Inset shows location and extent of area of study.

lie structurally above the Greater Himalayan sequence, are characterised by lower metamorphic grades and largely comprise limestone, sandstone, shale and quartzite (Gansser, 1983).

A study of the paleomagnetism of Tethyan Himalayan rocks (Antolín et al., 2012) has shown that in more recent stages of the Himalayan orogeny deformation, strain in Bhutan and southern Tibet has been partitioned between conjugate strike slip fault systems. Such fault systems are associated with clockwise rotation of southern Tibet with respect to India and with WNW-ESE extension and NNW-SSW shortening. The main structures on which such deformation takes place are NE-SW oriented faults and graben, such as the Lingshi fault and the Yadong-Gulu graben (the latter, expression of WNW-ESE extension) (Antolín et al., 2012). Faults belonging to the Lingshi fault set are sinistral strike slip faults with sub-vertical dip. The Lingshi fault is found in the NW of our study region, offsetting other important regional structures and running at mid-crustal depth through the exposed Tethyan sediments (Fig. 5-1). The conjugate set to this system includes dextral strike slip faults, oriented NNW-SSE. Faults belonging to this set have also been mapped in NW Bhutan in previous studies (Antolín et al., 2012; Wiesmayr et al., 2001).

All		***Mountain slope deformation (and rock slope deformation?)***		***Rock slides***	
Main scarp	*(B)*	*Double crest*	*(B)*	*Tension cracks*	*(N)*
Secondary failures	*(%)*	*Depression near crest*	*(B)*	*Depletion zone*	*(B)*
Enhanced rockfall	*(%)*	*Secondary scarps*	*(N)*	*Large accumulation*	*(B)*
Sympathetic failure	*(B)*	*Counterscarps*	*(N)*		
		Lineaments	*(%)*		
		Concave-convex profile	*(0-1-2)*		
		River displacement	*(B)*		
		Erosion at the toe	*(B)*		
		Slope steepness	*(B)*		

Table 5-1. Characteristics used to describe objects in the inventory and to generate a semi-quantitative landslide index. (B) value assigned is 0 (absence) or 1 (presence), (0-1-2) reflects the three profile possibilities described in the main text, (N) number corresponding to how many of the features are observed, (%) characteristics that are quantified in terms of percentage of total areaThe profile is assigned a 0 in case of linear profile, 1 if only bulging at the toe is visible and 2 if a concave upper profile is also present. Secondary failures, enhanced rock fall activity and lineaments are more difficult to quantify. Hence, they are assigned a percentage index which is describing the fraction of area of the whole polygon that they affect. Finally, the numbers assigned to secondary scarps, counterscarps and tension cracks are normalised, and then all indices added into a landslide index. Landslide indices are compiled separately for rock slides, rock slope or mountain slope deformations according to the parameters that are associated to each category (as shown in table) and they represent a semi-quantitative measure of the likelihood of a polygon in the inventory actually being a landslide.

5.3. Data

5.3.1. Landslides inventory based on optical images

In this work, a large landslide inventory was compiled for the study area through the analysis of GoogleEarth optical images and a high-resolution DSM (ALOS World3D, 5m Ground Sample Distance, (JAXA, 2017)). Landslides were mapped systematically, by subdividing the entire study region into a 10 km grid and analysing each square grid, focusing on the identification of morphological features (Table 1). Each identified landslide was classified as either a rock slide or rock slope deformation/mountain slope deformation, based on the classification of Hungr et al. (2014). The difficulty in associating a rock slide type on the basis of the available remote sensing data allowed only for a main distinction between rock slide (including and not differentiating translational, rotational, wedge, compound, irregular) or rock slope deformation and mountain slope deformation to be made. The inventory contains either potential instabilities or certain landslides, with different confidence levels. Qualitative levels of activity were assigned after scrutiny of the images, together with a description of the characteristics observed. Features such as increased rock fall activity with respect to surrounding, erosion at the toe and deep and active debris flow channels were used to qualitatively assess levels of activity. Moreover, a number of attributes, presented in Table 1, were collected for each identified landslide and the degree of certainty in the interpretation was quantified.

5.3.2. Landslide inventories based on DInSar

Active slope movements were mapped using Synthetic Aperture Radar differential interferometry (DInSar) in two previous works, this leading to the generation of two additional landslide datasets as explained in the following. A large-scale analysis of 521 interferograms obtained with data acquired by ALOS-1 and Envisat was performed in Dini et al. (2019a). Here, 693 potentially unstable slopes were mapped on the basis of displacement patterns observed in individual interferograms. A geomorphological analysis of the unstable areas detected revealed that around 77.5% of them are rock slope instabilities, whilst the rest are gravitational displacements either associated with soil creep or slide or rock glaciers. In Dini et al. (2019b), the same SAR dataset was used for small baseline subset (SBAS) processing, to retrieve velocity, cumulative displacements and time series of displacements at the regional scale and we mapped 550 areas with displacements compatible with slope instability. Only 10% were classified as potential rock slope instabilities and 14% remain of unknown type, the rest is attributed to rock glacier, soil creep/slide or reversible deformation. Given the intrinsic difficulties of the technique used (Dini et al., 2019a,b) the two approaches are complementary and do not allow necessarily the identification of the exactly the same displacement areas. In particular, the time series retrieval is complicated by the large scale and the land cover. On the other hand, the analysis of single interferograms with a shorter temporal interval than the whole time-series period may not allow the identification of slopes affected by low displacement rates. For these reasons, the areas mapped in these two works present only a partial overlap. Moreover, between the optical based inventory and the DInSAR based inventories, only a partial overlap is observed. This is because, the

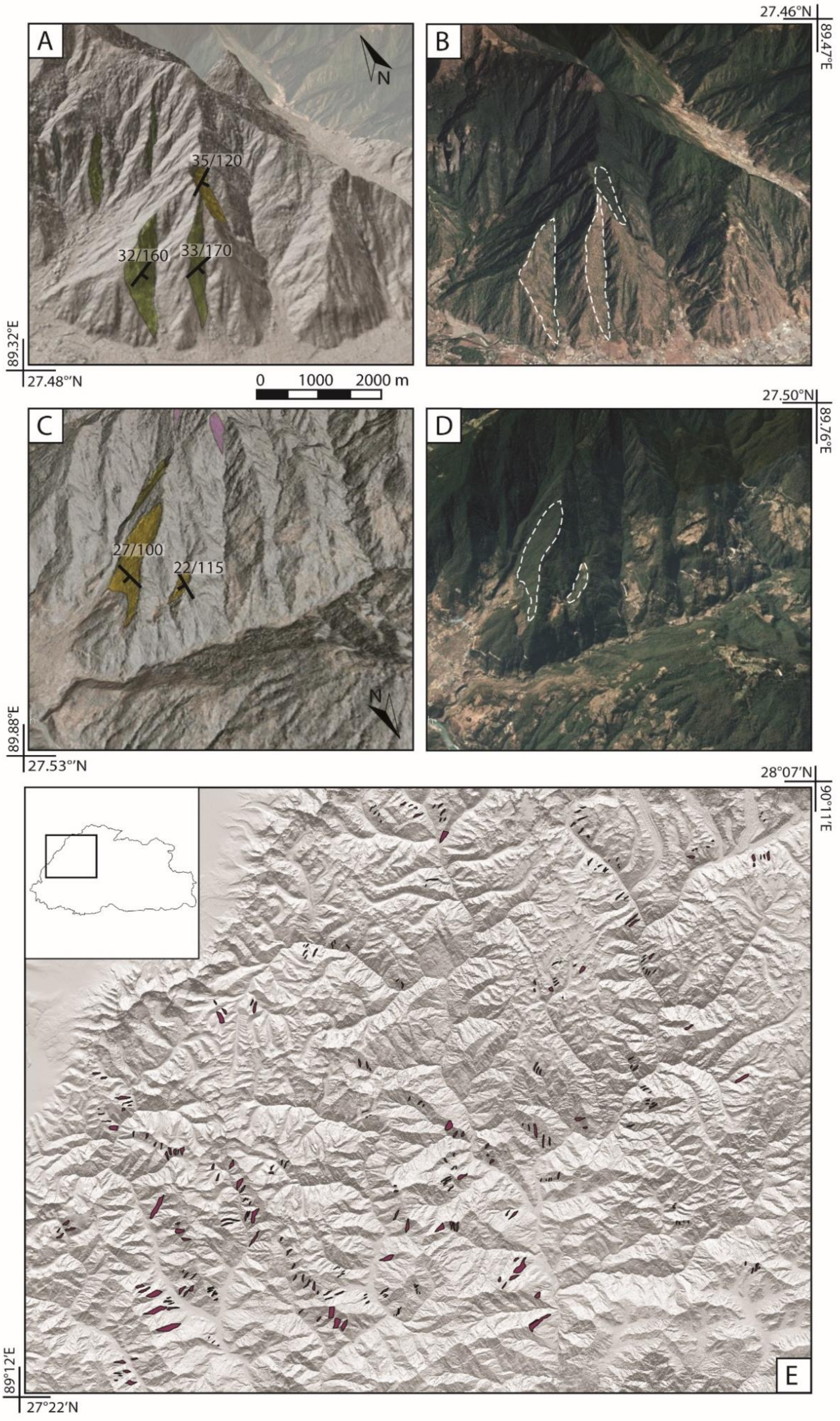

Fig. 5-2. A-C) Hillshade showing mapped planar valley flanks with remote sensing. The extracted orientations are shown. B-D) GoogleEarth image of the same valley flanks. E) large scale map of the mapped planar valley flanks.

first represents the mapping of not only ongoing instabilities, but of old instabilities and deposits, that may not be active in recent times. The DInSAR inventories, identify recent activity, which may not overlap with mapped past landslides. In the present work, of the DInSAR inventories, we only use the polygons corresponding to potential rock slope instabilities mapped on interferograms and on SBAS results.

5.3.3. Structural dataset and generation of lineaments map

The dataset used for the investigation of structural control on landslide distribution has a complex structure and is composed by the following layers: 1) in-situ measured foliation, 2) in-situ measured faults, 3) planar structures mapped on the high-resolution DSM and 4) lineaments mapped on DSM model and optical images. The location and orientation of foliation and faults were measured during two field campaigns (September 2016, October 2017), however their presence is restricted to the areas of Haa, Paro, Thimphu and Punakha, covering just over 20% of the entire study area (see Fig. 5-1 for place locations, and App. 5-1 for locations of field measurements). The foliation layer was enhanced through the addition of measurements digitised from Long et al. (2011) and of measurements recorded by D. Grujic (pers. comm., see App. 5-1). The foliation and faults layers contain respectively 493 data points unevenly distributed across the study area and 556 data points only in the south of the study area (App. 5-2 and 5-3).

Field observations in the lower valleys of Paro and Thimphu suggest that the morphology of some valley flanks, particularly those that are smooth and planar and display a flatter morphology than the opposite valley flank, must be controlled by planar geological structures, either faults or foliation planes (Fig. 5-2). Valley flanks that meet these criteria were mapped on GoogleEarth images and on the high resolution ALOS DSM, generating a layer containing 286 objects, sparsely, but relatively evenly, distributed across the entire study area (Fig. 5-2E and App. 5-4). The mean slope and mean aspect were calculated for each of them, in order to extract an orientation (as shown in Fig. 5-2A and C).

Finally, a lineament map was generated for the entire study region, containing 1973 objects distributed over the entire study area, with higher densities in the centre (App. 5-6). Lineaments were visually mapped on optical images and DSM, by subdividing the study area in a 10 km grid. Lineaments as short as 80 m and as long as 14 km were mapped (Figure 5-6). Lineaments were only mapped when they had a clear morphologic expression, so adjacent segments with similar orientation may be mapped as separate features. The potential bias introduced by this procedure is discussed in section

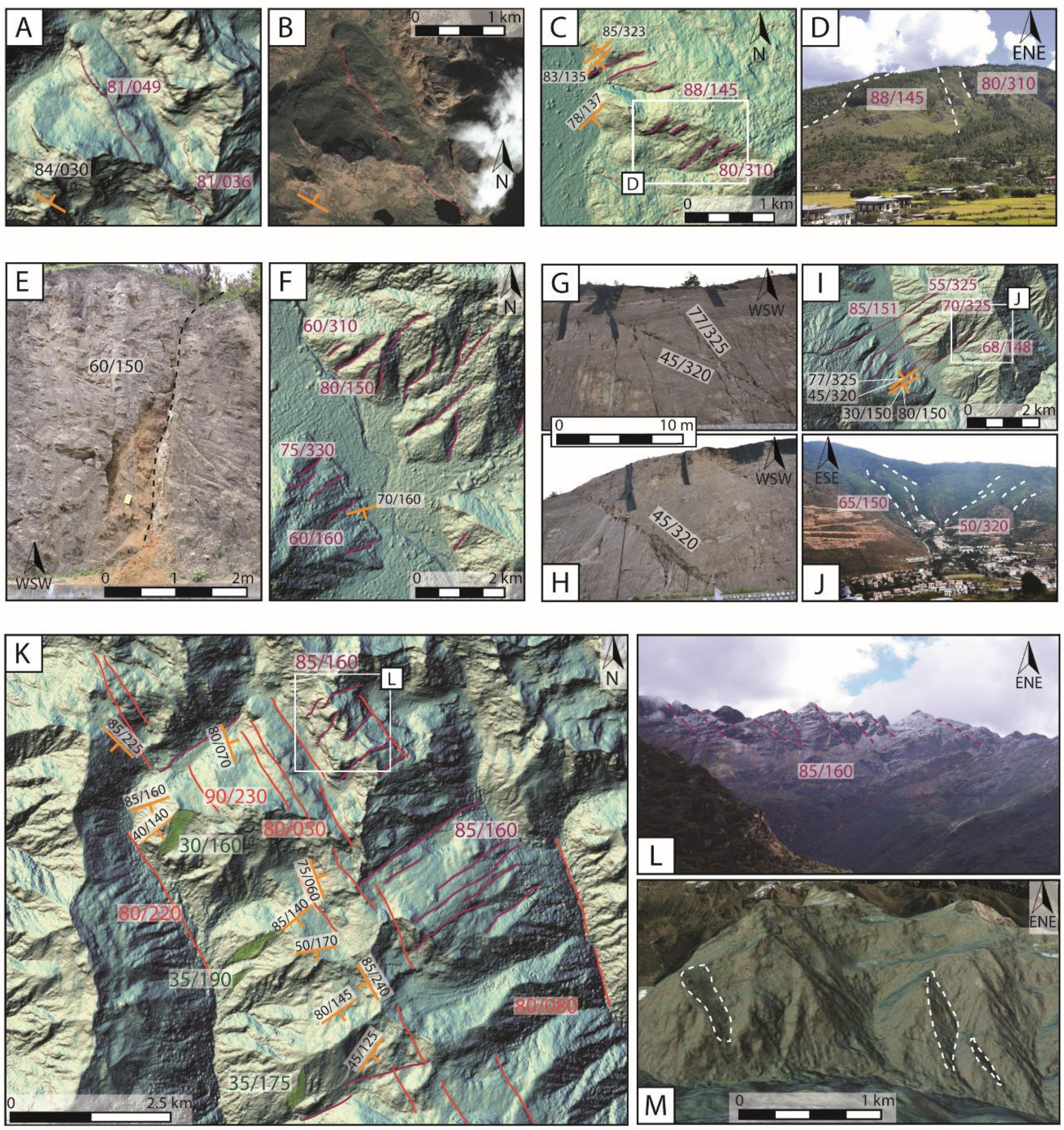

Fig. 5-3. Mapping of faults at different levels.

4.4.2. The mapping focused on identifying potential traces of large faults. In many instances, we were able to identify the effect on the landscape of faults that have also been recorded during field work, particularly for faults that were observed at a distance from a view point (Fig. 5-3). This is due to the fact that such faults are larger than many faults that were measured at the outcrop level, thus their morphological expression is stronger. Additionally, the identification of large faults is unambiguous in areas that are not covered by dense forest, snow or thick soil. The association of lineaments to faults is more uncertain in areas were ground cover obscures fresh morphological markers. In such areas, an effort was made to avoid the mapping of foliation traces, by cross-checking available information on foliation and/or searching for clear foliation expression on nearby bare rock slopes (assuming no change in foliation orientation). Valleys with a very linear axis were also mapped, as their morphology is potentially controlled by a large structure.

Orientations of planes forming the lineaments were then extracted through a 3D least square fitting method: each lineament was split into points at 20 m intervals, each point carrying X, Y, Z information and contributing to a point cloud. The results were then manually checked, by visually evaluating the plausibility of the obtained orientation with the mapped trace. For example, very shallow dip angles and dip directions similar to the strike of the trace associated with long, straight lineaments at valley bottoms were considered unreasonable. Intervention was clearly required in less than 9% of the cases, of these, 70% were reassigned steep dip angles (>70°).

5.4. Methods

5.4.1. Structural domains

The main lineament orientations were used to identify seven structural domains, for which separate kinematic analyses were successively performed. The domains (hereinafter D1, D2, D3, D4, D5, D6, D7) were selected so that some systematic, albeit sometimes small, changes in the main orientations of principal fault sets could be identified. Moreover, domains sizes are maintained large enough to contain enough data for the analyses (Fig. 5-1). In the domains obtained, often the systematic rotation of foliation or lineaments sets is sufficient to lead to clear differences in the stereoplot distributions (Fig. 5-1) and to cause variations in the kinematic analyses results (section 5.4.3). Geology was not considered as a criterion to identify suitable domains, for two main reasons. First, the distribution of lithological units causes a high homogeneity of crystalline rocks cover and the presence of sedimentary rocks only in a relatively small portion of the area. Second, the goal of this study is to identify structural control on landslides distribution, thus using structural data for the differentiation of domains seems more suitable.

5.4.2. Weighting system

We have identified the following biases that may be present in our structural data and can influence the results of the kinematic analyses:

I. Structural measurements have an uneven spatial distribution (Figures 5-2 and 5-5, App. 5-2 to 5-6);

II. For field measurements, many measurements are taken in a relatively small spatial area (outcrop). This area would then have an outsized influence on any analyses that follow;
III. Both small and long lineaments are given equal weight in the kinematic analysis;
IV. Some portions of the study area are difficult to map due to the surficial cover.

In order to explore the effect these biases may have on our analysis, we have adopted a weighting system based on the inverse of the density of each data point within an individual layer of the dataset (the four layers, measured foliation, measured faults, mapped planes and mapped lineaments, are described in section 5.3.2). This system assumes that the density of the information that each layer contains should be similar across the entire region, in the absence of a clear reason to believe the opposite. In this way, sparse measurements are given extra weight in the kinematic analyses and their influence on the results is enhanced. Individual layers are weighted independently of the others in order to avert adverse effects of uneven densities between different layers in the same area. For instance, a cluster of closely spaced foliation measurements should not reduce the weight of an individual fault measurement in the same area. At each point within a given structural layer, the number of measurements within a 10 km radius surrounding the point are calculated (see App. 5-2 through 5-6). This density is then normalized to the maximum density for this layer in the entire study area. The inverse of this normalised measurement density is then used as a weight for each measurement. Four variations of the weighting system were tested for the lineaments layer, these are described in detailed appendix 5-7, though here we illustrate only the one that was adopted for the analyses for the sake of simplicity. For lineaments, which may span 14 km length, density is calculated at points lying at 200 m intervals along the lineament length (App. 5-6). The weight is calculated as the inverse of the density at each point. However, this introduces a consequential problem, as the large amount of points generated causes the proportions of the initial dataset to change markedly and artificially. To overcome this issue, a scaling factor is applied to the weights, in order to maintain similar proportions to the initial ones between the four layers of the dataset (App. 5-7).

5.4.3. Kinematic analysis of structural control

We performed a series of kinematic analyses with the four weighted dataset layers in each of the seven structural domains for the four principal failure modes: planar (PS) and wedge sliding (WS), flexural (FT) and direct toppling (DT). The kinematic analyses are carried out for different slope angles, at 5° intervals between 35° and 50°, but up to 55° in domains 2 and 3, where steeper slopes are found. The geometric conditions used in each of these kinematic analyses are given in Hudson & Harrison (1997). Lateral limits were set to 20° for flexural and direct toppling.

The friction angle used for all analyses is 28°, as a common angle found in literature for various rock types. Competent metamorphic rocks may have friction angles higher than 28°, but, as the general conditions of the rock masses in the study area are not known, we chose to use a conservative value. There may be also cases, however, in which the friction angle may be lower than 28°, in the presence of phyllosilicates on a failure plane and high pore water pressures. The difficulty in accounting for heterogeneous and largely unknown geotechnical parameters across the region requires a simplification. Additionally, sensitivity analyses performed by varying the friction angle show that it does not have a large effect on the overall results. Finally, a sensitivity analysis is performed on all possible slope aspects (0°-359°), for the 4 (or 5) slope angles chosen. This sensitivity analysis, shown in the following section, illustrates the percentage of critical structures found among all structures in the given domain, indicating how many of the structures present may act as a critical discontinuity on which a given mode of failure can occur, for given slope parameters. This analysis highlights slope aspects that are more susceptible to the four kinematic failure modes, based on the regional structural data. The results of the kinematic analyses are then compared to the landslide density in each domain. The density here represents the distribution of landslides across slope angles and slope aspect values of mapped landslides.

Additionally, the results of the kinematic analyses are used to calculate a 'kinematic score' (KS) for each landslide in both the optical and DInSar databases (sections 5.3.1 and 5.3.2). This score represents a normalised percentage of critical structures (%CS) for a given failure mode, which is a function of a given landslide's aspect (α) and slope angle (β). It is calculated for each landslide in the database based on equation 1:

$$KS_{i,j} = \frac{\%CS(\alpha,\beta)_{i,j}}{\max\left(\%CS(\alpha,40°)\right)_{i,j}}$$

where j is a given landslide in the database, i is the failure mode (PS, WS and FT), and the maximum operator is calculated based on all the landslides with a given failure mode across all domains.

The kinematic scores were only calculated for PS, WS and FT, as low percentages of critical structures were consistently observed for DT across the domains (see section 5.5). For any given mode, the values of critical percentages found are normalised to the maximum value for a 40° slope angle found across all domains. 40° was chosen because it is the slope angle value that represents roughly the 90th percentile in all domains. In this way, the kinematic score is comparable across the entire study region and the maximum score reflects steep slopes that are present and relatively frequent across the region.

A cumulative kinematic score (CKS) was also calculated by adding the PS, WS and FT scores and normalising once again to the maximum value for a 40° slope, this time across all domains and also across all failure modes. The meaning of the kinematic score is relative, with absolute values comprised between 0 and 1, useful to allow a comparison between landslides in the inventory, in order to investigate a regional structural control. Kinematic scores of 0 are automatically assigned to slopes with angle < 24°. This value roughly represents, across all domains, the 10th percentile. Setting this value to 28°, which is the friction angle used for the analyses, is deemed unrealistically conservative. First of all, shallow sliding surfaces can occur, given suitable geological conditions. Second, the current slope values of large landslides such as old and deep mountain slope deformations may not be representative of original values.

5.4.4. Lithological control

With the aim of investigating the lithological control on landslides distribution, each landslide of the inventory (and each unstable slope from the DInSAR inventory mentioned 3.2) was assigned a geological attribute based on the geological map of Bhutan generated by Long et al. (2011). The lithologies are organised into the following groups: metasediments belonging to the Greater Himalaya sequences (mostly comprising paragneiss, schist, quartzite, thus likely characterised by anisotropic texture), isotropic crystalline rocks of the Greater Himalaya (consisting of orthogneiss, leucogranite), sediments belonging to the Tethyan sequence (largely composed of carbonaceous shale, limestone, sandstone, quartzite) and a fourth category in which shales are considered alone. The reason for this last category lies in the fact that shales, compared with all other lithologies in the area, are likely to be characterised by the poorest geotechnical parameters, thus representing the weakest lithology in the region. Given the very uneven distribution of different lithologies, we decided to analyse the density of landslides within each lithology group across the entire study area, rather than analysing it over each domain.

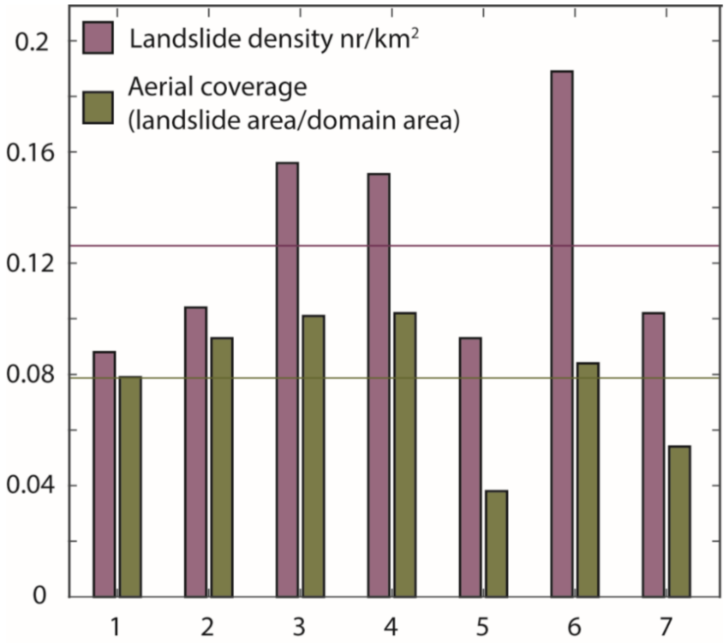

Fig. 5-4. Landslide density per domain and areal coverage. Red horizontal line represents average landslide density. Green horizontal line represents average areal coverage.

5.5. Results

5.5.1. Landslide density

The optical landslide inventory compiled for the study region includes 907 objects (black polygons in Fig. 5-1). These are divided into rock slides, rock slope and mountain slope deformations (Hungr et al., 2014). The inventory also includes an exiguous number of rock slide and rock avalanche deposits. The mapped landslides appear to be unevenly distributed across the entire study region, with clear clusters. Many of such clusters appear to correspond to main valleys in the south of the region. 5-Landslide density and total areal coverage were calculated for each domain (Fig. 5-4). This shows that domains D1 and D2 are characterised by a lower than average density but an average or higher than average spatial coverage, which indicates that larger landslides are present. On the contrary, domain D6 is characterised by a much higher than average density and an areal coverage which is only slightly above average, indicating the presence of many smaller landslides.

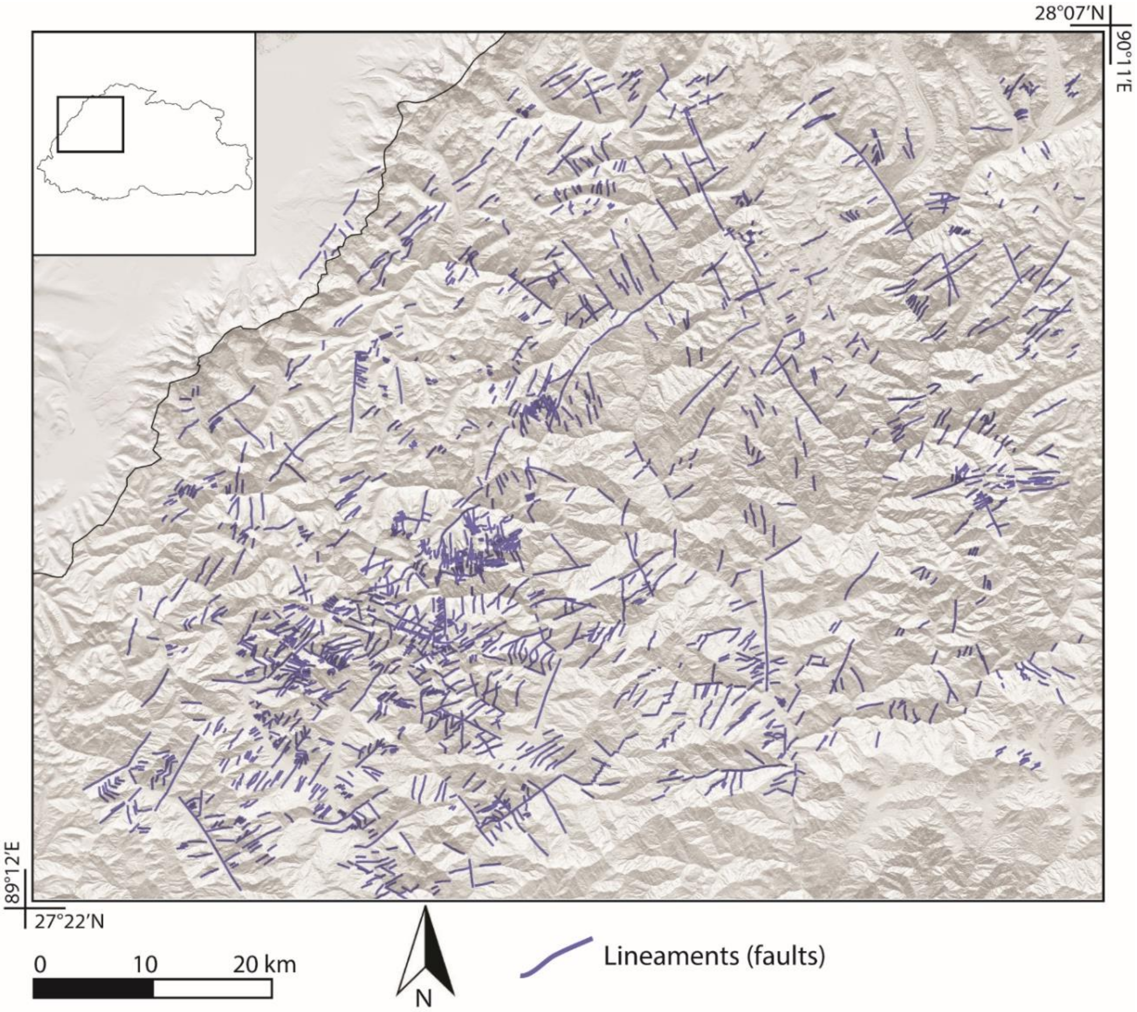

Fig. 5-5. Lineaments (fault traces) mapped through remote sensing.

5.5.2. Lineaments maps

The lineament maps contain 1973 traces of potential faults across the entire region (Fig. 5-5). Domains D6 and D4 have a higher density of mapped traces, but elsewhere the distribution is relatively even. The mapped trace lengths are between 80 m and 1300 m, they follow a skewed lognormal distribution peaking at 200 m (Fig. 5-6), presumably caused by undersampling at low trace lengths. Around 50% of the estimated fault planes have a dip above 70° and only roughly 15% is below 40°. This most probably also represents fault undersampling, as shallow dipping faults rarely develop lineaments visible on a DSM. In general, a very strong and persistent steep set striking NE-SW is visible across almost all domains, with the exception of the central domain D4. A slight eastwards rotation is observed from northwest to southeast (Fig. 5-1), with the northwestern domains showing a more marked NE-SW direction and the southern domains showing more ENE-WSW traces. This trend, albeit with the small differences highlighted, is on the whole similar to the Lingshi fault, already mapped by other authors (Antolín et al., 2012). Additionally, a NW-SE striking set is also present, this becoming very apparent in the east of the region, but nearly absent in the west. This is in agreement with what was mapped by Wiesmayr et al. (2001) in the Lunana region, just east of our study area. North south structures are observed in the central parts of the region (e.g. D4).

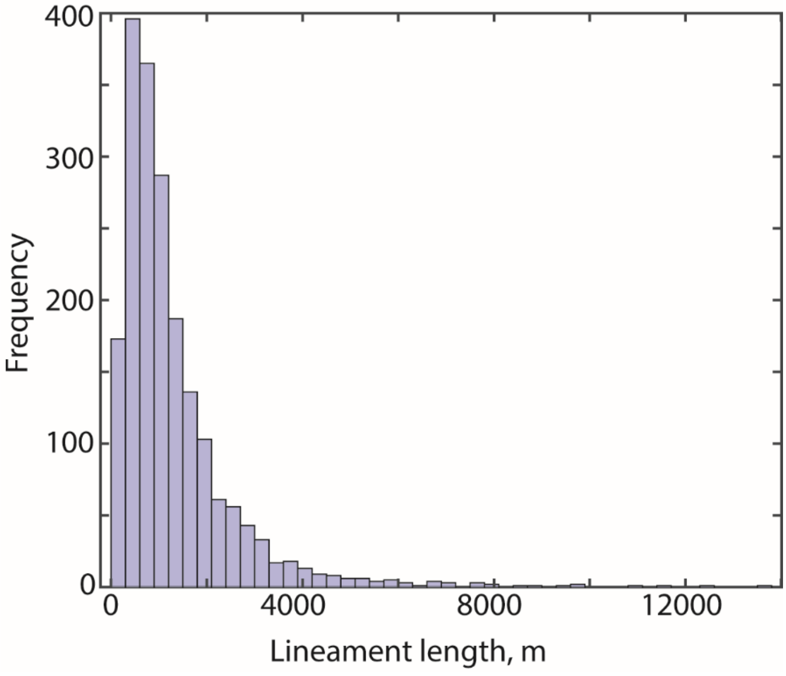

Fig. 5-6. Lineament lengths follow a lognormal distribution.

5.5.3. Kinematic analyses

The results of the kinematic analysis are shown in figures 5-7 to 5-13. The crosses on the plots show individual landslides mapped in each domain and the landslide density (2D bins of slope angle and aspect) is shown with the purple colour scale (equal on all graphs per domain). The curves in the graphs represent, for different slope angles from 35° to 50° (55° in domains 2 and 3) at 5° intervals, the percentages of critical out of the total structures in the domain for the corresponding failure mechanism. In domains D1, D2, D3, D5 and possibly D4 and D7 the highest densities of landslides correspond, for some failure modes, to peaks or portions in the curves of elevated critical percentages. In general, we find that the DT mechanism does not appear to control the landslides mapped in our study area. PS, WS and FT seem to have a clear influence in many areas, with the exceptions of domains D4 and D7, for which the correlation between curves peaks and landslide density is weak and D6, in which no correlation at all is observed. In particular, domain D5 shows two clear landslides clusters, these coinciding very well with the peaks observed in PS and WS between 80° and 180°, in PS and FT between 270° and 330° and between 130° and 180° in FT. This is particularly clear due to the bimodal nature of PS and FT curves and the two density maxima. Domains D4 and D6 do not show clear correlations between observed and modelled failure mechanisms for the given slope orientations. However, in domain D4, weak clusters are observed but these do not appear to be clearly associated with any particular percentage curves pattern, a part from perhaps FT between 45° and 180°. In D6, despite the large number of landslides, no clear clusters are seen at any aspect value, moreover, the curves for all four modes are, on the whole, quite muted.

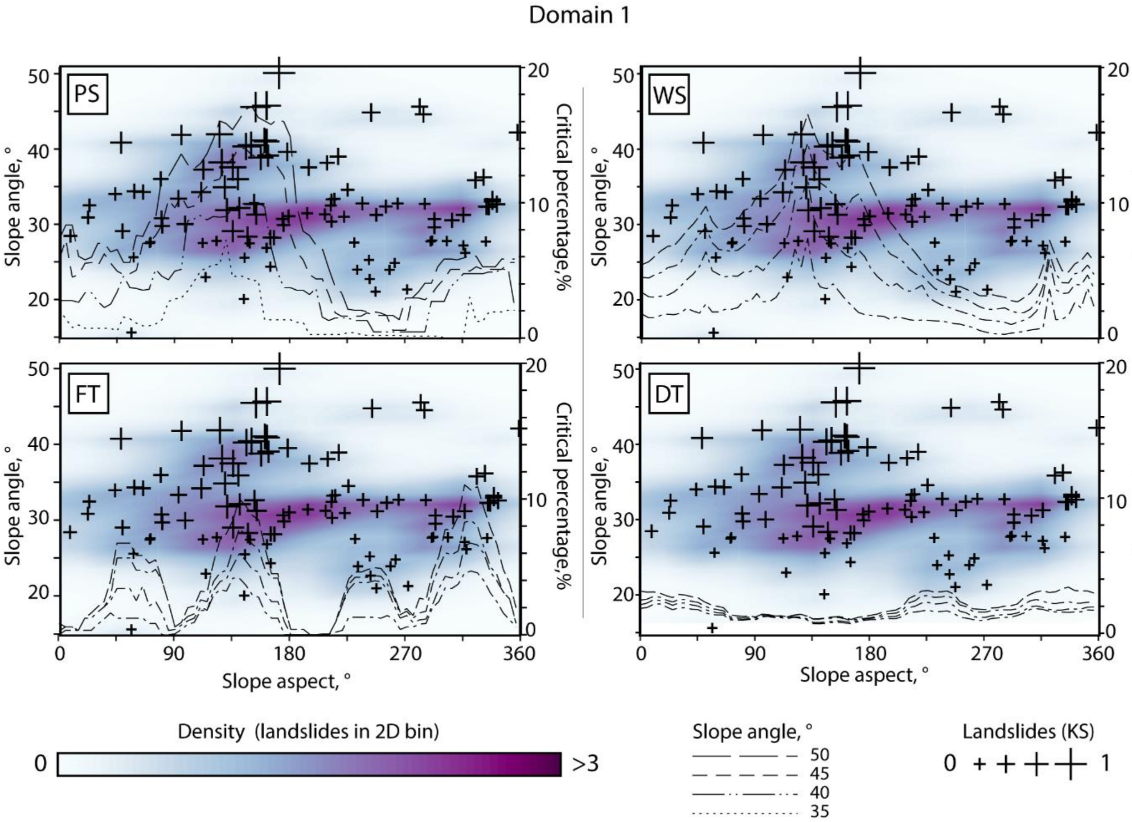

Fig. 5-7. Domain 1, kinematic analyses for the four failure modes. Different critical percentage curves represent different slope angles. Each cross represents a landslide in the domain. Larger crosses represent higher cumulative kinematic score. Colour scale represents 2D landslide density for given slope angles and aspects.

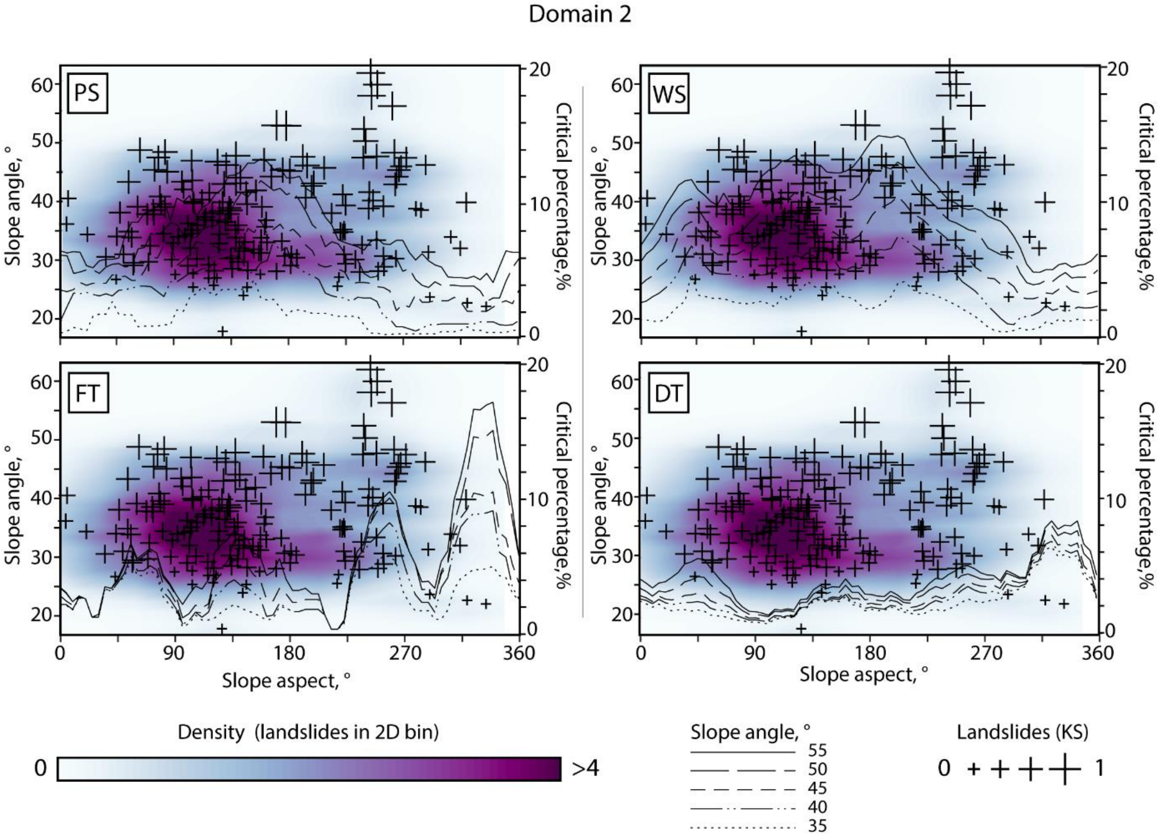

Fig. 5-8. Domain 2, kinematic analyses for the four failure modes. As above.

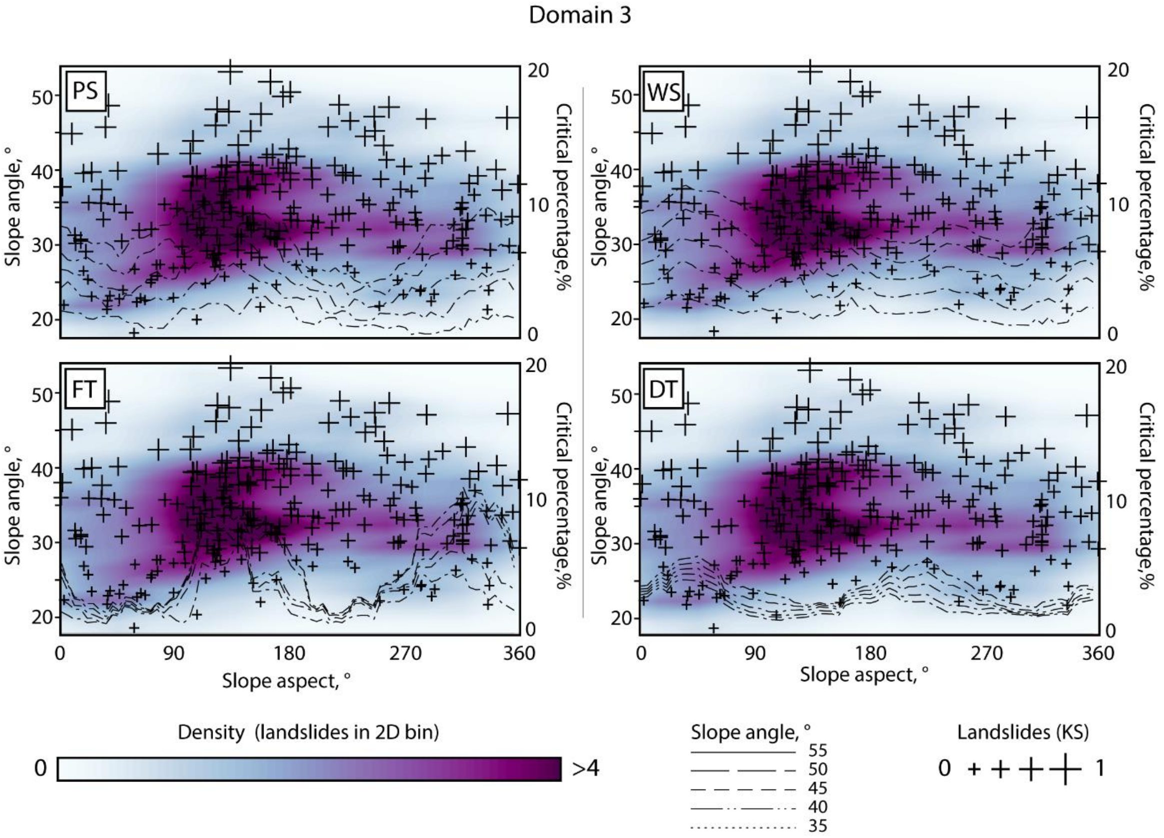

Fig. 5-9. Domain 3, kinematic analyses for the four failure modes. As above.

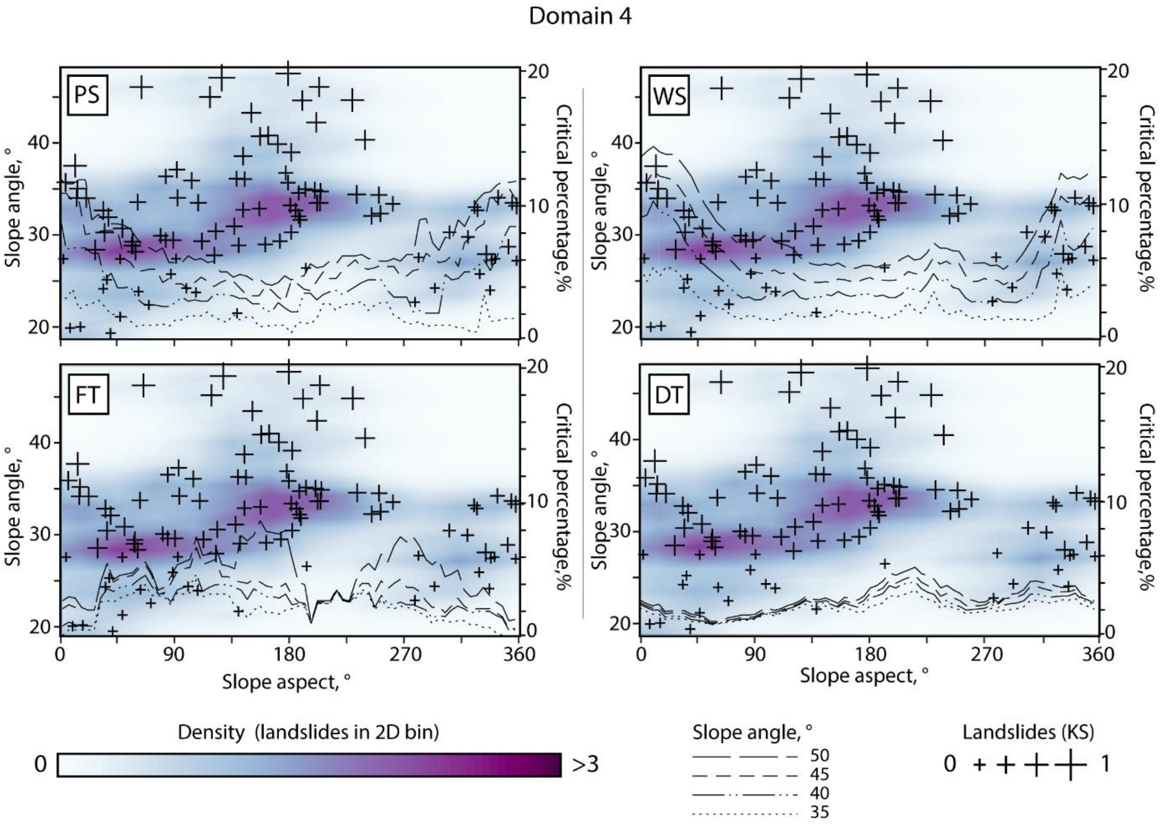

Fig. 5-10. Domain 4, kinematic analyses for the four failure modes. As above.

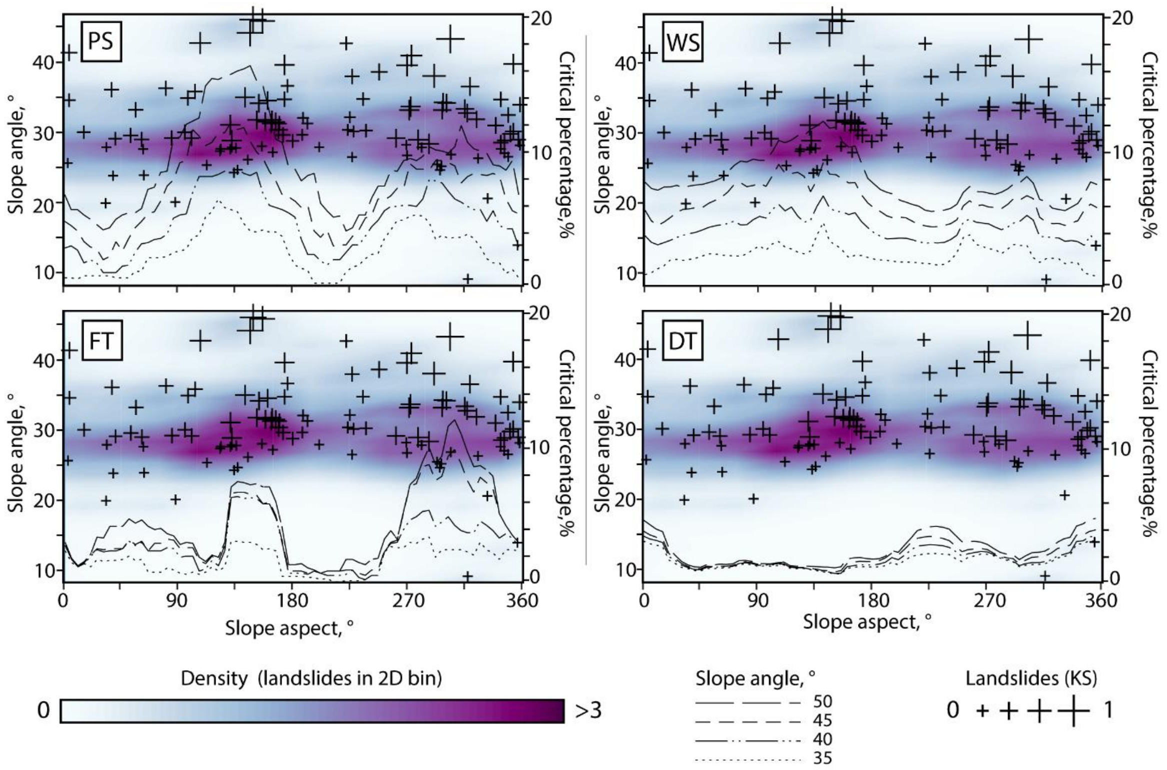
Domain 5

Fig. 5-11. Domain 5, kinematic analyses for the four failure modes. As above.

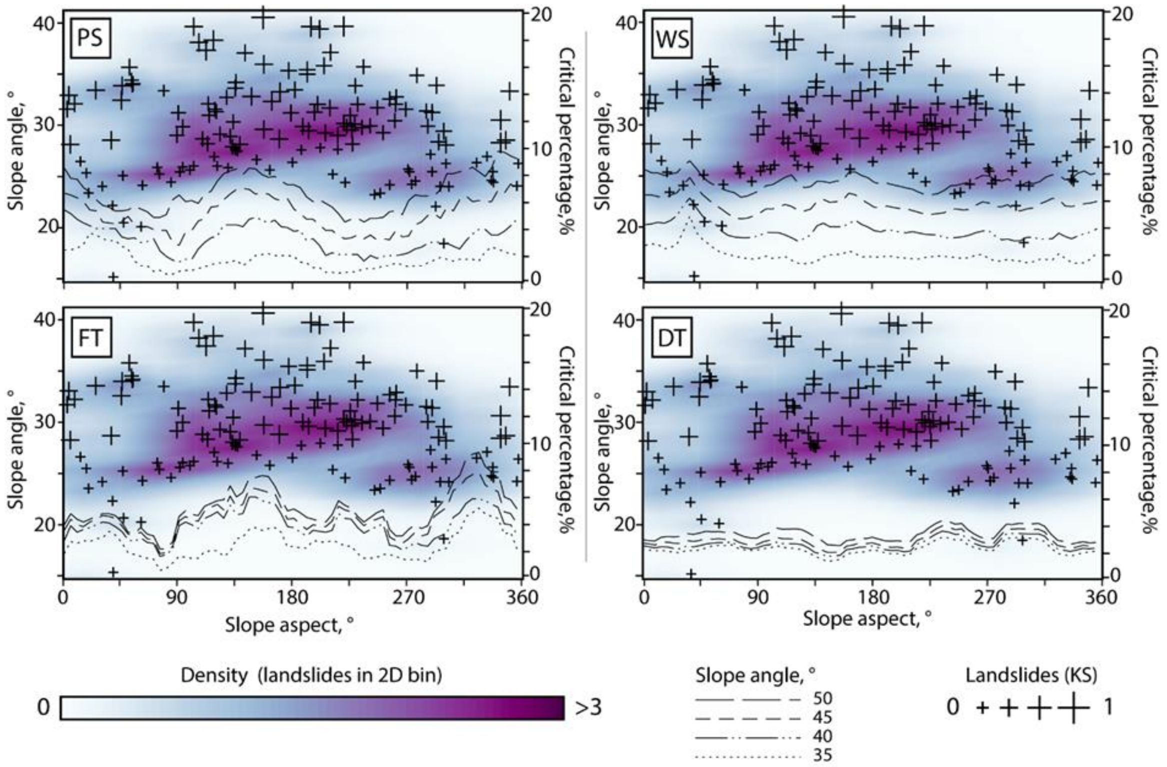
Domain 6

Fig. 5-12. Domain 6, kinematic analyses for the four failure modes. As above.

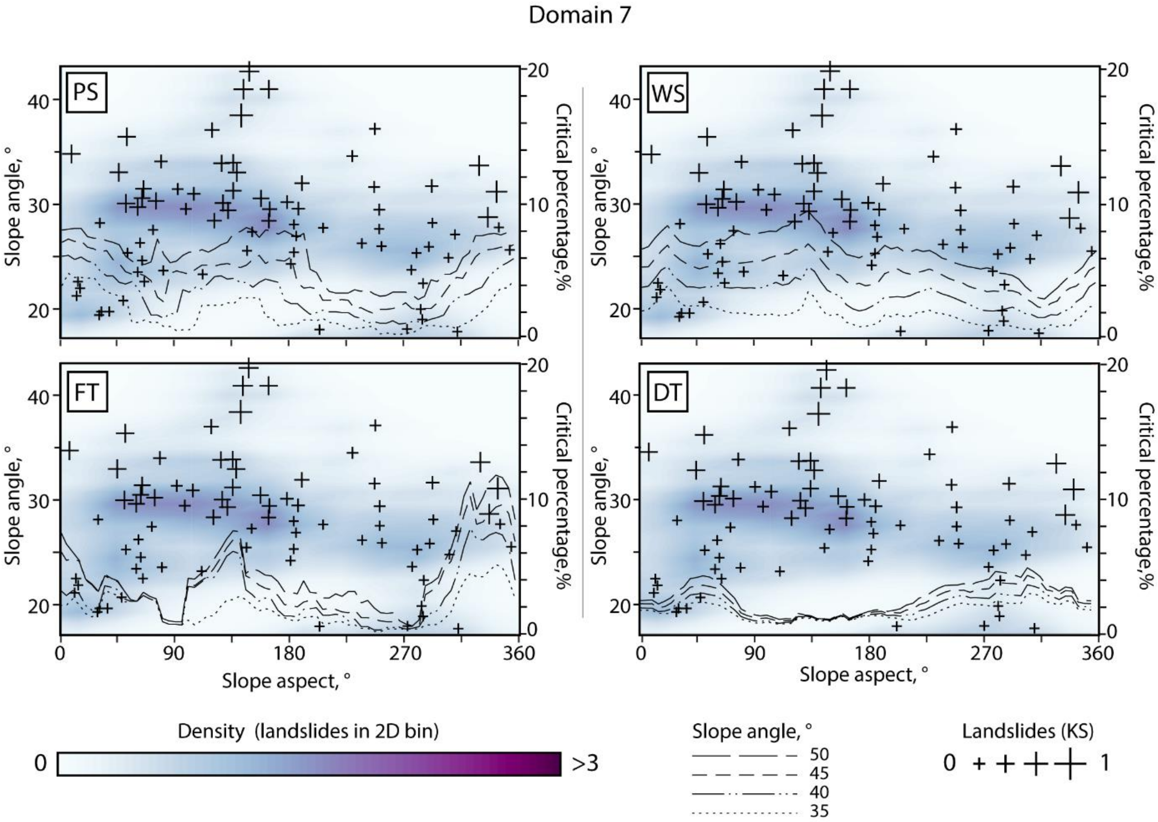

Fig. 5-13. Domain 7, kinematic analyses for the four failure modes. As above.

5.5.4. Kinematic scores

Figure 5-14 shows the cumulative kinematic score, CKS, for polygons belonging to the landslides inventory. Kinematic scores for the individual failure mechanism PS, WS, FT are shown in appendices 8 to 10. In addition, landslides extracted from the inventories of unstable slopes detected with DInSAR (Dini et al., 2019a) and with InSAR time series (Dini et al., 2019b, under review.) as explained in section 5.3.2 are also included in this part of the analysis, to explore further the kinematic control on rock slope instabilities spatial distribution across the area. Around 57% of the landslides in the optical inventory have a CKS ≥ 0.2. Just over 8% have a CKS of 0, which is automatically assigned when the slope angle is < 24°. Of the landslides extracted from the inventory of slope instabilities detected with DInSAR and InSAR time series we find that 37% and 18% respectively have a KCS ≥ 0.2, with roughly 17% and 8% having CKS = 0 due to shallow slope angle. Taking into account only the polygons with KCS ≥ 0.2, a clear elongated cluster of structurally controlled landslides is visible in the NW of the region, with a NE-SW orientation. Other clusters can be seen, one in the far NE of the region, with a N-S strike and another one in the SE, with a NE-SW strike.

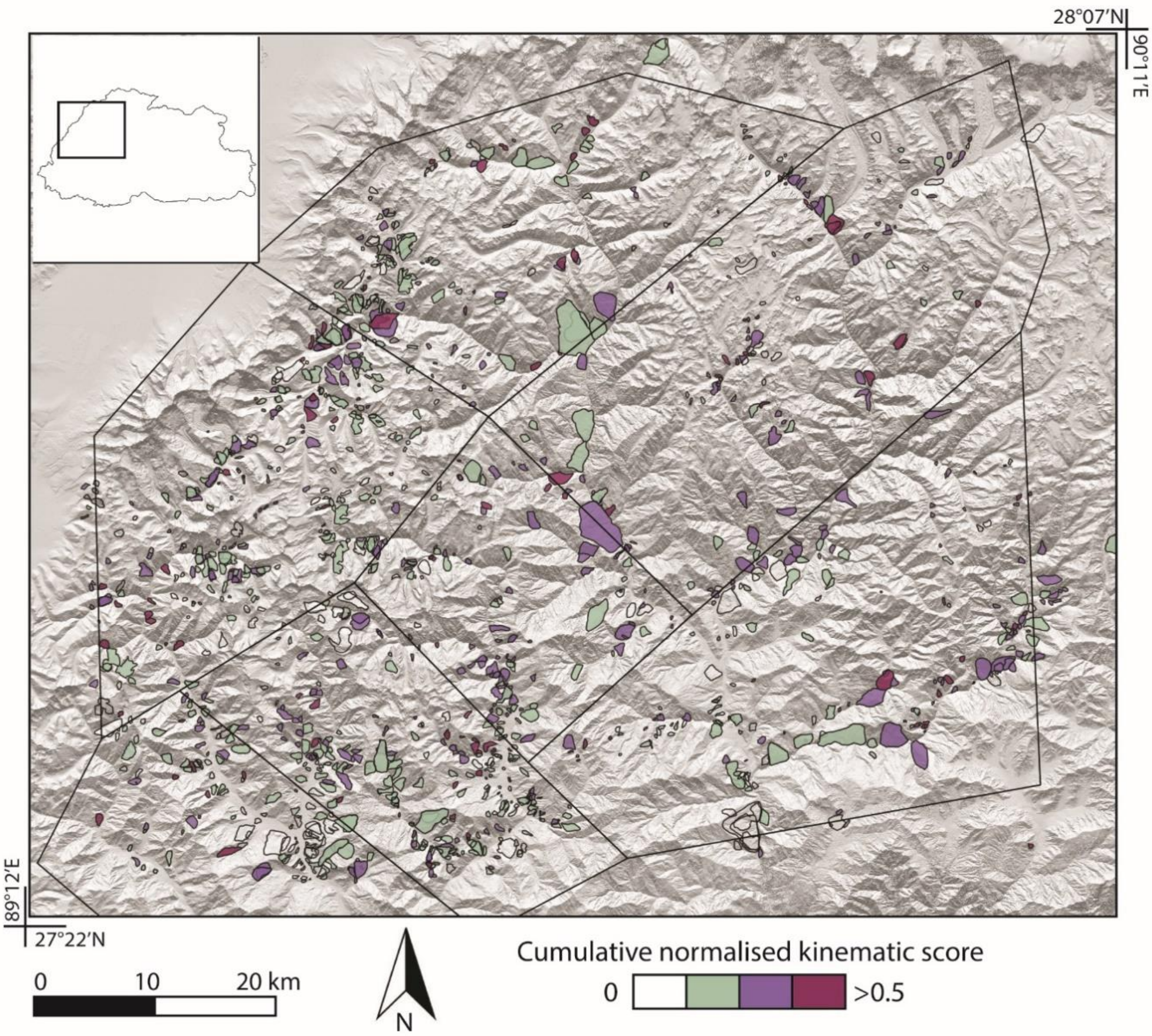

Fig. 5-14 Cumulative kinematic score for landslides of the inventory obtained with optical images and DSM analysis (black polygons in figure 5-1), for slope instabilities observed with DInSAR (single interferograms, Dini et al. 2019a) and with InSAR time series (Dini et al., 2019b).

5.5.5. Lithological control

Given the uneven distribution of lithologies in the study area, the various domains are characterised by very different ratios of the geological units. For this reason, we have analysed the landslides density in relation to geology in the entire region instead of over each individual domain. We compare overall landslides density (without lithological distinction) to the densities within different lithological categories as described in the previous section. What we observe is that the landslides density within anisotropic metamorphic rocks and isotropic crystalline rocks is slightly lower, but very similar, to total density, whilst the density within sedimentary Tethyan rocks is slightly above. However, when shales are considered alone, the landslide density is 75% higher than the total density value (Fig. 5-15).

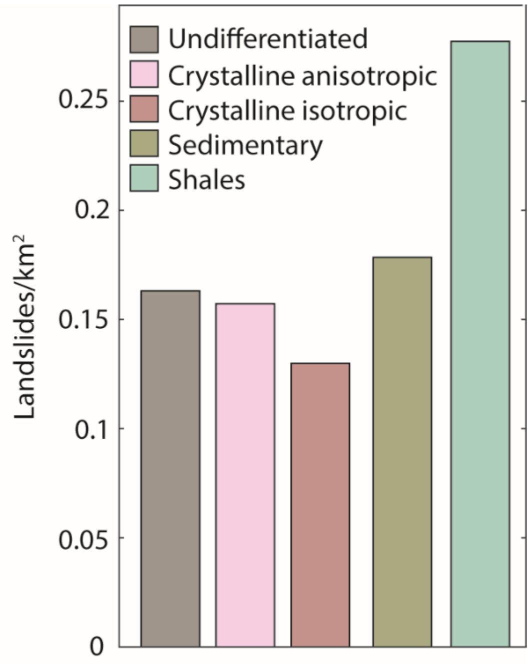

Fig. 5-15**.** Landslide distribution across different lithological groups.

5.6. Discussion

5.6.1. Faults and lineaments

As mentioned in section 5.3, there are some uncertainties associated with determining the attitude of the lineaments mapped with remote sensing. However, we note that the steep NE-SW and NNW-SSE sets that were mapped in this work (shown in Fig. 5-5) fit very well with the tectonic regime of the region (Antolín et al., 2012). The NE-SW set that is found across most domains (with the exception of D4) has a similar orientation to the Lingshi fault, whilst the NNW-SSE set likely corresponds to the dextral strike slip fault system observed in northern Bhutan by other authors (Antolín et al., 2012; Wiesmayr et al., 2001). These are the two conjugate sets that accommodate the NE-SW shortening and WNW-ESE extension in response to the clockwise rotation of southern Tibet with respect to India. In areas in which we collected field measurements, we were able to verify that the orientations extracted from the mapped lineaments were consistent with field data. Fig. 5-3 shows how information collected on the field and remote sensing information are pieced together to reconstruct an overall picture. Despite the uncertainties associated with the extraction of orientations from the lineaments map, we observe how the orientations obtained fit well the field measurements (e.g. Fig. 5-3 panels A-B-C-F-I-K). This increases the confidence on the validity of our dataset. Moreover, clear morphological expressions in the landscape also reinforce the overall orientations found in an area. In Fig. 5-3 D-I-J and L we show that the medium to steep NE-SW and NW-SE trending sets were observed in the landscape and that similar orientations were obtained through the lineament mapping based on remote sensing data for the same areas. Fig. 5-3K shows how not only the lineament mapping yields similar orientations to the field measurements, but also it indicates that even the mapping of planar valley flanks gives orientations that correspond to field measurements.

The meaning of the density of foliation measurements as opposed to that of the density of fault measurement is not the same. Fault measurements, although they are expected to be incompletely sampled in response to length, dip angle and soil coverage, represent the spatial distribution of discontinuities that locally condition slopes for large landslides formation. On the other hand, foliation planes are pervasive and densely spaced but not all of these planes correspond to large discontinuities that can potentially form a sliding or toppling surface. This means that the individual density of the layers of foliation and faults measurements should not to be expected to be the same or to have the same significance for the analyses, since they describe different objects. For this reason, we kept the measured foliation and measured fault layers separate in the weighting system (section 5.4.2), to ensure that the density of foliation would not influence the density of faults. This may also mean that the critical percentages of modes largely influenced by foliation may be artificially higher when compared with modes for which such influence is expected to be lower. However, this is not seen as a limitation of our method, since we are not aiming at identifying the specific failure modes that describe each landslide in the inventory, but more at exploring whether a structural control is present at all.

In-situ fault orientation measurements in our dataset are only available for domains 3, 4, 6 and 7. Though they provide a partial description of faults across the entire study region, we consider important to include them in the analyses of these domains, because they carry extra information, for which confidence is higher due to the direct observation. As the procedure of the inverse density weighting is applied to layers individually, the effect is to homogenise the density only in the areas in which they are present, without negatively influencing any of the other layers in the same and in other areas.

Additionally, we have analysed the sensitivity of the results of the kinematic analysis to the proposed weighting system, described in section 5.4.2. The sensitivity analysis was performed by running the kinematic analyses for the unweighted dataset as well as for the dataset weighted with the four variations of the weighting system (detailed in appendix 5-7). The results of this sensitivity analysis are shown in appendix 5-11. As shown in Appendix 5-11, the weighting system does not have a large influence on the identification of critical slope aspects, and, on the whole, the shape of the curves is similar between different weighting systems and the ranges of favourable aspects to a particular failure mode remains largely unchanged. This is because, as mentioned earlier (also shown in Fig. 5-16), with the weighting system introduced here we do not make up for data that was not collected, but only enhance or dampen the effects of existing data on the basis of their original and expected densities.

5.6.2. Observed preconditioning and effects of structures on kinematic analyses

Our results show that in 5 out of 7 domains (D1, D2, D3, D5, D7), landslide occurrence and type are on the whole influenced by the structural predisposition. In these domains we observe that there is some correlation between the mapped landslides density and higher percentages of critical structures for given failure modes for specific slope aspect ranges.

5.6.2.1. Planar sliding

Planar sliding has a pronounced influence in D1, D2, D3, D5 and, to a lesser extent, D6. In these domains, the slope aspects corresponding to the peaks in the critical percentage curves appear correlated with clusters of landslides. Planar sliding is largely controlled by the shallow foliation sets which can allow for the development of planar sliding surfaces daylighting the slopes. The spread of foliation orientation over two possible distinct shallow sets in domains D3, D5 and D6 causes PS to show two peaks, whilst the rotation of foliation induces a shift in the peaks as seen in D1 as opposed to D4.

5.6.2.2. Wedge sliding

Whilst PS is controlled by the shallower sets alone, generally associated with foliation, WS requires the intersection of foliation with the steep fault lineament sets for the generation of favourable dip slope intersections. Wedge sliding appears to be a dominant mechanism in domains D1, D2 and D5, due to the strength and low dispersion of the NE-SW steep set intersecting with the shallow SE dipping foliation. In other domains WS percentages are lower, due to the lower number of structures belonging to this important set. The intersections of the steep NW-SE set with a largely SE dipping foliation focus the higher percentages for WS on SE dipping slopes.

5.6.2.3. Flexural toppling

Given the shallow dip angles across the study area, foliation is not found to influence toppling. However, flexural toppling may play an important role in D1, D2, D3, D5 and arguably in D4. In these domains, FT is supported by the presence of two NE-SW and NNW-SSE steep lineaments sets (and a N-S set in D4). The presence of these sets leads to two or four peaks in the critical percentage curves, favouring the corresponding aspect ranges, depending on whether one or both conjugate sets are present. The relative strength of the peaks is directly proportional to the weighted strength of the sets and to slight variations in dip angle. In domain D2, only slope dip directions of 025° and 320° would allow for the intersection of the steep sets and the foliation to be in the critical zone. A stronger NE-SW steep set than the NW-SE in domain D1 allows for higher percentages of flexural toppling for SE and NW slopes. In domain D2, stronger SE and NE dip directions for the steep sets converts into higher FT percentages for slopes facing SW and NW.

5.6.2.4. Direct toppling

As mentioned in Section 5.4, we observe that DT percentages are very low in all domains and the curves do not show any more favourable aspect to this failure mechanism. Despite the abundance of vertical sets, the requirements for an intersection dipping into the slope and for near horizontal basal planes with suitable dip direction is not met.

5.6.2.5. Effects of data dispersion

The effects of data dispersion, sets rotation and presence of different sets in the various domains lead to the differences seen in the kinematic analyses results. In general, the dispersion of the orientations of discontinuity planes modulates the shape of the peaks in the critical percentage curves. For example, in domains D1 and D2 a more focused or spread peak in the PS and WS curves is respectively associated with a lower or higher variability of foliation orientations. Moreover, in domains D6 and D7, both PS and WS are relatively more muted, this is due to the high dispersion of structures orientations and to the unfavourable plunge (often too shallow with respect to the friction angle) of the intersection between shallow structures with the main steep sets. Data dispersion thus seems to have an effect on the detection of structural control. As the stereoplots show, domains D4, D6 and D7, which are the domains for which the kinematic analyses give less conclusive results, are those for which a higher data point dispersion exists. For domain D7 there could be a weak structural control imposed mostly by foliation (PS, WS), whereas in domain D6 the landslides distribution does not indicate any cluster. This seems to suggest that landslides are almost equally possible on all slope aspects, making it less likely that data dispersion alone is responsible for the muted results obtained for this domain. In fact, the uniform landslides distribution with respect to slope aspect may indicate that no structural control exists in this domain. Moreover, in D4 the mismatch between the highest densities of landslides and the weak peaks in PS, WS and FT curves is also an indicator of lack of structural control in the domain.

5.6.2.6. Causes for observed differences

The question regarding what causes structural control to be present in some domains (D1, D2, D3, D5, D7) and not in others (D4, D6) does not have a clear answer. Lithology, as described in the map of Long et al. (2011), does not appear to be the discriminating factor. Additionally, forest cover is also unlikely to be responsible for the differences observed in domain D4 and D6, since other domains, like D7 and D3 and the southern parts of D2, are covered by dense vegetation. The forest cover also follows the boundaries between the wet, tropical and the arid, alpine climate bands, thus similar climatic conditions as in D4 and D6 are also found elsewhere in the study area. One possible explanation is that different types of landslides, less susceptible to structural control, are more abundant in D4 and D6. Though an effort was made to include in the landslide inventory only large instabilities in rock, it is also possible that the nature of the study area, with thick soil covers in the south, may be conducive to large slides in soil. The morphological features of these landslides, made unclear by a smoothed topography, may be similar to those of relict rock slides that underwent long periods of erosion. If this is true, then it is possible that southern domains may also include large soil slides, in addition to rock slides. Northern domains are also characterised in general by larger landslides (D1, D2, Fig. 5-4) and the morphologies of the terrain is less dull, with more bare rock exposed. Moreover, domain D6, in particular, is characterised by relatively smaller landslides than in other domains, this also suggesting that there could be a higher number of landslides occurring in soil.

5.6.3. Limitations

We are aware of the limitations that affect our dataset and that may, in turn, also have an effect on the results of our analyses. In the following, we summarise and discuss these aspects.

The in-situ measurement of faults and foliation is biased by the accessibility during field visits. We have visited only a relatively small portion of the entire area, restricted to the lower valleys in the south and some higher ground areas in between them. We have enhanced our foliation/bedding layer by digitising data from the map of Long et al. (2011) (mainly in the east of the study region) and data obtained from Grujic (pers. comm., mainly in the northwest of the region). These layers of the dataset so compiled are rich in the southwestern quadrant of the region (own field campaigns) and more sparse elsewhere. In particular, there are large areas, namely in the east of the study region, for foliation, and in the northern half, for faults, that are characterised by a complete lack of measurements. Clearly, this means that there are areas of our structural domains for which we may be missing information regarding any changes in the foliation orientation as well as new faults orientations. Our weighting cannot make up for data that has not been recorded and can only enhance or reduce the influence of data points in areas where data exists (Fig. 5-16). The results of the kinematic analyses would change if new data, with different orientations from the known ones, would be introduced in the dataset. Though new structure sets may change the shape of the critical percentages curves, this would not necessarily invalidate the current result. Potential new sets may justify the presence of landslides where this is not explained by the current results, but even if strong sets would

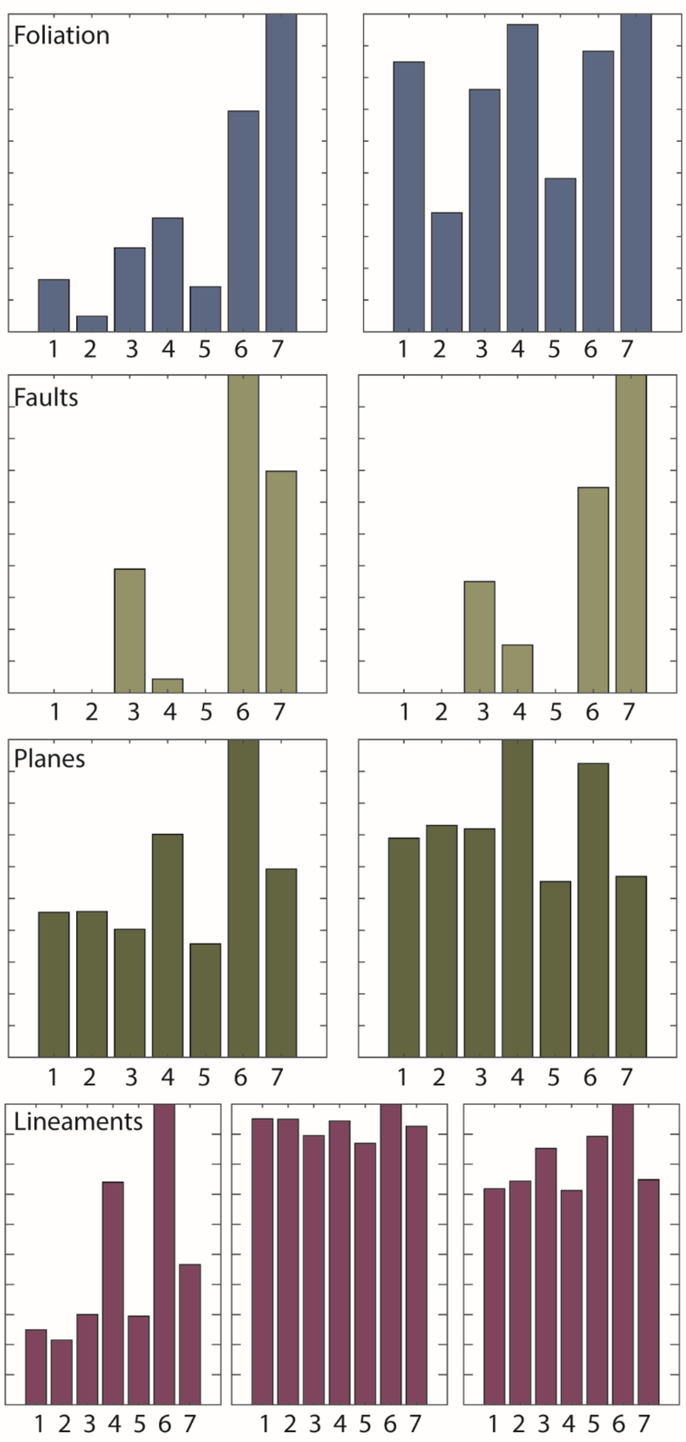

Fig. 5-16. Normalised density of data points in each domain, across the four layers. Left panels, non weighted, right panel, weighted. For lineaments, centre panel density is averaged from all 200m interval points along a lineaments, in the right panel density is rescaled.

cause the relative influence of currently known sets to decrease, this would unlikely completely overthrow the current picture (i.e. landslide clusters that are currently well explained by PS would most likely continue to be).

This bias associated with measurements collection does not affect the other two layers of the dataset (planes and lineaments mapped with remote sensing data) because the same sampling method has been applied during mapping. It is unlikely that a particular steeply set exists that we are systematically unable to identify with remote sensing mapping (though shallow sets are undersampled on the whole). However, these layers are affected instead by the difficulties caused by surficial cover (dense forest, perennial snow fields) in some areas. This is particularly true, for example, for the southeastern domain, where dense vegetation cover impairs visibility of the morphological expression of regional structures. Moreover, it is possible that some of the mapped lineaments represent intersections of planes instead of an individual plane. Although an effort was made in avoiding this, this effect may add to the observed data dispersion.

One of the issues introduced by the weighting system proposed here concerns the variability of orientations. Care must be taken when applying this weighting to the faults and lineaments layers, because faults with different orientations may be found and recorded at the same outcrop and it is questionable whether their weight should be reduced in order to homogenise the density over the whole area covered by the layer. On the other hand, an individual data point with different orientation compared to the homogeneous orientation of a larger amount of surrounding points will be given the same weight assigned to its surrounding points and it will remain an outlier compared to them. This would continue to reflect the picture obtained through mapping, which hopefully reveals the real distribution in the area, so that, although arguably locally important, one fault measurement at odds with surrounding ones should carry less weight at the regional scale.

5.7. Conclusions

In this work we present a new regional scale landslide inventory for a large area in Northwestern Bhutan. This inventory is largely based on the analysis of satellite optical images and a high-resolution DSM. We also present a new regional scale structural dataset for the area, based on different layers of data. These are measured faults and foliation orientations, mapped lineaments (fault traces) and mapped planar valley flanks. The first two were acquired in two field campaigns (September 2016 and October 2018) with the addition of data from other authors; the latter two are obtained through detailed analyses of high-resolution DSMs.

We present a new methodology that combines these datasets to investigate the structural control on spatial landslide distribution over a large, inaccessible region. We apply a weight to the structural layers that aims at addressing the problems associated with uneven sampling, thus reducing misleadingly higher or lower influence of particular fault sets. We carried out kinematic analyses for 7 structural domains identified in the region, with a sensitivity analysis performed on slope aspect. These analyses showed that for 6 out of 7 domains a structural control exist and that clusters of landslides around specific ranges of slope aspects and slope angles reflect the shape of curves of critical percentages of structures that could favour failure. In particular, we observe that planar sliding could be a dominant mechanism in the north and east of the region, wedge sliding in the north and flexural toppling across the northeastern parts of the region. We also generated a kinematic score for landslides in the inventory, as a relative measure to identify instabilities that show a higher predisposition to failure in response to the presence of certain sets of regional fault and foliation/bedding structures. The kinematic score is a normalised value based on the percentage of critical structures for a given slope and aspect. This reveals that around 57% of the landslides have a score between 0.2 and 1 and that clusters of higher kinematic scores exist across the region, these are elongated and reflect the strikes of the main conjugate NE-SW and NW-SE sets. We also observe a lithological control, with a higher landslide density in the shales of the Tethyan sediment sequence. However, the coarse nature of our information on lithology does not allow detailed investigations.

Though the importance of large tectonic structures in influencing the formation and distribution of large rock slope instabilities has largely been recognised in the literature (Stead and Wolter, 2015; Crosta et al., 2013; Brideau, 2009; Hermanns, 2006; Agliardi et al., 2001; Schramm et al., 1998), this study represents a novel methodology and data set for intersecting landslide and structural inventories at the scale of an entire mountain range, whilst using the kinematic analyses to explain the observed landslide density patterns. Our findings further the understanding of spatial landslide distribution across a large and remote mountainous region in NW Bhutan and it is replicable and applicable to other mountainous regions. Moreover, it can serve as a basis for regional landslide susceptibility mapping for hazard mitigation purposes.

Acknowledgements

We thank our colleague Kerry Leith and Larissa de Palezieux for the help during the field campaigns and for the discussions and interesting suggestions that sparked ideas during the project. We are grateful to Djordje Grujic for sharing field data and ideas that helped with the understanding of our data fits with the bigger picture and known structures. Thanks to Federico Agliardi for sharing his views and expertise regarding the mapping of structures. We also thank our Bhutanese partners for their support during field work, these include of the College of Natural Resources of the Royal University of Bhutan, in particular Jigme Thinley, Helvetas, Walo and of National Land Commission, Department of Disaster Management, Department of Hydrology, Department of Roads, National Soil Science and Department of Geology and Mines of the Royal Government of Bhutan. The project was funded by an ETH grant (ETH-38 15-2) and an ESA Alcantara project (ESA 4000117652/16/F/MOS).

5.8. References

Agliardi, F., Crosta, G. B., Frattini, P., and Malusà, M. (2013). Giant non catastrophic landslides and the long-term exhumation of the European Alps. . Earth and Planetary Science Letters, 365, 263-274. doi:http://dx.doi.org/10.1016/j.epsl.2013.01.030.

Agliardi, F., Crosta, G. B., and Zanchi, A. (2001). Structural constraints on deep-seated slope deformation kinematics. Engineering Geology, 59(1-2), 83-102. doi:doi.org/10.1016/S0013-7952(00)00066-1

Agliardi, F., Crosta, G. B., Zanchi, A., and Ravazzi, C. (2009). Onset and timing of deep-seated slope deformation kinematics. Engineering Geology, 59, 83-102. doi:10.1016/j.geomorph.2007.09.015

Antolín, B., Schill, E., Grujic, D., Baule, S., Quidelleur, X., Appel, E., and Waldhör, M. (2012). E-W extension and block rotation of the southeastern Tibet: Unravelling late deformation stages in the eastern Himalayas (NW Bhutan) by means of pyrrhotite remanences. Journal of Structural Geology, 42, 19-33. doi:dx.doi.org/10.1016/j.jsg.2012.07.003

Brideau, M.-A., Yan, M., Stead, D. (2009). The role of tectonic damage and brittle rock fracture in the development of large 2 rock slope failures. Geomorphology. doi:10.1016/j.geomorph.2008.04.010

Cerri, R. I., Reis, F. A. G. V., Gramani, M. F., Rosolen, V., Luvizotto, G. L., Giordano, L. C., and M., G. B. (2018). Assessment of landslide occurrences in Serra do Mar mountain range using kinematic analyses. Environmental Earth Sciences, 77(325). doi:doi.org/10.1007/s12665-018-7508-1

Clayton, A., Stead, D., Kinakin, D., and Wolter, A. (2017). Engineering geomorphological interpretation of the Mitchell Creek Landslide, British Columbia, Canada. Landslides, 14(5), 1655–1675. doi:doi.org/10.1007/s10346-017-0811-1

Crosta, G. B., Frattini, P., and Agliardi, F. (2013). Deep seated gravitational slope deformations in the European Alps. Tectonophysics, 605, 13-33. doi:http://dx.doi.org/10.1016/j.tecto.2013.04.028

Di Maggio, C., Madonia, G., and Vattano, M. (2014). Deep-seated gravitational slope deformations in western Sicily: Controlling factors, triggering mechanisms, and morphoevolutionary models. Geomorphology, 208, 173-189. doi:doi.org/10.1016/j.geomorph.2013.11.023

Dini, B., Manconi, A., and Loew, S. (2019a). Investigation of slope instabilities in NW Bhutan as derived from systematic DInSAR analyses. Engineering Geology, 259. doi:doi.org/10.1016/j.enggeo.2019.04.008

Dini, B., Daout, S., Manconi, A., and Loew, S. (2019b). Classification of slope processes based on multitemporal DInSAR analyses in the Himalaya of NW Bhutan. Remote Sensing of Environment, 233. doi:doi.org/10.1016/j.rse.2019.111408.

Fey, C., Wichmann, V., and Zangerl, C. (2017). Reconstructing the evolution of a deep seated rockslide (Marzell) and its response to glacial retreat based on historic and remote sensing data. Geomorphology, 298, 72-85. doi:doi.org/10.1016/j.geomorph.2017.09.025

Finlayson, B., and Statham, I. (1980). Hillslope Analysis. London.

Francioni, M., Coggan, J., Eyre, M., and Stead, D. (2018). A combined field/remote sensing approach for characterizing landslide risk in coastal areas. International Journal of Applied Earth Observation and Geoinformation, 57, 79-95. doi:doi.org/10.1016/j.jag.2017.12.016

Gansser, A. (1983). Geology of the Bhutan Himamalya.

Glueer, F., and Loew, S. (2015). Rock Bridge Failure Caused by the Aysèn 2007 Earthquake (Patagonia, Chile). Paper presented at the Engineering Geology for Society and Territory. Landslide processes. , Cham.

Gokceoglu, C., Sonmez, H., and Ercanoglu, M. (2000). Discontinuity controlled probabilistic slope failure risk maps of the Altindag (settlement) region in Turkey. Engineering Geology, 55, 277-296.

Grämiger, L. M., Moore, J. R., Gischig, V. S., Ivy-Ochs, S., and Loew, S. (2017). Beyond debuttressing: Mechanics of paraglacial rock slope damage during repeat glacial cycles. Journal of Geophysical Research: Earth Surface, 122(4), 1004-1036. doi:doi.org/10.1002/2016JF003967

Heim, A. (1932). Bergsturz und Menschenleben (Landslides and Human Lives). Vancouver: Bitech Oress.

Hermanns, R. L., Niedermann, S., Villanueva Garcia, A., Chellenberger, A. (2006). Rock avalanching in the NW Argentine Andes as a result of complex interactions of lithologic, structural and topographic boundary conditions, climate change and active tectonics. In S. G. E. e. al. (Ed.), Landslides from massive rock slope failure: Springer.

Hudson, J. A., and Harrison, J. P. (1997). Engineering Rock Mechanics – An Introduction to the Principles.: Elsevier Science Ltd. .

Hungr, O., Leroueil, S., and Picarelli, L. (2014). The Varnes classification of landslide types, an update. Landslides, 11, 167-194. doi:10.1007/s10346-013-0436-y

Hutchinson, J. (1988). General report: Morphological and geotechnical parameters of landslides in relation to geology and hydrogeology. Paper presented at the 5th intarnational symposium on landslides, La Coruna, Spain.

Ivy-Ochs, S., Martin, S., Campedel, P., Hippe, K., Alfimov, V., Vockenhuber, C., . . . Viganò, A. (2017). Geomorphology and age of the Marocche di Dro rock avalanches (Trentino, Italy). Quaternary Science Reviews, 169, 188-205. doi:doi.org/10.1016/j.quascirev.2017.05.014

JAXA. (2017). ALOS World 3D. Retrieved from http://www.eorc.jaxa.jp/ALOS/en/aw3d30/index.htm

McColl, S. T., and Davies, T. R. H. (2013). Large ice-contact slope movements: glacial buttressing, deformation and erosion. Earth Surface Processes and Landforms, 38(10), 1102-1115. doi:doi.org/10.1002/esp.3346

Mishra, B. K., Bhattacharjee, D., Chattopadhyay, A., and Prusty, G. (2018). Tectonic and lithologic control over landslide activity within the Larji–Kullu Tectonic Window in the Higher Himalayas of India. . Natural Hazards, 92(2), 673-697. doi:doi.org/10.1007/s11069-018-3219-x

Park, H.-J., Lee, J.-H., Kim, K.-M., and Um, J.-G. (2016). Assessment of rock slope stability using GIS-based probabilistic kinematic analysis. Engineering Geology, 203, 56-69. doi:dx.doi.org/10.1016/j.enggeo.2015.08.021

Pedrazzini, A., Humair, F., Jaboyedoff, M., and Tonini, M. (2016). Characterisation and spatial distribution of gravitational slope deformation in the Upper Rhone catchment (Western Swiss Alps). Landslides, 13(2), 259-277. doi:https://doi.org/10.1007/s10346-015-0562-9

Robinson, D., Davies, T. R. H., Wilson, T. M., Orchiston, C., and Barth, N. (2015). Evaluation of coseismic landslide hazard on the proposed Haast-Hollyford Highway, South Island, New

Zealand. Georisk: Assessment and Management of Risk for Engineered Systems and Geohazards, 10(2), 146-163. doi:doi.org/10.1080/17499518.2015.1077974

Santangelo, M., Marchesini, I., Cardinali, M., Fiorucci, F., Rossi, M., Bucci, F., and Guzzetti, F. (2015). A method for the assessment of the influence of bedding on landslide abundance and types. . Landslides, 12(2), 295-309. doi:doi.org/10.1007/s10346-014-0485-x

Schramm, J.-M., Weidinger, J. T., and Ibetsberger, H. J. (1998). Petrologic and structural controls on geomorphology of prehistoric Tsergo Ri slope failure, Langtang Himal, Nepal. Geomorphology, 26(1-3), 107-121. doi:doi.org/10.1016/S0169-555X(98)00053-1

Stead, D., and Wolter, A. (2015). A Critical Review of Landslide Failure Mechanisms. Journal of Structural Geology, 74, 1-23. doi:doi.org/10.1016/j.jsg.2015.02.002

Tonini, M., Pedrazzini, A., Penna, I., and Jaboyedoff, M. (2014). Spatial pattern of landslides in Swiss Rhone Valley. Natural Hazards, 73, 97-110. doi:DOI 10.1007/s11069-012-0522-9

Wiesmayr, G., Edwards, M. A., Meyer, M., Kidd, W. S. F., Leber, D., Häusler, H., and Wangda, D. (2001). Evidence for steady fault-accommodated strain in the High Himalaya: progressive fault rotation of the southern Tibet detachment system in NW Bhutan (Vol. 200). London: Geological Society of London.

5.9. Appendix

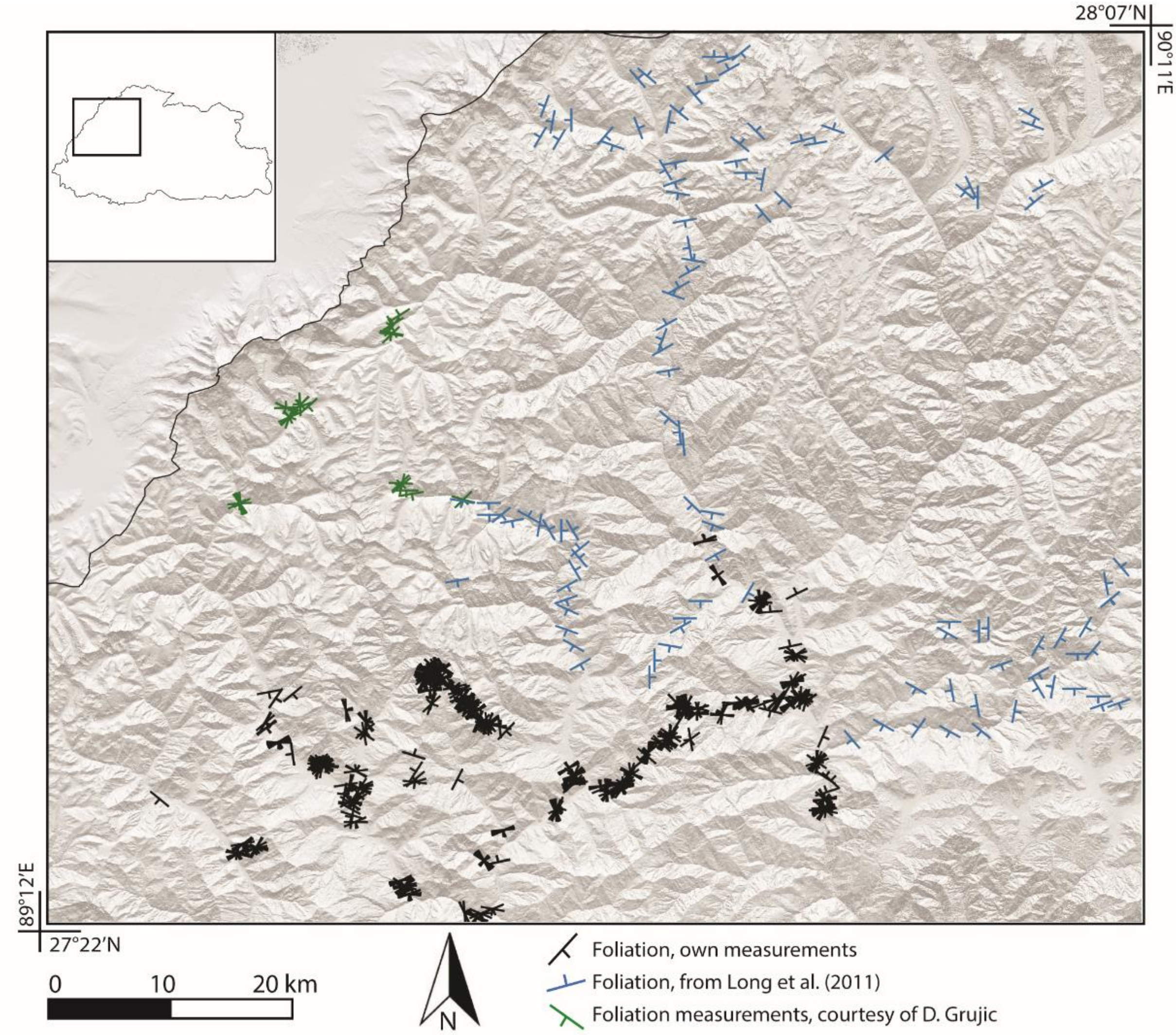

App. 5-1**.** In black, areas in which foliation and faults orientations were acquired during our two field campaigns. In green, foliation measurements courtesy of Djordje Grujic, in blue foliation measurements digitised from Long et al. (2011).

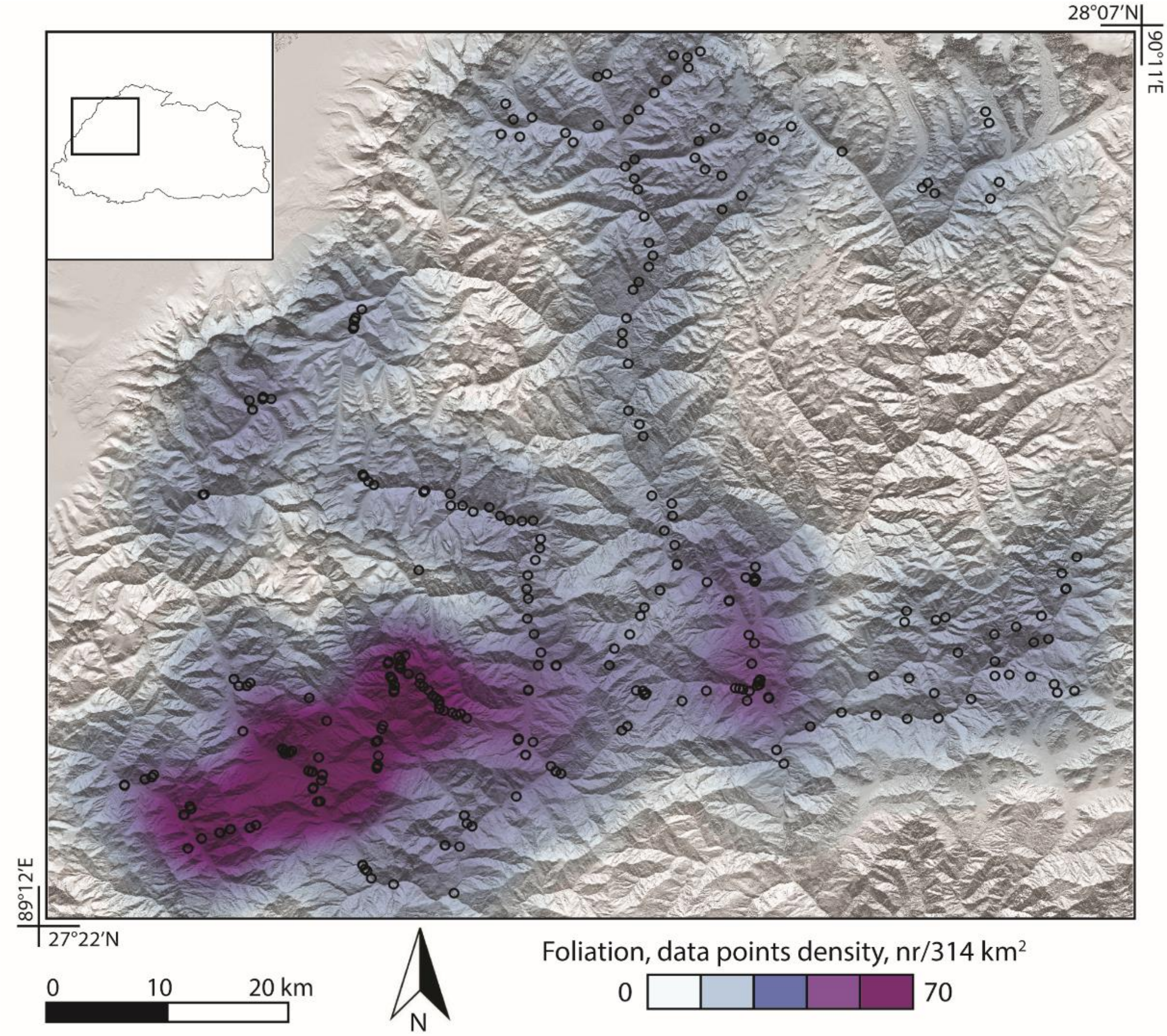

App. 5-2 Heatmap of the enhanced foliation including own measurements in the south. In addition, measurements courtesy of D. Grujic and those digitised from Long et al. (2011) are shown.

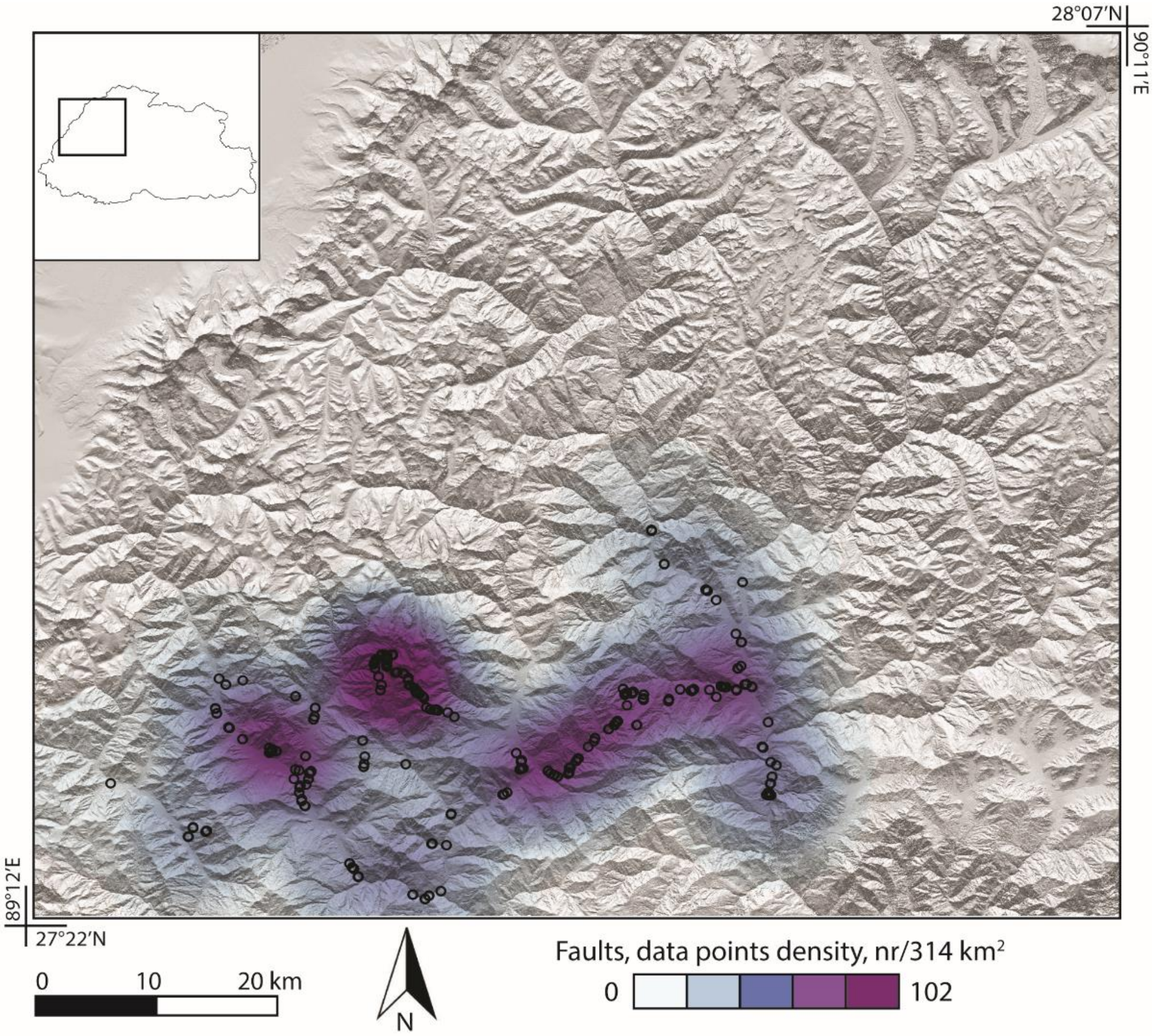

App. 5-3 Heatmap of the fault measurements acquired during our field campaign.

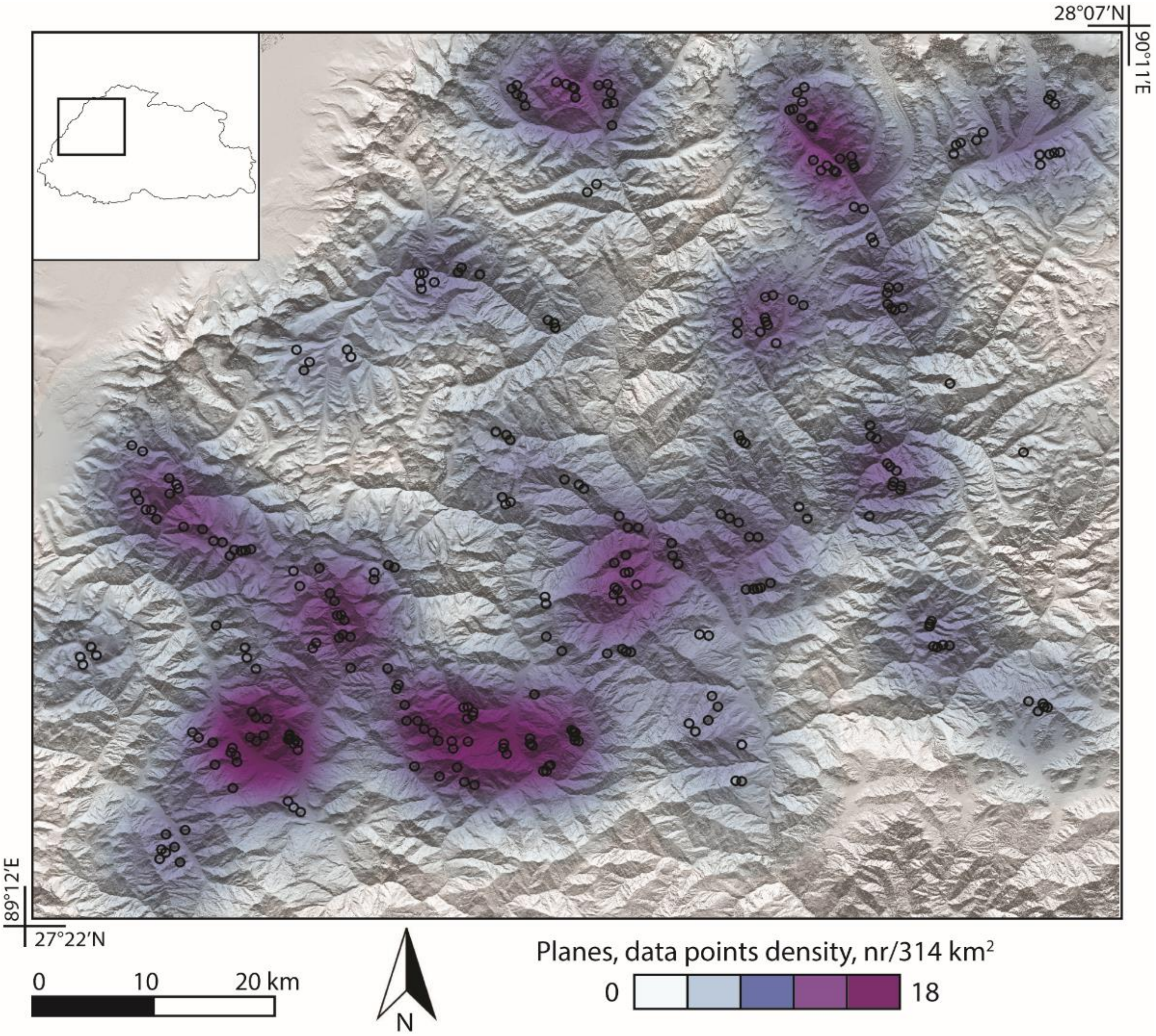

App. 5-4 Heatmap of the mapped planar valley flanks (acquired through remote sensing).

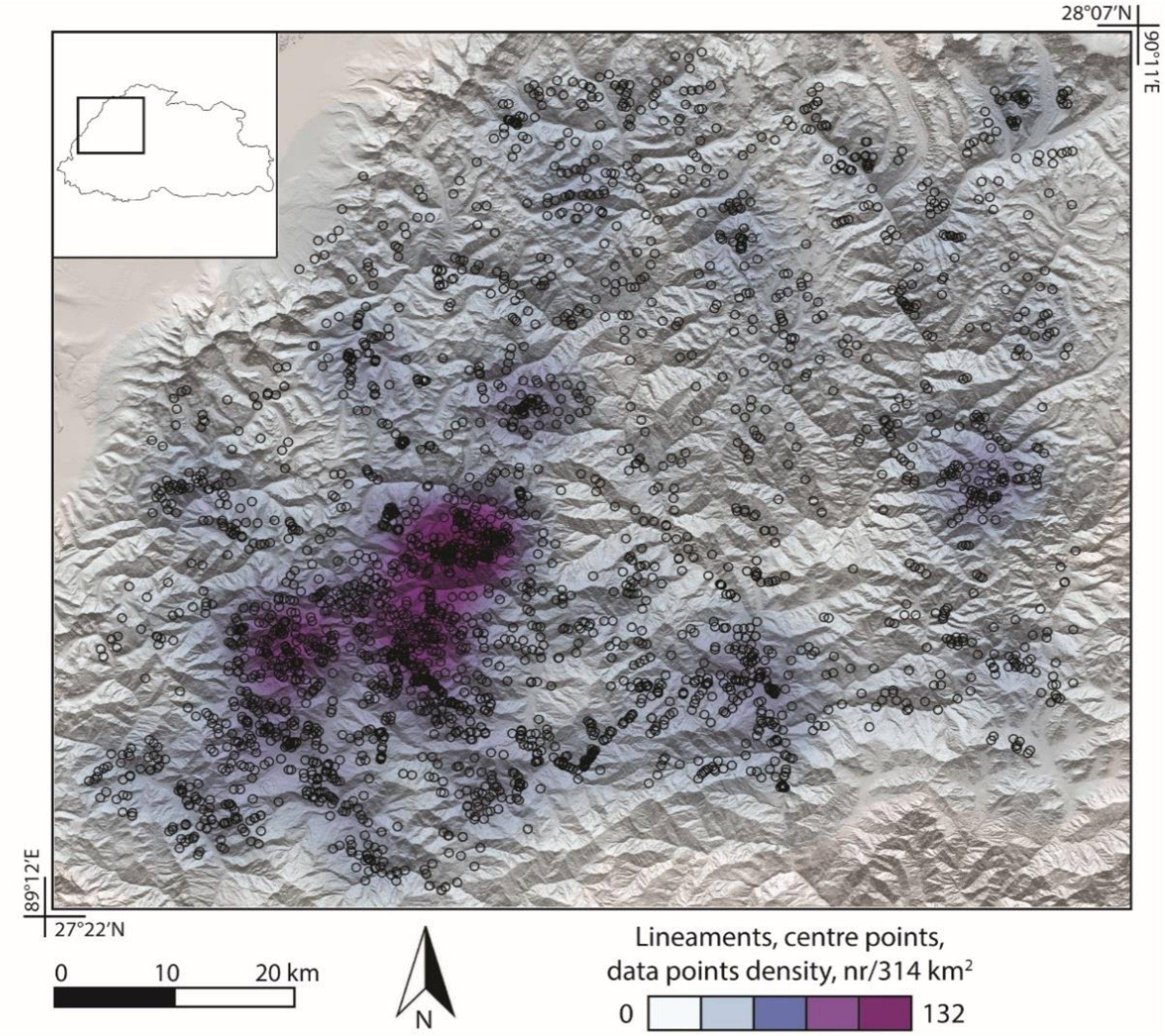

App. 5-5. Heatmap of the mapped lineaments (fault traces) acquired through remote sensing. Points refer to the centre of an individual lineament.

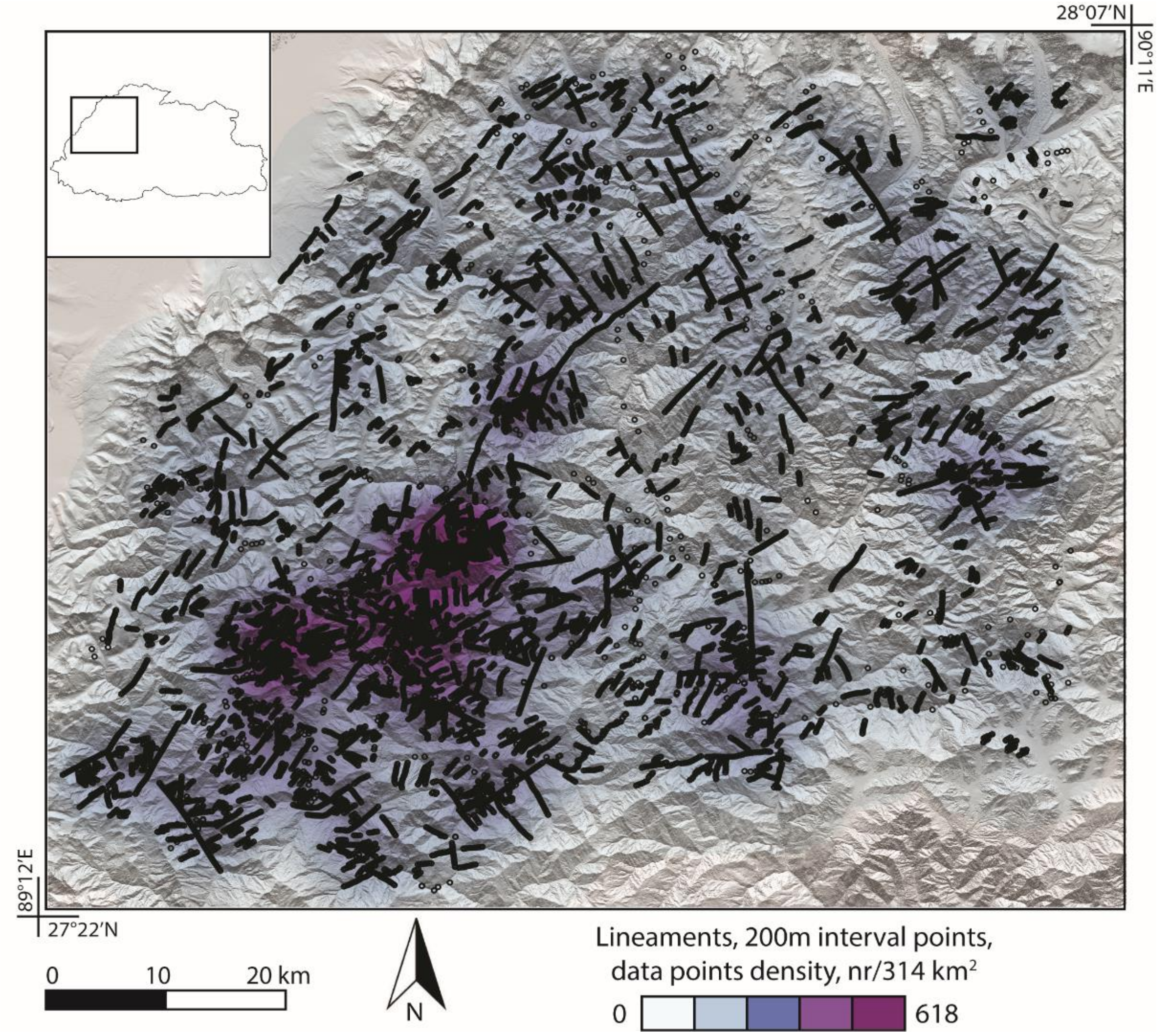

App. 5-6. Heatmap of the mapped lineaments (fault traces) acquired through remote sensing. Points sample each lineament at 200m intervals.

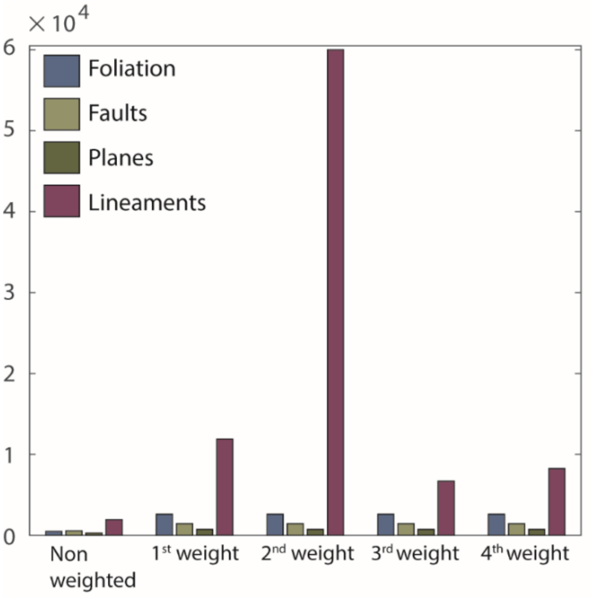

	Non-weighted	Centre point	200 m interval points	Rescaling 200 m points	Average of 200 m points
Foliation	493	2614	2614	2614	2614
Faults	556	1444	1444	1444	1444
Planes	286	739	739	739	739
Lineaments	1951	11900	60005	6700	8258

App. 5-7. The histograms show the effect on the four structural layers of the weighting system. In particular, in the first weighting system each segment is assigned one point at its centre. In the second, each segment is split into a number of points, lying at 200 m intervals along its length, though no correction is made to re-establish proportions. In the third, the proportions are re-established by using the average of the density, the latter sampled at 200 m interval points. In the fourth, which is the system used for the analyses, a scaling factor is applied. Below, table showing datapoints in the different layers and weighting systems.

Four variations of the weighting method are explored. In the first one, each segment is assigned one point at its centre. In the other three, each segment is split into a number of points, lying at 200 m intervals along its length. Heat maps are generated for each of the four layers (twice for the lineaments layer, one for centre points and one for 200 m interval points), all of them based on a 10 km radius (Appendix 5-2 to 5-6). The heat maps describe the density of data points of a layer over a circular area of 314 km2. The density is then sampled at all data points within each layer and normalised for the layer's maximum. The reciprocal of the normalised density at each data point is used as the dimensionless weight which is then assigned to a data point as the bogus quantity of points with the same orientation. Individual layers are weighted independently of the others in order to avert adverse effects of uneven densities between layers in the same area. For instance, a cluster of closely spaced foliation measurements should not reduce the weight of an individual fault measurement in the same area.

The four variations of the method differ in the way that density is calculated for the lineaments layer. A long lineament (i.e. > 2000 m) would have a different density if the density is calculated by generating a heat map of the centre points or of points spaced every 200 m along each trace (clearly generating a much higher number of points). When calculating and sampling density at the centre point, the density may be biased to higher or lower values depending on where the point happens to fall with respect to surrounding points. When a lineament is assigned points at every 200 m along its length, this issue is overcome because the higher number of equally spaced points is more reflective of the real density of the lineaments, therefore being less reliant on the position of a centre point, better representing density overall. The fact that longer lineaments are given higher densities implies that they get a lower weight, this effect though being counteracted by the large amount of points that are assigned to each lineament. Although assigning points at 200 m intervals to each segment improves the density calculation as opposed to using centre points, this method introduces a consequential problem, as the large amount of points generated multiplied by their weights, causes the proportions of the initial dataset to change markedly (table 2).

In the original dataset we have 493 foliation measurements, 556 faults measurements, 286 planes, 1951 lineaments. What we note is that in the same area (roughly 1800 km2) covered by our own fault measurements (containing the whole 556 data points) we find roughly 620 mapped lineaments. The strong relation of the two layers, due to the fact that they indicate a similar type of discontinuity, makes them more comparable and we consider reasonable a rough ratio of 0.9. In fact, if one is the morphological expression of the other, then an unbiased fault dataset should yield an expected ratio of roughly 1. Moreover, it would be unsafe and highly speculative to skew the original ratios without a good basis on which to build new ones. Thus, in order to maintain similar ratios between layers as the initial ones, and assuming that fault density is the same across the study area (there is no clear reason to believe any different), the weight applied should increase the lineaments by around 240% of the initial number. In fact, 620 lineaments in roughly 1800 km2 should correspond to approximately 2600 non weighted lineaments in 7600 km2 (whole study area). The weighting of the faults layer (see table 2 and inset bar graph) yields a total of 1444 weighted data points. In order to keep the same ratio between faults and lineament layers, there should be around 6700 weighted lineaments in the whole region. Any higher proportion would risk to bias the dataset even further, thus arguably deteriorating the dataset quality from its initial conditions. Assigning points every 200 m of lineament lengths yields to a high amounts of points (13505 vs 1951) and when the inverse of density weight is applied they count in total as 60005 data points. This is almost 9 times more than there should be in order to maintain the initial ratios observed in the area with fault measurements. This may introduce a bias in the analyses results towards the effects of the lineaments. In order to solve this problem, we envisage two possible variations: 1) either we rescale all points by a factor 0.112 which is what is required to maintain the proportion we deem more realistic, or 2) instead of using all the points into which the lineaments are divided, the density sampled at all points along a lineament is averaged and then used to calculate the weight which is applied only to one point per lineament. When we average the density of all 200 m points of a lineament and then use one point per lineament, we obtain a total weighted lineament amount of 8258. This is much better in keeping the wanted proportion than the 60005 or even the 11900 of the second and first variation of the weighting system respectively. Table

2 summarises the quantity of non-weighted and weighted data points in each layer. For our analyses we will use the third variation of the method, with lineament density calculated and sampled with points at 200 m interval and then rescaled to keep the initial proportions of the dataset. In this way, the length of the lineaments is also taken into account without the need of additional length-based weighting.

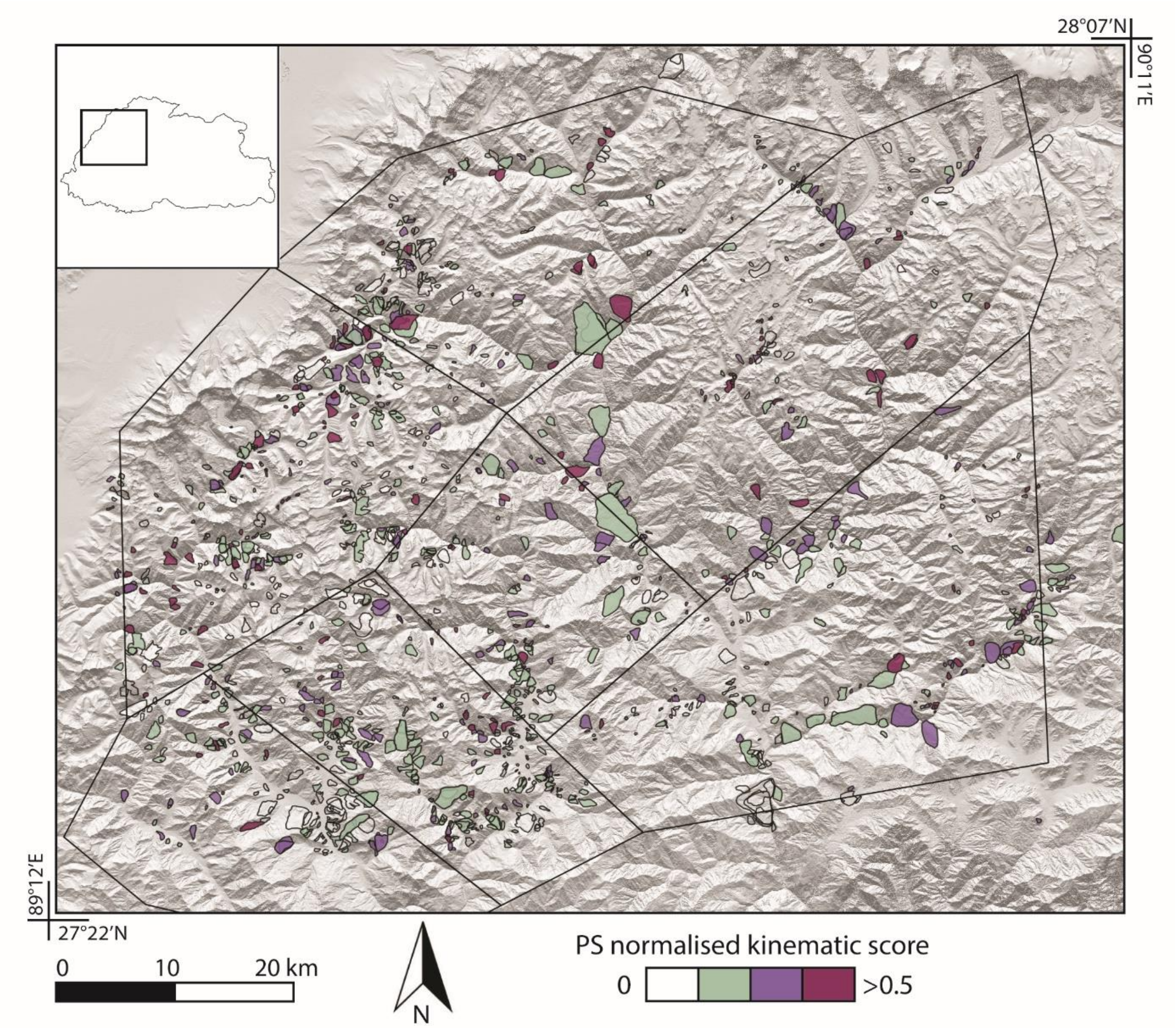

App. 5-8. Kinematic score for PS for landslides (optical) and instabilities from DInSAR and InSAR time series.

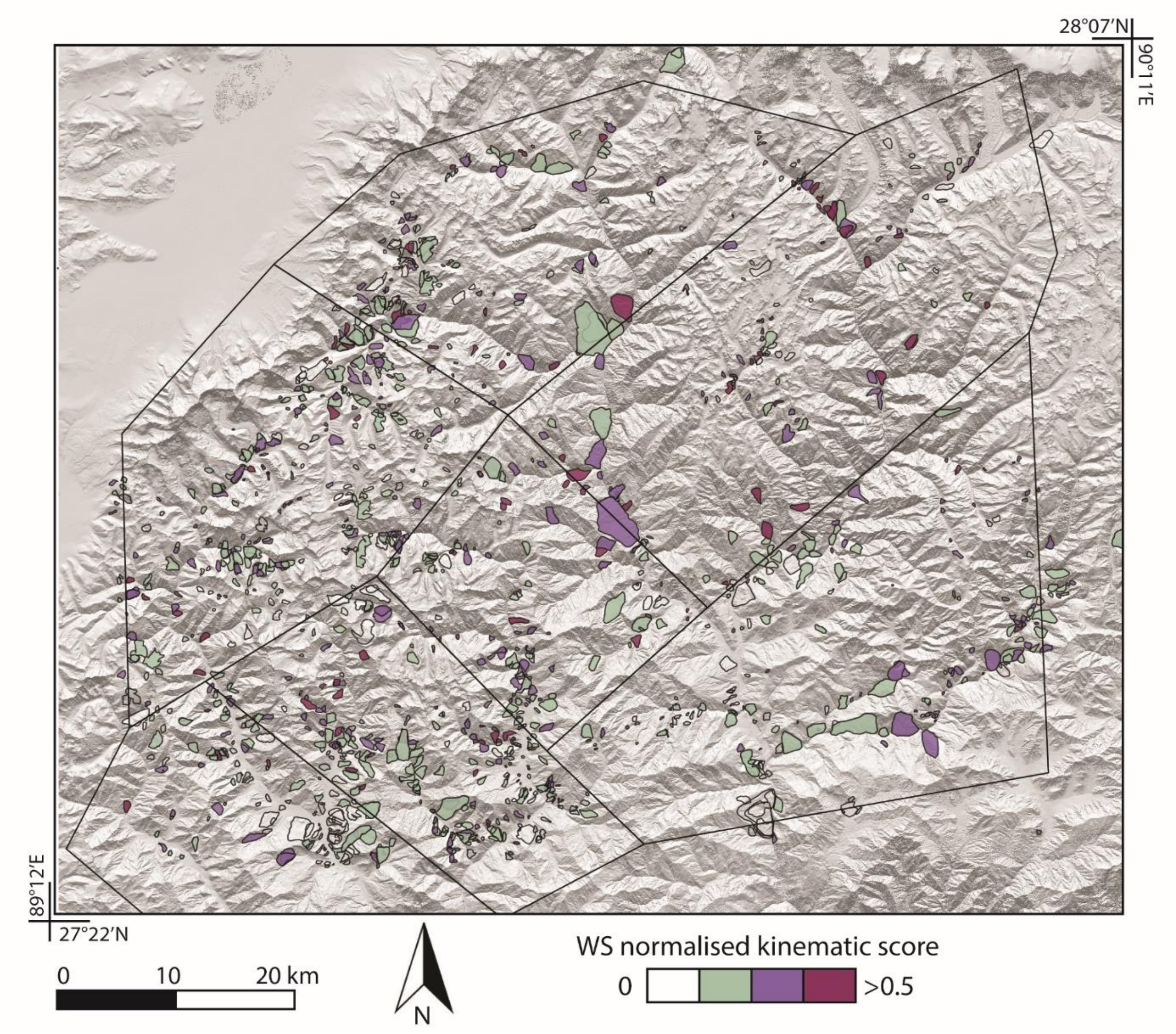

App. 5-9. Kinematic score for WS for landslides (optical) and instabilities from DInSAR and InSAR time series

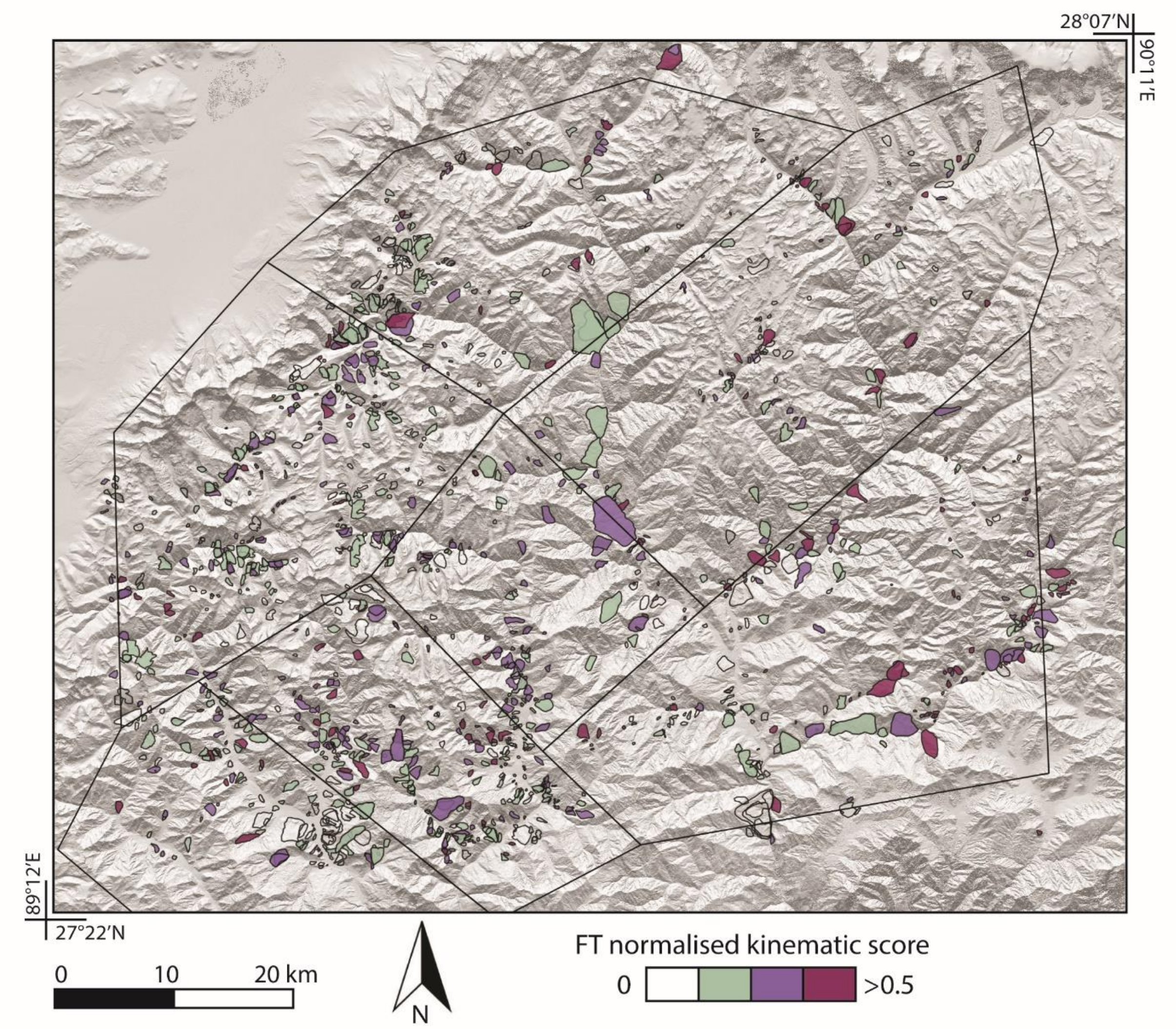

App. 5-10**.** Kinematic score for FT for landslides (optical) and instabilities from DInSAR and InSAR time series.

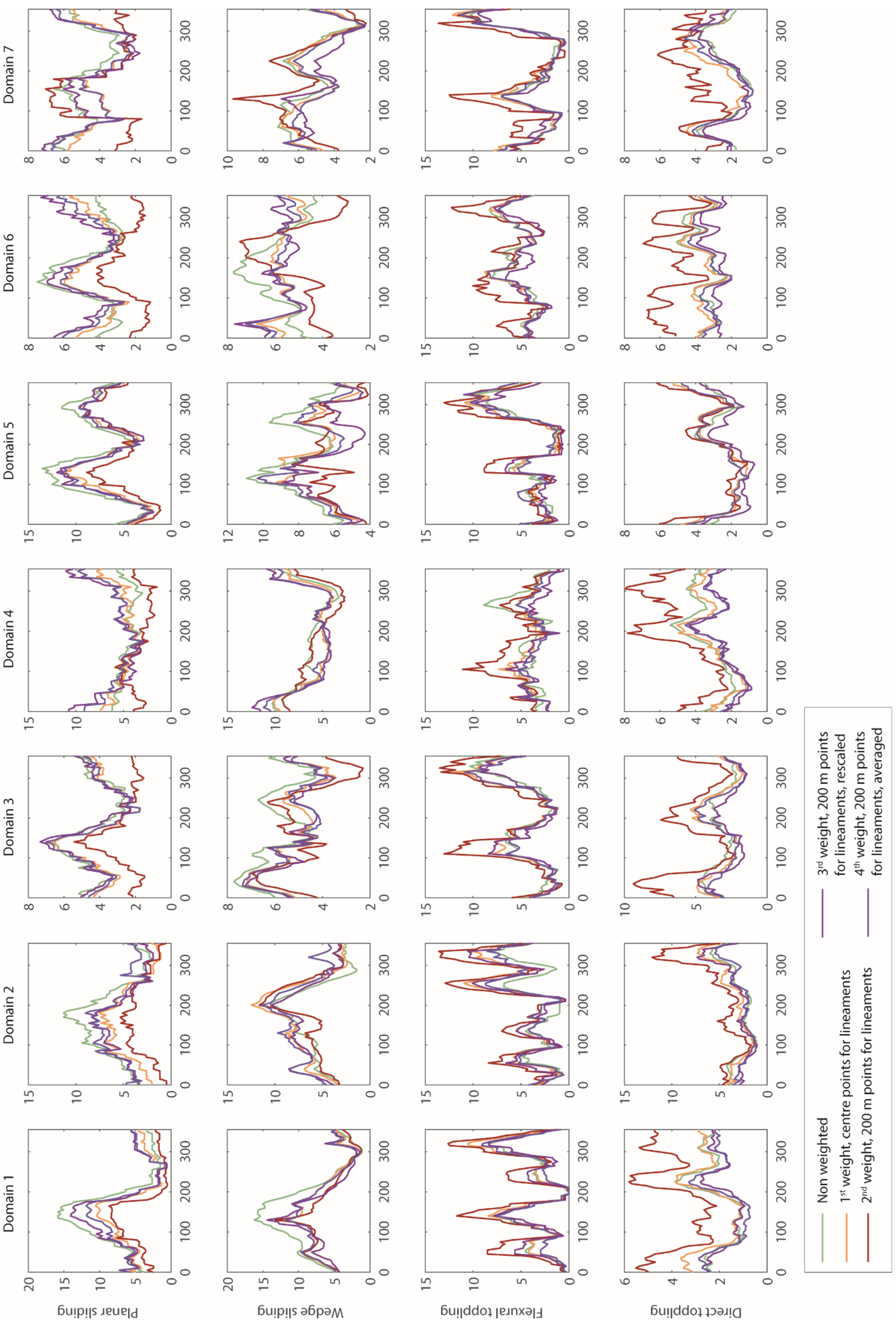
Domain 1
Domain 2
Domain 3
Domain 4
Domain 5
Domain 6
Domain 7
Planar sliding
Wedge sliding
Flexural toppling
Direct toppling
0
100
200
300
Non weighted
1st weight, centre points for lineaments
2nd weight, 200 m points for lineaments
3rd weight, 200 m points for lineaments, rescaled
4th weight, 200 m points for lineaments, averaged

App. 5-11 Previous page. Comparison between the results of the kinematic analyses for PS, WS, FT and DT, using different weighting systems. On the whole, the shape of the curves is similar between different weighting systems and the ranges of favourable aspects to a particular failure mode remains largely unchanged. This is because, with the weighting system introduced here we do not make up for data that was not collected, but only enhance or dampen the effects of existing data on the basis of their original and expected densities. However, the application of the weighting proposed here has an effect on the critical percentages obtained for a given failure mode. For example, for the two toppling modes, the red curve always shows higher critical percentages. The red curve is associated to the weighting variation according to which a really large number of points is associated to the lineaments layers. In this way, the steep sets are given a very large influence on the results and are favoured with respect to less steep sets. Since toppling is largely controlled by steep sets or their intersections, it comes to no surprise that toppling percentages are skewed to higher values. For sliding modes, the red curves are often, though not always, showing lower percentages with respect to the other curves, whilst the green curve (non-weighted data) is often showing high percentages. The reason for this is that sliding is often favoured by foliation or by medium to shallow dipping structures (either associated with the measurements, the planes or the lineaments layers). When data is not weighted, the relative abundance of foliation measurements in some domains, for example, has a stronger influence on the results than the lineaments have. The curves associated with the other variations of the weighting system lie somewhere in the middle and tend to smoothen out peaks and troughs, flattening the curves. The shape of the curve may of course change if new data (new orientations) were collected or if certain orientations in the dataset are currently severely subsampled.

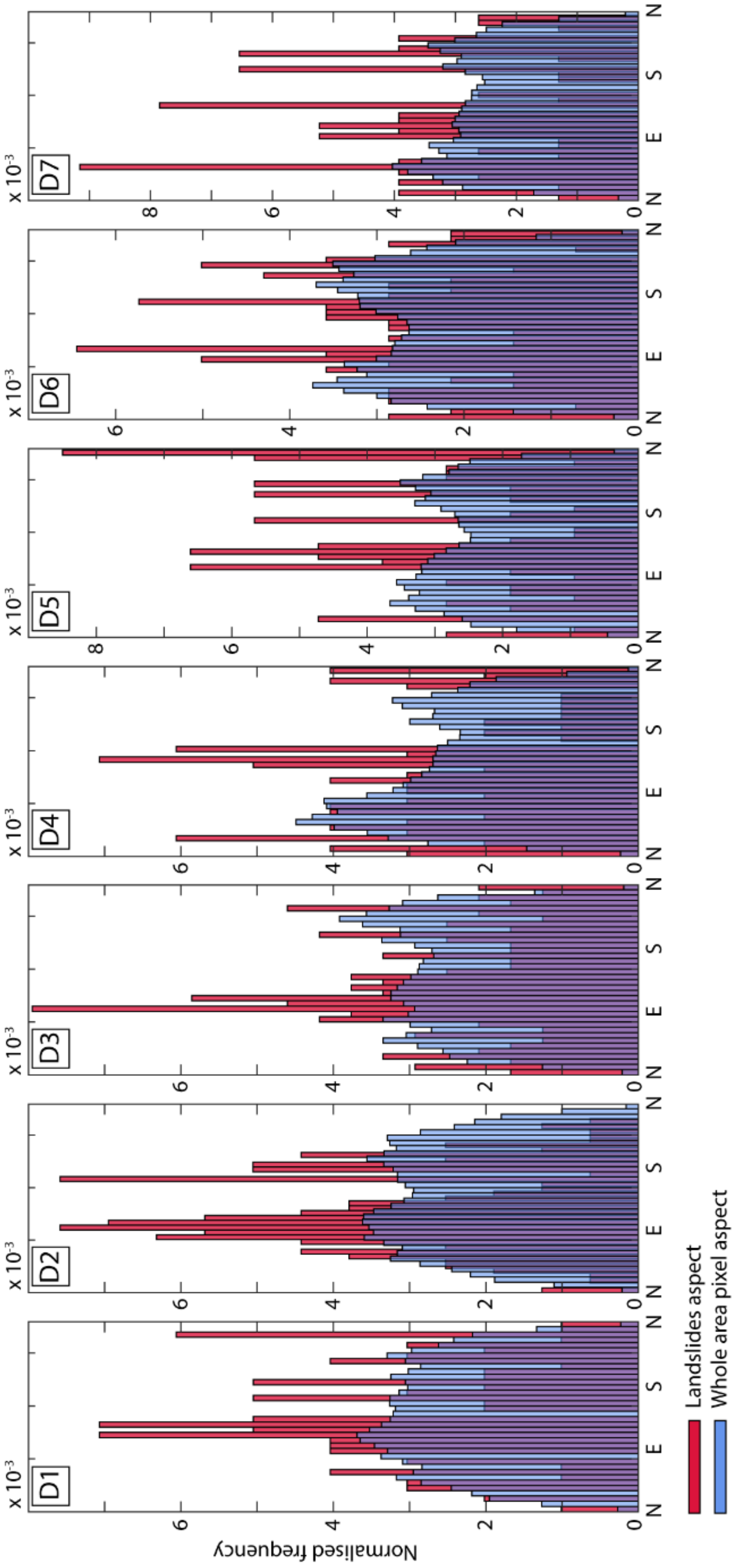

App. 5-12. Comparison between landslide aspect distribution (blue) and pixel axpect distribution (red). In order to ensure that the non-uniform landslides distribution is not biased by topographic factors, we have compared the landslides distribution with the slope aspect distribution in all domains. The abundance of roughly N-S oriented valleys causes troughs in the distributions of slope aspect for pixels oriented north and south. However, we note that in the majority of cases the peaks in the landslide distribution show a shift compared to the peaks in the distribution of pixel aspect values. Moreover, at least for southern aspects, the maximum peak-trough difference is very small compared to the total amount pixels, likely yielding to differences in pixel numbers too low to justify a strong control on landslides distribution.

6. Conclusions and outlook

In this work we have established methodologies for the extraction of slope instability data and the analysis of their displacement rates and their predisposing factors. These methodologies are largely based on remote sensing data and are replicable in other mountainous regions. We have produced a large amount of valuable, new geological data for northwestern Bhutan, a region that had been previously relatively unexplored from the point of view of slope instabilities, the underpinning processes and their relation with other geological factors such as, for example, structural features and permafrost distribution. We have obtained new insights for the region, generating an overview of slope instabilities and their displacement rates that were previously unknown.

6.1. Methodologies presented: values, limitations and practical implications

Among the methods presented in this work, we have established a way to not only identify potentially active areas, but also to assess their likelihood. This is important because the retrieval of information from interferometric analyses, in challenging environments and at the regional scale, can be quite difficult. Making judgements on the hazard level based, for example in the case of landslides, on the creep velocities, can be consequently complicated. High topographic gradients, landcover, large scale are all limiting factors for DInSAR analyses, causing problems related to temporal decorrelation and unwrapping among others. The limitations of this approach correspond to the inherent limitations of DInSAR, the main one in our case being landcover and temporal decorrelation. The gap we observe in the most densely vegetated part of our study region, the southeastern quadrant, is likely related to the difficulties of retrieving displacements with DInSAR in vegetated areas or where landcover changes markedly through time (agricultural land). However, though unlikely exhaustive across all land cover types, our likelihood of activity map generated with wrapped interferograms essentially represents a hazard index map, showing an overview of the recent slope instability situation and comparing, in a semi-quantitative way, how different areas are affected by slope deformation. This has a value in terms of land-use planning and development of infrastructure and can serve as a basis for site selection and as a guide for the identification of sites where risk may be elevated and which thus require in depth local investigations.

The analysis of time series and velocities/cumulative displacements could in principle offer more in terms of quantifying the actual displacements. Though we obtained interesting results in this sense, multi-temporal interferometric processing at the large scale is limited by difficulties related to the unwrapping of the phase, thus again a limitation intrinsic to the technique. Moreover, the ability to retrieve small displacement rates would require long temporal windows and high-level processing, the first becoming increasingly available now with the launch of new generations satellites, the latter at the large scale being indeed challenging. In order to obtain a picture at the large scale with a multi-temporal analysis in our work, we compromised coverage. We show that we can separate the linear and seasonal signals, after applying some correction for long wavelength artifacts, revealing deformation related to interesting processes, some of which had not been identified before with satellite based InSAR. Namely, we exploited the information of amplitude and timing of corrected seasonal signals to identify freeze-thaw cycles in the permafrost region and groundwater table driven reversible slope deformation below the permafrost region. Though cycles related to permafrost may have an interest from a scientific point of view, we believe that revealing seasonal cycles of valley closure and opening can again have practical implications for planning purposes of infrastructure that may be sensitive to millimetric displacements, such as concrete arch dams.

We have also shown a method to create a compound structural dataset also largely based on remote sensing, to address some of the intrinsic biases related to data availability and unevenness and to use it, in combination with a landslide inventory, to perform probabilistic kinematic analyses. The clear advantage of this method is that we take into account the distribution of structures that have either been measured in the field or mapped through remote sensing techniques, the reliability of which is corroborated by the good fit with the expected tectonic environment. One limitation is related once again to land cover and the difficulty of mapping structures using remote sensing data in densely vegetated regions. Moreover, shallower dipping sets are much harder to observe and map, given their muted expression on the topography. Though again our dataset is likely not exhaustive of all structures, it has the advantage of using all available real data, and the possibility to extend it to the large region. The results can be used to identify what slopes, within a given structural domain, may be affected by what type of rock slope instability. This is not only important to investigate predisposing factors, thus to understand the observed landslide distribution, but also as a guidance for stakeholders and local investigators on the failure modes that are more likely on certain slope orientations in a given area.

Our analyses of optical images, interferograms and velocity/displacement maps were carried out in a non-automated way, thus are affected by a degree of subjectivity related to the visual mapping. However, we strived to contain this subjectivity, by making the analyses as systematic as possible and dividing the area into a grid of 10 km squares. Therefore, we believe that the maps we have produced are reliable for large scale analyses. Moreover, the use of ascending and descending geometries should limit problems related to layover and shadow that would impair activity detection with DInSAR on specific slope orientations. This cannot exclude that some slope instabilities may have been missed. This is particularly true for densely vegetated areas (southeastern quadrant of the region), and for instabilities which do not show clear morphological signs nor active displacements above measurement error (1-2 mm/year for annual velocities and 5-10 mm for displacement, see chapter 2). Moreover, our mapping of optical images focused on large rock slope instabilities. Though it is possible that large landslides in soil have been erroneously mapped as rock slope instabilities, we generally avoided mapping soil slides. We also did not map debris flows (active channels or fans) and rockfall. Not only our original focus was on large rock slides, but we also had a size cut-off imposed by the resolution of the imagery we worked with. For instance, we observed in the field a large amount of small instabilities in rock faces caused by new road cuts, these releasing material on the road during the monsoon. For as much as these relatively small events can be dangerous and damaging and cause disruption to the network, we were not able to map them on optical images nor were we able to detect their activity due to their limited size.

Our activity maps and optical based landslide inventory, though likely not exhaustive, can be used by the relevant Royal Government of Bhutan’s departments to inform communities and to make land-use plans. They should also prove useful for stakeholders involved in the development of new infrastructure, as a basis to identify suitable sites or sites that would require in-depth local investigations.

6.2 New datasets generated and what their analysis reveals about the region

We present a new dataset of unstable slopes characterised by displacements in the period between 2006 and 2011, with a likelihood of activity and a geomorphological classification which allows to identify different types of landslides and also rock glaciers. We show another new inventory based on DInSAR multitemporal analyses, which illuminated not only rock slope instabilities and rock glaciers quantifying the creep velocities at the regional scale, but also reversible deformation associated with freeze-thaw cycles in the permafrost region and with ground water table variations below the permafrost region. We also propose a new inventory of past large rock slope instabilities based on optical images and DSM analysis alone and a large structural dataset articulated on a variety of sources, but largely retrieved from remote sensing data. Moreover, an interesting case study is analysed, highlighting the importance and potential of DInSAR multi-temporal analyses and time series to identify, quantify and monitor large rock slope instabilities, and to play a key role in the planning of critical infrastructure. We observed that 350 rock slope instabilities contained in the optical inventory have some activity information based on either the interferogram analysis or the multi-temporal DInSAR analysis or both. This leaves 557 rock slopes instabilities mapped on optical images without any activity information retrieved with DInSAR. It is possible that for some of the landslides mapped on optical images no activity is detected either due to land cover or due to displacements being within the error of the measurement, thus too small to be detected. However, it is also possible, and in fact we believe likely, that many of the landslides mapped on optical images are not active during our DInSAR observation window. This means that landslide activity is on the whole lower than it may have been in the past in the region, as we state in chapters 2 and 4. Insight obtained through the different analyses are summarised below.

6.2.1 Investigation of slope instabilities in NW Bhutan as derived from systematic DInSAR analyses

DInSAR standard analyses based on wrapped interferograms allowed the detection of 693 previously unknown rock slope instabilities in northwestern Buthan. A geomorphological classification was performed to distinguish between different landslide types into the following groups: 1) rock slides, rock slope deformation, mountain slope deformation, 2) soil creep, 3) soil slide, with the addition of 4) rock glaciers. This geomorphological classification revealed that almost 78% of the identified instabilities are rock slope instabilities (group 1), thus more likely involving large depths and volumes as opposed to shallow soil movements. The spatial distribution observed of potentially unstable rock slopes is non-uniform and seems to be influenced by the presence of regional tectonic structures. Moreover, active unstable rock slopes seem to be less abundant in recent times (between 2006-2011) than in the past. During field campaigns in September 2016 and October 2017 a large number of past rock slides deposits were identified, often covered by thick soil layers. The fact that the number of actively unstable slopes across the region does not match that of past rock slides observed in the field attests a relatively low level of current rock slope activity in the region. This may be related to the lack of large earthquakes to act as trigger or to initiate instabilities in the last three centuries (a recent study placed the latest magnitude 8 earthquake in 1714). Whilst the lowest limit of displacement detectability is more difficult to pin point, but it is not lower than roughly 1/5-1/6 of a fringe for a single interferogram (around 5 mm for Envisat and 20 mm for ALOS-1), the highest bound of a full fringe has never been reached, for any of the mapped instabilities. Indeed, the actual velocity depends on the history of each area affected by displacements over the observation period. Only for some rock glaciers, displacements corresponding to a gradient of almost a full fringe have been observed. Occasionally, debris mantled slopes and talus cones show patterns that appear to be decorrelated within a more coherent area, this showing that the maximum detectability threshold is reached by faster displacements in these cases. Though it is possible that large rock slope instabilities which are affected by faster displacements than can be detected were missed, we paid attention to the identification of areas of displacements adjacent to decorrelated signal. This would indicate that some sectors of a slope moved too fast to be detected. However, such instances were not recorded during our mapping.

6.2.2 Classification of slope processes based on multitemporal DInSAR analyses in the Himalaya of NW Bhutan

Large scale DInSAR multitemporal processing was carried out with the SBAS approach, generating velocity maps and time series of displacements. In this part of the work, we identified unstable slopes by analysing the velocity and cumulative displacement maps, from the temporal behaviour we discerned between gravitational and reversible processes and quantified the activity of different types of landslides, rock glaciers and reversible processes on the basis of the observed time series trend and pattern. Mountain slope and rock slope deformations were shown to have low creep velocities mostly not exceeding 160 mm/year, thus confirming the findings that rock slope activity in the region, in recent times, is relatively low. Though it is possible that some fast-moving landslides were missed by the analysis due to decorrelation, we believe this is unlikely to have happened on a widespread basis for the following reasons. 160 mm/year for the wavelength of ALOS (~23 cm) and a temporal sampling between 82 and 98 days is well below the upper limit of detection, which is more likely to be somewhere around 240 mm/year for adjacent pixels. Moreover, the areas of the detected deformation generally are much larger than a few pixels, which means that the detection threshold could even be higher. Finally, we would expect to observe a gradient in the velocities then followed by a gap in the data (no information retrieved with SBAS over decorrelated areas). Though it is possible that decorrelating or partly decorrelating landslide displacements occurred in areas with no coverage at all (extensive data gaps in the maps due to low coherence), we did not observe any of such instances in our displacements and velocity maps, apart from in the case of some rock glaciers. Rock glaciers are also shown to have low velocities in comparison to those in the Alps, with detected creep rates generally around 300 mm/year. The complete absence of destabilising rock glaciers, with accelerating creep related to increasing temperatures, could be related to more muted effects of climatic changes at such latitudes. Reversible deformation was also illuminated for the first time at such a large scale and associated with different processes on the basis of their position with respect to permafrost but also in relation to their aspect dependency. Amplitudes of the seasonal signal lie between 5 and 17 mm for hydromechanical effects and on average around 10 mm, with maxima up to 28 mm for freeze-thaw related displacements.

6.2.3 Regional scale investigation of preconditioning factors of rock slope instabilities in NW Bhutan

We present a new regional scale past rock slope instabilities inventory for northwestern Bhutan obtained through the analysis of optical images and the high resolution ALOS World3D DSM. We also introduce a new regional scale structural dataset for the area, also largely based on remote sensing, but with the addition of field data (either own or obtained in previous studies).

Exploiting the structural dataset, in conjunction with the rock slope instabilities inventory, we identified structural and lithological control on rock slope instabilities across some parts of the study region. A higher predisposition to failure seems to be associated to the presence of specific sets of regional faults and foliation/bedding structures and in association with certain lithologies. In particular, wedge sliding appears to be an important mechanism in the eastern branch of the Paro valley and in the Thimphu valley. The northwest of the study region seems to be dominated by planar sliding. Our analyses aimed at furthering the understanding of spatial landslide distribution across a large and remote mountainous region in northwestern Bhutan. They are replicable and applicable to other mountainous regions and potentially leading to results that constitute a basis for regional landslide susceptibility mapping for hazard mitigation purposes.

6.2.4 The Punatsangchhu landslide illuminated by satellite based DInSAR time series

The analysis of single interferograms performed in chapter 1 showed that displacements have been occurring on the right slope directly impending on the dam construction site. The successive generation of velocity and cumulative displacements maps and the generation of time series of displacements showed that significant downslope displacements occur in various sectors of the entire valley flank during the observation period. Acceleration phases were also observed, these within the period in which stabilisation measures were put in place, thus raising concerns regarding their effectiveness.

Multi-temporal InSAR analyses performed at a large scale, without previous knowledge, were able to indicate the presence of the instability. Moreover, despite the relatively small observation window, DInSAR analyses alone would have allowed to raise concern regarding the location of the dam. This shows the potential of DInSAR to help assessing the suitability of a site for a project of this kind, focusing efforts and investigating the effectiveness of stabilisation measures and allowing future monitoring.

6.3 Outlook

We have looked into the spatial distribution of unstable slopes which showed displacements in the period 2006-2011. We have then analysed the history of slope movements in the same observation window, by generating velocity and cumulative displacement maps and time series of displacements. Successively, we focused on investigating the predisposition of mapped landslides, thus providing a static picture of the distribution of instabilities in the region. An open question remains that concerning the cause for landslide activity today and in the future. One possibility to address this question would be to produce landslide susceptibility and hazard maps for the region, taking into account different earthquake scenarios that may reactivate previous instabilities or cause failure of meta-stable old rock slide deposits and of colluvium slopes. In the scenario in which Bhutan were to be struck by a major earthquake, many coseismic landslides could be triggered: old rock slides could be reactivated, incipient rock slope instabilities and the large number of slopes composed of colluvium originated from paleo landslides could also fail. Certainly, heavy rainfall events during the monsoon could also act as a trigger for catastrophic slope failures, or cause seasonal accelerations, though coseismic landslides could occur simultaneously on a very widespread scale, their effects being thus more devastating in terms of disruption and interruptions to lifelines. Though it is difficult to predict where landslides will be triggered in the case of a major earthquake, landslides that were identified in this study as presenting clear, fresh morphological features (mapped on optical images), high activity likelihood (analysis of interferograms) or recent downslope trends (multi-temporal analysis) are potential candidates. Moreover, a field investigation of the materials composing slopes identified here as potentially unstable would be required to obtain estimates of geotechnical parameters important for stability analyses. Large earthquakes also lead to an increase in sediment production in relation to debris flow and soil slips which will add to the damaging effects to agricultural land, roads and other infrastructure. The Royal Government of Bhutan should begin to focus on assessing the hazard level in different scenarios for the populated area of Thimphu, but also for important corridors. This is for a number of reasons: the largest concentration of population lives in the valley of Thumphu, we observed in the area several slopes composed of colluvium and old rock slides deposits, moreover, the valley of Thimphu sits in a rather strategic position, on the main east-west highway. If a large landslide were to occur south of Thimphu, this could potentially block access to Paro airport and would cut accessibility between the east, west and south of the country. Additionally, the three more populated valleys of Paro, Thimphu and Punakha may be subject to exceptional floods in the scenario in which a large failure occurred causing a landslide dam even several km upstream and this were to be subsequently breached during the wet season. This represents an important secondary hazard that needs to be taken into account and an in-depth analysis and field validation of the potentially unstable slopes mapped upstream of these settlements should be carried out.

Individual, high-risk sites could be looked at in more detail, such as that of the Punatsangchhu landslide. Cases like this, the damage potential of which lies at large distances from the site of the instability, would deserve in depth field investigations, associated with the modelling of different failure scenarios to assess the hazard in the immediate vicinity and downstream. The integration with in-situ data would also allow to provide information regarding potential volumes involved and failure mechanisms. Further InSAR analyses could be improved through the installation of corner reflectors, where land cover is not ideal for interferometric analyses.

Integrating the analysis of individual sites, future locations of key infrastructure, with DInSAR analyses would be beneficial for a developing country such as Bhutan. Establishing procedures to transparently analyse the geological situation of critical sites would empower stakeholders and governmental departments to take informed decisions.

Establishing channels to pass knowledge on DInSAR analyses and procedures would represent a great benefit for the country and it would allow for the generation of a new scientific, valuable expertise for the region.

The addition of Sentinel-1 data into the large-scale analysis would add value to the work presented here. Sentinel-1 with its better baselines control and its frequent repeat pass would grant better correlation over areas with patchy, low vegetation. Moreover, the continuous acquisition of Sentinel-1 would increase the temporal window of observation, shedding more light on ongoing instabilities and on changes in creep velocities in time and perhaps even detecting transient and precursory events. The evolution of the observed instabilities could potentially be monitored, allowing for valuable information for hazard assessment purposes but also enhancing the possibility to investigate environmental controls over their distribution.